

AD_____

Award Number: W81XWH-07-1-0228

TITLE: Developing a Zebrafish Model of NF1 for Structure-Function
Analysis and Identification of Modifier Genes

PRINCIPAL INVESTIGATOR: Jonathan A. Epstein, M.D.

CONTRACTING ORGANIZATION: University of Pennsylvania
Philadelphia, PA 19104

REPORT DATE: April 2012

TYPE OF REPORT: Revised Final

PREPARED FOR: U.S. Army Medical Research and Materiel Command
Fort Detrick, Maryland 21702-5012

DISTRIBUTION STATEMENT: Approved for Public Release;
Distribution Unlimited

The views, opinions and/or findings contained in this report are those of the author(s) and should not be construed as an official Department of the Army position, policy or decision unless so designated by other documentation.

REPORT DOCUMENTATION PAGE				<i>Form Approved</i> OMB No. 0704-0188	
Public reporting burden for this collection of information is estimated to average 1 hour per response, including the time for reviewing instructions, searching existing data sources, gathering and maintaining the data needed, and completing and reviewing this collection of information. Send comments regarding this burden estimate or any other aspect of this collection of information, including suggestions for reducing this burden to Department of Defense, Washington Headquarters Services, Directorate for Information Operations and Reports (0704-0188), 1215 Jefferson Davis Highway, Suite 1204, Arlington, VA 22202-4302. Respondents should be aware that notwithstanding any other provision of law, no person shall be subject to any penalty for failing to comply with a collection of information if it does not display a currently valid OMB control number. PLEASE DO NOT RETURN YOUR FORM TO THE ABOVE ADDRESS.					
1. REPORT DATE April 2012		2. REPORT TYPE Revised Final		3. DATES COVERED 1 April 2007 – 31 March 2012	
4. TITLE AND SUBTITLE Developing a Zebrafish Model of NF1 for Structure-Function Analysis and Identification of Modifier Genes				5a. CONTRACT NUMBER	
				5b. GRANT NUMBER W81XWH-07-1-0228	
				5c. PROGRAM ELEMENT NUMBER	
6. AUTHOR(S) Jonathan A. Epstein, M.D. A. Thomas Look, M.D. E-Mail: epsteinj@mail.med.upenn.edu				5d. PROJECT NUMBER	
				5e. TASK NUMBER	
				5f. WORK UNIT NUMBER	
7. PERFORMING ORGANIZATION NAME(S) AND ADDRESS(ES) University of Pennsylvania Philadelphia, PA 19104				8. PERFORMING ORGANIZATION REPORT NUMBER	
9. SPONSORING / MONITORING AGENCY NAME(S) AND ADDRESS(ES) U.S. Army Medical Research and Materiel Command Fort Detrick, Maryland 21702-5012				10. SPONSOR/MONITOR'S ACRONYM(S)	
				11. SPONSOR/MONITOR'S REPORT NUMBER(S)	
12. DISTRIBUTION / AVAILABILITY STATEMENT Approved for Public Release; Distribution Unlimited					
13. SUPPLEMENTARY NOTES					
14. ABSTRACT This final report summarizes the activity of this project which was focused on the identification and characterization of the zebrafish orthologs of the neurofibromatosis type 1 (NF1) gene. This project involved work within the Epstein laboratory and collaboration with the laboratory of Dr. Thomas Look at the Dana Farber Cancer Institute as a sub-contract. This report summarizes the collaborative work including results from both groups. Significant progress was made toward the proposed aims and several publications resulted from the work. The major discoveries included the isolation and characterization of two zebrafish orthologs, nf1a and nf1b. The genes have been sequenced and their expression patterns identified. Gene knockdown phenotypes have been characterized and include overgrowth of glia and cardiovascular abnormalities. Perhaps most critically, independent and compound mutations in these genes have been engineered in zebrafish using zinc finger nucleases producing germ-line transmission of the mutations. Thus, critical reagents and a new animal model of type 1 neurofibromatosis has been produced which is amenable to high throughput drug and genetic screening.					
15. SUBJECT TERMS Zebrafish model of neurofibromatosis, Morpholino knockdown, Engineered zinc fingered nuclease, Tilling, Vascular Patterning, Endocardial Cushion, Glia					
16. SECURITY CLASSIFICATION OF:			17. LIMITATION OF ABSTRACT UU	18. NUMBER OF PAGES 122	19a. NAME OF RESPONSIBLE PERSON USAMRMC
a. REPORT U	b. ABSTRACT U	c. THIS PAGE U			19b. TELEPHONE NUMBER (include area code)

Table of Contents

	<u>Page</u>
Introduction.....	4
Body.....	4
Key Research Accomplishments.....	8
Reportable Outcomes.....	8
Conclusion.....	8
Appendices.....	9
(2011 Accepted Final Report and recent publications)	

Introduction:

This report covers a one year extension of our award. Last year we submitted an extensive report that summarized our findings to date. The scientific portion of that report is appended to this report ("2011 annual scientific report").

As described in previous iterations of this report, the primary goal of this project was to develop a zebrafish model of the autosomal dominant genetic disorder type 1 neurofibromatosis (NF1). This very common disorder affects approximately 1 in 3000 live births and results from mutations in the NF1 gene. Utilizing the awesome power of the zebrafish model system will allow us to further our understanding of the pathophysiology of this disorder. The judicious application of high throughput strategies for screening libraries of chemical compounds will permit us to identify small molecules that may modulate NF1-associated phenotypes. A zebrafish NF1 model will also allow for rapid and costeffective structure-function analysis of neurofibromin, the large protein product of the NF1 gene. Zebrafish offer a number of advantages over other model systems, including rapid development and there optical clarity throughout early development. This permits the easy visualization of many developing tissues, including the cardiovascular and nervous systems. Additionally, the availability of various transgenic reporter lines that express fluorescent proteins under the control of tissue-specific promoters allows for real-time visualization of complex developmental processes. An added benefit of the zebrafish model system is that it is also tenable to forward genetic screens, which will allow for the identification of enhancers and suppressors of NF1 phenotypes in an unbiased fashion. Prior to the efforts funded by this award, the zebrafish orthologues of the human NF1 gene had not been described or characterized. Through a very active and dynamic collaboration between two established laboratories, we have been able to coordinate our collective efforts to develop and subsequently exploit a zebrafish model of this very important genetic disease.

Body of Work:

The Epstein and Look laboratories have continued to collaborate to complete the proposed aims. The past year (a one year extension period) was spent characterizing zebrafish with engineered mutations (induced by zinc-finger nucleases) in the *nf1a* and *nf1b* genes. The extensive phenotypic and molecular characterization of these fish has been submitted for publication to *Disease Models and Mechanisms* and has been accepted. This manuscript, entitled "Zebrafish neurofibromatosis type 1 genes have redundant functions in tumorigenesis and embryonic development" by Shin et al. is appended. Detailed results provide evidence of neural, cardiovascular and melanocyte defects in mutant animals. Thus, we have developed and characterized a new animal model of NF1, which will allow for chemical and genetic screens to find new therapies.

The specific experiments that were conducted during the no cost extension are summarized below.

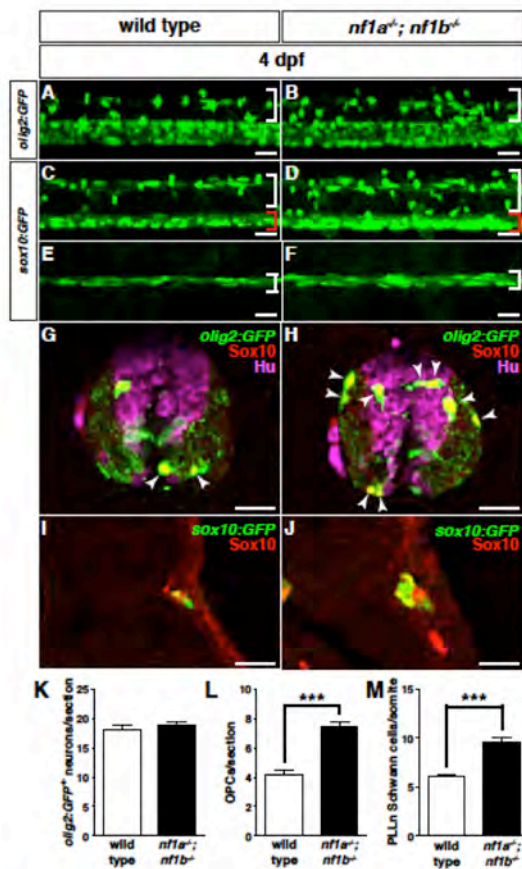


Fig. 1. Loss of *nf1a* and *nf1b* causes hyperplasia of oligodendrocyte progenitor cells (OPCs) and Schwann cells. (A,B) Confocal images of spinal cords in *nf1a*^{-/-}; *nf1b*^{-/-}; Tg(*olig2*:GFP) larvae (B) demonstrate increased numbers of dorsally migrating (white brackets) *olig2*:GFP-positive OPCs when compared with wild type;; Tg(*olig2*:GFP) larvae (A) at 4 dpf. Scale bars: 20 μ m. (C,D) Confocal images of spinal cord in *nf1a*^{-/-}; *nf1b*^{-/-}; Tg(*sox10*:GFP) larvae (D) demonstrate increased numbers of both dorsally (white brackets) and ventrally (red brackets) positioned *sox10*:GFP-positive OPCs when compared with wild type;; Tg(*sox10*:GFP) larvae (C) at 4 dpf. Scale bars: 20 μ m. (E,F) *nf1a*^{-/-}; *nf1b*^{-/-}; Tg(*sox10*:GFP) larvae (F) show an increased number of *sox10*:GFP-positive Schwann cells associated with the peripheral lateral line nerve (PLLn;; white brackets) when compared with wild type;; Tg(*sox10*:GFP) larvae (E) at 4 dpf. Scale bars: 20 μ m. (G,H) Neuronal numbers (*olig2*:GFP- [green], HuC/D- [magenta] positive) do not increase in concert with OPCs (*olig2*:GFP- [green], *Sox10*- [red] positive;; arrowheads) in transverse sections through the spinal cord of *nf1a*^{-/-}; *nf1b*^{-/-}; Tg(*olig2*:GFP) larvae (H) as compared to wild type;; Tg(*olig2*:GFP) larvae (G) at 4 dpf. Scale bars: 20 μ m. (I,J) Increased numbers of PLLn Schwann cells (*sox10*:GFP- [green], *Sox10*- [red] positive) are appreciated in transverse sections of *nf1a*^{-/-}; *nf1b*^{-/-}; Tg(*sox10*:GFP) larvae (J) when compared with wild type;; Tg(*sox10*:GFP) (I) larvae at 4 dpf. Scale bars: 20 μ m. (K,L) Quantification of neurons (*olig2*:GFP-, HuC/D-positive cells) (K) and OPCs (*olig2*:GFP-, *Sox10*- positive cells) (L) from transverse sections through the spinal cord of wild type;; Tg(*olig2*:GFP) and *nf1a*^{-/-}; *nf1b*^{-/-}; Tg(*olig2*:GFP) larvae at 4 dpf. Values indicate mean \pm SEM per section (n=30 from 5 each of wild type and *nf1a*^{-/-}; *nf1b*^{-/-} larvae;; ***P<0.001). (M) Quantification of *sox10*:GFP-positive Schwann cells in the PLLn of wild type;; Tg(*sox10*:GFP) and *nf1a*^{-/-}; *nf1b*^{-/-}; Tg(*sox10*:GFP) larvae at 4 dpf. Values indicate mean \pm SEM per hemisegment (n=5 each for wild type and *nf1a*^{-/-}; *nf1b*^{-/-} larvae;; ***P<0.001).

We previously described oligodendrocyte progenitor cell (OPC) hyperplasia after *nf1a* and *nf1b* morpholino knockdown in the context of a homozygous *p53* mutant background (Lee et al., 2010). To examine *nf1a* and *nf1b* function in OPCs and other tissues beyond the first few days of life, we crossed several cell-type specific zebrafish reporter lines into *nf1a/nf1b* mutant backgrounds generated by zinc-finger mutagenesis. *nf1a*^{-/-}; *nf1b*^{-/-} larvae exhibited increased numbers of OPCs at 4 dpf when compared to controls, as evidenced by an excess of dorsally migrated *olig2*:GFP-positive OPCs (Fig. 1A,B) along with increased numbers of both dorsally and ventrally positioned *sox10*:GFP- positive OPCs (Fig. 1C,D), consistent with our analyses of *nf1* morphants. In addition, we observed an increase in *sox10*:GFP-positive Schwann cells associated with the PLLn (posterior lateral line) (Fig. 1E,F). To determine whether neuronal numbers increased in concert with OPCs in *nf1a/nf1b* mutant larvae, we used anti-HuC/D and anti-SOX10 antibodies to discriminate between *olig2*:GFP-positive neurons and OPCs, respectively. No difference between the number of *olig2*:GFP-, HuC/D-positive neurons was appreciable in 4 dpf spinal cord sections from wild type and *nf1a*^{-/-}; *nf1b*^{-/-} larvae (Fig. 1G,H, green and magenta; Fig. 1K). However, the numbers of *olig2*:GFP-, *Sox10*-positive OPCs (Fig. 1G,H, arrowheads; Fig. 1L) and PLLn Schwann cells (Fig. 1I,J,M) were significantly increased at 4 dpf in *nf1a*^{-/-}; *nf1b*^{-/-} larvae relative to wild type controls. **Taken together, these results (and additional data contained in**

the manuscript) strongly support a defect in gliogenesis in the mutant fish.

Deficits in motor coordination and cognition, including learning and memory, are characteristic of NF1 patients and animal models. To examine motor behavior and cognition in *nf1a*^{-/-}; *nf1b*^{-/-} larvae, we performed kinematic analysis of the short-latency C-start (SLC), a highly stereotyped yet modifiable acoustic startle reflex in the zebrafish that has been previously described by our collaborator, Dr. Granato, at Penn. Briefly, over time, normal fish will learn to react less dramatically (less of a startle response) when exposed to repeated loud sounds. Unlike their siblings, *nf1a*^{-/-}; *nf1b*^{-/-} larvae showed a deficit in short-term SLC habituation when presented with repetitive acoustic stimulation (Fig. 2). Furthermore, *nf1a*^{-/-}; *nf1b*^{-/-} larvae performed kinematically weaker SLC responses, as indicated by decreased head turning angle, maximum angular velocity, and distance traveled following delivery of an acoustic stimulus. **These results suggest a learning and/or memory defect in mutant fish.**

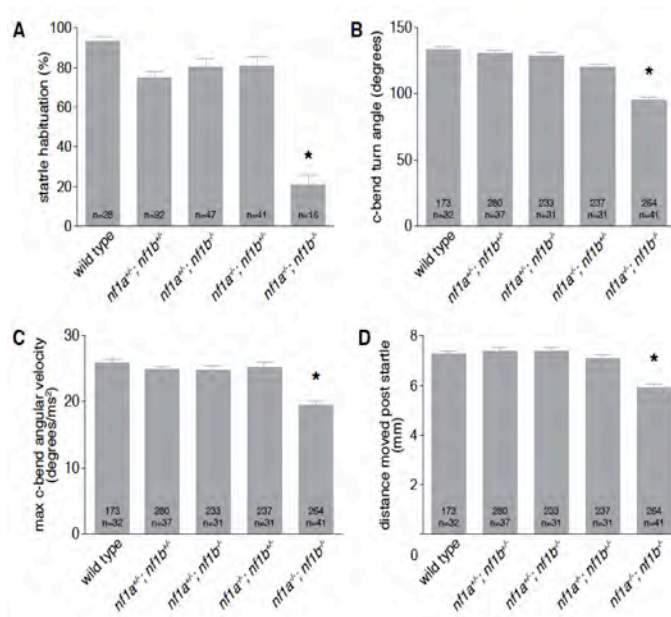


Fig. 2. *nf1a*;*nf1b* mutants exhibit acoustic startle behavioral deficits. (A) Mean degree of short-term SLC habituation is reduced in 5 dpf *nf1a*^{-/-}; *nf1b*^{-/-} larvae. (B-C) Measurement of mean head turning angle (B) and mean maximum angular velocity (C) of initial C-bend following delivery of acoustic stimulus demonstrates a significant reduction of both behavioral measures in 5 dpf *nf1a*^{-/-}; *nf1b*^{-/-} larvae. (D) Mean distance traveled over 90 milliseconds following delivery of acoustic stimulus, as a result of short latency C-start behavioral response, is also significantly reduced in 5 dpf *nf1a*^{-/-}; *nf1b*^{-/-} larvae. The total number of short latency C-bends and number of larvae tested per genotype appear at the base of each bar graph (*P<0.001).

Pigmentation defects are characteristic of human NF1, yet are not evident in mouse models. Interestingly we identified pigmentation defects in mutant fish. Notably, *nf1* null larvae displayed aberrant lateral stripe pigmentation when compared to wild type controls at 6 dpf (Fig. 3A-D). This phenotype was first appreciable at 4 dpf and was manifested as a disruption in the uniform pattern of melanophores arranged along the lateral stripe (Fig. 3B,D, brackets). At 6 dpf, *nf1a*^{-/-}; *nf1b*^{-/-} larvae exhibited a significant reduction in the number of lateral stripe melanophores (Fig. 3E). Less severe, but still significant, decreases were also noted in larvae carrying two or three mutant *nf1* alleles (Fig. 3E). To assess the regeneration and metamorphic lineage of melanophores, we suppressed melanin synthesis after 3 dpf by treatment with N-phenylthiourea (PTU) allowing us to identify newly formed melanophores by their melanin-negative and pale appearance. Removal of PTU at 5 dpf restores melanin synthesis and regeneration and metamorphic melanophores appear melanin-positive by 6 dpf. The abnormal appearance of the lateral stripe in mutant larvae can be attributed to defects in

patterning of regeneration and metamorphic melanophores, suggesting abnormal migration or differentiation of this lineage. **Collectively, these data demonstrate a specific defect in lateral stripe melanophore numbers following *nf1* allele loss, most prominent in the setting of biallelic *nf1a/nf1b* loss.** This finding provides a new and unique animal model in which to study the cause and potential treatment of pigmentation defects in NF1. Taken together, our work has provided a potentially important new animal model of this human disease, which is amenable to high throughput drug screening and to genetic modifier screens in the future. We believe that our detailed characterization of this model, in addition to the creation of the model, will provide an important foundation for the discovery of novel treatment options in the future.

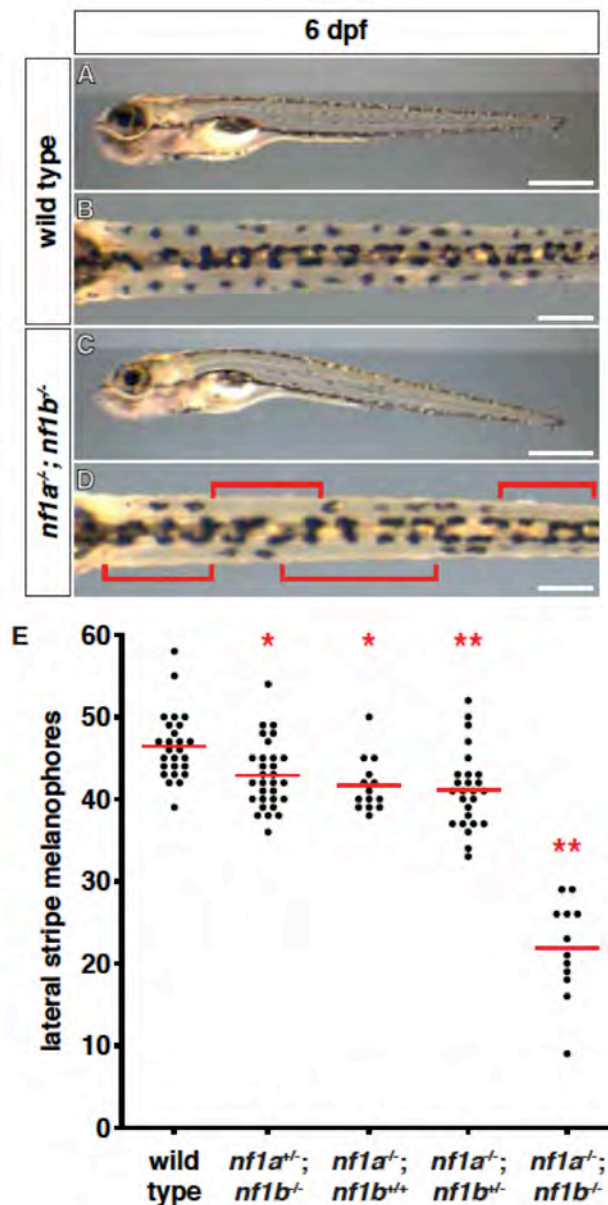


Fig. 3. ***nf1* mutants display decreased lateral stripe melanophores.** (A-D) Lateral stripe melanophores of wild type (A,B) larvae demonstrate a normal uniform pattern that is absent in *nf1a*^{-/-}; *nf1b*^{-/-} larvae (C,D) at 6 dpf. The brackets in (D) highlight regions where melanophores are absent. Scale bars 0.5 mm (A,C); 150 μ m (B,D). (E) Quantification of lateral stripe melanophores from wild type (n=26), *nf1a*^{+/-}; *nf1b*^{-/-} (n=30), *nf1a*^{-/-}; *nf1b*^{+/-} (n=14), *nf1a*^{-/-}; *nf1b*^{+/-} (n=26), and *nf1a*^{-/-}; *nf1b*^{-/-} (n=12) larvae at 6 dpf. Each point represents the number of lateral stripe melanophores in an individual embryo and red lines indicate mean values (*P<0.05; **P<0.01).

Key research accomplishments:

- Characterization of zebrafish orthologs: nf1a and nf1b.
- Additional analysis of gene expression of nf1a and nf1b.
- Additional analysis of morpholino knockdown phenotypes for nf1a and nf1b.
- Generation and validation of zebrafish lines harboring mutations in nf1a and nf1b via TILLING and through the use of engineered Zinc Finger Nucleases.
- Extensive characterization of nf1a/nf1b double homozygous mutant zebrafish embryos.

Reportable outcomes:

The following manuscripts were published as a result of this funding:

1. Lee JS, Padmanabhan A, Shin J, Zhu S, Guo F, Kanki JP, Epstein JA, Look AT. Oligodendrocyte progenitor cell numbers and migration are regulated by the zebrafish orthologs of the NF1 tumor suppressor gene. *Hum Mol Genet.* 2010;19(23):4643-53.
2. Padmanabhan A, Lee JS, Ismat FA, Lu MM, Lawson ND, Kanki JP, Look AT, Epstein JA. Cardiac and vascular functions of the zebrafish orthologues of the type I neurofibromatosis gene NFI. *Proc Natl Acad Sci U S A.* 2009;106(52):22305-10. PMID: 2799742.
3. Zhu C, Smith T, McNulty J, Rayla AL, Lakshmanan A, Siekmann AF, Buffardi M, Meng X, Shin J, Padmanabhan A, Cifuentes D, Giraldez AJ, Look AT, Epstein JA, et al. Evaluation and application of modularly assembled zinc-finger nucleases in zebrafish. *Development.* 2011;138(20):4555-64. PMID: 3177320.

A 4th manuscript has been accepted for publication:

4. Shin J, Padmanabhan A, de Groh ED, Lee J, Haidar S, Dahlberg S, Guo F, Wolman MA, Granato M, Lawson ND, Wolfe SA, Kim S, Solnica-Krezel L, Kanki JP, Ligon KL, Epstein JA, Look AT. Zebrafish neurofibromatosis type 1 genes have redundant functions in tumorigenesis and embryonic development. *Disease Models and Mechanisms*, *In press*.

In addition, multiple abstracts and oral presentations stemming from this work have been presented at various local, national, and international meetings.

Conclusion:

We have created and characterized a zebrafish model for NF1. This model, which displays features reminiscent of the human disease, including a predisposition to tumors, neural defects, cardiovascular abnormalities and melanocyte defects (which have not been noted in other animal models) will provide an important new tool for the identification of potential novel therapeutics.

Award Number: W81XWH-07-1-0228

TITLE: Developing a Zebrafish Model of NF1 for Structure-Function
Analysis and Identification of Modifier Genes

PRINCIPAL INVESTIGATOR: Jonathan A. Epstein, M.D.

CONTRACTING ORGANIZATION: University of Pennsylvania
Philadelphia, PA 19104

REPORT DATE: April 2011

TYPE OF REPORT: Final Report

PREPARED FOR: U.S. Army Medical Research and Materiel Command
Fort Detrick, Maryland 21702-5012

DISTRIBUTION STATEMENT: (Check one)

- Approved for public release; distribution unlimited
- X Distribution limited to U.S. Government agencies only;
report contains proprietary information

The views, opinions and/or findings contained in this report are those of the author(s) and should not be construed as an official Department of the Army position, policy or decision unless so designated by other documentation.

Table of Contents

	<u>Page</u>
Introduction.....	4
Body.....	4
Key Research Accomplishments.....	73
Reportable Outcomes.....	73
Conclusion.....	73

Appendix includes publications derived from funded work.

Introduction:

As described in previous iterations of this report, the primary goal of this project was to develop a zebrafish model of the autosomal dominant genetic disorder type I neurofibromatosis (NF1). This very common disorder affects approximately 1 in 3000 live births and results from mutations in the *NF1* gene. Utilizing the awesome power of the zebrafish model system will allow us to further our understanding of the pathophysiology of this disorder. The judicious application of high throughput strategies for screening libraries of chemical compounds will permit us to identify small molecules that may modulate NF1-associated phenotypes. A zebrafish NF1 model will also allow for rapid and cost-effective structure-function analysis of neurofibromin, the large protein product of the *NF1* gene. Zebrafish offer a number of advantages over other model systems, including rapid development and their optical clarity throughout early development. This permits the easy visualization of many developing tissues, including the cardiovascular and nervous systems. Additionally, the availability of various transgenic reporter lines that express fluorescent proteins under the control of tissue-specific promoters allows for real-time visualization of complex developmental processes. An added benefit of the zebrafish model system is that it is also tenable to forward genetic screens, which will allow for the identification of enhancers and suppressors of NF1 phenotypes in an unbiased fashion. Prior to the efforts funded by this award, the zebrafish orthologues of the human *NF1* gene had not been described or characterized. Through a very active and dynamic collaboration between two established laboratories, we have been able to coordinate our collective efforts to develop and subsequently exploit a zebrafish model of this very important genetic disease.

Body of work:

Through the coordinated efforts of the Epstein and Look laboratories, we have accomplished or made significant inroads towards the major objectives of this award. Below, we outline our progress since the inception of this award reiterating important aspects described in previous annual reports and expanding on those data where relevant as well as describing new and ongoing efforts underway in both the Epstein and Look laboratories.

Identification of *nfla* and *nflb*

We utilized a bioinformatics approach to identify the zebrafish orthologues of human *NF1*. Analysis of the eighth assembly (Zv8) of the zebrafish genome revealed two genes highly similar to *NF1* at the amino acid level (90.4% and 90.7% respectively), which we named *nfla* and *nflb*. These genes are highly related to one another (87.4% identical and 93.7% similar) with *nfla* and *nflb* sharing similar genomic structures and each containing 57 exons (Figure 1A-B). *nfla* is located on chromosome 15 (Figure 1A) and predicts a 311 kD protein composed of 2755 amino acids while *nflb* is located on chromosome 10 (Figure 1B) and predicts a 310 kD protein composed of 2747 amino acids.

Comparison to *Drosophila*, murine, and human neurofibromin protein sequences reveals significant conservation in the GAP and IRA homology domains and also in extensive areas flanking these regions, suggesting additional functional motifs that have been conserved across evolution (Figure 2). A phylogenetic tree (Figure 1C) demonstrates a tight clustering of the zebrafish neurofibromin orthologues with other mammalian neurofibromins and a divergence from the *Drosophila* neurofibromin orthologue. Human/zebrafish synteny maps and bioinformatics analyses suggest that *nfla* and *nflb* likely arose via gene duplication (Figure 1D). Upstream of the human *NF1* gene on chromosome 17 are genes encoding WD repeat and SOCS box-containing 1 (*WSB1*), Kinase suppressor of ras 1 (*KSR1*), and Galectin-9 (*LGALS9*) while A kinase anchor protein 1 (*AKAP1*) and RNA-binding protein Musashi homolog 2 (*MSI2*) both lie downstream of *NF1*. Similar genes flank *nfla*, while *nflb* is flanked only by

orthologues of *KSRI* and *MSI2*. The identification of duplicated genes is common in zebrafish and reflects the well-described chromosomal doubling event occurring early in teleost evolution.

The GenBank EST database identified expressed sequence tags for both zebrafish *nf1* genes in many tissues including the heart (Figure 3A) suggesting that neither gene is likely to be a pseudogene and that they are expressed in overlapping tissues. We examined the expression of both genes by whole mount *in situ* hybridization between the 4-cell stage and 4 days post fertilization (dpf) and found that both genes are expressed ubiquitously during early development with later restriction to regions of the head and anterior central nervous system (Figure 4A1-7, B1-7, Figure 3C1-C7, D1-D7). Notably, at 48 hours post fertilization (hpf) and 3 dpf both genes are expressed in the heart (Figure 4A4, B4, A6, B6, Figure 3C5-6, D5-6) and in the dorsal vessel (Figure 4A3, B3, A5, B5, Figure 3C7, D7). Reverse transcription and polymerase chain reaction (RT-PCR) using RNA from wild type 24, 72, and 84 hpf whole embryos or 3 dpf *Tg(kdrl:GRCFP)zn1* GFP-positive sorted cells confirmed expression, particularly in the vascular endothelium (Figure 3E-G), while RNAs from 1-cell embryos indicated that both genes are expressed maternally (Figure 3B). Queries of an expression database generated from sorted endothelial cells from *Tg(fli1:egfp)y1* zebrafish identified *nf1a* and *nf1b* in both GFP+ and GFP- cell populations, consistent with the expression of these genes in vascular endothelium.

Morpholino knockdown of *nf1a* and *nf1b*

We employed morpholino antisense oligonucleotides (MOs) to inhibit expression of *nf1a* and *nf1b* at early stages of development. Effectiveness of gene knockdown by translation blocking MO was confirmed by Western blot analysis (Figure 5A). The ability of neurofibromin to function as a ras-GAP, thereby down-regulating levels of active GTP-bound ras, can result in decreased phosphorylation of downstream effectors including Erk/MAPK. Western blots of 3.5 dpf whole embryo extracts derived from *nf1a*, *nf1b*, or *nf1a/nf1b* morphants revealed a marked up-regulation of phospho-Erk in knockdown tissue, while levels of total Erk were unchanged (Figure 5B). Efficacy of splice blocking MOs was assessed by RT- and quantitative PCR using RNA collected from 24 hpf embryos (Figure 5C-G).

Morpholino knockdown of *nf1a* and *nf1b* results in cardiovascular defects

nf1a and *nf1b* morphant embryos displayed gross abnormalities of cardiovascular development appreciable to the blinded observer by 48 hpf. Frequently, blood was seen to move back and forth from atrium to ventricle in morphants, suggesting a malfunctioning atrioventricular valve. At the resolution afforded to us by histological analysis, we observed no readily apparent structural defects in the atrioventricular valves of morphants despite the observed functional deficits (Figure 6). In addition, we observed pooling of blood in the common cardinal vein and a paucity of blood flow along the dorsal aorta and posterior cardinal vein. Valvular insufficiency and reduced blood flow were not seen in control morphants or wild type embryos. Despite these cardiac defects, overall development of the embryos was relatively preserved through the first 3 days. Histological analysis revealed a thinned ventricular myocardium and large pericardial effusions in MO-treated embryos (Figure 7K-L, Figure 8A-B, F-G). Immunohistochemical analysis of 3.5 dpf *nf1a*, *nf1b*, and *nf1a/nf1b* morphant zebrafish also revealed increases in phospho-Erk staining (Figure 7M-N, Figure 8C-E, H-K). Gross morphological analysis showed an increased incidence of pericardial effusions beginning at 48 hpf, reflecting cardiac dysfunction, in *nf1a* and *nf1b* morphants when compared with controls (Figure 7A-G, Figure 8L-M). Non-specific toxicity arising from MO exposure as a cause of the observed cardiovascular defects was unlikely as unrelated control or scrambled MOs failed to produce similar levels of abnormalities, defects were observed even at low doses of specific MOs, and similar defects were observed with several unrelated but specific MOs directed against *nf1a* and *nf1b*. In addition,

injection of specific MOs in *p53* mutant embryos also produced similar cardiovascular defects (Figure 7H-J), and off-target effects due to MO exposure are known to be partially mediated through *p53* activation. Defects in cardiac valve morphogenesis and a thinning of the ventricular myocardium are also seen in *Nf1*^{-/-} murine embryos.

We performed knockdown experiments using zebrafish embryos in which endothelial cells are marked by expression of a cytoplasmic enhanced green fluorescent protein (GFP) in order to allow for a more detailed analysis of vascular development. Dramatic abnormalities of vascular patterning in the intersomitic vessels of morphant embryos were seen at 48 and 72 hpf (Figure 9). In *nf1a* MO-treated embryos, the leading edge of the sprouting vessels displayed claw-like projections at 48 hpf (Figure 9C) and failed to pattern normally such that the dorsal longitudinal anastomotic vessel (DLAV) either did not form, or developed in a rudimentary fashion (Figure 9F). This occurred in embryos that were otherwise normal in overall size and maturity. These defects were also noted in *nf1a/nf1b* compound morphants, and were present but less severe in *nf1b* morphants. Vascular patterning defects did not appear to correlate directly with cardiac defects, as we observed embryos with vascular abnormalities that did not display pericardial effusion or valvular insufficiency as assessed by a “to-and-fro” movement of blood within the heart. In embryos with isolated vascular abnormalities, blood flow within the dorsal aorta and posterior cardinal vein appeared intact.

At 24 hpf, analysis using zebrafish embryos expressing a nuclear-localized GFP in endothelial cells indicated that morphants displayed a complete (Figure 10A4) or partial absence of intersomitic vessels emanating from the dorsal aorta when compared with stage-matched controls (Figure 10A3). Overall morphology of morphant and control embryos appeared equivalent (Figure 10A1-2) ruling out non-specific developmental delay. These defects were apparent following MO-mediated knockdown of *nf1a* or *nf1b* while knockdown of both together had an additive effect (Figure 10B). The small percentage of embryos with defects produced by the 5MP MO may have been due to low-level knockdown of *nf1a*. Again, similar defects were observed with several unrelated but specific MOs directed against *nf1a* and *nf1b* (Figure 11A). Our analysis of morphant embryos at 24 hpf also revealed a caudal vessel defect. Morphant embryos displayed a cystic expansion in the region of the caudal vein and exhibited inappropriate anastomoses between the caudal vein and artery (Figure 11D2-D4) when compared with controls (Figure 11D1). Identity of the expanded tissue as vascular was confirmed by expression of GFP (Figure 11D6-D8) and the observation of a pooling of red blood cells in the expanded region. This defect was present following knockdown of *nf1a*, *nf1b*, or both together (Figure 11C-D).

Additional confirmation of the role of *nf1a/nf1b* in vascular development derives from studies using a genetic background sensitized to vascular insult. Previous studies employed MOs directed against *flt4*, the zebrafish VEGF receptor-3 orthologue, to investigate genetic interactions during zebrafish artery development. *flt4* morphant zebrafish embryos display variable defects in segmental artery formation reminiscent of those identified in our *nf1a/nf1b* morphants. Endothelial-GFP expressing zebrafish embryos were injected with *flt4* MO alone and in combination with a MO directed against *nf1a*, *nf1b*, or a combination of both. At low MO doses, 85% of *flt4/nf1a*, 24% of *flt4/nf1b*, and 36% of *flt4/nf1a + nf1b* compound morphants, displayed abnormal vascular shunts at 48 hpf compared to only 3-8% of individual *flt4*, *nf1a*, or *nf1b* morphants (Figure 10C, Figure 11B). This defect was not apparent in control morphants. The shunts occur between the dorsal aorta and the dorsal longitudinal anastomotic vessel with retrograde flow through segmental arteries back into the dorsal aorta or through intersegmental veins into the posterior cardinal vein. In some cases, there were interruptions of the dorsal aorta.

Human *NF1* GRD RNA does not rescue abnormal vascular shunts in *flt4/nf1a* compound morphants

Given neurofibromin's role as a negative regulator of ras, it stands to reason that phenotypes arising from transient knockdown of the orthologous zebrafish proteins may well be downstream of supraphysiological levels of activated ras. Combining MO treatment with an RNA species encoding the isolated GAP activity of neurofibromin can directly test this hypothesis. Indeed, such an RNA rescue would additionally serve as the most stringent assay to demonstrate MO specificity in the elaboration of these phenotypes. Given the size of the *nf1a*, *nf1b*, and human *NF1* transcripts, performing a similar rescue experiment using full-length mRNAs poses a significant technical hurdle given the size limitations associated with *in vitro* transcription reactions. The approximately 1 kb transcript encoding the human neurofibromin GRD, however, is not subject to these restraints. Endothelial-GFP expressing zebrafish embryos were injected with human *NF1* GRD RNA tagged with an N-terminal monomeric Cherry red fluorescent protein (mcRed) alone or with a combination of *flt4* and *nf1a* MOs and were screened for vascular shunts at 48 hpf. This phenotype is particularly amenable to this type of analysis as it is highly penetrant and readily scored by simple microscopic observation. Administration of *flt4* and *nf1a* MOs was associated with the development of abnormal vascular shunts in 61% of injected embryos as compared to 46% of embryos in which mcRed-GRD RNA was added ($p < 0.08$; NS) (Figure 12). These results suggest that forced expression of the human *NF1* GRD, at the levels used in these experiments, does not rescue the vascular shunt phenotype induced by concomitant administration of MOs directed against *nf1a* and *flt4*. This, however, does not rule out the possibility that these defects are secondary to increased ras signaling.

Vascular patterning defects in mouse embryos lacking *Nf1*

Although cardiac defects have been reported in mouse embryos lacking *Nf1*, a phenotype that has been attributed to a role for neurofibromin in endothelium, abnormalities in vascular patterning have not been previously identified. *Nf1*^{-/-} mice succumb during mid-gestation and exhibit significant peripheral hemorrhage that has been hypothesized to be secondary to the intracardiac defects, although similar hemorrhage is not a common feature of mouse embryos with congenital heart disease. In light of our observation of peripheral vascular patterning defects in *nf1* morphant zebrafish embryos, we reevaluated murine *Nf1* knockouts by whole mount platelet/endothelial cell adhesion molecule-1 (*PECAM-1*) staining to visualize endothelium at E10.5-E11.5, time points prior to the development of overt cardiac failure or significant endocardial cushion defects. Although no overt differences were appreciated in E11.5 yolk sacs (Figure 13), we identified vascular abnormalities in embryos including an increase in overall vascularity and a failure of the primitive vascular plexuses in the somitic region and head to remodel as seen in wild type embryos (Figure 14). These findings suggest that peripheral hemorrhage commonly noted on *Nf1*^{-/-} mouse embryos may be related to an intrinsic vascular defect similar to that identified in MO knockdown zebrafish.

MO knockdown of the *nf1a* and *nf1b* results in neural defects

We observed a marked increase in the intensity and domain of expression of glial fibrillary acidic protein (*GFAP*), a marker of Schwann and glial cells, by whole mount *in situ* hybridization in *nf1a/nf1b* compound morphants (Figure 15). This result is consistent with the increase in neural crest-derived tissue in *Nf1*^{-/-} mice and the presence of neural crest-derived tumors in NF1 patients. We also examined the expression of *myelin basic protein (mbp)*, *sex-determining region Y-box 10 (sox10)*, *forkhead box d3 (foxd3)*, and *crestin* but did not observe changes. Therefore, the alterations observed in

nf1a and *nf1b* morphant embryos appear to be restricted to the Schwann-glia lineages in the neural compartment.

The number of OPCs is increased upon *nf1a/nf1b* knockdown

NF1 patients often have symptoms that may be related to glial abnormalities such as macrocephaly, and they are prone to develop glia-derived cancers including optic pathway glioma and astrocytoma. To complement the expression data presented in Chapter 2, we verified that *nf1a* and *nf1b* are expressed in oligodendrocyte precursor cells by performing RT-PCR for these transcripts using RNA prepared from sorted cells of 3 dpf *Tg(olig2:EGFP)* zebrafish embryos (Figure 16). In this transgenic zebrafish line, oligodendrocyte precursor cells are marked throughout oligodendrocyte development by expression of an enhanced green fluorescent protein (GFP). *nf1a* and *nf1b* transcripts are expressed in both the GFP-positive and GFP-negative cell populations. In order to test the roles of *nf1a* and *nf1b* in zebrafish oligodendrocyte development, we again used morpholinos (MOs) to knockdown the expression of each gene or both together in this transgenic line. These transgenic zebrafish were bred into both wild type and *p53* mutant backgrounds. We again utilized a *p53* mutant background to circumvent any off-target effects arising from MO toxicity (Figure 17). In addition to the *nf1a*-SBe1 and *nf1b*-SBe4 MOs described in Chapter 2, we designed and injected a third MO directed against the splice donor region of *nf1a* exon 7 (*nf1a*-SBe7 MO). The efficacy of this MO was confirmed by RT-PCR at 3 dpf, where the observed aberrant bands demonstrate inappropriate splicing due to MO knockdown (Figure 18). Because *nf1a*-SBe7 MO injection led to several aberrant bands, likely due to multiple cryptic splice donor sites within exon 7 of *nf1a*, the knockdown of *nf1a* could not be evaluated by quantitative PCR. However, cloning and sequencing of these aberrant bands identified deletions of exon 7 or insertions of additional intronic sequence that resulted in frame shifts in the coding sequence that would generate truncated peptides.

In oligodendrocyte precursor cell-GFP expressing zebrafish, a subset of GFP-positive OPCs that arise in the ventral spinal cord migrate dorsally and differentiate into oligodendrocytes (brackets in Figure 19A-C), while another GFP-positive OPC subpopulation remains in the ventral spinal cord, intermingled with GFP-positive motoneurons and interneurons (Figure 19A-C). These GFP-positive motoneurons and interneurons labeled by the *olig2:EGFP* transgene can often be distinguished from OPCs because of their lower level of *EGFP* expression, relatively round shape devoid of processes, and their failure to migrate dorsally. When *nf1a* and *nf1b* were knocked down by MOs, we consistently found an increased number of dorsally positioned OPCs at 3 dpf (Figure 19A-C). Similar results were appreciated using multiple MOs directed against *nf1a* and *nf1b* (Figure 20). The most dramatic OPC increase relative to the control was observed when both the *nf1a* and *nf1b* genes were knocked down simultaneously in the *p53* mutant background (Figure 19C), although significant increases in OPC numbers were also observed in embryos with knockdown of *nf1a* or *nf1b* alone (Figure 19M, Figure 20). These results indicate that both *nf1a* and *nf1b* contribute to the regulation of normal OPC numbers, and that knockdown of these genes results in an increased number of dorsally positioned OPCs.

We then extended our analysis to include ventrally positioned OPCs by co-immunostaining with an anti-sox10 antibody that labels OPCs, but not the motoneurons or interneurons, located in the ventral spinal cord at this stage. Although an increase in *olig2:EGFP*-positive; sox10-positive OPCs was not apparent upon *nf1a/nf1b* knockdown at 2 dpf (Figure 21), transverse sections of the spinal cord at 3 dpf revealed increased numbers of OPCs (Figure 19J-L, compared to Figure 3.5D-F and Figure 3.5I G-I). The mean number of OPCs was determined for *nf1a/nf1b* compound morphants and control embryos by counting these double-positive cells in immunostained transverse sections. The *nf1a/nf1b* morphants were found to have 36% more OPCs than control *p53* mutant embryos (9.0 vs. 6.6, n=23 and 26,

respectively, $p < 0.0001$; Figure 19M). These findings indicate that *nf1a* and *nf1b* negatively regulate OPC number during development.

The observed increase in OPCs in *nf1a/nf1b* compound morphants could be due to aberrant dorsal migration of OPCs that normally remain in the ventral spinal cord or could result from an overall increase in OPC number throughout the spinal cord. To distinguish between these possibilities, we assessed the differences in OPC numbers in dorsal and ventral spinal cord regions. A 36% increase in dorsally migrating OPCs (4.0 vs. 2.9; $n=11$; $p < 0.05$) and a 26% increase in ventrally localized OPCs (4.6 vs. 3.7; $n=11$; $p < 0.05$) was observed in *nf1a/nf1b* morphants when compared with control morphants in the *p53* mutant background. These results indicate that increases in OPC numbers occur in both locations rather than reflecting an aberrant displacement of ventral cells to more dorsal regions. A slight increase in OPC numbers was appreciated in the *p53* mutant background, presumably due to the survival of cells that would otherwise succumb to MO toxicity. However, it is important to note that significant increases in OPCs in *nf1a/nf1b* morphants were observed in the wild-type background as well (Figure 19M; Figure 20).

To further document the increase in OPC numbers in *nf1a/nf1b* compound morphants, we employed a second approach to block the apoptosis and early cell death evident in wild type embryos upon simultaneous knockdown of *nf1a* and *nf1b*. While our first approach utilized a *p53* mutant background, this approach involved co-injecting *in vitro* transcribed zebrafish *bcl-X_L* RNA, which is known to block most cell death during early embryogenesis. The majority of the *bcl-X_L* RNA/*nf1a*-SBe7 MO/*nf1b*-SBe4 MO injected embryos (>90%) did not exhibit cell death in the brain at 1 dpf (Figure 22), and developed relatively normally to 3 dpf. The numbers of OPCs in these *Tg(olig2:EGFP)* embryos was significantly increased compared to those in embryos co-injected with *bcl-X_L* RNA and the control MO (63.3 vs. 52.9, $p < 0.05$; Figure 22E-G).

MO-mediated loss of *nf1a* and *nf1b* did not appear to affect differentiation of OPCs into oligodendrocytes, as no significant difference in the number of myelin basic protein-positive oligodendrocytes in the dorsal spinal cord at 3 dpf was apparent between control and *nf1a/nf1b* double morphants as assessed by whole mount *in situ* hybridization (Figure 23). This finding suggests that the extra OPCs fail to differentiate during the 3-day time period shown in Figure 23. Given that the effectiveness of MOs is diluted over time, a more thorough analysis at time points beyond 3 dpf will require the creation of stable *nf1a/nf1b* mutant lines.

***nf1a/nf1b* loss specifically affects OPCs from the pMN of the ventral spinal cord**

Since OPCs and motoneurons are derived from common precursors in the *olig2:EGFP*-positive pMN domain of the ventral spinal cord during development, we examined whether *nf1a/nf1b* deficiency might affect the development of motoneurons and contribute to the increased numbers of OPCs. Islet protein (Isl) is expressed in primary and secondary motoneurons, interneurons, and sensory neurons of the spinal cord, and zn5 is a marker specific for developing secondary motoneurons. Quantitation of cell numbers using anti-Isl and zn5 antibodies did not reveal significant differences in the number of cells expressing either of these markers in *nf1a/nf1b* compound morphant embryos compared to controls at 80 hpf (Figure 24F compared with 3.10B; 3.10N compared with 3.10J; 3.10Q compared with 3.10R, $n=15$). Additionally, *nf1a/nf1b* loss did not affect the overall size or shape of developing secondary motoneurons (Figure 24N compared with 3.10J). These results suggest that *nf1a/nf1b* knockdown acts specifically on cells of the oligodendrocyte lineage, while the neuronal lineages from the pMN domain, such as motoneurons, remain unaffected.

Loss of *nf1a/nf1b* causes an increase in OPC proliferation

We identified no difference in the number of TUNEL-positive OPCs in the spinal cord of control-MO injected *p53* mutant *Tg(olig2:EGFP)* zebrafish embryos when compared with *nf1a*-SBe7 + *nf1b*-SBe4 compound morphants. In fact, TUNEL-positive OPCs were extremely rare in embryos injected with either control or experimental MOs with only 2-4 cells identified in over 40 sections. This suggests that the observed increase in OPCs following *nf1a/nf1b* knockdown does not occur as a result of reduced apoptosis.

To assess for increased proliferation of OPCs, we pulse-labeled control MO- and *nf1a*-SBe7 + *nf1b*-SBe4 MO-injected embryos with BrdU at 54 hpf and 80 hpf, fixed them immediately, and examined BrdU incorporation in GFP/sox10 double-positive OPCs. At 80hpf, BrdU-positive cells were much more abundant in sections of the spinal cord (>40% of total sections) and BrdU-positive OPCs could be identified in both control morphants as well as *nf1a*-SBe7 + *nf1b*-SBe4 compound morphants. Importantly, when GFP/sox10/BrdU triple-positive cells were counted, the numbers of BrdU-labeled and total OPCs in *nf1a/nf1b* morphants was significantly higher when compared to controls (1.08 compared to 1.83 per section, n=12, p<0.005; Figure 25). These results indicate that *nf1a/nf1b*-deficient OPCs proliferate at a greater rate, thus accounting for the observed increase in OPC numbers. In contrast, at 54 hpf, when OPC numbers are not yet affected by *nf1a/nf1b* loss (Figure 21), GFP/sox10/BrdU triple-positive cells in the spinal cord of both control and *nf1a/nf1b* compound morphant embryos were very rare and no significant differences were appreciated between these groups (1/60 sections of control and 4/43 sections of *nf1a*-SBe7 + *nf1b*-SBe4 morphants, p>0.05; Figure 26).

The increase in OPCs that we observe upon *nf1a/nf1b* knockdown may also result from an expansion of OPC progenitor cells. Newly forming OPCs in the adult and juvenile spinal cord are thought to arise from a population of slowly dividing *olig2:EGFP*-positive radial glial cells. Thus, increased proliferation or transdifferentiation of these radial glial cells into OPCs is a possible mechanism that could contribute to our observed phenotype. We assessed the number of these radial glial cells, which are *olig2:EGFP* and GFAP double-positive, in control morphants and *nf1a*-SBe7 + *nf1b*-SBe4 compound morphants and observed no significant difference between these groups (1.17 vs. 1.11, n=18, p>0.7, Figure 27). We also detected no change in the number of proliferating radial glial cells (*olig2:EGFP*/GFAP/BrdU triple-positive cells) in the spinal cord at 54 and 80 hpf upon *nf1a/nf1b* knockdown when compared with controls (3 BrdU-positive radial glial cells in 109 sections in control morphants and 1 BrdU-positive radial glial cell in 138 sections for *nf1a/nf1b* compound morphants at 80 hpf, p>0.3; Figure 27G-N). Taken together, these data suggest that *nf1a/nf1b* loss leads to increased proliferation of OPCs, following their appropriate specification, between 54 and 80 hpf.

nf1a/nf1b* regulation of OPC number relies on the GRD of *NF1

The best-known function of human *NF1* is as a negative regulator of ras signaling, an activity encoded by its gap-related domain (GRD). To test whether the increased proliferation of OPCs observed in *nf1a/nf1b* morphants was dependent upon the GAP activity of these proteins, we co-injected mRNA encoding the human *NF1* GRD into *nf1a*-SBe7 + *nf1b*-SBe4 compound morphant embryos (*p53* mutant; *Tg(olig2:EGFP)*) and assessed OPC number in the dorsal spinal cord. Expression of the isolated *NF1* GRD was verified by fusion of an in-frame N-terminal monomeric Cherry red fluorescent (mcRed) protein. Embryos injected with monomeric Cherry red fluorescent (mcRed) in combination with *nf1a*-SBe7 + *nf1b*-SBe4 MOs served as a positive control, displaying the expected increase in OPC cell number when compared with controls (Figure 28B-D). Importantly, *nf1a/nf1b* morphant embryos injected with *NF1* GRD RNA exhibited a reduction in dorsal spinal cord OPCs (from 67.7 per embryo to 48.5 per embryo, n=10, p<0.001; Figure 28A, B, E). This did not differ significantly from the number of OPCs present in control MO- and control RNA- injected embryos (48.5 as compared with 47.5, p>0.7

and 48.5 as compared with 57.5, $p > 0.1$, respectively; Figure 28A, C-E). These results demonstrate that the isolated GRD of human *NF1* is sufficient to rescue the increase in OPCs that results from transient knockdown of *nf1a/nf1b*, indicating that the zebrafish neurofibromin orthologues regulate OPC proliferation through their GAP activity.

***nf1a/nf1b* loss promotes OPC migration**

Zebrafish offer a distinct advantage over many other model organisms in that embryos develop outside the mother's body and are optically clear, allowing for direct observation of developmental events. Coupled with availability of transgenic lines that mark specific cell types with the expression of fluorescent proteins, complex biological processes can be visualized and quantitatively assessed *in vivo* in zebrafish. We utilized these unique features to examine the behavior of OPCs following *nf1a/nf1b* knockdown by live *in vivo* time-lapse imaging. In these experiments, we monitored *olig2:EGFP* transgene-expressing animals for a period of 12 hours beginning at 60 hpf, when OPCs start to actively migrate away from the ventral spinal cord. Compared with uninjected control animals, *nf1a/nf1b* compound morphants displayed an increase in the number of OPCs migrating into the dorsal spinal cord (Figure 29A, B). These findings are consistent with our observations from fixed sections (Figure 19). Interestingly, the time-lapse study also revealed that *nf1a*-SBe7 + *nf1b*-SBe4 morphant OPCs traveled longer distances, both in the dorsal and rostrocaudal directions, relative to control animals (Figure 29E). Representative migratory traces of individual cells are outlined in Figure 29C, D. A comprehensive analysis of all individual moving OPCs observed over the 12-hour imaging period revealed a 35% increase in total distance traveled by the OPCs in *nf1a/nf1b* knockdown animals (32.05 μm in control as compared with 43.27 μm in *nf1a/nf1b* morphants, $p < 0.05$; $n = 9$ and $n = 23$, respectively; Figure 29E). In all cases, the OPCs display repeated cycles of intermittent movements consisting of active migration separated by pauses before continuing, often in directions different from the original path. After *nf1a/nf1b* knockdown, the OPCs paused for shorter periods of time relative to controls (413.9 min in control as compared with 324.3 min in *nf1a/nf1b* morphants; $p < 0.005$; Figure 29F), with no significant difference in the frequency of the pauses (2.28 per hour in control as compared with 2.58 per hour in *nf1a/nf1b* morphants; $p > 0.1$). Furthermore, the migration velocity of OPCs, determined by dividing the distance traveled by the total traveling time (which excluded the periods when they were stationary), was also found to be unaffected by *nf1a/nf1b* knockdown (0.5203 $\mu\text{m}/5\text{min}$ in control as compared with 0.5343 $\mu\text{m}/5\text{min}$ in *nf1a/nf1b* morphants; $p > 0.7$; Figure 29G). Together, these findings demonstrate that OPCs in *nf1a/nf1b* morphants spend more time actively migrating with shorter pauses when compared with controls, a novel *in vivo* phenotype made accessible by our use of the zebrafish model system.

***nf1a/nf1b* loss leads to the hyperactive ERK signaling in the spinal cord**

Given the role of *NF1* in negative regulation of ras signaling, we investigated two principal pathways downstream of activated ras by evaluating the status of phosphorylated ERK (pERK) and phosphorylated S6 (pS6) to assess the Raf/ERK and PI3K/Akt/mTOR pathways, respectively. Labeling transverse sections of the spinal cord in *p53* mutant *Tg(olig2:EGFP)* embryos at 54 hpf with a pERK antibody revealed few pERK-positive cells in controls or *nf1a/nf1b* morphants, suggesting low ERK signaling in the spinal cord at this stage that is unresponsive to *nf1a/nf1b* loss (Figure 30). However, at 80 hpf, *nf1a/nf1b* knockdown resulted in a marked increase in the number of pERK-positive cells throughout the spinal cord of *p53* mutant *Tg(olig2:EGFP)* embryos relative to controls; this indicates aberrant ras activation resulting from *nf1a/nf1b* deficiency (Figure 31). Interestingly, we did not identify pERK as being elevated in OPCs (arrows in Figure 31A-H), but rather in neighboring neurons, which were identified by the co-expression of HuC/D, a pan-neuronal marker (arrows in Figure 32). There was

a small subpopulation of OPCs that were weakly pERK-positive in both control and *nf1a/nf1b* morphants (asterisks in Figure 31A-H); however, no significant change in pERK levels in this cell population were detected upon *nf1a/nf1b* loss. No significant differences in the levels of pS6 were appreciated in any cell type in the spinal cord at 3dpf in *nf1a*-SBe7 + *nf1b*-SBe4 morphants as compared with controls (Figure 33). Thus, *nf1a/nf1b* deficiency causes aberrant activation of the ERK signaling pathway in spinal cord neurons, coincident with the hyperproliferation and abnormal migration of OPCs.

TILLING for mutations in *nf1a* and *nf1b*

An important aspect of our proposal requires the generation of stable zebrafish lines harboring mutations in *nf1a* and *nf1b*. We will use these animals to verify the data we collected from our morpholino studies as well as to extend our analysis to time points beyond those accessible using transient knockdown assays. Towards this end, we have utilized multiple approaches to generate zebrafish harboring germline mutations in *nf1a* and *nf1b*.

TILLING is a target-selected mutagenesis strategy and relies on the detection of heterozygous mutations directly in the genomic DNA of individuals from a mutagenized population. An overview of the TILLING procedures that followed is outlined in Figure 35 and Figure 36. As in forward mutagenesis, male zebrafish are treated with *N*-ethyl-*N*-nitrosurea (ENU), inducing base pair substitutions in pre-meiotic germ cells. These animals are subsequently outcrossed to wild type females to generate a large population of F₁ animals harboring random heterozygous mutations in their genomes. Genomic DNA is isolated from these animals and subjected to a screening methodology that will identify mutations in a specific gene of interest. Given the challenges associated with maintaining a large “live library” of F₁ animals, these animal may be sacrificed if sperm is also extracted from these animals and cryopreserved to generate matching libraries of genomic DNA and sperm that can be used to respectively screen for mutations and recover mutant lines through *in vitro* fertilization. The success of this strategy is highly dependent upon not only the efficiency of mutagenesis but also the number of individuals screened. Therefore, a robust and high-throughput means of screening genomic DNA from individually mutagenized F₁ males is tightly coupled with the successful application of this technique.

We began by screening samples from a genomic DNA/cryopreserved sperm library of approximately 10,000 ENU mutagenized F₁ animals, generated by the combined efforts of the laboratories of Thomas Look at the Dana-Farber Cancer Institute and Cecilia Moens at the Fred Hutchinson Cancer Research Center, for mutations in *nf1a* using a direct sequencing method. The zebrafish *nf1a* gene spans a genomic region of approximately 120 kilobases and contains 57 exons encoding a 2755 amino acid protein. The very large size of this gene, coupled with the number of samples in our library and the costs associated with sequencing an individual sample, precluded our screening the entire coding sequence for mutations. In light of these practical considerations, we established screening criteria which required that our PCR amplicons contained portions of *nf1a* coding sequences of appropriate size such that they could be sequenced in their entirety by a single dye terminator Sanger sequencing reaction.

Another important consideration in the development of our screening strategy was the nature of the mutations induced by the ENU mutagen that the animals comprising this library were subjected to. ENU alkylates DNA leading to point mutations being randomly distributed throughout the genome. These single base pair substitutions may be synonymous mutations or, in the context of our present purpose, the more desirable missense and nonsense changes. When considering the probabilities associated with the possible outcomes of point mutations in a particular coding sequence of DNA, missense mutations would be predicted to occur at a greater frequency than nonsense mutations. Therefore, by focusing on sequences in *nf1a* that encode known functional domains of the protein, we

maximize the likelihood that a missense mutation will result in a null allele. In our initial screening strategy, we amplified a 574 bp region of genomic DNA that contained exons 28 (162 bp) and 29 (104 bp) of *nf1a*, a feat made possible by the short intervening intron separating them.

Given the size of our library, it was particularly important to ensure that our screening strategy could be scaled up rapidly. Thus, PCR reactions were carried out in a 96-well format, with purification and sequencing of the products outsourced to a third party vendor with a high-performance single pass sequencing pipeline that was optimized for long reads, high pass rates, and rapid turnaround. Analysis of the sequencing results was automated, with sequencing data delivered directly to a dedicated server established for this purpose. We developed and validated a novel Perl script that compared the nucleotide sequences of exons 28 and 29 contained within each read to the wild-type sequence and, in the case of the identification of a putative mutation, compared the translated amino acid sequence to that of the wild type peptide sequences encoded by these exons. Our analysis platform was thus able to filter out silent mutations and would report only samples with mutations leading to changes in protein coding sequence. We also developed criteria to remove samples from the analysis that represented poor or failed sequencing reactions. Samples reported to contain mutations were reviewed and confirmed by resequencing the opposite strand. Using this approach, we screened approximately 3000 samples and isolated a single missense allele (Table 1).

Despite extensive optimization to maximize the throughput of samples through our direct sequencing screening methodology, the cost and time associated with this approach remained a significant hurdle. Therefore, along with our work described above, we further collaborated with the laboratory of Dr. Lilianna Solnica-Krezel to screen an independent panel of approximately 5,000 genomic DNA samples from ENU mutagenized F₁ animals maintained as a living library. These animals were subjected to a higher dose of ENU resulting in a greater mutation rate. Samples from this library were screened for mutations within the GRD of *nf1a* using an enzyme-mediated heteroduplex cleavage approach. Along with screening *nf1a* exons 28 and 29, we extended our analysis to include a second PCR amplicon containing exon 21 (504 bp). An overview of this approach is outlined in Figure 36.

The CEL-I enzyme, an extracellular plant-specific glycoprotein isolated from bulk celery, cleaves heteroduplex DNA at all single nucleotide mismatches. In this approach, pooled genomic DNA samples are subjected to PCR amplification using primers carrying different fluorescent labels. These PCR products, when denatured and allowed to re-anneal, will form mismatched heteroduplexes at the sites of ENU-induced mutations as well as pre-existing polymorphisms. Re-annealed products are incubated with CEL-I and the purified digested products are then separated by acrylamide electrophoresis using a LI-COR DNA analyzer. Upon identification of a mutation in pooled sample, the individuals that constitute that pool are rescreened to determine which sample contains the mutation. This screening method has the advantages of being faster and less expensive than our direct screening approach. In addition, as all of the F₁ animals are maintained as a “live library” in this approach, both males and females may be screened for mutations. Through this collaboration, the Solnica-Krezel laboratory screened approximately 4000 samples, again identifying predominantly missense alleles (Table 1). However, this screen yielded a single nonsense allele arising from a T to G mutation in codon 21 of *nf1a* exon 28, converting a leucine residue to a translation stop codon (Table 1). The entire collection of mutants generated from our TILLING approach is summarized in Figures 37 and 38.

***nf1a* and *nf1b* mutant alleles generated by retroviral insertional mutagenesis**

We also searched the ZeneMark library, a commercial library of zebrafish mutants alleles generated by retroviral insertional mutagenesis, for insertions in *nf1a* or *nf1b*. We identified one sample

that reported a proviral insertion 6 bp upstream of *nfla* exon 1. For *nflb*, we identified two samples with proviral insertions located 18 bp upstream of the *nflb* start codon and 137 bp downstream from the first exon. We attempted to purchase all three lines from this vendor; however, they were unable to recover the single *nfla* insertional mutant line. We received one *nflb* insertional mutant line (proviral insertion 137 bp downstream of exon 1) prior to the company terminating all operations, at which time they were still working to isolate the second *nflb* insertional mutant line (proviral insertion 18 bp upstream of *nflb*). Analysis of the single *nflb* insertional mutant line we obtained, designated ZM_00346420, indicated that the proviral insertion (located within intron1/2) was spliced out of the *nflb* mRNA and its presence did not appear to alter *nflb* expression. The mutant lines we identified in the ZeneMark library are summarized in Table 2.

Targeted inactivation of *nfla* and *nflb* using zinc-finger nucleases

As previously outlined in our proposal, the generation of stable *nfla* and *nflb* mutant zebrafish lines remains a necessary prerequisite to performing the large scale chemical and genetic screens we argue will be invaluable to furthering our understanding of NF1 biology and lead to the development of novel therapeutic agents. While we encountered some success in generating *nfla* mutant lines using the TILLING approach, this method lacked the efficiency necessary to generate multiple loss-of-function mutant alleles. Therefore, we turned to emerging technologies that promised a more efficient rate of specific lesion-induction in the zebrafish genome.

Excitingly, a cutting-edge strategy for targeted mutagenesis was developed for zebrafish using zinc finger nuclease (ZFN) technology (Figure 34). We were fortunate to have the opportunity to collaborate closely with the laboratories Nathan Lawson and Scot Wolfe in the application of this exciting technology. We successfully engineered ZFNs that target *nfla* and *nflb* using a modular assembly approach. Though this task is generally associated with a low efficacy rate, a number of factors worked in our favor during this process. First, we began with a library of 71 ZFPs whose binding specificities had been extensively characterized by the Wolfe laboratory. Additionally, the *nfla* and *nflb* genes are both extremely large with over 8000 bp of coding sequence, providing a large number of potential target sites. Using an algorithm developed by the Wolfe laboratory, we scanned the coding sequences of *nfla* and *nflb* to identify potential regions that conformed to the requirements for effective ZFN activity. Namely, we searched for tandem 9 bp target sites separated by 5 to 6 bp in an inverted orientation that could be bound by combining individual fingers from the various ZFPs present in the library. The Wolfe laboratory has extensive experience and expertise in the construction of sequence-specific ZFPs and their collective knowledge of how a particular finger would behave in the context of another finger was incorporated into the search algorithm resulting in a numerical score for each potential ZFN pair. Based on this analysis, we generated a list of eight ZFN sites each for *nfla* and *nflb* (Table 3). Another important feature taken into account by the search algorithm was whether or not a restriction site was contained within the spacer separating the two 9 bp ZFN target sites that was unique to a small region extending in either direction of the ZFN target site large enough to be amplified by PCR and resolved by gel electrophoresis. As non-homologous end joining (NHEJ) can lead to microinsertions, microdeletions, or a combination of both at the site of the double strand break, site-specific mutations induced by the injected ZFNs should cause loss of this restriction site. Thus, PCR amplification of this region followed by restriction digestion provides a molecular screening tool to detect somatically induced ZFN mutations.

Initially, we focused on ZFN pairs targeting the first exons of *nfla* and *nflb*; however, we were unable to demonstrate that these ZFNs caused site-specific mutations using a PCR/restriction digestion based genotyping strategy. Therefore, we next concentrated our efforts on the highest scoring ZFN pairs

from the computational analysis; namely, those targeting exon 25 of *nf1a* and exon 19 of *nf1b* (Table 3, highlighted in green). Schematics depicting these ZFN proteins and their target sites in *nf1a* and *nf1b* are depicted in Figure 39.

The desired three-finger ZFP cassettes for the *nf1b* ZFNs were assembled by splice overlap extension PCR and transferred into a pCS2 expression plasmid containing a nuclear localization signal, epitope tag, and one of two complementary FokI nuclease domain variants (EL or KK; DD or RR). These versions of the FokI nuclease domain harbor mutations at the dimerization interface that reduce the ability of individual ZFN to homodimerize and cleave at off-target sites. A second version of these constructs was made in which the *nanos1* (*nos1*) 3' untranslated region (UTR) was appended to the end of the FokI nuclease domain variant. Expression of *nanos1* is restricted to primordial germ cells by a posttranscriptional control mechanism, with its 3' UTR directing rapid degradation of the transcript in the soma and protection of the transcript from degradation in germ cells (Köprunner, Thisse et al. 2001). We predicted that stabilizing these transcripts in germ cells might increase their efficiency in inducing heritable targeted gene mutations. We used *in vitro* transcribed mRNAs from the constructs with and without the *nos1* 3' UTR in our subsequent experiments, but did not quantitatively assess their relative abilities to induce mutations at their specified target sites. One-cell fertilized zebrafish embryos were injected with a total dose of 10 pg or 20 pg of the DD/RR FokI ZFN pair mRNAs or 50 pg of the EL/KK FokI ZFN pair mRNAs (Figure 40). At 24 hpf, dead embryos were noted in all three conditions, with increasing concentrations of ZFN mRNAs causing higher degrees of lethality (Figure 41B). Morphological assessment of living embryos revealed two phenotypic classes, normal embryos that appeared indistinguishable from uninjected controls and embryos displaying nonspecific developmental abnormalities ("monsters") (Figure 41A). Embryos with a monster phenotype were exceedingly rare upon injection of the DD, RR, EL, or KK FokI ZFN monomer mRNAs, suggesting that this phenotype arises from excessive nonspecific off-target cleavage of the ZFN heterodimeric complex. The percentage of living embryos with a monster phenotype increased in a dose-dependent manner with the amount of DD/RR FokI ZFN mRNAs injected (Figure 41C). However, the EL/KK FokI ZFN mRNAs appeared to be better tolerated as injection of 50 pg induced a similar level of the monster phenotype as only 10 pg of the DD/RR FokI ZFN mRNAs.

We used a combination of PCR and restriction digestion to molecularly screen for site-specific mutations at the desired target site. Wild type samples contain a BslI restriction site in the 6 bp spacer separating the two individual ZFN binding sites. PCR amplification of a region roughly centered on this site generates a 223 bp PCR product that, upon restriction digestion with BslI, yields two products of 119 bp and 104 bp. Injection of functional ZFN mRNAs would lead to DNA cleavage specifically in this spacer region, leading to combinations of microinsertions or microdeletions when repaired by NHEJ, collectively resulting in the loss of the BslI restriction site (Figure 42A). Thus, retention of an uncut PCR product would indicate that the ZFNs were functioning appropriately at the intended target site.

Pooled genomic DNA was collected at 24 hpf from uninjected embryos as well as normal and monster DD/RR or EL/KK FokI ZFN mRNA injected embryos and used as a template for PCR with aforementioned primers (Figure 42A). An aliquot of these PCRs was separated by agarose gel electrophoresis to verify amplification of the 223 bp products (Figure 42B, top). The remainders of these reactions were subsequently digested with BslI and separated by gel electrophoresis (Figure 42B, bottom). The PCR products generated by templates from the uninjected embryos as well as the embryos injected with 10 pg or 20 pg of the DD/RR FokI ZFN mRNAs were digested to completion by BslI. However, following BslI digestion, a faint undigested band remained in both the normal and monster embryos injected with 50 pg of EL/KK FokI ZFN mRNAs, indicating that the genomic DNA from these

pools included individual samples in which the BslI restriction site had been lost, a finding consistent with ZFN-directed site-specific mutagenesis. Importantly, this undigested band was detected in embryos that appeared morphologically normal at 24 hpf. These data suggested that injecting 50 pg of the EL/KK FokI ZFN mRNAs could presumably induce mutations at the *nf1b* locus with adequate specificity such that off-target cleavage events did not lead to generalized developmental abnormalities. These embryos were predicted to be mosaic for ZFN-induced mutations, with some having undergone cleavage events early enough in development that the mutations introduced by NHEJ would be transmitted to the germ line.

Having designed, constructed, and validated a ZFN pair that targets the *nf1b* locus, we next turned our attention to verifying that we could transmit these ZFN-induced mutations to the zebrafish germ line. A schematic outlining the workflow we followed for generating stable zebrafish lines harboring ZFN-induced mutations in *nf1b* is outlined in Figure 43. Approximately 800 fertilized zebrafish embryos were injected at the 1-cell stage with 50 pg of EL/KK FokI ZFN mRNAs, with roughly 50% dying by 24 hpf. All embryos with monster phenotypes were discarded and genomic DNA was prepared from three individual pools of 5-10 ZFN mRNA-injected embryos along with uninjected controls to verify retention of an uncut PCR product by our PCR/Restriction Endonuclease (RE) genotyping strategy. Upon confirming successful ZFN-induced mutagenesis, the remaining live embryos with a normal phenotype were bleached and transferred into our fish facility to be raised to sexual maturity.

Based upon previous work, we expected approximately 50% of these embryos to survive to adulthood. Incrossing founder animals and screening individual progeny using our PCR/RE assay identified putative founder pairs bearing germ line ZFN-induced mutations in *nf1b*. Given the novelty of the technological platform we were using, it was unclear how efficient our modularly assembled ZFNs would be in generating site-specific lesions in the germ line. Coupled with the 3-4 months necessary for zebrafish to reach mating age, we opted to err on the side of excess and generated a large number of founder animals.

A high-throughput method was developed to identify F₀ animals positive for germ line transmission of a mutant *nf1b* allele that allowed up to 24 animals to be screened in a single 96-well plate (Figure 44). After screening approximately 100 F₀ animals, we identified 3 founders harboring 4 different mutant alleles of *nf1b* (Figure 45). We characterized the ZFN-induced lesions in *nf1b* by cloning and sequencing PCR fragments from exon 19 that were resistant to BslI digestion in the progeny from each of these founders. The mutations were combinations of the microinsertions of 2-13 bp and microdeletions of 1-3 bp. The founder animal 37P.F contained two different mutations in the germ line, a 1 bp deletion and 4 bp insertion (*nf1b*^{Δ1;+4}) as well as a 2 bp deletion and 4 bp insertion (*nf1b*^{Δ2;+4}). All of these mutant alleles led to frame shifts that resulted in premature translation stop codons. These founders were outcrossed to wild type fish and entire clutches of F₁ animals were raised to mating age. Heterozygous F₁ carriers were identified by PCR/RE genotyping of tail fin DNA. For the 37P.F founder, the two different *nf1b* mutant alleles were differentiated by cloning and sequencing BslI-resistant exon 19 PCR fragments amplified from tail fin DNA of F₁ animals. A similar strategy was carried out for *nf1a* by Jimann Shin in the laboratory of Thomas Look at the Dana-Farber Cancer Institute, leading to the isolation of two *nf1a* mutant alleles, one harboring a 53 bp deletion and the other a 8 bp deletion, both in exon 25 (Figure 46). Again, these mutations lead to frame shifts that produce premature translation stop codons.

Redundant function of the *nf1a* and *nf1b* alleles

We generated single homozygous mutant alleles of *nf1a* and *nf1b*, however they failed to show any significant abnormalities from embryogenesis through adulthood. However, when *nf1b*-specific morpholinos were injected into *nf1a* homozygous mutant embryos, an increased OPC phenotype, similar to *nf1a* and *nf1b* double morphants, was observed (data not shown). This result suggests that our *nf1a* mutant allele yields no functional *nf1a* protein and that *nf1b* shares redundant function with *nf1a*.

Due to the lack of a mutant phenotype *nf1a* and *nf1b* single homozygous mutants, we generated *nf1a;nf1b* double mutants. We crossed two ZFN-induced *nf1a* mutant alleles and the *nf1a*-nonsense tilling mutant with two mutant alleles of *nf1b*. To analyze tissue-specific phenotypes we intercrossed 6 different transgenic lines with the *nf1a;nf1b* double mutants (Table 4) to ascertain cell type-specific phenotypes in the CNS and PNS. We also found that *nf1a;nf1b* double homozygous mutants start to die around 7 dpf and that the majority fail to survive beyond 9 to 10 dpf. The double mutants exhibit severe brain degeneration that may be a primary cause of lethality. All three combinations of *nf1a;nf1b* double mutant alleles exhibited the identical phenotype supporting the redundant roles of *nf1a* and *nf1b* and that they are essential for survival as in mammals.

Hyperplastic OPCs and SCG in the *nf1a;nf1b* double mutant

Although *nf1a;nf1b* double homozygous mutant larvae do not survive beyond 10 dpf, their general morphology appears relatively normal until 7 or 8 dpf (see Figure 47 of confirmed mutant genotypes). Most double mutant larvae lacked melanocytes in the lateral stripe, which could first be detected at 4 dpf and persisted until death (Figure 47C and D). Furthermore, the double mutant larvae exhibited increased yellow pigmentation, indicative of altered xanthophore development and may correlate with increased café-au-lait spots often seen in human NF1 patients. We have now confirmed that we can use this phenotype to identify double mutant animals prior to PCR genotyping, which simplifies our experimental protocols immensely.

Because *nf1a* and *nf1b* double morphants have excess OPCs in the spinal cord, we promptly confirmed this phenotype in *Tg(olig2:egfp);nf1a;nf1b* double homozygous mutants and found that they had more dorsally migrated OPCs in the spinal cord than wild-type control animals at 6 dpf (Figure 47E and F). Increased numbers of OPCs could be detected as early as 3 dpf in the double mutants, which persisted up to their death (data not shown). This result is consistent with our morphant data and the mouse *Nf1*-loss phenotype.

The earliest report of *Nf1* knockout mice demonstrated the *Nf1* homozygous mutant had hyperplasia in the neurons of sympathetic ganglion tissue. To check whether zebrafish *nf1a* and *nf1b*-loss induces a similar defect, we examined superior cervical sympathetic ganglion (SCG) tissue by crossing the mutant to the *Tg(dbh:gfp)* transgenic line. As shown in Figure 47G and H, the *nf1a;nf1b* double homozygous mutant animals have an enlarged SCG relative to wild type animals, indicating that the function of *nf1* genes in zebrafish is conserved with *Nf1* function in mice.

In order to address whether Ras signaling is activated in the double mutant, we performed immunohistochemistry using phospho-ERK 1/2 antibody. At 5 dpf, a few neurons in the spinal cord of wild-type larvae express pERK1/2 strongly, while most other cells express it weakly (Figure 47I). However, in the double mutant, in addition to a subset of neurons, the white matter of neurons in the spinal cord are show strong expression, indicating that ERK signaling is highly active in the axons of neurons in the mutant (Figure 47J). Furthermore, the basal level of ERK1/4 phosphorylation appears relatively higher in most tissues (Figure 47J). These findings suggest that *nf1a* and *nf1b* loss leads to activation of the ERK pathway, which is one of the main downstream signaling of Ras pathway.

Ongoing efforts with *nf1a* and *nf1b* stable mutant lines

Why does the absence of *nfla* and *nflb* result in early larval degeneration? This question is certainly of great importance and we are actively working to uncover the answer. While there are certainly a number of possible explanations, an attractive hypothesis is that gross defects in the microvasculature due to *nfla/nflb* loss may contribute to tissue necrosis and degeneration. It is interesting to note that the liver and brain are both highly metabolic organs, which would make them particularly sensitive to such a lesion. Indeed, a careful analysis of the vasculature of double mutant embryos is warranted not only to address this possibility, but also to confirm the vascular patterning defects identified in our MO studies. The transgenic animals we are generating that fluorescently label endothelial cells with cytoplasmic and nuclear markers in the background of our *nfla* and *nflb* mutant alleles will be important tools for performing these studies.

Consistent with our MO data, *nfla;nflb* double homozygous mutant embryos displayed an increase in OPCs detectable as early as 3 dpf when compared with their clutchmates (Figure 47E and F). Examination of clutches from *nfla;nflb* compound heterozygous incrosses further revealed a number of embryos demonstrating a regurgitant valve phenotype, in which blood was seen to move back and forth between the atrium and the ventricle (data not shown). Genotyping of samples exhibiting this phenotype revealed that these animals included only *nfla;nflb* compound homozygous mutant embryos, *nfla*^{Δ/Δ}; *nflb*^{+Δ} embryos, and *nfla*^{+Δ}; *nflb*^{Δ/Δ} embryos. These preliminary findings are consistent with our MO studies in which we observed a similar cardiac phenotype. Interestingly, this phenotype is not fully penetrant, as we observe embryos of the same genotypes that do not display cardiac dysfunction. A careful quantitative analysis of this phenotype is certainly warranted and is presently underway. Taken together, however, these preliminary studies not only lend credence to our MO data but further suggest that the *nfla* and *nflb* alleles we isolated are in fact null alleles. Quantitative Western analysis in mutant populations from our various *nfla* and *nflb* alleles will provide additional evidence supporting this assertion.

While MOs serve as a powerful tool to rapidly assess the consequences of transient gene knockdown, they have a number of limitations including a relatively short duration of efficacy. Excitingly, we identified a novel melanophore phenotype in our double homozygous mutant animals that was not apparent until 4 dpf, a time period outside the window of MO effectiveness. Double homozygous mutant embryos show increased pigmentation over the dorsal aspect of the head (Figure 48A, D, B, E) and lack melanophores at positions along the lateral strip (Figure 48A, D, C, F). In addition, the repetitively arranged clusters of melanophores that compose the lateral strip appear enlarged in double homozygous mutant embryos (Figure 48C, F). These defects did not appear to be limited to the melanophore lineage, as double mutant larvae also appear to have an increased yellow pigmentation, consistent with abnormal xanthophore development. These phenotypes persist until death and are fully penetrant in double homozygous mutants, providing a robust means to identify double homozygous mutants prior to genotyping. It is also interesting to note that all embryos that have been identified as positive for a valvular regurgitation phenotype display pigmentation phenotypes (Figure 49).

An enticing possibility is that these abnormalities in the zebrafish melanocyte lineage of double homozygous mutant embryos may serve as a clinical correlate to the hyperpigmented lesions in the skin of NF1 patients. Indeed, biallelic loss of *NF1* in melanocytes has been shown in NF1-related café au lait macules. Importantly, no other animal model of NF1 has duplicated these common disease associated lesions. Unraveling the mechanism by which this phenotype occurs will certainly be of interest. The high penetrance and robust readout of this phenotype may serve as a powerful platform to identify non-GAP activities of neurofibromin.

Although homozygous loss of both *nfla* and *nflb* results in early larval lethality, some embryos harboring three inactivated zebrafish *NF1* orthologues (*nfla*^{Δ/Δ}; *nflb*^{+/^Δ} or *nfla*^{+/^Δ}; *nflb*^{Δ/Δ}) are viable and fertile. In preliminary examinations of these adult animals, we observed what appeared to be hyperpigmented regions along portions of the caudal fin (data not shown). Do these lesions arise from loss of heterozygosity of the single remaining *nfla* or *nflb* allele in clonal populations of melanophores in these animals? This intriguing finding certainly warrants additional examination of these adult animals to resolve this question as well as to carefully screen them for neoplasms commonly associated with NF1.

Importantly, we have also found that *nfla*^{+/-}; *nflb*^{-/-}; *p53*^{e7/e7} fish develop tumors that resemble high grade glioma and malignant peripheral tumors (MPNST) with significantly earlier onset and with higher penetrance, whereas *nflb*^{-/-}; *p53*^{e7/e7} fish rarely develop tumors, suggesting that zebrafish NF1 orthologs, *nfla* and *nflb*, possess a strong tumor suppressor function that is conserved among vertebrates. These findings support a major aim of our studies, to establish an NF1 zebrafish model that demonstrated tumor suppressor function, and could be used to dissect the underlying molecular and cellular pathways through which *nfl* exerts its tumor suppressor function.

We have crossed the various aforementioned *nfla* and *nflb* alleles into a number of different transgenic lines to assess the consequences of loss of these genes specific tissues during development (Table 4). As these various transgenic lines we have crossed our *nfla* and *nflb* mutant alleles into reach mating age, we will perform additional descriptive analyses to carefully define the phenotypic spectrum of compound homozygous deficiency of *nfla* and *nflb*. These studies serve as a necessary prerequisite for the application of these lines to high-throughput chemical screens to identify small molecules that can modify NF1-associated phenotypes as well as for performing reverse genetic screens to identify enhancers and suppressors of NF1 phenotypes *in vivo*.

In summary

- Transient loss-of-function of *nfla* and *nflb* in zebrafish yields a range of cardiac, vascular, and neural phenotypes that we have carefully defined and characterized.
- Several stable lines of zebrafish harboring loss-of-function alleles for *nfla* and *nflb* have been identified and validated, with significant work having been completed towards phenotypic characterization.

Homo sapiens *NF1* ETVLADRFRERLVELVTMMGDGELPIAMALANVVPCSQWDELARVLVTLFDSRHLLYQLLWNMFSEVELADSMQTLFRGNSLASKIMTF
 Mus musculus *Nf1* ETVLADRFRERLVELVTMMGDGELPIAMALANVVPCSQWDELARVLVTLFDSRHLLYQLLWNMFSEVELADSMQTLFRGNSLASKIMTF
 Danio rerio *nf1a* ETVLADRFRERLVELVTMMGDGELPIAMALANVVPCSQWDELARVLVTLFDSRHLLYQLLWNMFSEVELADSMQTLFRGNSLASKIMTF
 Danio rerio *nf1b* ETVLADRFRERLVELVTMMGDGELPIAMALANVVPCSQWDELARVLVTLFDSRHLLYQLLWNMFSEVELADSMQTLFRGNSLASKIMTF
 Drosophila melanogaster *Nf1* ETVLADRFEQLVQLVMTISDRGELPIAMALANVVTTSQMDELARVLVTLFPAKHLSPLLWNMFYREVEVSDCHQTLFRGNSLGSKIMAF
 Homo sapiens *NF1* CFKVVYCATYLQKLLDPLLRVIITSSDQHQHVSFEVDPTRELPSSSELEENQNRNLLQMTKEKFFHAIISSESEFFPPQLRSVCHCLYQATCHSLL
 Mus musculus *Nf1* CFKVVYCATYLQKLLDPLLRVIITSSDQHQHVSFEVDPTRELPSSSELEENQNRNLLQMTKEKFFHAIISSESEFFPPQLRSVCHCLYQATCHSLL
 Danio rerio *nf1a* CFKVVYGAAYLQKLLLEPLLRGIITTPHQQISFEVDPTRELAENLEENQKLLQITDRFFLAITNSSEFFPPQLRSVCHCLYQATCHSLL
 Danio rerio *nf1b* CFKVVYCATYLQKLLLEPLLRVIAGTEWHMLSFEDVDPTRENGENLEENQNRNLLRMTERFFKAIISSESEFFPPQLRSVCHCLYQATCHSLL
 Drosophila melanogaster *Nf1* CFKITYGASYLQMLLEPLIRPLLD--EEETCFEVDPARLDPTEDIEQHRNNLIALTQKVFDAITNSSEFFPPQLRSVCHCLYQ-----
 Homo sapiens *NF1* NKATVKEKKENKKSQVVSQRFP---QNSIGAVGSAMFLRFINPAIVSPYEAGILDKKPPPRIERGLKLMISKILOSIAHNVLFTEEHMRPF
 Mus musculus *Nf1* NKATVKEKKENKKSQVVSQRFP---QNSIGAVGSAMFLRFINPAIVSPYEAGILDKKPPPRIERGLKLMISKILOSIAHNVLFTEEHMRPF
 Danio rerio *nf1a* NKATVKEKKENKKSQVVSQRFP---QNSIGAVGSAMFLRFINPAIVSPYEAGILDKKPPPRIERGLKLMISKILOSIAHNVLFTEEHMRPF
 Danio rerio *nf1b* SEASVKKDRKEVKKAVVSQRFP---QNSIGAVGSAMFLRFVNPVAVSPYEAGILDKKPPPRIERGLKLMISKILOSIAHNVLFTEEHMRPF
 Drosophila melanogaster *Nf1* -----VLSKRFPPNLLQNHIGAVGTIVIFLRFINPAIVSPQELGIVDKQVHSSAKRGLMLMSKILQNIANHVEFSKEQHMLCF
 Homo sapiens *NF1* NDFVKSNFDAARRFFLDIASDCPTSDAVNHSLSFISDGNVLALHRLLLWNNQEKIGQYLSSNRDHKAVGRRPPFDKMATLLAYLGPPER
 Mus musculus *Nf1* NDFVKSNFDLARRFFLDIASDCPTSDAVNHSLSFISDGNVLALHRLLLWNNQEKIGQYLSSNRDHKAVGRRPPFDKMATLLAYLGPPER
 Danio rerio *nf1a* NDFVKSNFDAARRFFLDIASDPSDVSNNHSLSFISDGNVLALHRLLLWNNQEKIGQYLSSNRDHKAVGRRPPFDKMATLLAYLGPPER
 Danio rerio *nf1b* NDFVKSNFDAARRFFLDIASDCPASDSLNHSLSFISDGNVLALHRLLLWNNQEKIGQYLSSNRDHKAVGRRPPFDKMATLLAYLGPPER
 Drosophila melanogaster *Nf1* NDFFLRQHFAGRRFFIQIASDCETVDOTSHSMSPISDAHVLAHRLLLWTHQEKIGDYLSNRDHKAVGRRPPFDKMATLLAYLGPPER

Figure 2. Zebrafish *NF1* orthologues are highly conserved within the GAP-related domain.

Amino acid sequence alignment reveals a remarkably high degree of protein conservation within the human, mouse, zebrafish, and drosophila neurofibromin GAP-related domains (identical amino acid highlighted grey, similar amino acids highlighted yellow, and mismatched amino acids not highlighted). Alternatively spliced exon 23a in human *NF1* (not depicted) is present in both *nf1a* and *nf1b*.

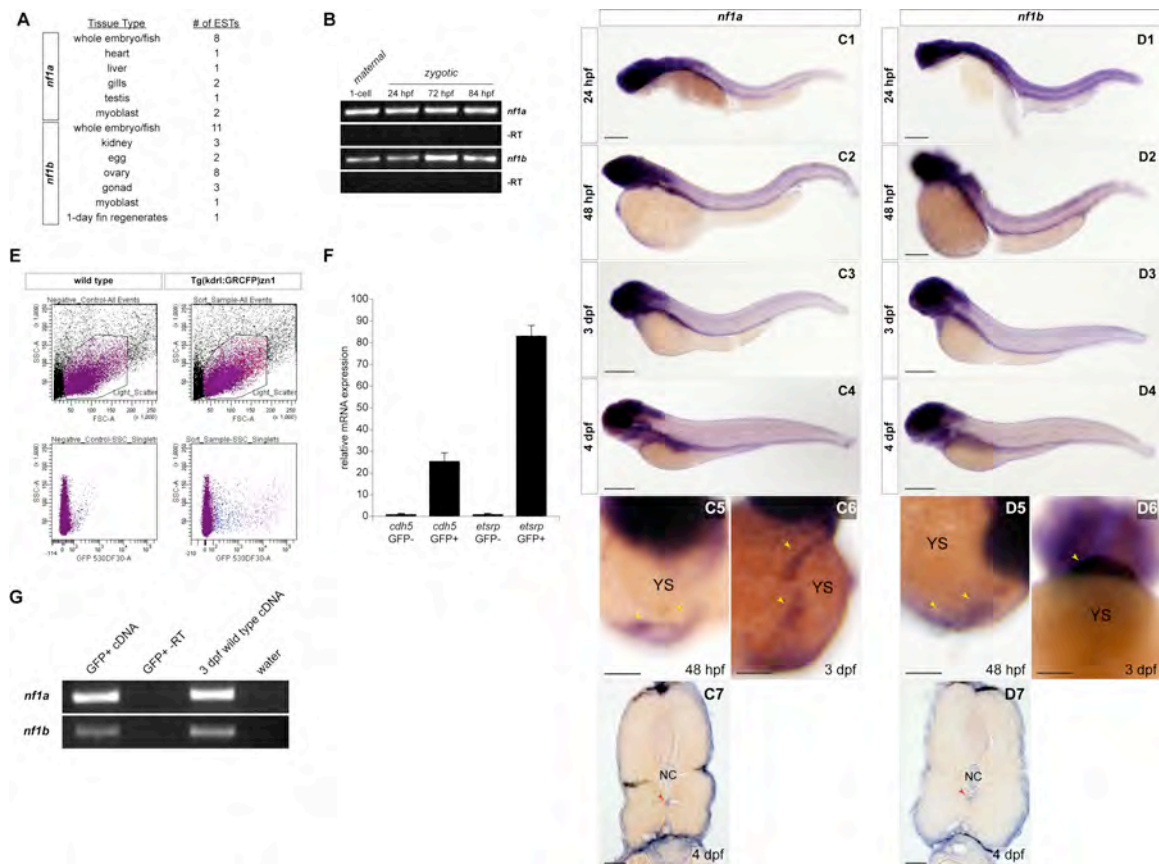


Figure 3. Zebrafish *nfla* and *nflb* are expressed during embryonic development.

(A) Distribution of ESTs mapping to *nfla* or *nflb* in dbEST including tissue of origin. (B) RT-PCR analysis verifying maternal (1-cell) and zygotic (24, 72, and 84 hpf) expression of *nfla* and *nflb*. (C1-C6, D1-D6) Whole-mount *in situ* hybridization of 24 hpf, 48 hpf, 3 dpf (all magnifications of insets in Figure. 2), and 4 dpf zebrafish embryos shows temporal and spatial expression patterns of *nfla* and *nflb*. (C5-6, D5-6) Both *nfla* and *nflb* are expressed in cardiac tissue at 48 hpf and 3 dpf as seen in these anteroventral images. Notably, analysis of 14 μ m (C7, D7) cross sections of whole-mount stained 4 dpf zebrafish embryos reveals strong *nfla* and *nflb* expression in the region of the dorsal vessel (arrows) directly below the notochord (NC). (E) Parameters utilized for sorting GFP-positive and GFP-negative cells from 3.5 dpf Tg(kdrl:GRCFP)zn1 zebrafish embryos. (F) Quantitative PCR analysis of the GFP-positive cell fraction reveals marked enrichment for endothelial-specific genes, including *cdh5* and *etsrp*, relative to the GFP-negative fraction. (G) Reverse-transcription and polymerase chain reaction (RT-PCR) for *nfla* and *nflb* was performed using first strand cDNA synthesized from endothelial cell RNA (GFP-positive cell fraction), confirming expression of both genes in vascular endothelium. Scale bars: 25 μ m.

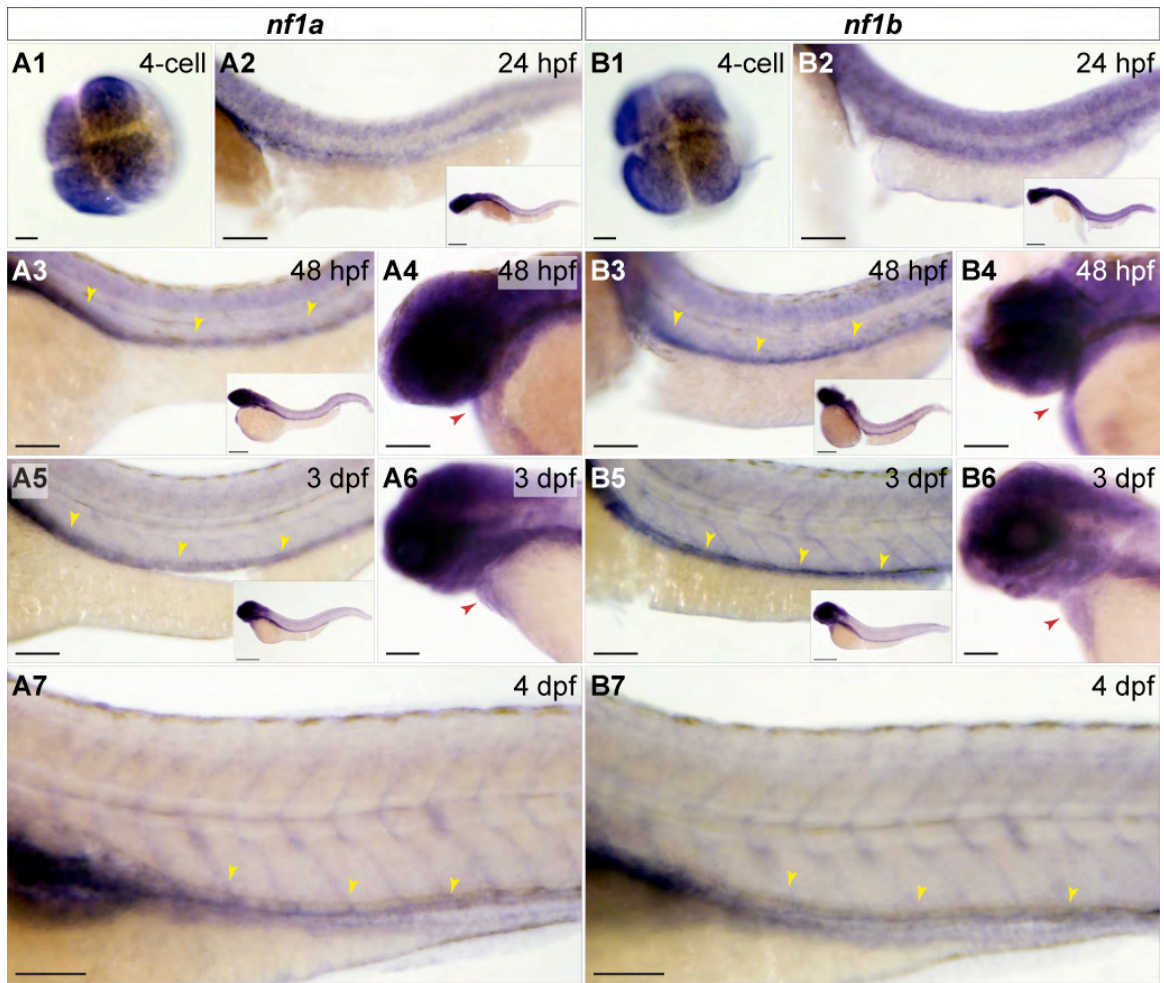


Figure 4. *nf1a* and *nf1b* are expressed maternally and in the developing zebrafish cardiovascular system.

Whole-mount *in situ* hybridization for *nf1a* and *nf1b* at the 4-cell stage, 24 hpf, 48 hpf, 3 dpf, and 4 dpf. (A1, B1) At the 4-cell stage, *nf1a* and *nf1b* are expressed throughout the animal pole of the developing embryo. (A2, B2) Both genes are expressed broadly at 24 hpf (inset), with strong expression along the spinal cord. (A3, B3) At 48 hpf, expression of *nf1a* and *nf1b* is noted in the head and regions of the anterior trunk (inset). Spinal cord expression of both genes persists and positive staining is observed along the dorsal vessel for *nf1a* and *nf1b*. (A4, B4) Cardiac expression for both genes is observed at 48 hpf. (A5, B5) Expression of *nf1a* and *nf1b* become progressively restricted to regions of the head at 3 dpf (insets). *nf1a* and *nf1b* expression along the dorsal vessel (A5, B5) and in the embryonic heart (A6, B6) persist at 3 dpf. (A7, B7). At 4 dpf, robust vascular staining is apparent for *nf1a* and *nf1b*. Scale bars: 25µm (100µm for insets).

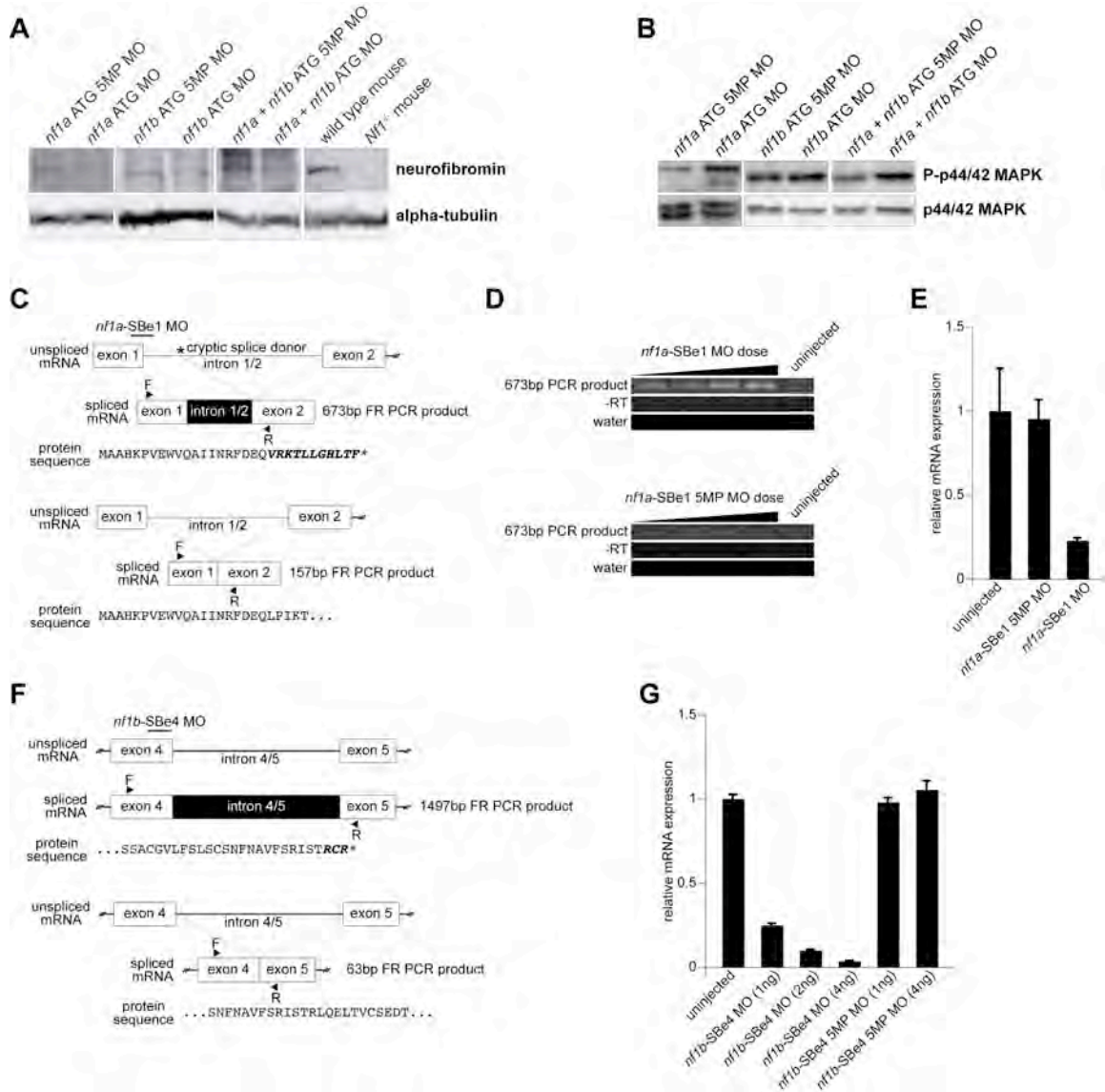


Figure 5. Transient knockdown of *nf1a* and *nf1b* is achieved by specific translational- and splice-blocking MOs.

(A) Western blot analysis of *nf1a* ATG 5MP MO (2ng), *nf1a* ATG MO (2ng), *nf1b* ATG 5MP MO (10ng), *nf1b* ATG MO (10ng), *nf1a + nf1b* ATG 5MP MO (2ng), and *nf1a + nf1b* ATG MO (2ng)-treated 3.5 dpf zebrafish embryos. Administration of MOs specific for *nf1a*, *nf1b*, or both together leads to a marked decrease in neurofibromin at the protein level (wild type and *Nf1*^{-/-} mouse lysates are included as controls for antibody specificity). (B) Activation of effector pathways downstream of Ras, as assessed by increased P-p44/42 MAPK, are observed by Western blot analysis in 3.5 dpf *nf1a* (~3ng), *nf1b* (~5ng), and *nf1a + nf1b* (~2ng) ATG morphant zebrafish embryos when compared to dose-matched controls. (C) Schematic representation of site targeted by *nf1a*-SBe1 MO. Administration of *nf1a*-SBe1 MO leads to activation of a cryptic splice donor and the generation of an mRNA transcript harboring a premature stop codon. MO-mediated inclusion of intronic sequence in the mRNA transcript generates a 673bp PCR product by RT-PCR using the depicted primer pair. (D) RT-PCR analysis from 1, 2, 3, and 5ng *nf1a*-SBe1 MO-treated samples using the depicted primer pair reveals a dose-dependent increase in the amount of the 673bp PCR product that is absent in uninjected embryos. Injection of *nf1a*-SBe1 5MP MO does not lead to the generation of the 673bp PCR product. (E) Quantitative PCR analysis of uninjected, *nf1a*-SBe1 MO-, and *nf1a*-SBe1 5MP MO-treated samples using the depicted primer pair (mean fold change \pm SD). Administration of 3ng of an *nf1a*-SBe1 MO leads to a 77% reduction in the wild type *nf1a* transcript when compared to uninjected or 3ng injected *nf1a*-SBe1 5MP MO-treated samples. (F) Schematic representation of site targeted by an *nf1b*-SBe4 MO. Administration of *nf1b*-SBe4 MO leads to the inclusion of intron 4/5 in the *nf1b* mRNA transcript, which harbors a premature stop codon. MO-mediated inclusion of intronic sequence in the mRNA transcript generates a 1497bp PCR product by RT-PCR using the depicted primer pair while the wild type transcript generates a 63bp PCR product. (G) Quantitative PCR analysis of uninjected, *nf1b*-SBe4 MO-, and *nf1b*-SBe4 5MP MO-treated samples using the depicted primer pair (mean fold change \pm SD). Administration of 1, 2, or 4ng of *nf1b*-SBe4 MO leads to a dose-dependent decrease in the wild type *nf1b* mRNA transcript when compared to uninjected or *nf1b*-SBe4 5MP MO-treated samples.

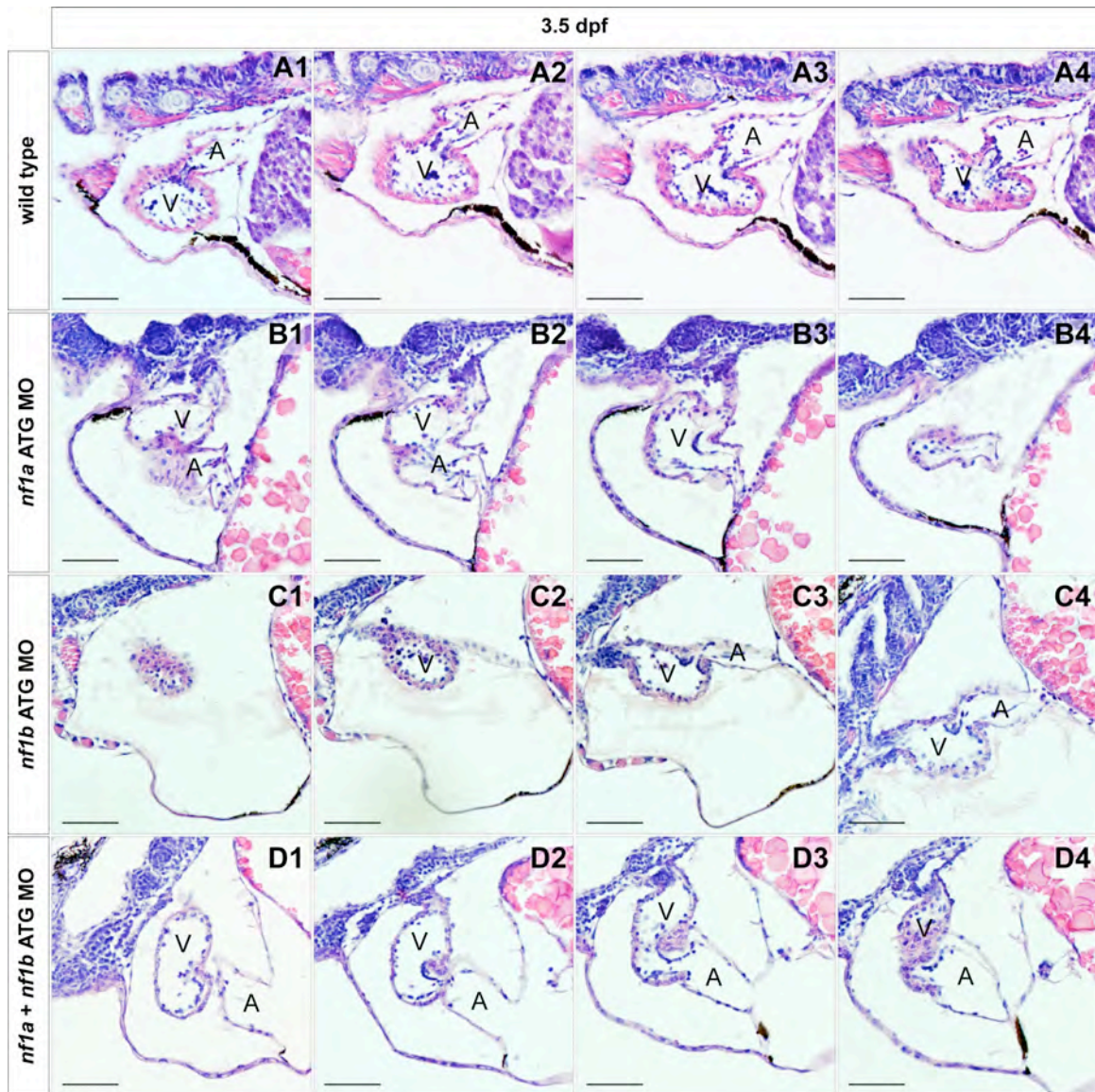


Figure 6. Histological analysis of MO knockdown cardiac valves.

Serial transverse histological sections through the atrio-ventricular valves of wild type (A1-4) or ~2ng morphant *nf1a* ATG (B1-4), *nf1b* ATG (C1-4), and *nf1a + nf1b* ATG (D1-4) 3.5 dpf zebrafish embryos reveal no readily apparent defects at the resolution afforded to us by histological analysis (A, atrium; V, ventricle). Scale bars: 50µm.

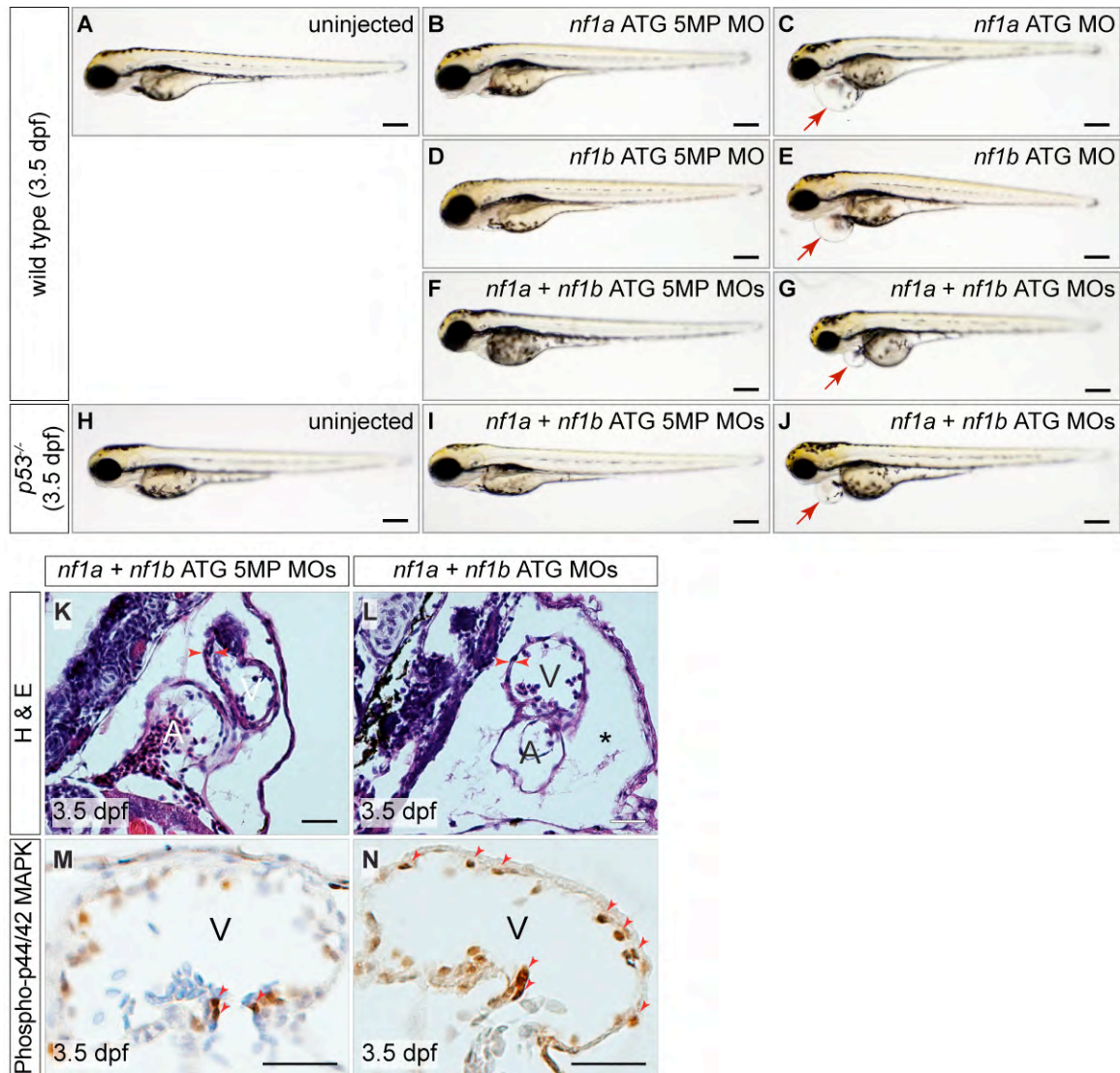


Figure 7. MO knockdown of *nf1a*, *nf1b*, or both together results in pericardial effusions at 3.5 dpf and increased phospho-p44/42 MAPK in cardiac tissue.

Analysis of 3.5 dpf wild type (A), *nf1a* ATG 5-mispair (5MP) MO- (B), *nf1b* ATG 5MP MO (D), or *nf1a + nf1b* ATG 5MP MO- (F) injected embryos reveal no apparent defects in gross morphology. Treatment with *nf1a* ATG MO (C), *nf1b* ATG MO (E), or a combination of both (G), however, results in a dilation of the pericardial space. (H-J) Injection of *p53*^{-/-} embryos with *nf1a + nf1b* ATG MO results in a gross dilation of the pericardial space (J), while uninjected (H) and *nf1a + nf1b* ATG 5MP MO-injected *p53*^{-/-} embryos (I) appear normal. Scale bars: 0.25mm. (K-L) Transverse sections of 3.5 dpf *nf1a/nf1b* combined morphant embryos reveals a thinning of the ventricular myocardium and pericardial effusion (*) when compared with controls (A, atrium; V, ventricle). (M-N) Immunohistochemical analysis of transverse sections of 3.5 dpf *nf1a/nf1b* combined morphant embryos reveals an increase in the ratio of phospho-p44/42 MAPK positive cardiac cells (arrows) to the total number of cardiac cells when compared to controls. Scale bars: 25μm.

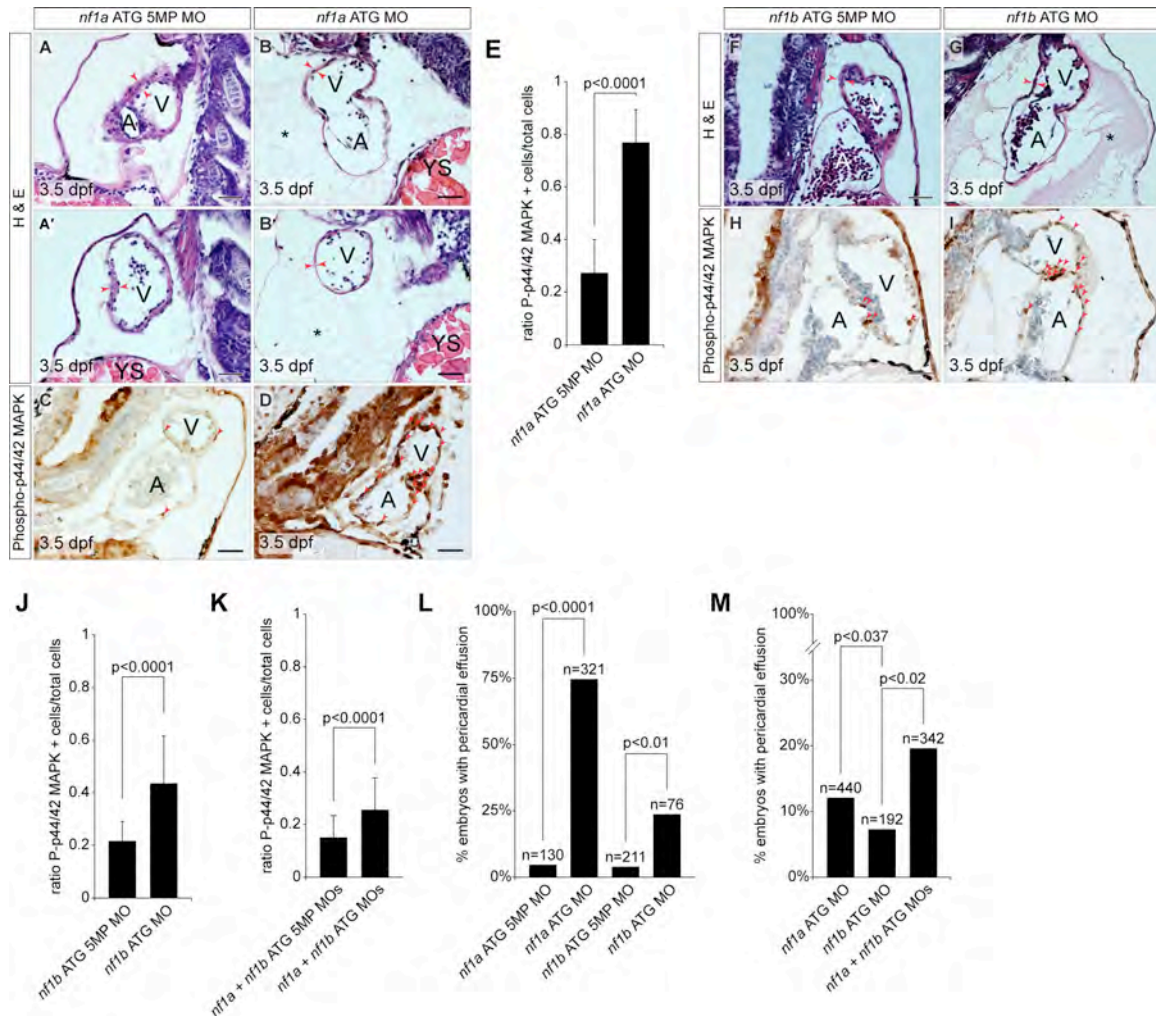


Fig 8. MO knockdown of *nf1a* or *nf1b* results in a thinning of the ventricular myocardium and increased phospho-Erk staining in cardiac tissue.

(A, A', B, B', F, G) Transverse histological sections through the heart of 3.5 dpf zebrafish embryos reveals a thinning of the ventricular myocardium (red arrows) of zebrafish treated with *nf1a* or *nf1b* ATG MOs when compared with the corresponding controls (A, atrium; V, ventricle; YS, yolk sac). Notably, a large pericardial effusion can be appreciated in *nf1a* and *nf1b* morphants (*). (C, D, H, I) Immunohistochemical analysis of transverse sections through 3.5 dpf zebrafish hearts reveals an upregulation of phospho-p44/42 MAPK (phospho-Erk) in *nf1a* or *nf1b* morphants when compared to the appropriate 5MP controls. The ratio of phospho-Erk positive cardiac cells to the total number of cardiac cells was quantified over multiple sections for *nf1a* MO (2ng), *nf1b* MO (2ng), and *nf1a* + *nf1b* MO (2ng) groups (mean ratio phospho-p44/42 MAPK positive cardiac cells/total cardiac cells \pm SD) (E, J, K). (L) Quantification of percentage of embryos displaying a pericardial effusion phenotype at 3.5 dpf following injection of approximately 2ng of *nf1a* ATG 5MP MO, *nf1a* ATG MO, *nf1b* ATG 5MP MO, or *nf1b* ATG MO. 75% of *nf1a* ATG morphants displayed pericardial effusions as compared to 5% of *nf1a* ATG 5-mispair (5MP) morphant controls ($p < 0.0001$). 24% of *nf1b* ATG morphants displayed pericardial effusions as compared to 4% of *nf1b* ATG 5MP morphant controls ($p < 0.01$). (M) Quantification of percentage of embryos displaying a pericardial effusion phenotype at 3.5 dpf following injection of *nf1a* ATG MO, *nf1b* ATG MO, or *nf1a* + *nf1b* ATG MO. A suboptimal dose (1ng) of *nf1a* ATG MO resulted in a 12% incidence of pericardial effusion, while a suboptimal dose (1ng) of *nf1b* ATG MO resulted in a 7% incidence of pericardial effusion. Injection of 1ng of a combination of *nf1a* + *nf1b* ATG MO, however, resulted in a 20% incidence of pericardial effusion. Scale bars: 25 μ m.

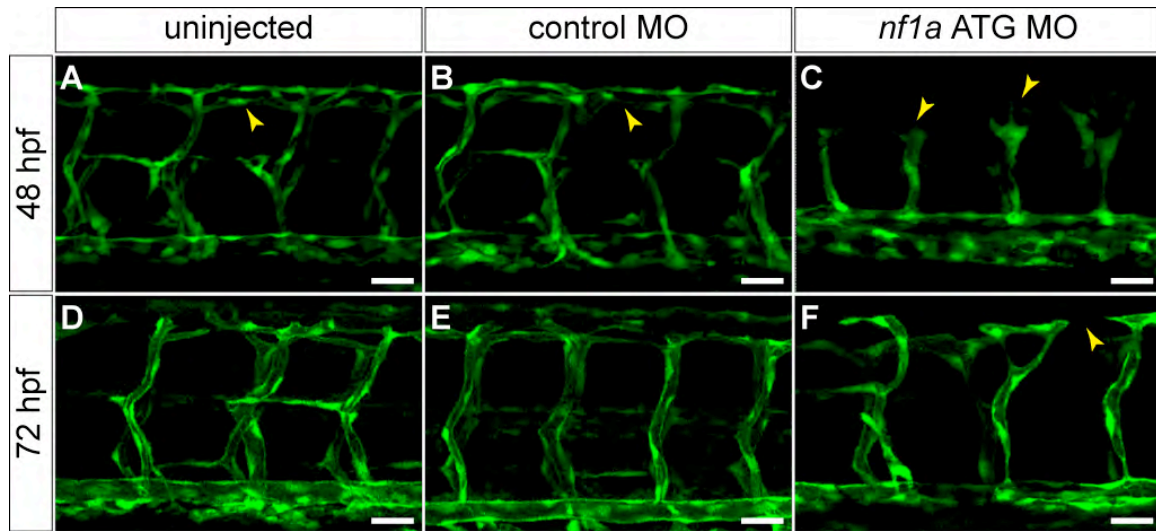


Figure 9. MO knockdown of *nf1a* results in vascular patterning defects at 48 and 72 hpf.

(A-C) At 48 hpf, *nf1a* ATG MO-treated Tg(fli:egfp)y1 (endothelial-specific GFP transgenic) zebrafish embryos display gross defects in vascular development compared with control MO-treated or uninjected samples. Morphant embryos (C) display abnormal claw-like projections at the leading edge of the developing intersomitic vessels and fail to develop the dorsal longitudinal anastomotic vessel (DLAV) present in both control MO-treated (B) and uninjected (A) samples. (D-F) At 72 hpf, *nf1a* ATG morphant embryos display only rudimentary DLAVs and a general disorganization of the trunk vasculature (F) when compared with control MO-treated (E) or uninjected (D) embryos. Scale bars: 25µm.

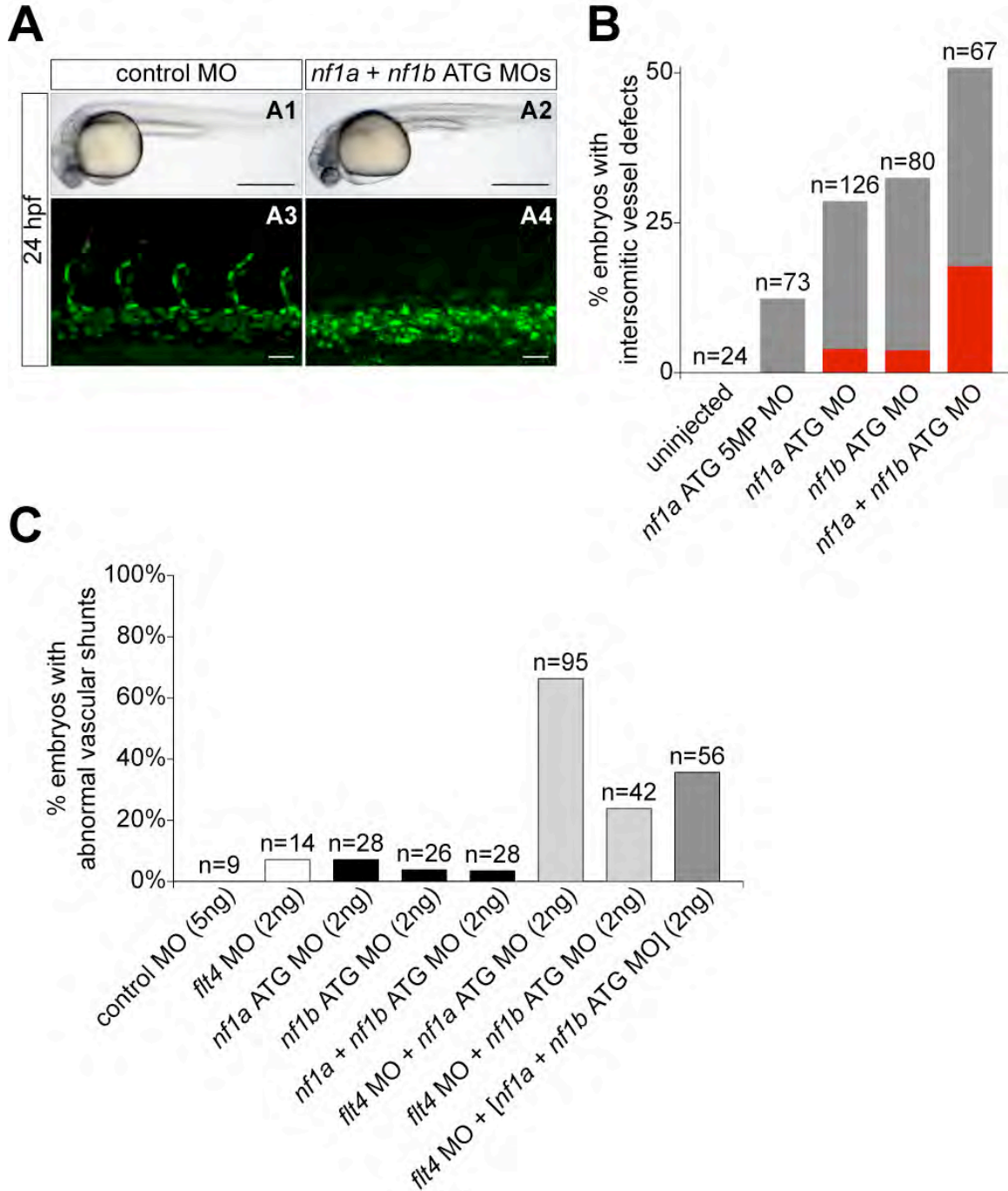


Figure 10. MO knockdown of *nf1a*, *nf1b*, or both together result in vascular defects at 24 at 48 hpf.

(A, B) Analysis and quantification of vascular defects at 24 hpf in uninjected and morphant Tg(*fli:negef*)y7 (endothelial-specific nuclear GFP transgenic) zebrafish embryos. Control MO- (A1) and combined *nf1a/nf1b* MO-treated (A2) zebrafish embryos appear similar by gross morphological analysis at 24 hpf (scale bars: 500µm). Development of intersomitic vessels is deficient at 24 hpf in *nf1a/nf1b* combined morphants (A4) when compared to controls (A3) (scale bars: 25µm). (B) Intersomitic vessel formation between somites 17-30 at 24 hpf was scored as absent (red), intermediate (grey), or normal following administration of 2ng of the indicated MO(s). (C) MO-mediated knockdown of *flt4*, providing a sensitized background for the detection of vascular defects, was combined with *nf1a*, *nf1b*, and *nf1a* + *nf1b* ATG MO knockdown. 24%-85% of combined *flt4/(nf1a, nf1b, nf1a + nf1b)* MO-treated embryos display abnormal vascular shunts compared with 3-8% of individual *flt4*, *nf1a*, *nf1b*, or *nf1a* + *nf1b* MO-treated embryos.

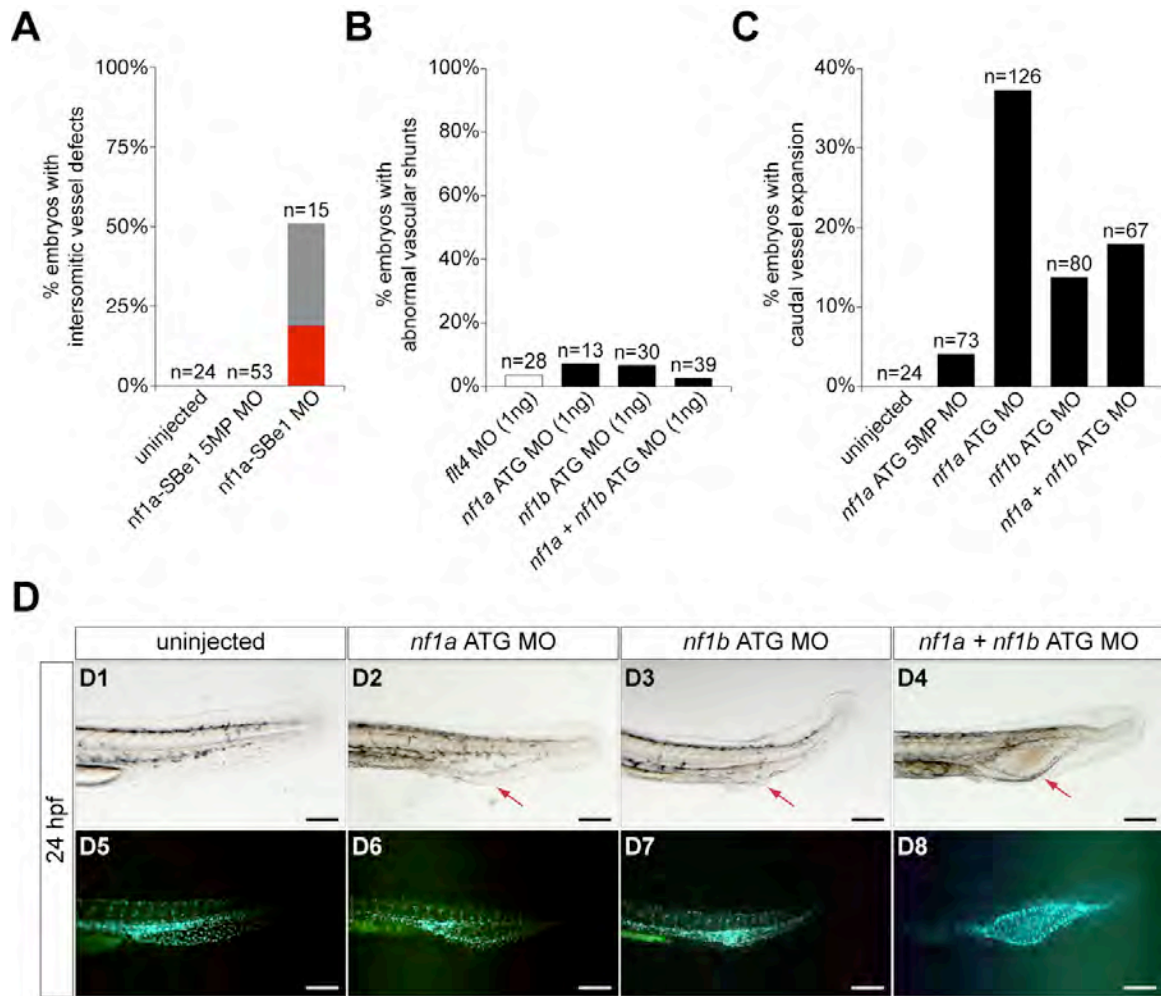


Figure 11. MO knockdown of *nf1a*, *nf1b*, or both together result in vascular defects at 24 at 48 hpf.

(A) Quantification of vasculature at 24 hpf in uninjected and morphant Tg(fli:negfp)y7 (endothelial-specific nuclear GFP transgenic) zebrafish embryos. Uninjected, *nf1a*-SBe1 5MP (1ng), and *nf1a*-SBe1 (1ng) morphant embryos were qualitatively assessed for presence, absence (red), or an intermediate phenotype (grey) with regard to the developing trunk intersomitic vessels between somites 17-30 at 24 hpf. (B) Quantitation of vascular shunt phenotype seen with low (1ng) doses of *flt4*, *nf1a*, *nf1b*, or *nf1a* + *nf1b* MOs. (C) Quantitation of cystic expansion phenotype observed in morphant Tg(fli:negfp)y7 embryos treated with 2ng of the indicated MO(s). (D1-D8) Treatment of Tg(fli:negfp)y7 zebrafish embryos with an *nf1a* ATG MO, *nf1b* ATG MO, or *nf1a* + *nf1b* ATG MOs leads to a cystic expansion in the region of the caudal artery and vein (arrows, D2-D4) not present in uninjected embryos (D1). The expanded tissue was confirmed to be vascular by GFP expression (D6-D8). Scale bars: 50μm.

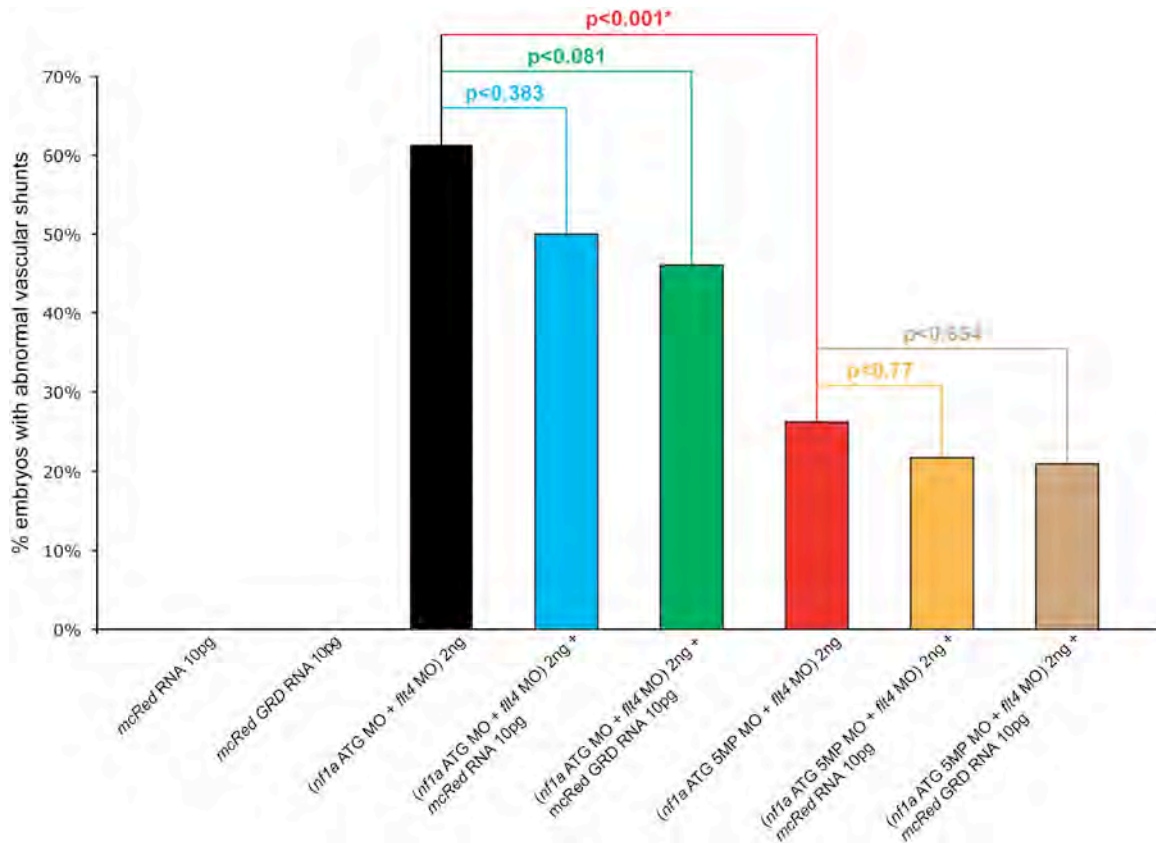


Figure 12. Expression of *NF1 GRD* RNA does not rescue *flt4/nfla* compound MO-induced abnormal vascular shunts.

MO-mediated knockdown of *flt4* and *nfla* results in a highly penetrant abnormal vascular shunt phenotype (61% of combined morphants). Addition of 10 pg of mcRed-GRD RNA results in a reduction to 46% ($p < 0.08$; NS). Administration of 10 pg of either mcRed-GRD RNA or mcRed RNA alone produced no vascular shunts, while combination of an equal amount of mcRed RNA or mcRed GRD RNA with *nfla/flt4* combined morphants or *nfla* control/*flt4* combined morphants also yielded no statistically significant difference in the percentages of embryos demonstrating vascular shunts.

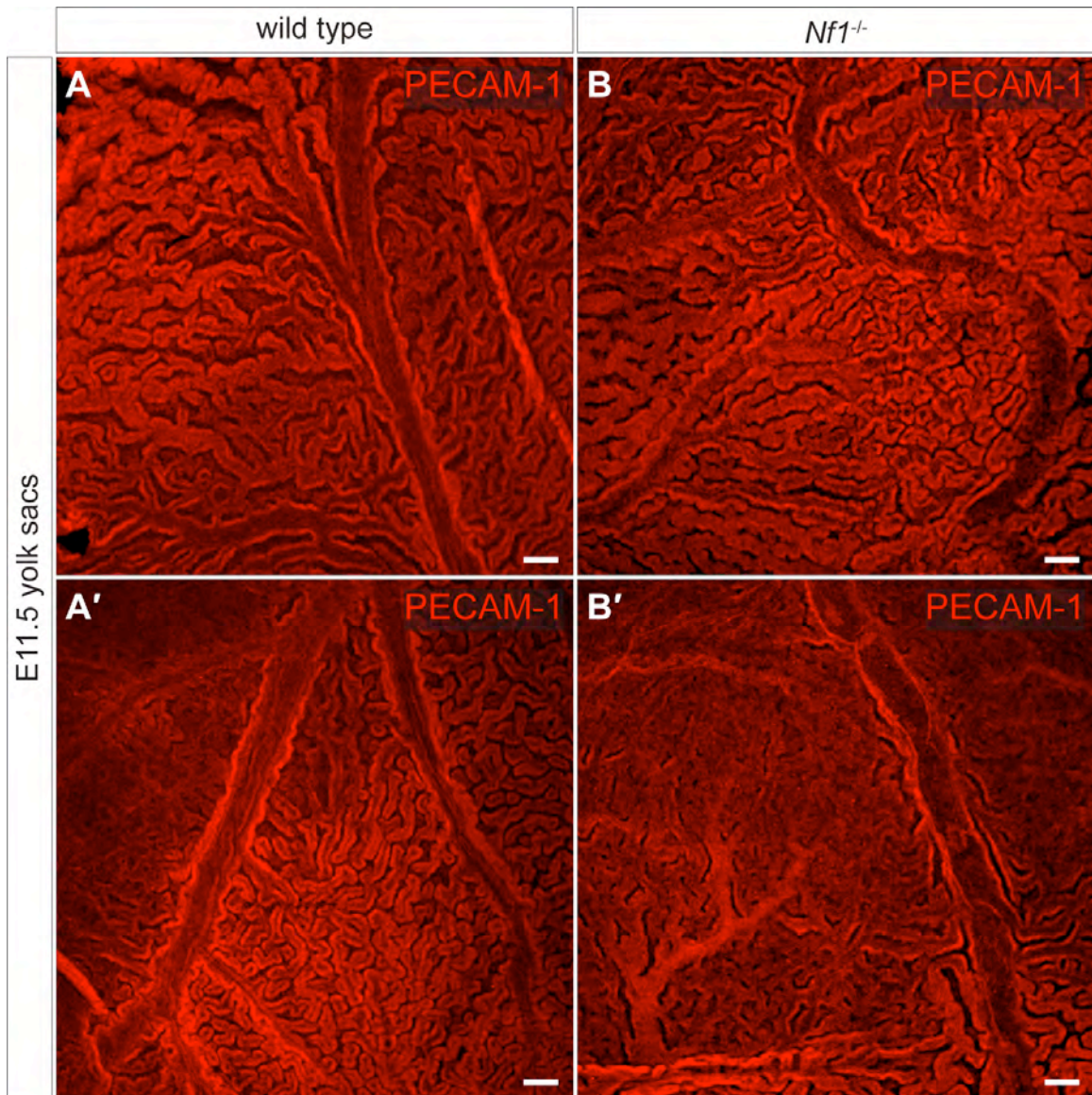


Figure 13. Loss of *Nf1* is not associated with defects in patterning of the mouse yolk sac vasculature.

(A, A', B, B') Comparison of confocal maximum projections through E11.5 whole mount PECAM-1 stained wild type (A, A') and *Nf1*^{-/-} (B, B') mouse yolk sacs reveals no overt differences in patterning of the developing yolk sac vasculature. Scale bars: 100μm.

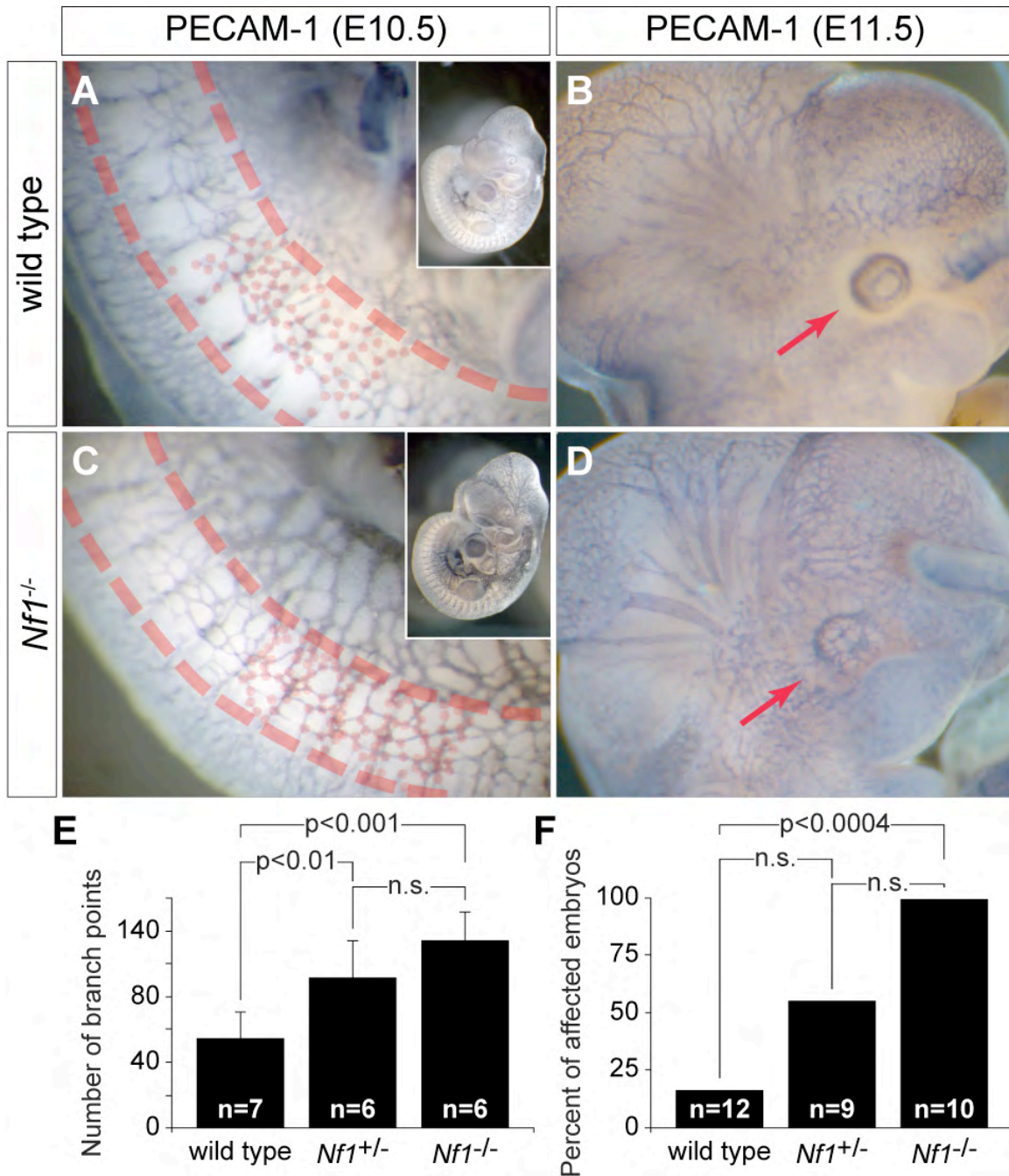


Figure 14. *Nf1*^{-/-} mouse embryos display defects in vascular patterning.

(A, C) Whole mount PECAM-1 staining of E10.5 wild type (A) and *Nf1*^{-/-} (C) mouse embryos reveals abnormal vascular patterning in *Nf1*^{-/-} embryos with an increased number of vessels and branching (dots at branch points), particularly evident in the somites (between dashed lines). Low-magnification insets show an overall increase in vascular staining in *Nf1*^{-/-} embryos. (E) Quantification of vessel branch points over 4 somites immediately rostral to the anterior limb buds at E10.5 shows a significant increase in *Nf1*^{+/-} and *Nf1*^{-/-} embryos compared to wild type (\pm SD). (B, D) Similar staining of stage-matched littermates at E11.5 reveals loss of the normal avascular zone around the developing eye (D) in *Nf1*^{-/-} embryos compared to wild type (B). (F) Quantification of abnormal eye vasculature shows a significant increase in the number of affected *Nf1*^{-/-} embryos compared to wild types ($p < 0.004$).

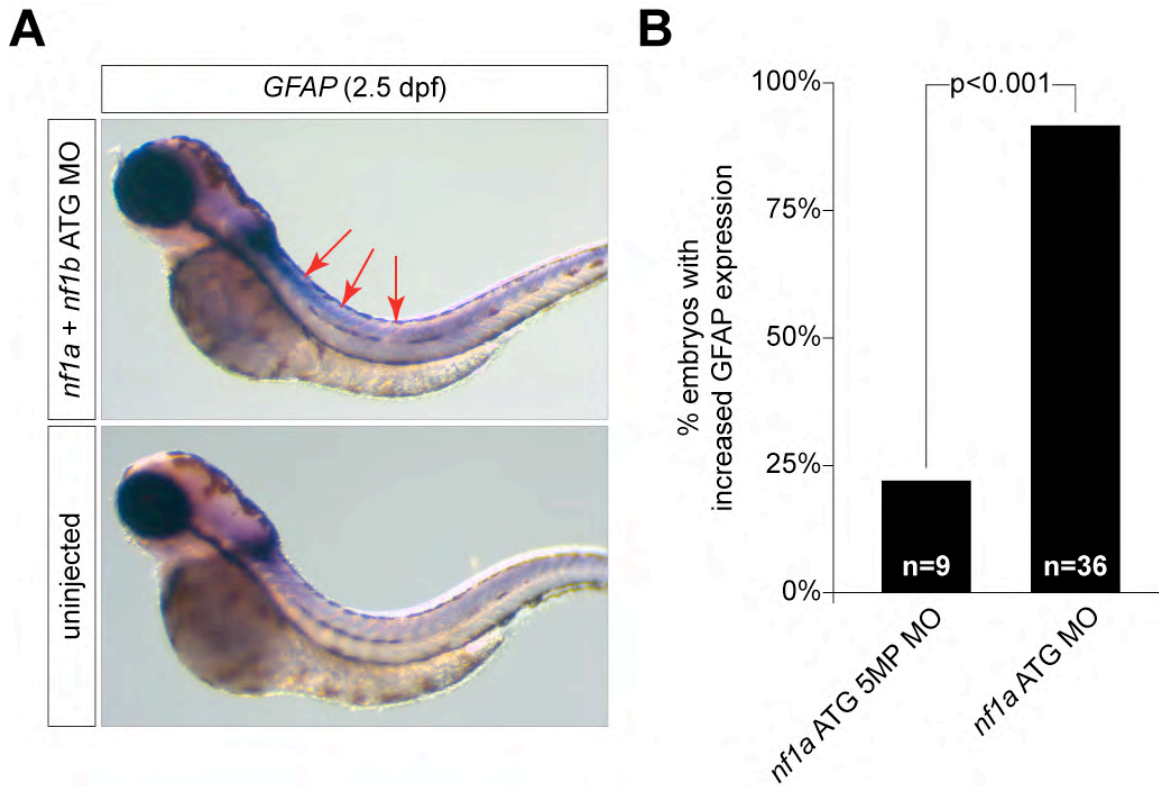


Figure 15. MO knockdown of *nf1a* and *nf1b* results in neural defects

(A) 2.5 dpf *nf1a/nf1b* compound morphant zebrafish embryos display a marked increase in the intensity and domain of *GFAP* expression by whole mount *in situ* hybridization when compared with stage-matched controls. (B) 92% of *nf1a* ATG morphant embryos were scored as having high levels of *GFAP* expression as compared to 22% of *nf1a* ATG 5MP MO (*nf1a* ATG 5-mispair control MO) injected embryos by blinded quantitative analysis ($p < 0.001$).

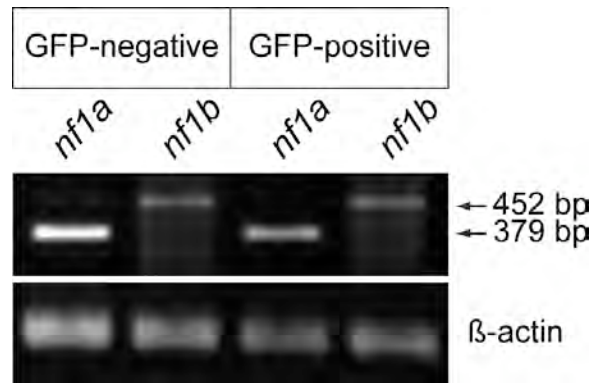


Figure 16. *nf1a* and *nf1b* are expressed in oligodendrocyte precursor cells at 3 dpf.

RT-PCR for *nf1a* and *nf1b* transcripts using RNA prepared from FACS-sorted cells of the 3 dpf spinal cord of *Tg(olig2:EGFP)* embryos based on GFP expression (GFP-positive or GFP-negative). Both *nf1a* and *nf1b* transcripts are expressed in each cell population.

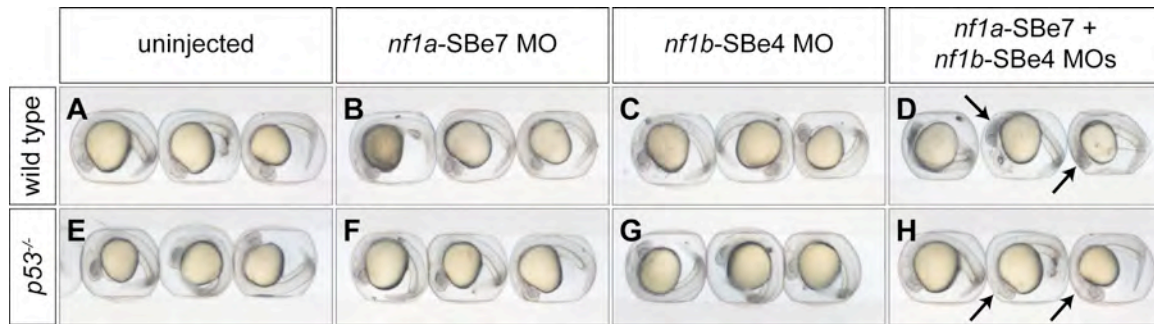


Figure 17. Brain necrosis due to morpholino toxicity is circumvented in *p53* mutant zebrafish.

The simultaneous knockdown of *nf1a* and *nf1b* transcripts by injecting *nf1a*-SBe7 and *nf1b*-SBe4 MOs induces brain necrosis, due to morpholino toxicity, by 24 hpf (arrows in D). This nonspecific side effect is rescued in the *p53* mutant background (arrows in H), improving embryo survival and allowing the phenotype of *nf1* deficiency to be analyzed at later stages.

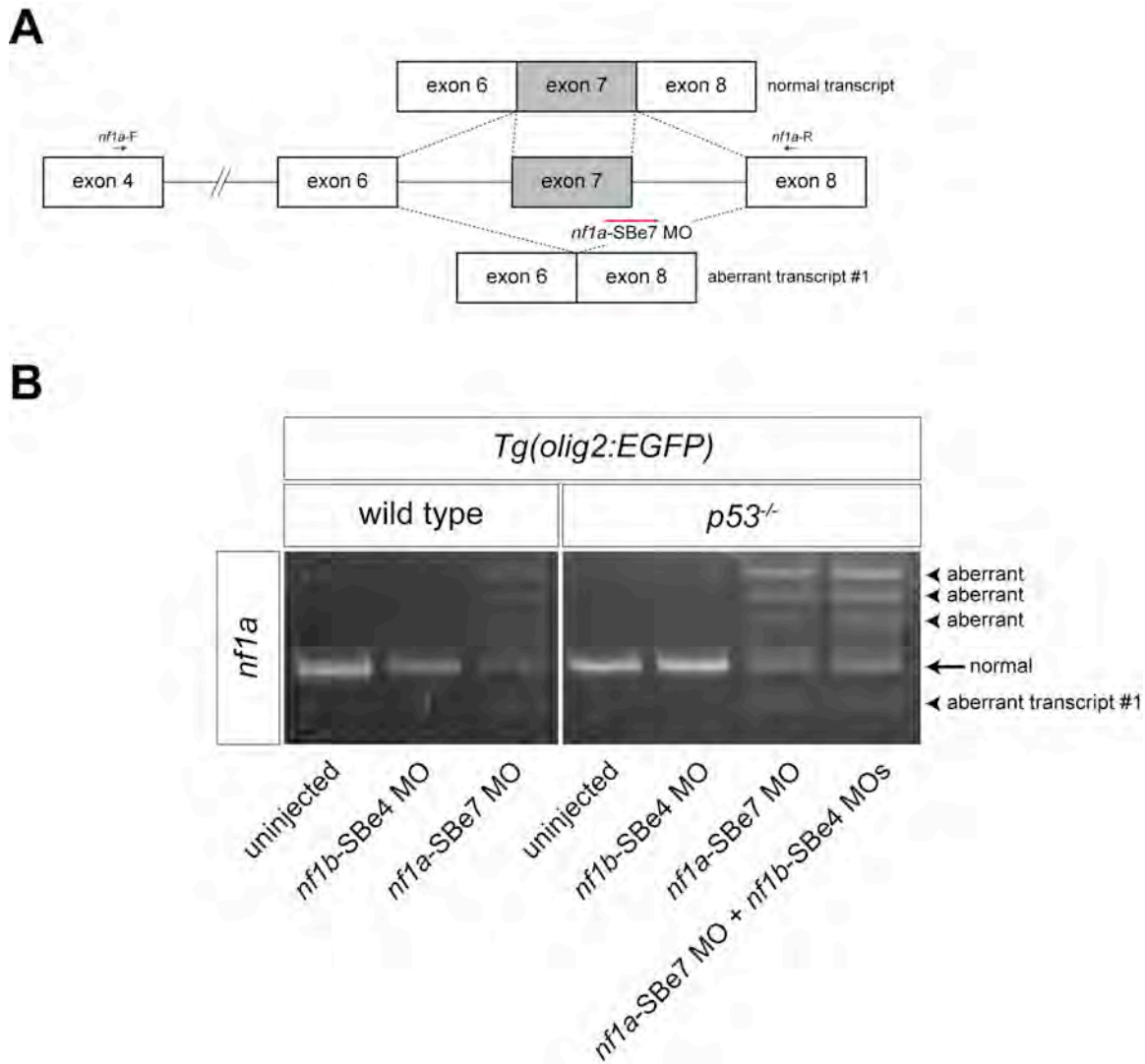


Figure 18. Morpholino against *nf1a* exon 7 splice donor efficiently blocks the normal splicing of its target.

(A) Diagram depicting the exon-intron boundaries, the normal transcript, and resultant aberrant transcript upon morpholino knockdown with *nf1a*-SBe7 MO, together with the positions of the primers and morpholino. (B) *nf1a*-SBe7 MO knockdown leads to several aberrant bands but only the lower aberrant band (aberrant transcript #1 in panel B) is depicted in the diagram for simplicity. When these aberrant bands were subcloned and sequenced, they contained either deletions of exon or the retention of additional intronic sequences between exons 6 and 7 or exons 7 and 8, all resulting in frame shifts in the coding sequence that would generate truncated peptides.

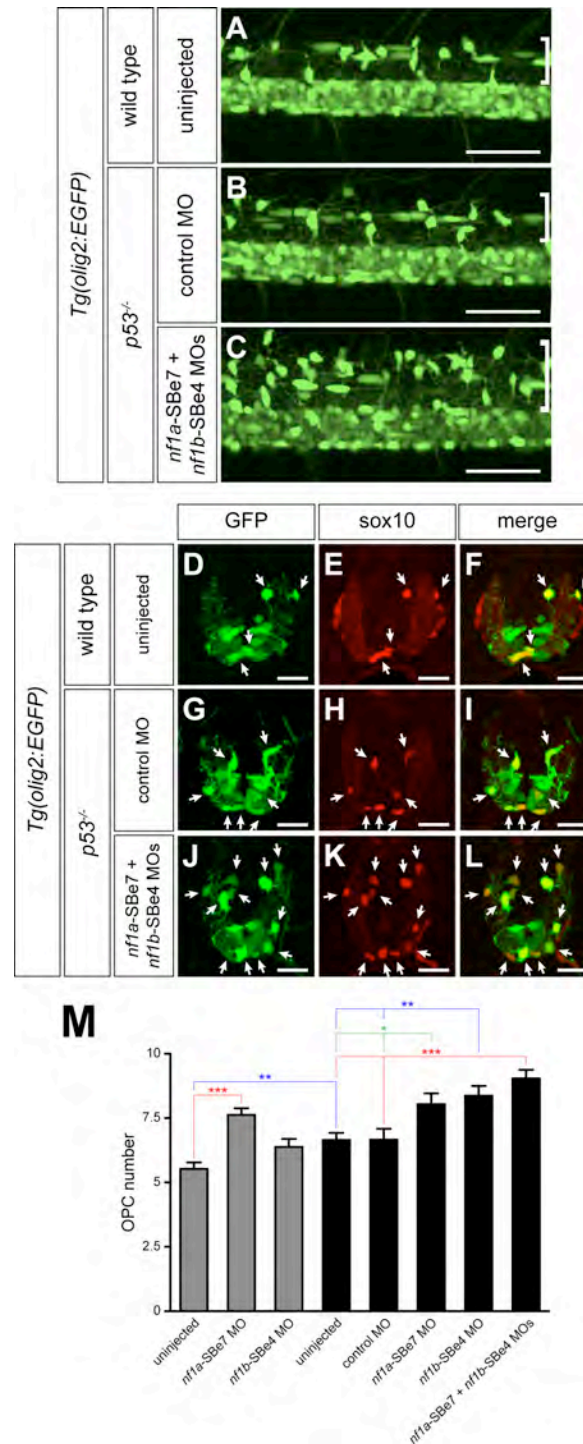


Figure 19. Knockdown of *nf1a* and *nf1b* leads to increased numbers of OPCs.

(A-C) Projected confocal images showing a lateral view of the spinal cord in live transgenic animals at 3 dpf. (A, D-F) Uninjected wild type *Tg(olig2:EGFP)* transgenic zebrafish. (B, G-I) Control morpholino injected *p53* mutant *Tg(olig2:EGFP)* embryo. (C, J-L) *p53* mutant *Tg(olig2:EGFP)* embryo injected with *nf1a* and *nf1b* morpholinos. (D-L) Transverse sections through the spinal cord of embryos at 3 dpf, with GFP (green) and sox10 (red) labeling to specifically visualize co-expressing OPCs (arrows). (M) Statistical analysis of mean \pm SEM numbers of GFP-positive/sox10-positive cells per section in *nf1a* MO-, *nf1b* MO-, or *nf1a* + *nf1b*-MO injected embryos at 3 dpf. Asterisks indicate statistical significance (* $p < 0.05$; ** $p < 0.005$; *** $p < 0.0005$). A-C Scale bars: 50 μ m; F, I, and L Scale bars: 20 μ m.

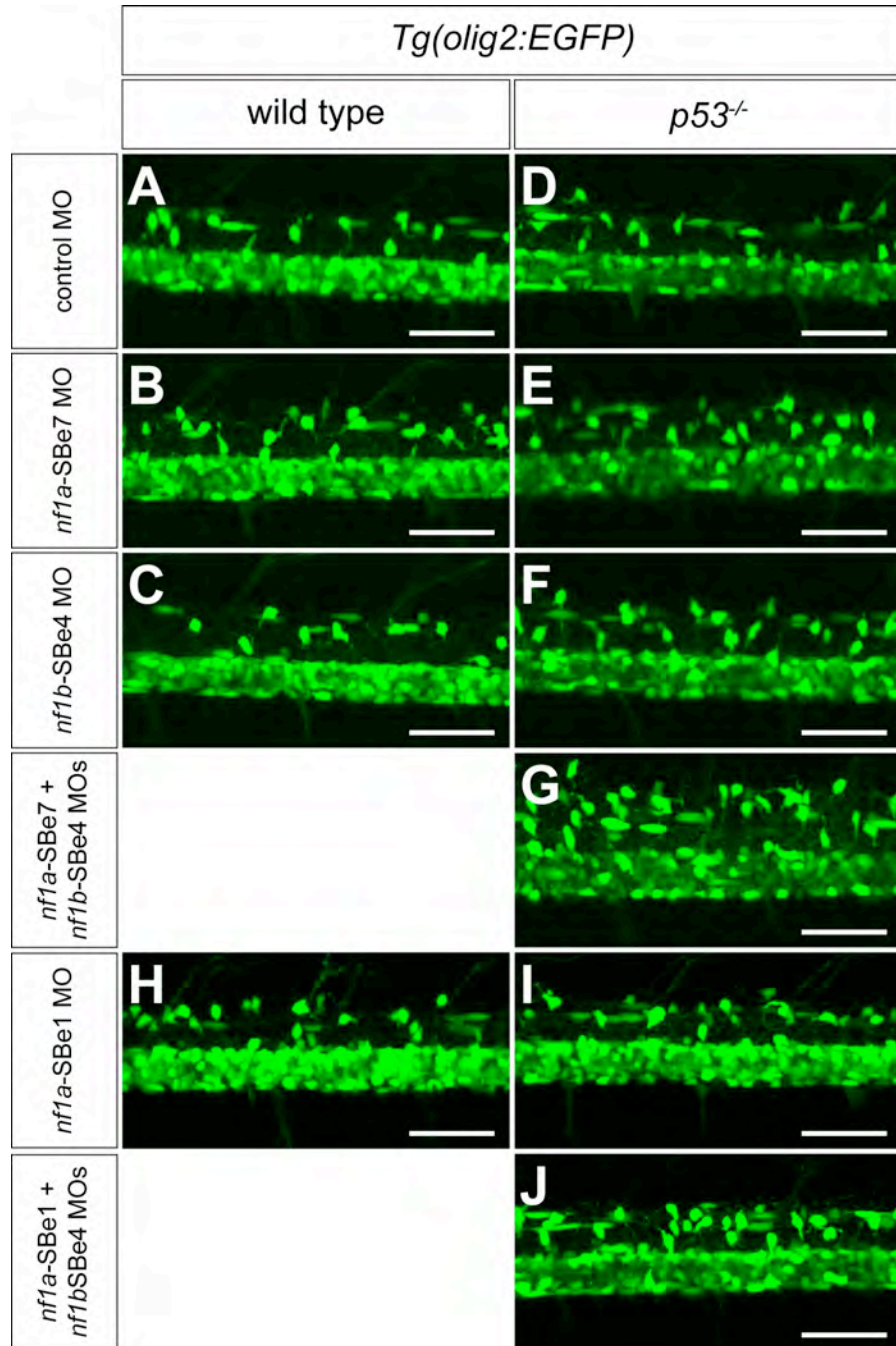


Figure 20. Increase in OPC number upon *nf1a/nf1b* knockdown is reproducible with multiple morpholinos.

(A-C, H) Wild type *Tg(olig2:EGFP)* embryo at 3dpf. (D-G, I-J) *p53* mutant *Tg(olig2:EGFP)* embryo at 3dpf. Panels A and D represent control MO- injected embryos; panels B and E, *nf1a*-SBe7 MO-injected; panels C and F, *nf1b*-SBe4 MO-injected; panel G, *nf1a*-SBe7 + *nf1b*-SBe4 MO-injected; panels H and I, *nf1a*-SBe1 MO-injected; and panel J, *nf1a*-SBe1 + *nf1b*-SBe4 MO-injected. Wild type *Tg(olig2:EGFP)* embryos injected with *nf1a*-SBe7 + *nf1b*-SBe4 MOs and *nf1a*-SBe1 + *nf1b*-SBe4 MOs are omitted because their developmental abnormalities, due to morpholino toxicity, compromise their survival to later stages of development. All are projected confocal images of the lateral spinal cord. Scale bars: 50 μ m.

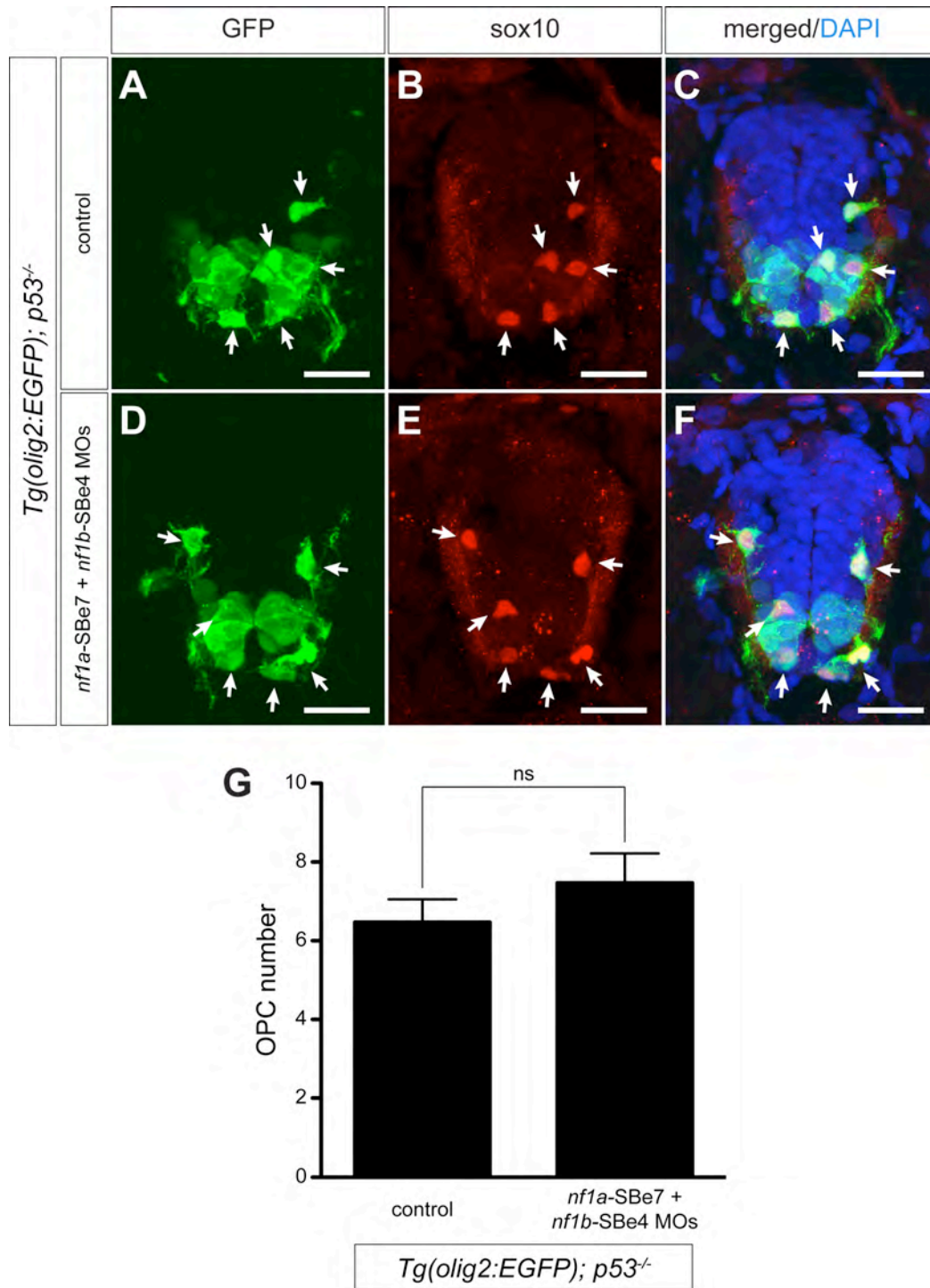


Figure 21. The number of *olig2:EGFP*; *sox10* double-positive OPCs does not increase significantly during early stages of OPC dorsal migration.

(A-C) control MO-injected *p53* mutant *Tg(olig2:EGFP)* embryo. (D-F) *nf1a-SBe7* MO + *nf1b-SBe4* MO-injected *p53* mutant *Tg(olig2:EGFP)* embryo. Transverse sections through the spinal cord of embryos at 2 dpf, labeling GFP (green) and *sox10* (red), to visualize double-positive OPCs (arrows). DAPI (blue) stains cell nuclei. (G) Statistical analysis of average numbers of *olig2:EGFP*; *sox10* double-positive cells per section in control or *nf1a-SBe7 + nf1b-SBe4* morphants at 2 dpf. Error bar indicates SEM; ns, not significant. Scale bars: 20 μ m.

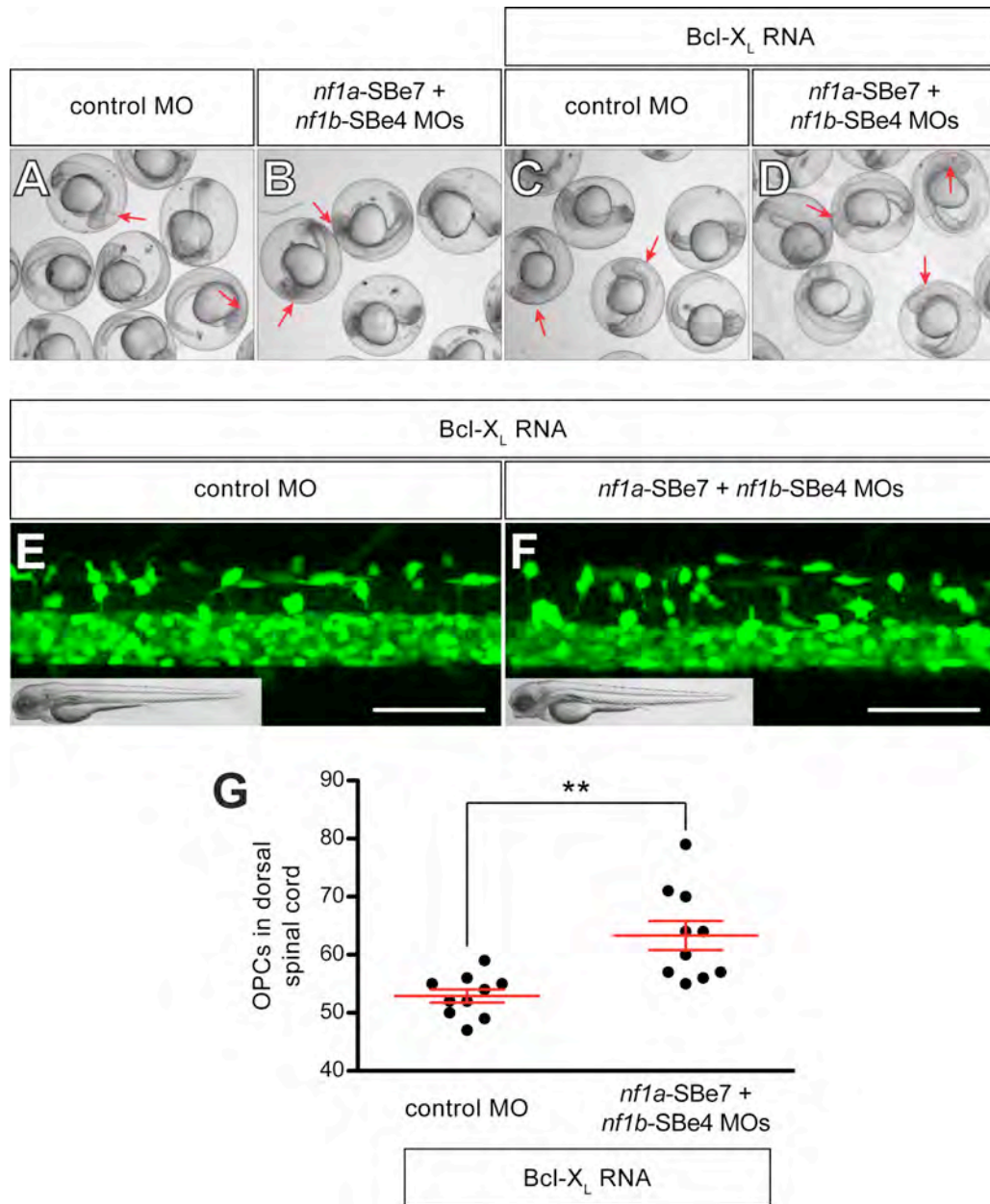


Figure 22. Co-injection of zebrafish *bcl-X_L* RNA in *nf1a/nf1b* double morphants blocks MO-induced apoptosis in wild type embryos.

(A, C) control MO; (B, D) *nf1a*-SBe7 + *nf1b*-SBe4 MOs; (A, B) no additional RNA-injected; (C, D) zebrafish *bcl-X_L* RNA-injected; (A-B) Wild type embryos injected with control MO or *nf1a*-SBe7 + *nf1b*-SBe4 MOs depicted 1 dpf. Note the apoptotic cell death in the brain of *nf1a*-SBe7 + *nf1b*-SBe4 morphants (arrows in B). (C-D) Wild type embryos injected with control MO or *nf1a*-SBe7 + *nf1b*-SBe4 MOs, together with zebrafish *bcl-X_L* RNA. The apoptosis in the brain due to *nf1a/nf1b* toxicity is prevented by addition of zebrafish *bcl-X_L* RNA (arrows in D). (E-F) Projected confocal images showing lateral view of the spinal cord in 3 dpf *Tg(olig2:EGFP)* embryos. An increased number of OPCs is appreciated in the *nf1a*-SBe7 + *nf1b*-SBe4 injected animals co-injected with *bcl-X_L* RNA (F) as compared with controls (E). Insets show the bright field images of the embryos used for confocal imaging. Scale bars: 50 μ m. (G) Quantitation of OPC number in the dorsal spinal cord (SC) of 10 embryos per condition, demonstrating significantly increased numbers of OPCs in *nf1a/nf1b* compound morphants (** $p < 0.005$). The data is presented as means \pm SEM.

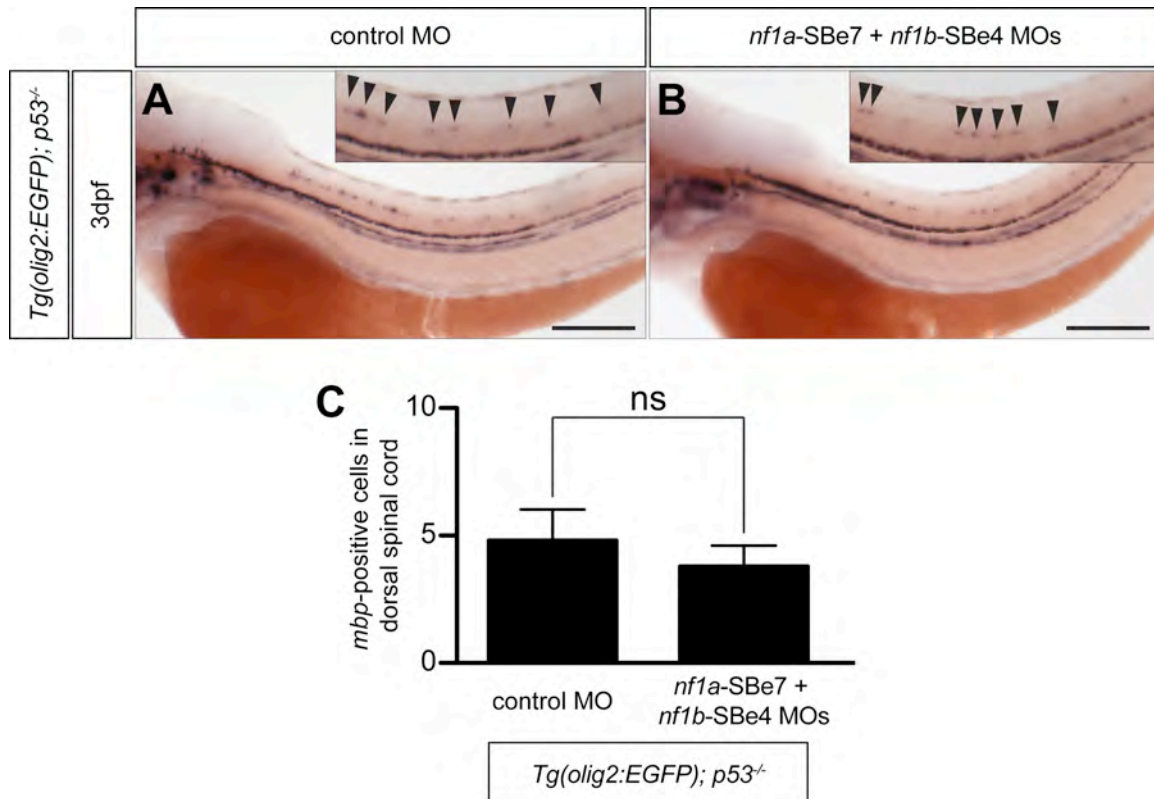


Figure 23. No difference in the differentiation of OPCs into oligodendrocytes upon *nf1a/nf1b* knockdown by whole mount *myelin basic protein (mbp)* in situ hybridization.

(A) Control MO-injected *p53* mutant *Tg(olig2:EGFP)* embryo at 3dpf. (B) *nf1a*-SBe7 + *nf1b*-SBe4 MO-injected *p53* mutant *Tg(olig2:EGFP)* at 3dpf. Scale bars: 200 μ m. Arrows in insets of A and B indicate the *mbp*-positive oligodendrocytes. (C) Statistical analysis of the number of *mbp*-positive oligodendrocytes of the dorsal spinal cord (SC) over the yolk extension. Ten embryos were analyzed for each condition.

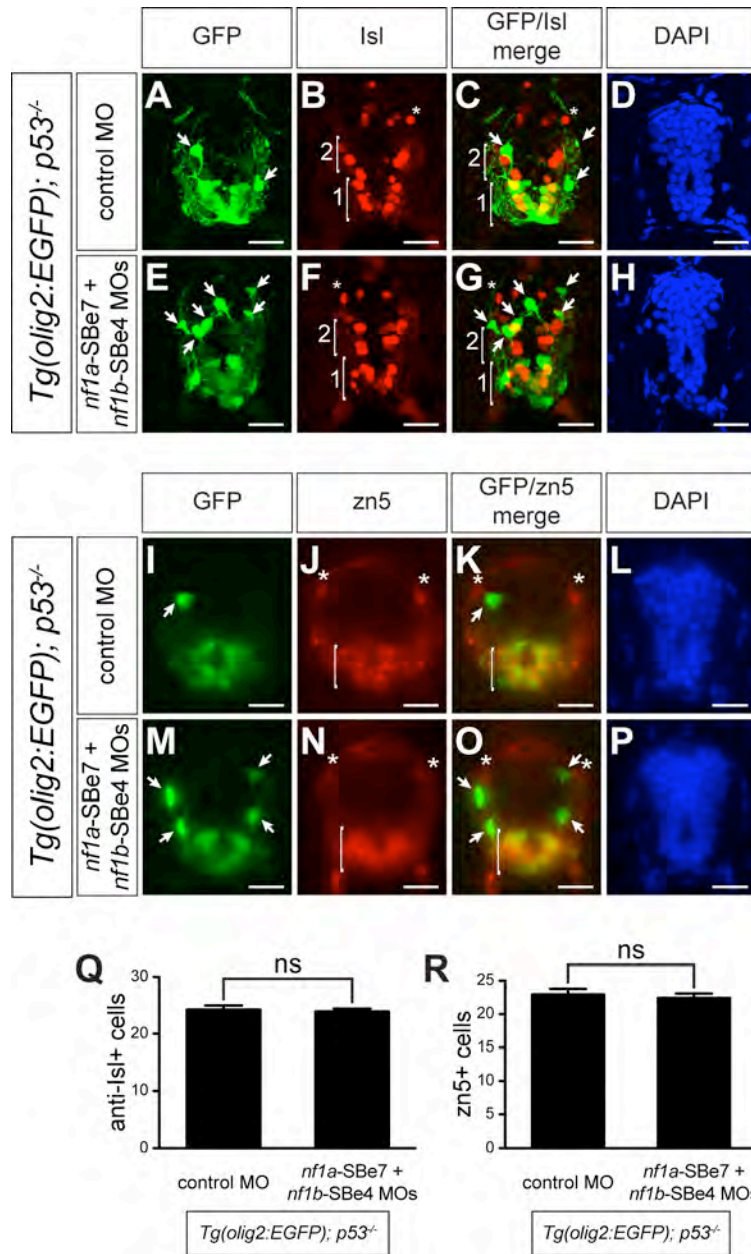


Figure 24. Spinal cord neurons are not affected by *nf1a/nf1b* loss.

(A-D, I-L) *p53* mutant *Tg(olig2:EGFP)* embryos injected with control morpholino. (E-H, M-P) *p53* mutant *Tg(olig2:EGFP)* embryo injected with *nf1a*-SBe7 and *nf1b*-SBe4 morpholinos. (A-H) Projected confocal images of transverse sections labeled with the anti-Isl antibody show subsets of primary/secondary motor neurons (bracket 1), interneurons (bracket 2), and putative Rohon Beard sensory neurons (asterisk). Green, *olig2:EGFP*; red, anti-Isl; blue, DAPI. Arrows in panels A, C, E, and G designate dorsal OPCs. (I-P) Fluorescence images of transverse sections labeled with the zn5 antibody showing secondary motor neurons. Statistical analyses of the numbers of anti-Isl- (Q) or zn5- (R) positive cells show no significant differences. Green, *olig2:EGFP*; red, zn5; blue, DAPI. Arrows in panels I, K, M, and O indicate dorsal OPCs; asterisks in J, K, N, O indicate the dorsal lateral fasciculus; brackets in J, K, N, O indicate secondary motoneurons. Scale bars: 20 μ m.

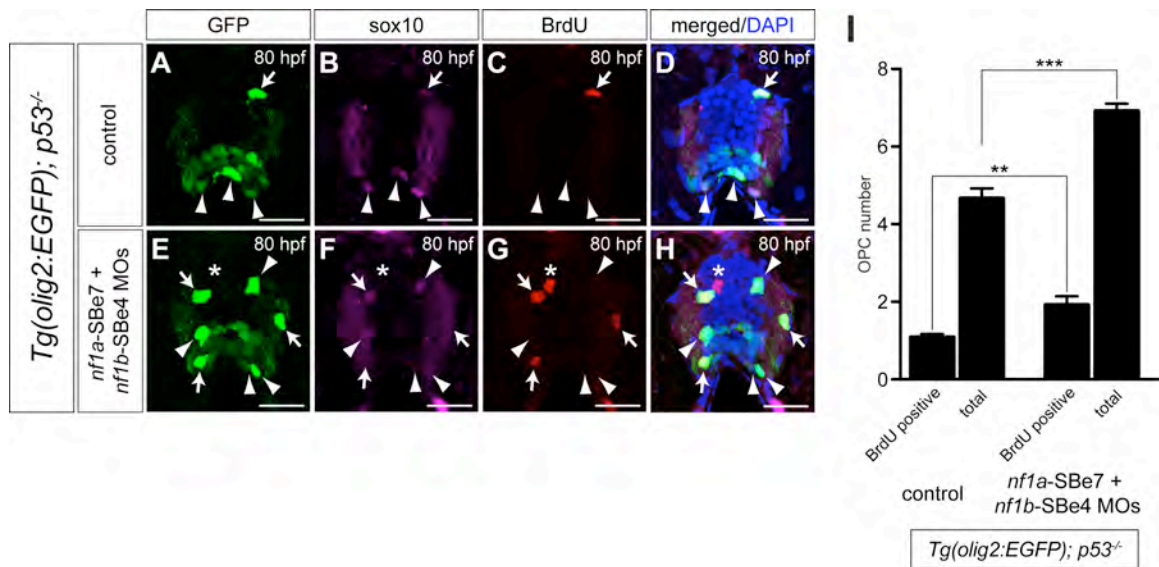


Figure 25. *nf1a/nf1b* loss leads to increased BrdU incorporation in OPCs. Projected confocal images of transverse spinal cord sections through *p53* mutant *Tg(olig2:EGFP)* at 80 hpf. (A, E) Green, *olig2:EGFP*; (B, F) magenta, anti-sox10; (C, G) red, anti-BrdU; (D, H) overlay merged with DAPI (blue). (A-D) Embryos injected with control morpholino. (E-H) Embryos injected with *nf1a-SBe7* and *nf1b-SBe4* morpholinos. (A-H) Arrows indicate dividing OPCs (GFP/sox10/BrdU triple-positive), while arrowheads denote non-dividing OPCs (GFP/sox10 double-positive; BrdU-negative). (E-H) Asterisks denote a GFP/sox10 double-negative; BrdU-positive cell in the spinal cord, representing a dividing neuron. (I) Statistical analysis of mean \pm SEM numbers of GFP/sox10/BrdU triple-positive ('BrdU') or total OPCs ('tOPCs') per section in control or *nf1a-SBe7 + nf1b-SBe4* morphants at 3 dpf. OPCs incorporating BrdU are increased in the *nf1a-SBe7 + nf1b-SBe4* morphants compared to controls, indicating higher proliferative activity. Asterisks indicate statistical significance (** $p < 0.005$; *** $p < 0.0005$). Scale bars: 20 μ m.

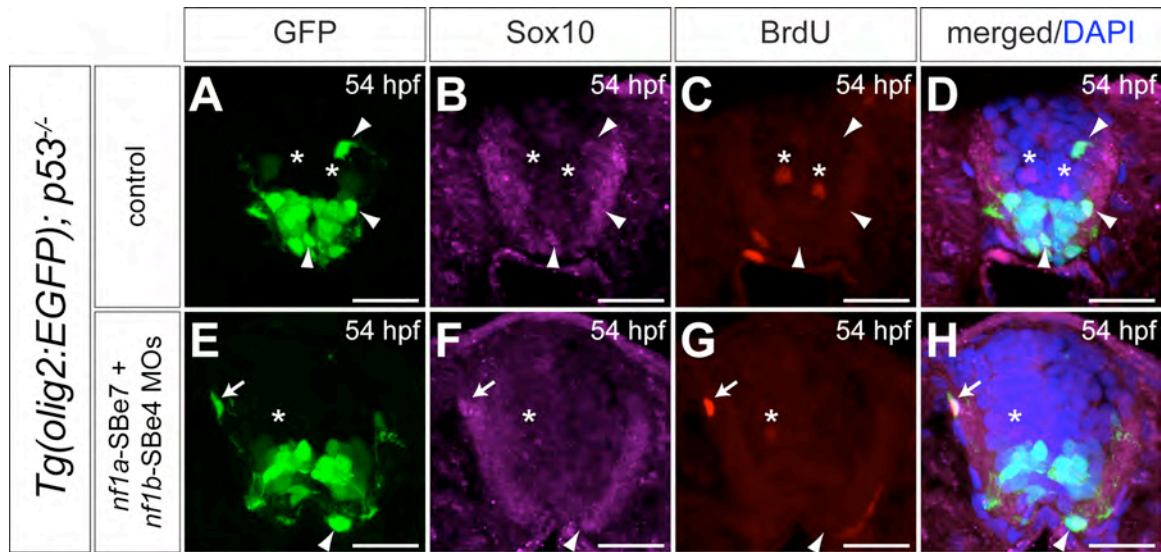


Figure 26. The proliferative activity of OPCs during early stages of OPC dorsal migration is at basal level irrespective of *nf1a/nf1b* knockdown.

Projected confocal images of transverse spinal cord sections of *p53* mutant *Tg(olig2:EGFP)* zebrafish embryos at 54 hpf. (A, E) Green, *olig2:EGFP*; (B, F) magenta, anti-sox10; (C, G) red, anti-BrdU; (D, H) overlay merged with DAPI (blue). (A-D) Embryos injected with control morpholino. (E-H) Embryos injected with *nf1a*-SBe7 + *nf1b*-SBe4 morpholinos. (A-H) Arrowheads denote non-dividing OPCs (GFP/sox10 double-positive; BrdU-negative) while asterisks denote dividing cells in the spinal cord that are non-OPCs (GFP/sox10 double-negative; BrdU-positive), presumably a subset of neurons. (E-H) Arrows denote dividing OPCs (GFP/sox10/BrdU triple-positive). Although there is a rare population of dividing OPCs at 54hpf (E-H), BrdU-positive cells in the spinal cord are generally very rare in either control or *nf1a/nf1b* compound morphants and no significant difference is found at this stage. Scale bars: 20 μ m.

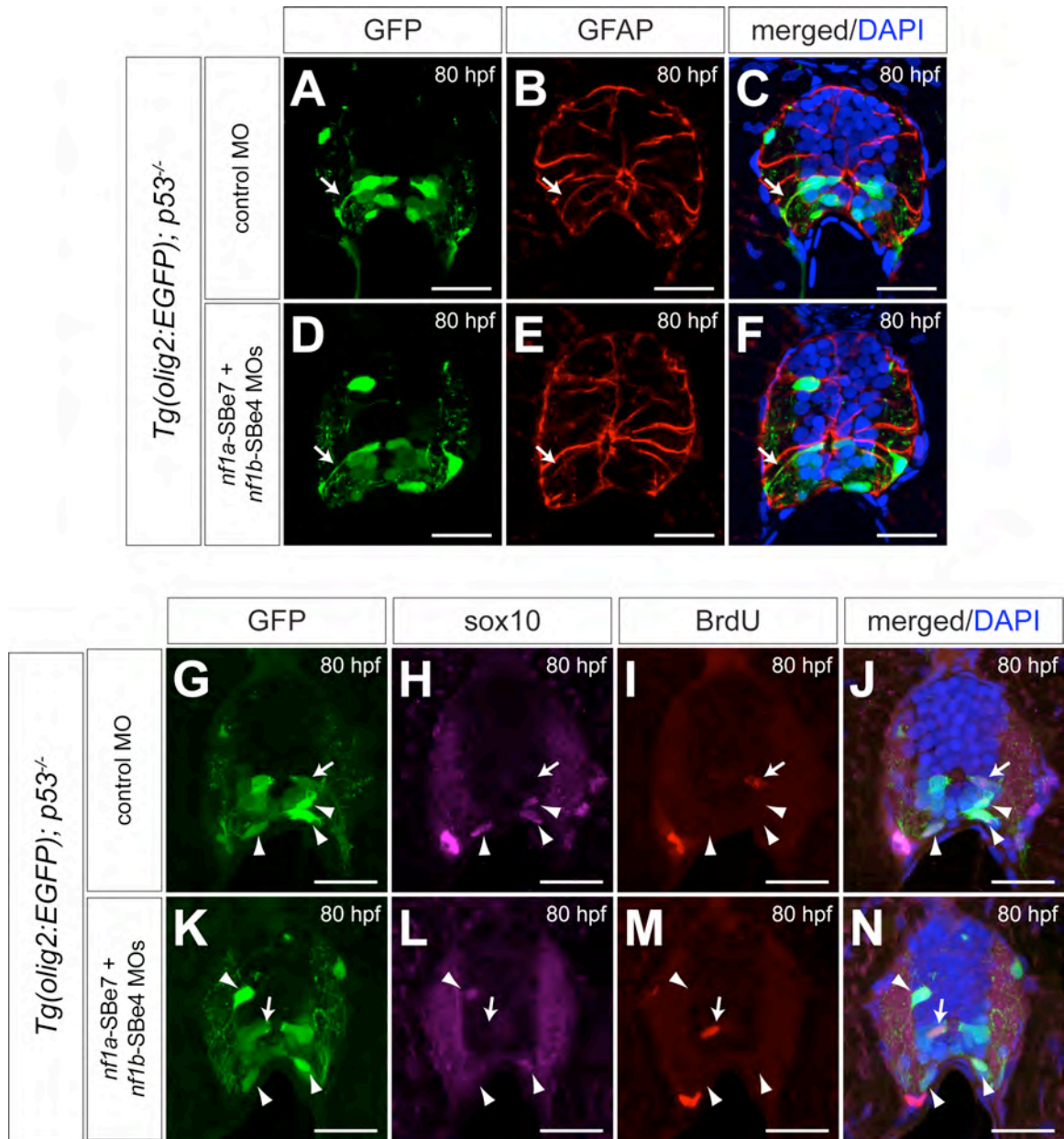


Figure 27. The number and proliferative activity of radial glia in the spinal cord remain unchanged upon *nf1a/nf1b* knockdown.

Projected confocal images of transverse spinal cord sections of *p53* mutant *Tg(olig2:EGFP)* embryos at 80 hpf. (A, D, G, K) Green, *olig2:GFP*; (H, L) Magenta, anti-sox10; Red, (B, E) anti-GFAP or (I, M) anti-BrdU; (C, F, J, N) Overlay merged with DAPI (blue). (A-C, G-J) Embryos injected with control MO. (D-F, K-N) Embryos injected with *nf1a*-SBe7 + *nf1b*-SBe4 morpholinos. Arrows in A-F denote radial glial cells with the characteristic fusiform-shaped cell body and process (GFP/GFAP double-positive) that extends to the pial surface of the spinal cord. Arrows in G-N denote dividing radial glia (GFP-positive/sox10-negative/BrdU-positive, based on their cell morphology with the processes). No difference in the number of average or dividing radial glia was appreciated. The projection thickness of images in A-F is 4 μ m for the clear visualization of the radial glia. Scale bars: 20 μ m.

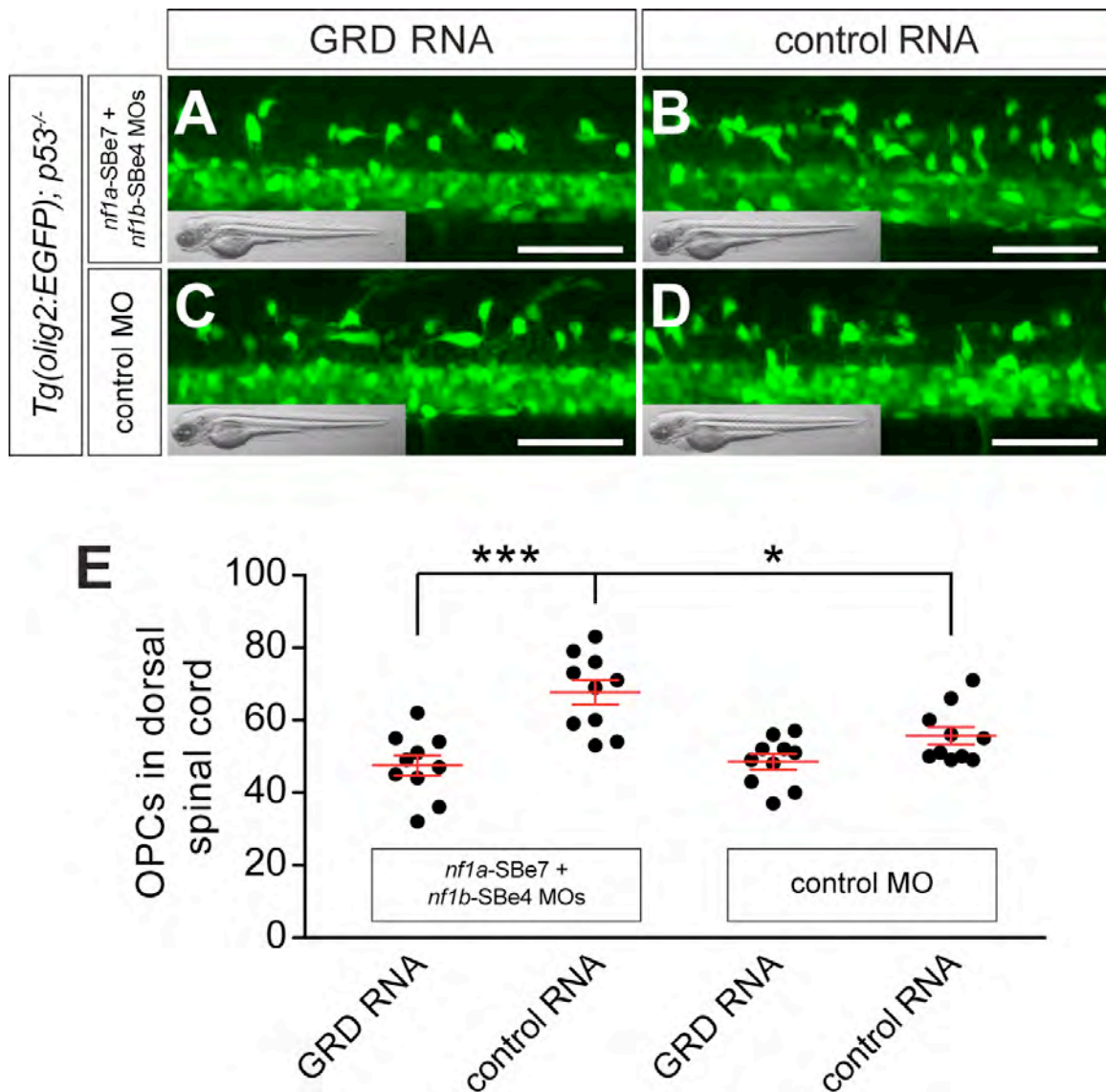


Figure 28. Forced expression of the human *NF1* GRD is sufficient to rescue the proliferative OPC phenotype resulting from *nf1a/nf1b* knockdown.

(A-D) Projected confocal images showing the lateral view of the spinal cord of a *p53* mutant *Tg(olig2:EGFP)* zebrafish embryo at 3 dpf. (A, B) *nf1a*-SBe7 + *nf1b*-SBe4 MOs; (C, D) control MO; (A, C) human *NF1* GRD RNA-injected; (B, D) mCherryRed (control) RNA-injected. Insets show the bright field images of the embryos used for confocal imaging and demonstrate normal overall morphologies in all cases. Scale bars: 50 μ m. (E) Graph showing the number of OPCs, represented by individual points, in the dorsal spinal cords of 10 embryos for each condition at 3 dpf. (* $p < 0.05$; *** $p < 0.001$). The data is presented as means \pm SEM.

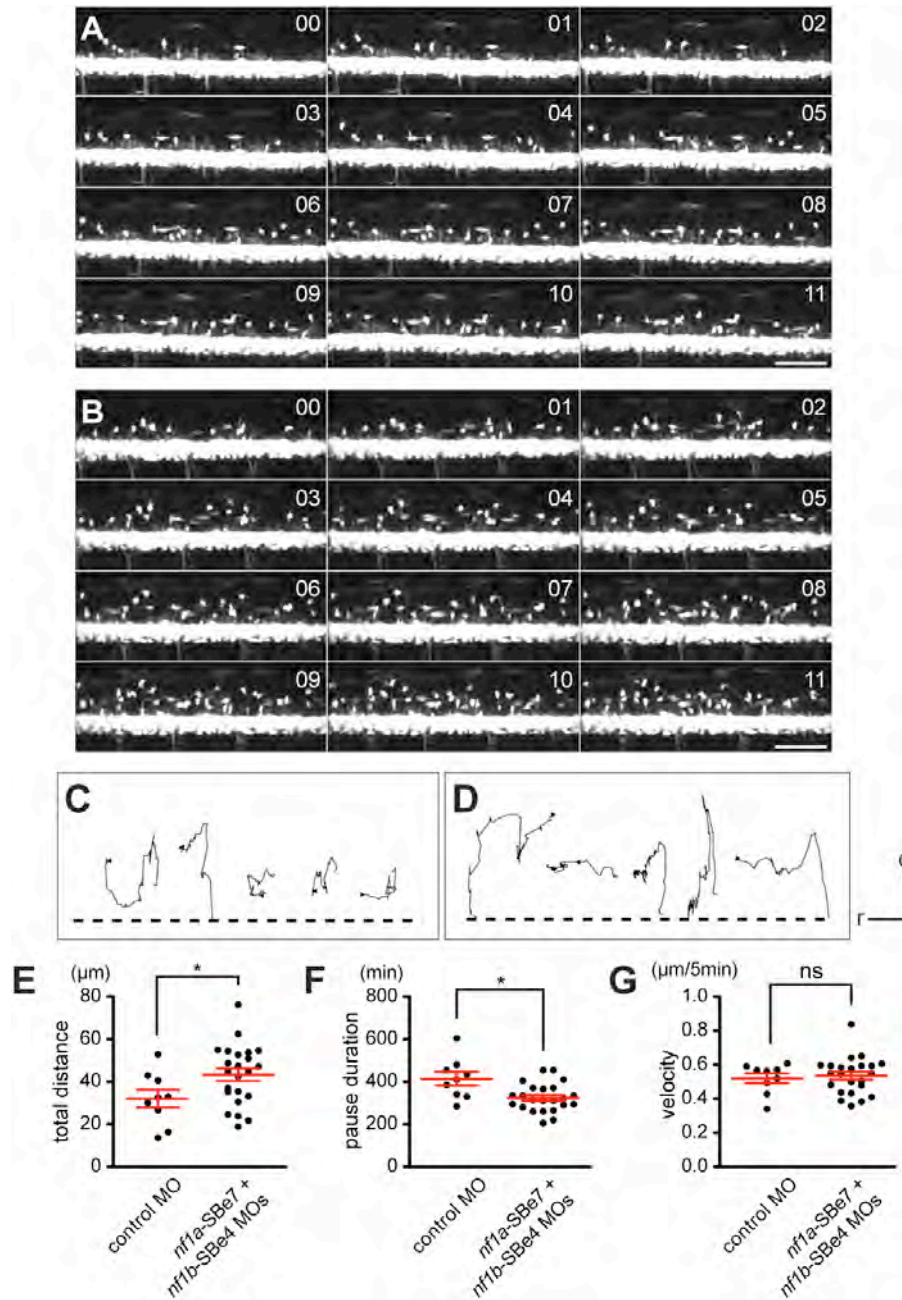


Figure 29. *nf1a/nf1b* loss affects the migration of OPCs.

(A, C) An uninjected *p53* mutant *Tg(olig2:EGFP)* control zebrafish embryo; (B, D) A *p53* mutant *Tg(olig2:EGFP)* zebrafish embryo injected with *nf1a*-SBe7 + *nf1b*-SBe4 MOs. (A, B) Montage of images from 12-hour time-lapse movies between 60 hpf to 72 hpf showing the movements of OPCs every hour. Numbers in each panel denote the hour(s) after the start of imaging. (C, D) Cell migration paths are shown for five OPCs that traveled the farthest during the observation period. In both conditions, migration patterns are highly dynamic. Arrowheads indicate the endpoint of the cell's migration. The dashed lines represent the dorsal-most GFP-positive domains of the ventral spinal cord (top, dorsal (d); left, rostral (r)). (E) Graph showing the total distance OPCs travel with or without *nf1a/nf1b* loss. (F) Graph showing the total time individual OPCs spent pausing. (G) Graph showing the velocity of OPCs calculated from when they were actively migrating. All individual OPCs (represented by single points) that could be observed in the field of view throughout the entire 12-hour imaging period were traced and used in this analysis (n=9 for uninjected control embryos, n=23 for *nf1a/nf1b* morphant embryos). The data in E-G are reported as mean \pm SEM; asterisks indicate nonparametric statistical significance (* p<0.05; ns, not significant). Scale bars (A, B): 25 μ m. Scale bars (C, D): X-axis (10 μ m) and Y-axis (5 μ m).

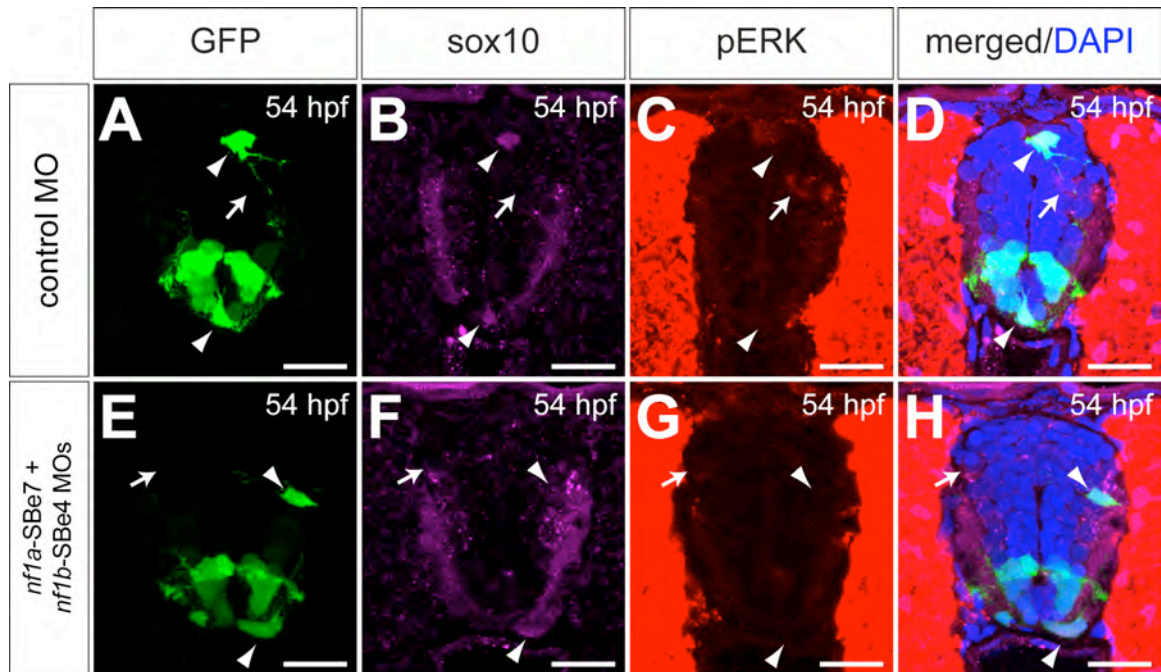


Figure 30. ERK signaling in the spinal cord is not upregulated upon *nf1a/nf1b* knockdown during early stages of OPC dorsal migration.

Projected confocal images of transverse spinal cord sections of *p53* mutant *Tg(olig2:EGFP)* zebrafish embryos at 54 hpf. (A, E) Green, *olig2:EGFP*; (B, F) Magenta, anti-sox10; (C, G) Red, anti-pERK; (D, H) overlay merged with DAPI (blue). (A-D) Embryo injected with control MO. (E-H) Embryo injected with *nf1a*-SBe7 + *nf1b*-SBe4 MOs. Arrows indicate the pERK-positive cells in the spinal cord, while arrowheads indicates OPCs (GFP/sox10 double-positive) that are pERK-negative. No difference in pERK staining is found between control and *nf1a*-SBe7 + *nf1b*-SBe4 morphants at this stage. Scale bar: 20 μ m.

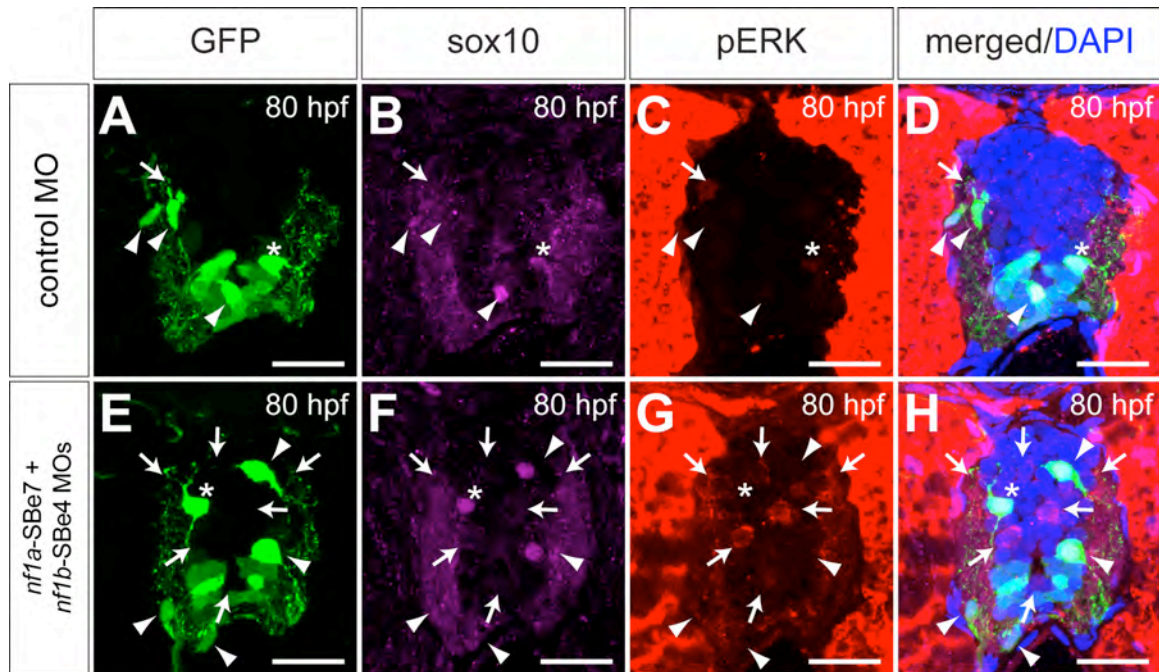


Figure 31. *nf1a/nf1b* loss activates the ERK pathway in the spinal cord at 80 hpf.

Projected confocal images of transverse spinal cord sections at 80 hpf of *p53* mutant *Tg(olig2:EGFP)* zebrafish embryos. (A, E) Green, *olig2:EGFP*; (B, F) Magenta, anti-sox10; (C, G) Red, anti-pERK; (D, H) overlay merged with DAPI (blue). (A-D) Control morphants; (E-H) *nf1a*-SBe7 + *nf1b*-SBe4 morphants. Increased numbers of pERK-positive cells were detected in the spinal cord of *nf1a*-SBe7 + *nf1b*-SBe4 morphants (arrows in G), compared to controls (arrow in C). Arrowheads denote GFP/sox10 double-positive OPCs, which are predominately pERK negative. A minor OPC population is pERK-positive (asterisks). Scale bars: 20 μ m.

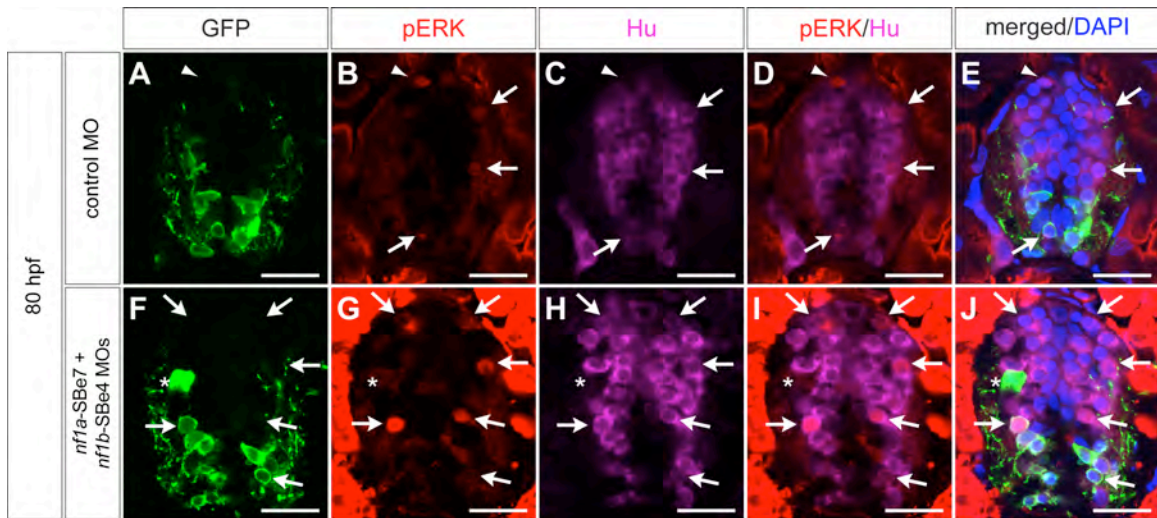


Figure 32. pERK-positive cells in the spinal cords if *nf1a/nf1b* morphants are neurons.

Projected confocal images of transverse spinal cord sections of *p53* mutant *Tg(olig2:EGFP)* zebrafish embryos at 80hpf. (A, E) Green, *olig2:EGFP*; (B, F) Magenta, anti-pERK; (C, G) Red, anti-Hu; (D, I) merge of anti-pERK and anti-Hu; (E, J) overlay merged with DAPI (blue). (A-E) Embryo injected with control MO. (F-J) Embryo injected with *nf1a*-SBe7 + *nf1b*-SBe4 MOs. Most pERK-positive cells co-localize with the neuronal marker HuC/D (arrows), indicating that they are neurons, while a small population of GFP-negative and Hu-negative cells of unknown identify are observed (arrowheads in panels A-E). Although relatively weak, OPCs are occasionally pERK-positive (asterisks in panels F-J). Scale bars: 20 μ m.

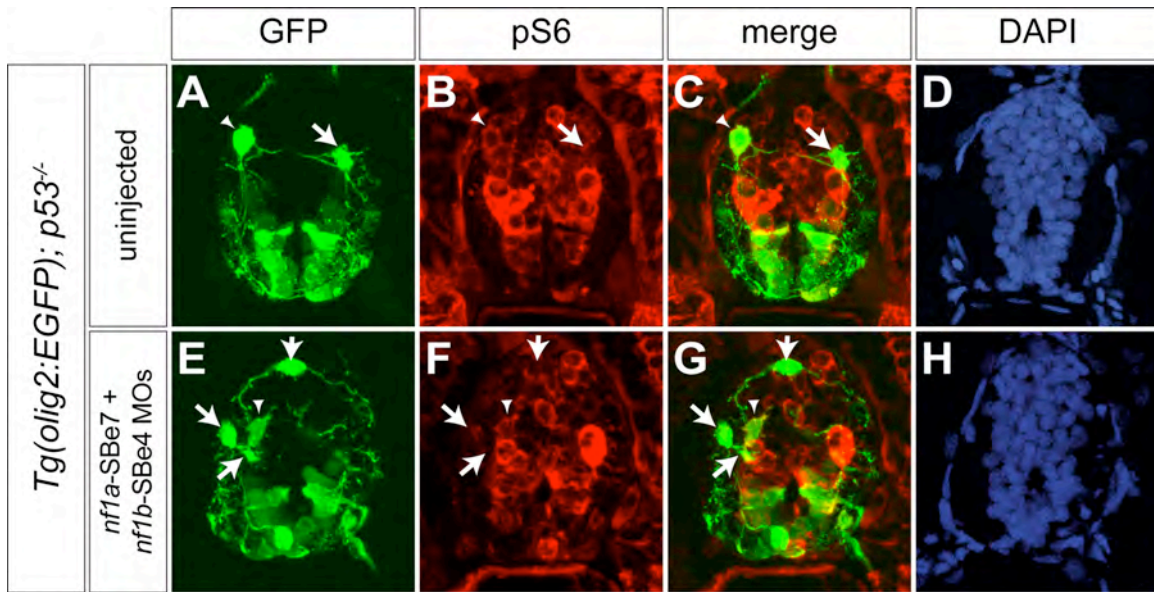


Figure 33. Phosphorylation of S6 ribosomal protein is not perturbed in the spinal cord at 3 dpf following *nf1a/nf1b* loss.

Projected confocal images of transverse spinal cord sections from *p53* mutant *Tg(olig2:EGFP)* zebrafish embryos. (A, E) Green, *olig2:EGFP*; (B, F) Red, pS6; (C, G) merge; (D, H) Blue, DAPI. (E-H) *nf1a*-SBe7 + *nf1b*-SBe4 MO-injected embryos display no obvious differences in pS6 staining in the spinal cord when compared with uninjected controls (A-D). GFP-positive OPCs were rarely pS6-positive (arrowheads) and were more often found to be pS6-negative (arrows denote GFP-positive/pS6-negative cells).

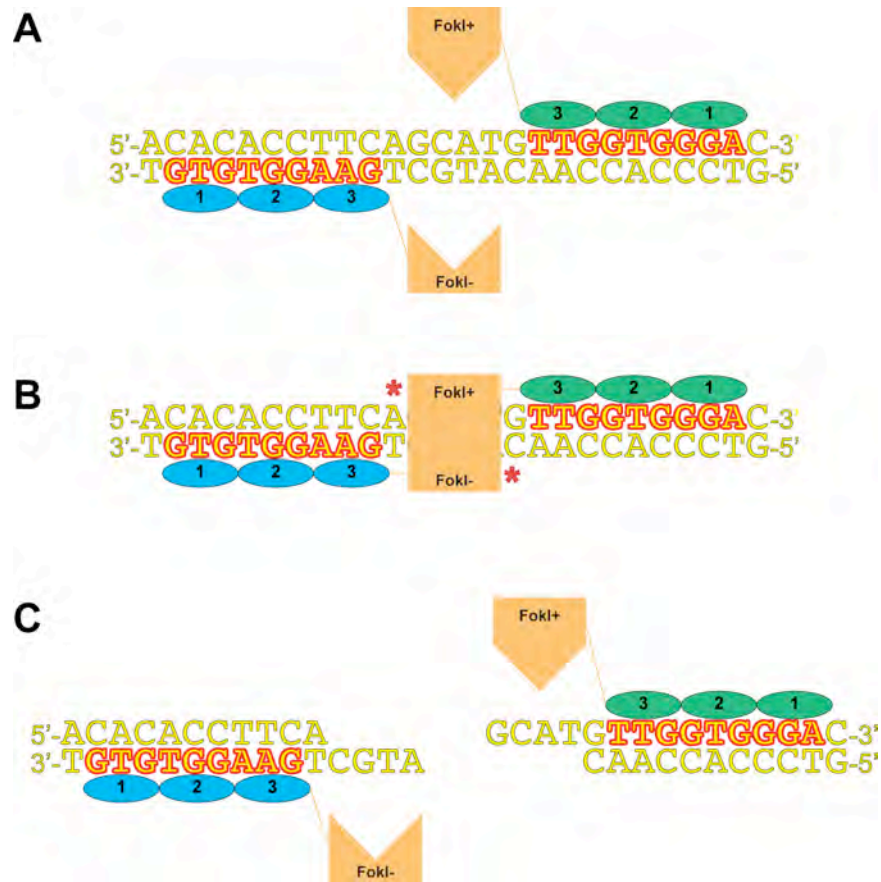


Figure 34. Overview of ZFN-mediated DNA cleavage.

ZFN-mediated DNA cleavage requires assembly of individual ZFNs on the DNA target with a specific geometry. (A) The portion of the ZFN that imparts sequence-specific binding recognizes a 9 bp element, with three individual fingers each responsible for binding a 3 bp subsite. The paired recognition elements must be in an inverted orientation and separated by a 5 to 6 bp spacer in order for the nuclease domains of the ZFNs to effectively dimerize and mediate DNA cleavage (represented by asterisks) (B). (C) A double strand break is introduced at the target site of the ZFNs.

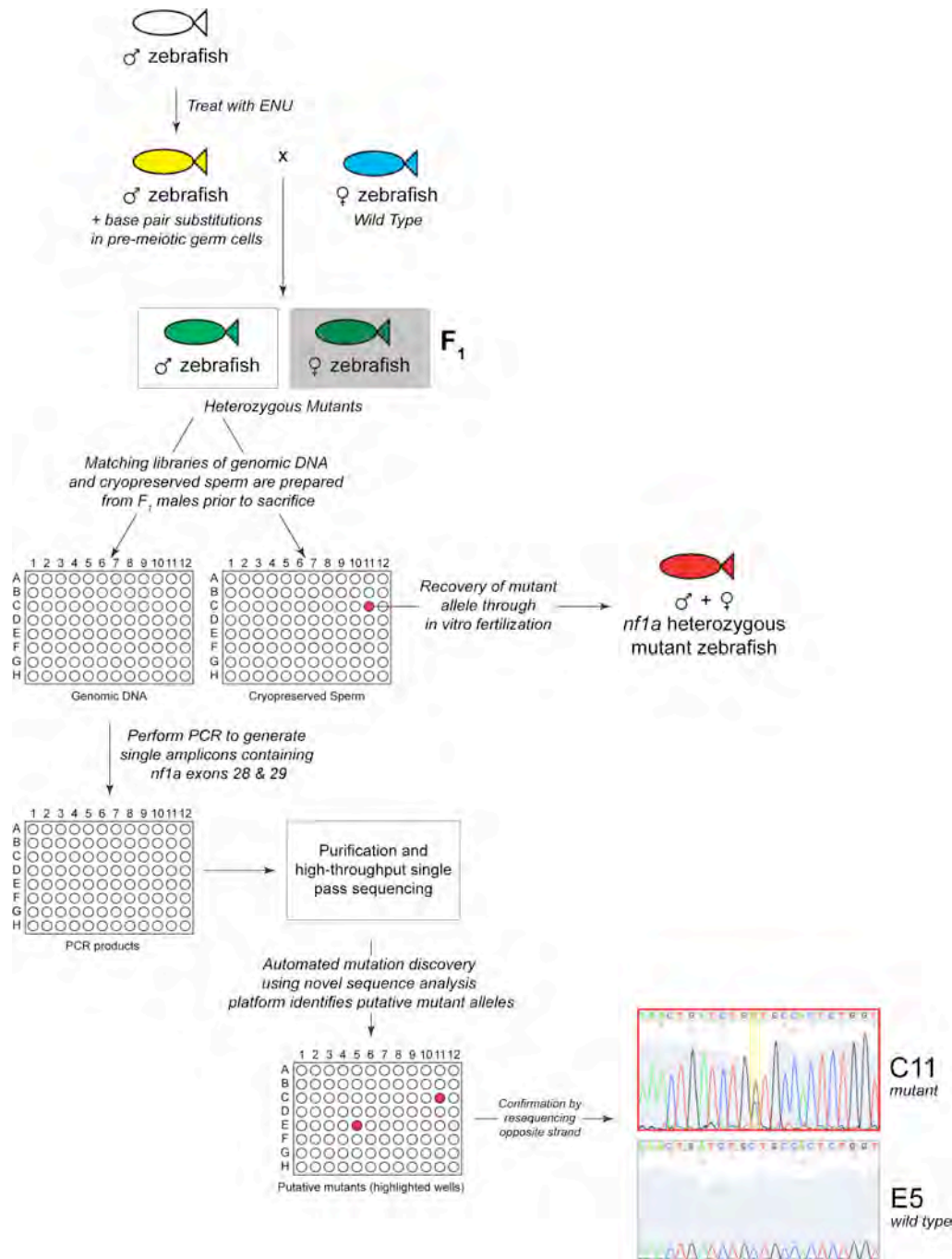


Figure 35. Overview of TILLING procedure with screening by direct sequencing.

An overview of the TILLING procedure using a direct sequencing approach for screening. Briefly, male zebrafish are treated with ENU, inducing single base pair substitutions in pre-meiotic germ cells. These fish are outcrossed to wild type females, generating F₁ animals that are heterozygous for these mutations. Dual libraries of genomic DNA and cryopreserved sperm are constructed from F₁ male animals, which are subsequently sacrificed. Genomic DNA is PCR amplified in a specific region of interest (in our case *nf1a* exons 28 and 29), which is sequenced by single pass Sanger dye-terminator sequencing. Results are analyzed to identify putative mutations that lead to amino acid changes, with samples identified as positive rescreened by sequencing the opposite strand.

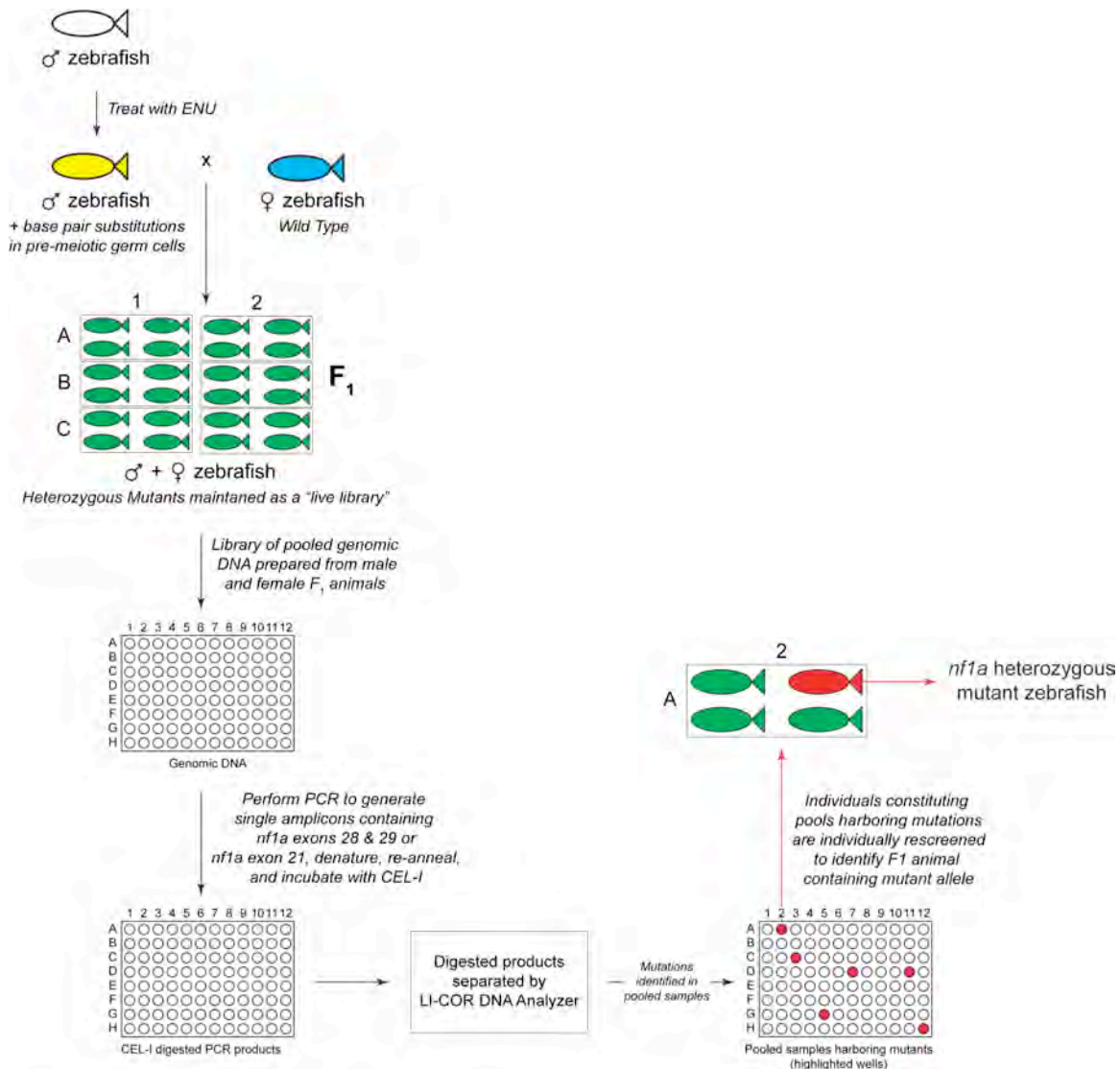


Figure 36. Overview of TILLING procedure with screening by CEL-I method.

An overview of the TILLING procedure using the CEL-I method for screening. Again, male zebrafish are treated with ENU, inducing single base pair substitutions in pre-meiotic germ cells. These fish are outcrossed to wild type females, generating F₁ animals that are heterozygous for these mutations. Genomic DNA samples from male and female F₁ animals are combined to generate a pooled library, with the F₁ animals maintained as a "live library". Genomic DNA is PCR amplified in a specific region of interest (in our case *nf1a* exons 28 and 29 as well as *nf1a* exon 21). In this case, the PCR primers are labeled with fluorescent probes. The PCR products are heated, allowed to re-anneal, and incubated with CEL-I enzyme. The products of the CEL-I digestion are separated by acrylamide electrophoresis using a LI-COR DNA analyzer. In pools identified to contain putative mutants, the individual animals comprising that pool are rescreened to identify which contains the mutation.

```

-----Exon 21-----
Ala Trp Glu Asp Thr Tyr Ala Lys Trp Glu Gln Ala Thr Lys Gln
GCA TGG GAA GAC ACA TAT GCA AAG TGG GAG CAA GCT ACA AAA CAG

-----Exon 21-----
Ile Leu Asn His Pro Lys Asn Lys Val Glu Asp Gly Gln Val Val
ATA CTC AAC CAC CCA AAA AAC AAA GTG GAA GAT GGA CAG GTA GTT

-----Exon 21-----
Asn Ile Arg Leu Val Asn Tyr Phe Ile Phe Phe Ser Ile His Gly
AAC ATA AGA TTG GTC AAT TAT TTC ATC TTT TTT TCC ATT CAT GGT

-----Exon 21-----
His Leu Phe Ser Val Arg Pro Gln Glu Trp Ile Asn Met Thr Gly
CAT CTA TTT TCT GTT CGT CCT CAG GAG TGG ATC AAC ATG ACT GGT

-----Exon 21-----
Phe Leu Cys Ala Leu Gly Gly Val Cys Leu Gln Gln Arg Ser Thr
TTC TTG TGC GCT CTG GGA GGT GTT TGT CTC CAA CAG CGC AGC ACG

(M82) Met
(M82) ATG

-----Exon 21-----
Pro Ser Leu Gly Thr Tyr Ser Pro Pro Met Gly Pro Leu Thr Glu
CCG AGT CTG GGC ACC TAC AGT CCT CCA ATG GGC CCC CTG ACC GAA

Lys (M211)
CTG (M211)

-----Exon 21-----
Arg Lys Gly Ser Met Ile Ser Met Ser Ser Cys Glu Val Asn Ser
CGC AAG GGG TCC ATG ATT TCC ATG AGC TCC TGC GAG GTA AAC AGC

-----Exon 21-----
Glu Thr Ser Leu Asn Arg Phe Leu Glu Arg Leu Leu Ala Leu Met
GAA ACA TCC CTG AAT CGC TTT CTG GAG CGT CTG CTG GCT CTG ATG

-----Exon 21-----
Val Cys Thr His Glu Lys Val Gly Val Gln Ile Arg Thr Asn Val
GTC TGC ACA CAT GAG AAA GTG GGA GTG CAA ATT CGC ACC AAC GTC

-----Exon 21-----
Lys Asp Leu Val Gly Leu Glu Leu Ser Pro Ala Leu Tyr Ser Met
AAA GAC CTG GTG GGA CTG GAG CTC AGT CCG GCT CTC TAT TCA ATG

-----Exon 21-----
Leu Phe Thr Lys Leu Arg Asn Ser Ile Gly Arg Phe Phe Asp Thr
CTC TTC ACT AAG CTG CGC AAC AGC ATC GGA CGC TTC TTT GAC ACC

--Exon 21--
Gln Gly Pro
CAG GGG CCG

```

Figure 37. Summary of mutations from TILLING *nfla* exon 21.

Our TILLING effort isolated two missense alleles of *nfla* in exon 21 of the gene. This schematic shows the nucleotide and amino acid sequence of the wild type *nfla* exon 21 with the nucleotide changes from our two isolated mutant alleles highlighted in yellow. The corresponding amino acid changes are depicted in red.

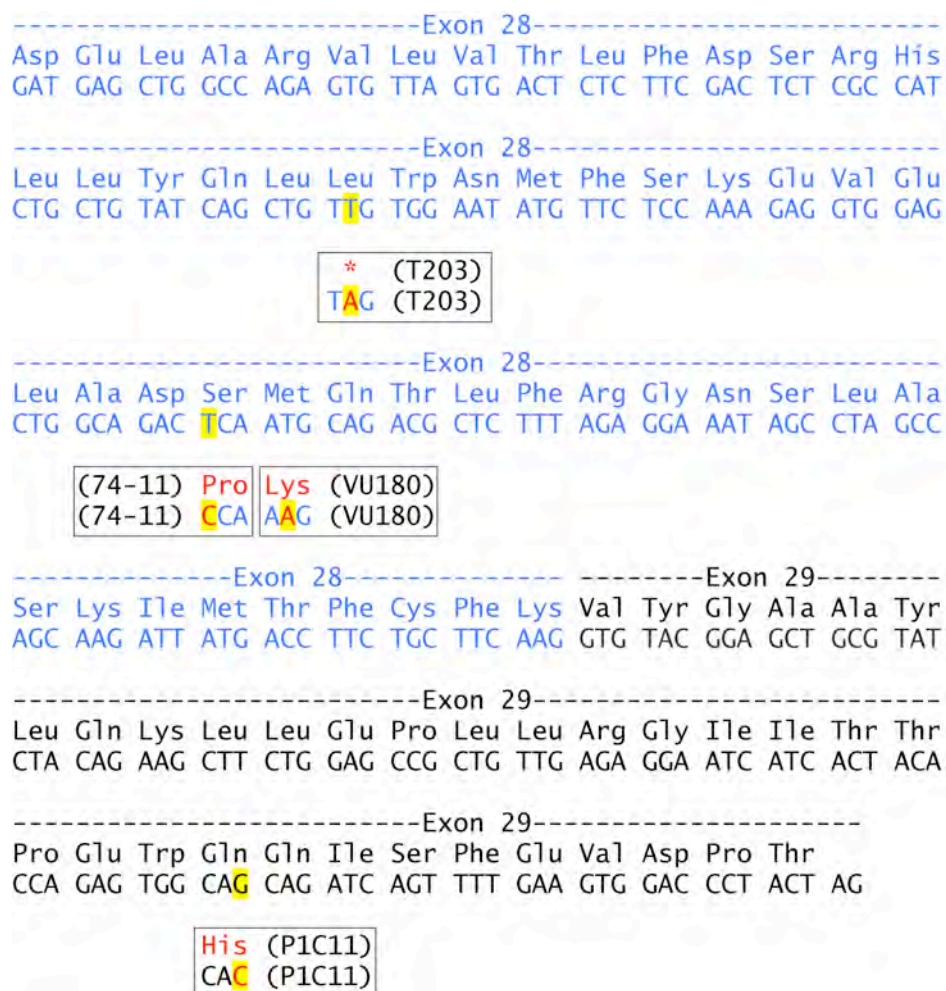


Figure 38. Summary of mutations from TILLING *nfla* exons 28 and 29.

Our TILLING effort isolated three missense alleles and one nonsense allele of *nfla* in exons 28 and 29 of the gene. This schematic shows the nucleotide and amino acid sequence of the wild type *nfla* exons 28 and 29 (exon 28 in blue, exon 29 in black) with the nucleotide changes from our four isolated four mutant alleles highlighted in yellow. The corresponding amino acid changes are depicted in red.

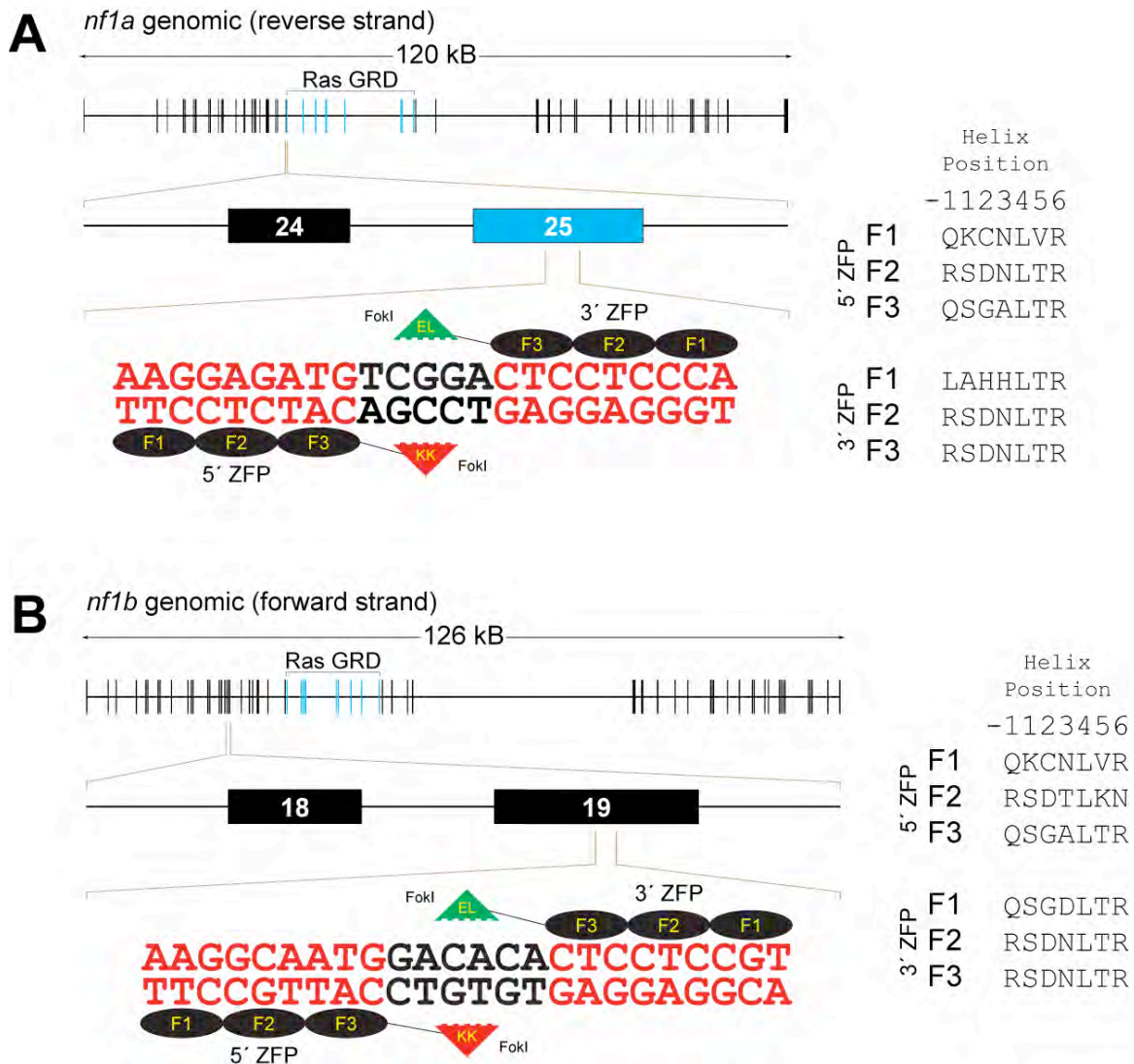


Figure 39. ZFN proteins and their recognition site within *nf1a* and *nf1b*.

A schematic depiction of the engineered ZFN proteins bound to their recognition sites within *nf1a* and *nf1b*, including the amino acid sequences of the three individual fingers that bind to each 9 bp recognition element. (A) For *nf1a*, the ZFN pair binds within exon 25. A BspCNI restriction site is contained within the spacer (not shown). (B) For *nf1b*, the ZFN pair binds within exon 19. A BslI restriction is contained within the spacer (not shown).

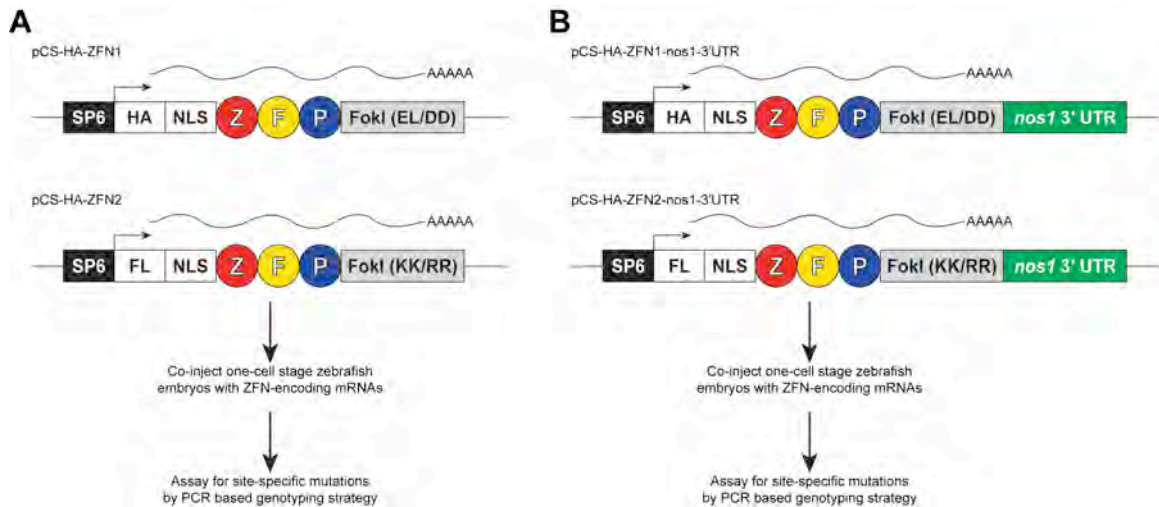


Figure 40. Overview of ZFN-targeted mutagenesis approach in zebrafish embryos.

(A, B) ZFPs cassettes constructed by a modular assembly approach are transferred into expression plasmids with an upstream nuclear localization signal and epitope tag as well as a downstream FokI complementary domain variant (EL or KK; DD or RR). *In vitro* transcribed mRNA from these constructs were injected into one-cell zebrafish embryos which, upon being translated into protein, will bind to their respective targets leading to double strand breaks and the introduction of mutagenic lesions. (B) A second version of these constructs was made in which the *nanos* 3' untranslated region (UTR) was appended to the end to increase mRNA stability in primordial germ cells.

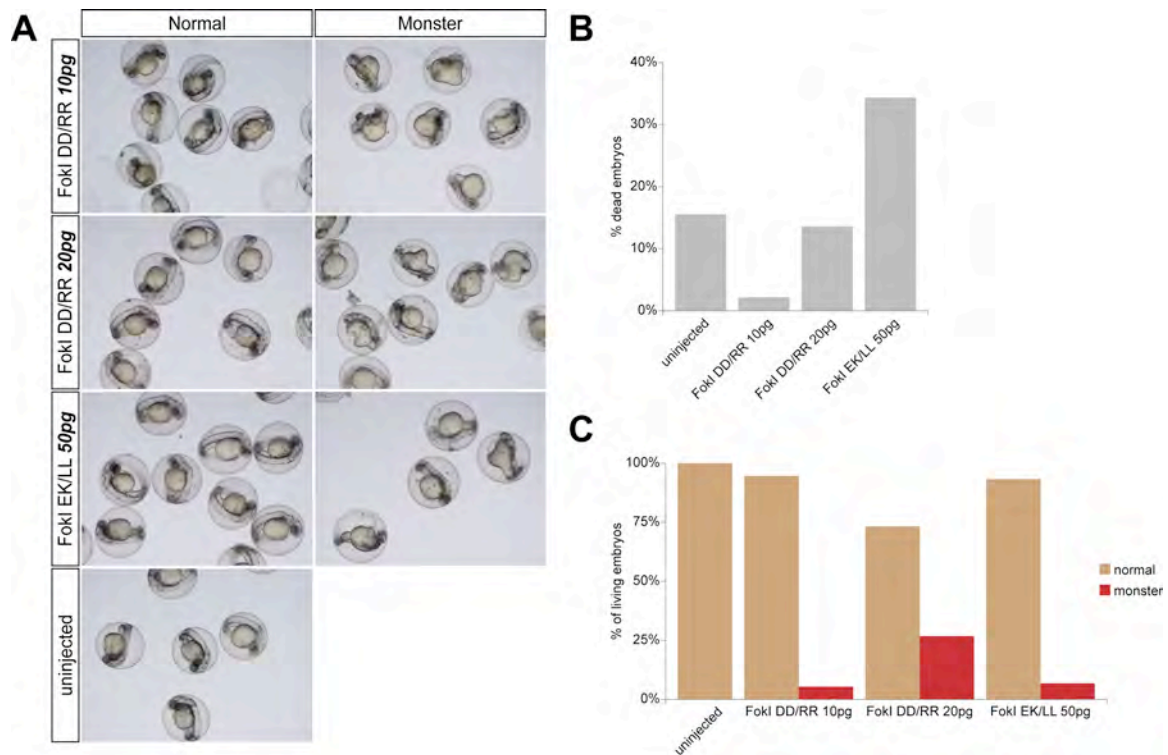


Figure 41. Effects of ZFN mRNA injection on zebrafish embryos.

(A) Gross morphological analysis of embryos injected with varying amounts of DD/RR or EK/LL FokI ZFN mRNAs at 24 hpf reveals two phenotypic classes with embryos appearing either normal or with nonspecific developmental defects (“monsters”). (B) Increasing amounts of DD/RR or EK/LL FokI ZFN mRNAs resulted in greater lethality at 24 hpf. (C) Injection of DD/RR FokI ZFN mRNAs resulted in a dose-dependent increase in the number of monster embryos, however EK/LL FokI ZFN mRNA injection was better tolerated at higher doses.



Figure 42. PCR based genotyping strategy to detect site-specific function of injected ZFN mRNAs. (A) PCR amplification of a wild type sample using the depicted primers (upper-case letters) will generate a 223 bp region of genomic DNA containing a BslI restriction site in the spacer between the targets of the two individual ZFNs (blue box). Introduction of mutagenic lesions by the ZFNs at this site would lead to microinsertions, microdeletions, or a combination of both at this site leading to loss of the BslI restriction site in mutants. The individual ZFN target sites are highlighted in yellow. (B) Pooled genomic DNA was collected at 24 hpf from uninjected embryos as well as normal and monster embryos following injection of DD/RR (10 pg or 20 pg) or EL/KK (50 pg) FokI ZFN mRNAs and used as a template for PCR using the primers outlined. Appropriately sized PCR products were generated for all samples, and subsequently digested with BslI. Following addition of this restriction endonuclease, a faint undigested band remained in both the normal and monster embryos injected with 50 pg of EL/KK FokI ZFN mRNAs. This suggests that the genomic DNA from these pools included individual samples in which the BslI restriction site had been lost presumably due to site-specific mutagenesis.

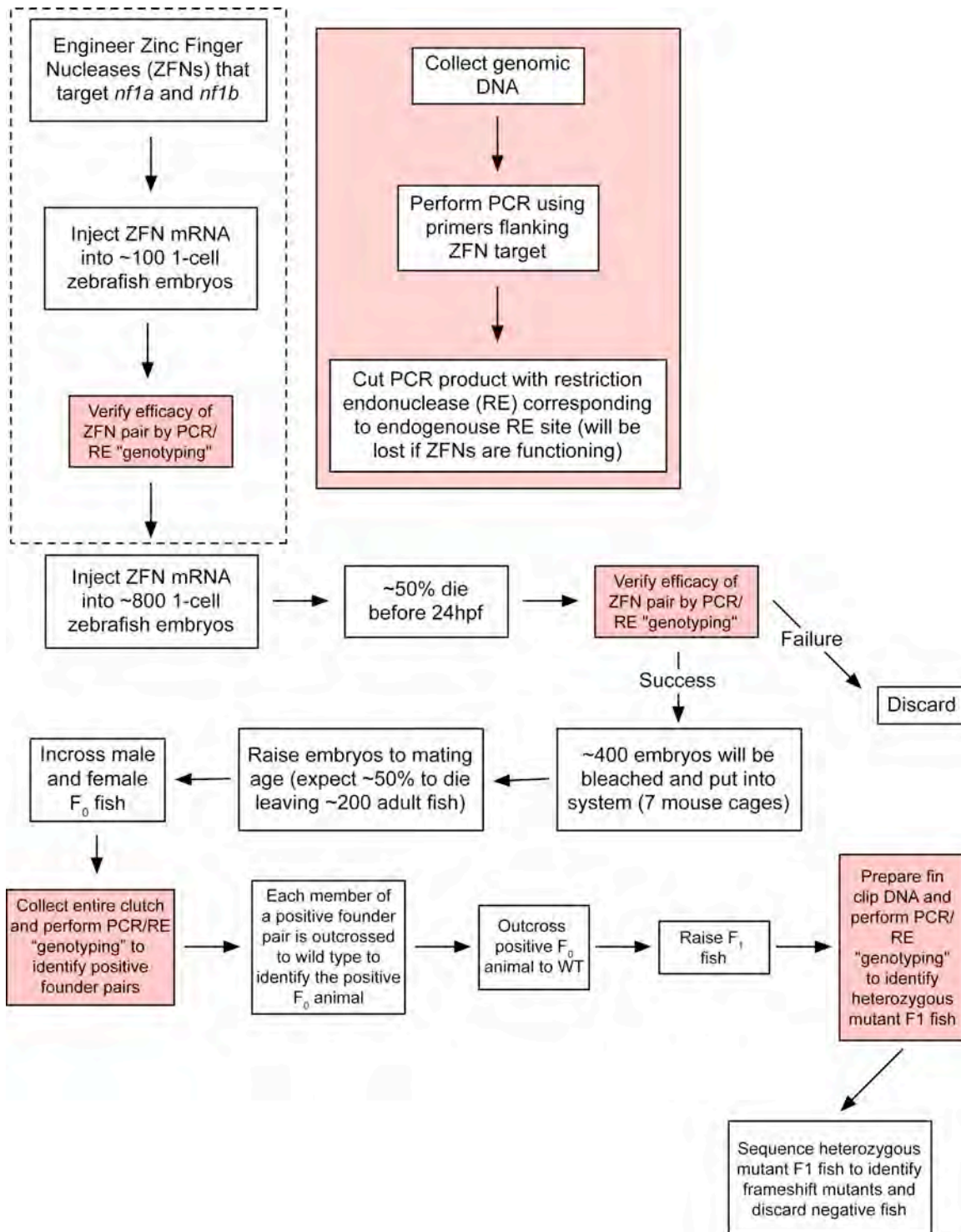


Figure 43. Workflow for generating stable *nf1b* mutant line by germ line transmission of a ZFN-induced mutation.

A schematic diagram reviewing the procedures followed to generate stable *nf1b* mutant lines by germ line transmission of a ZFN-induced mutation. The individual red boxes correspond to the three steps contained within the large red box that describe the PCR/RE genotyping assay that allows molecular assessment of the *nf1b* locus for any mutagenic lesions. The steps boxed by a dotted line represent the initial work of designing, assembling, and validating ZFNs that target *nf1a* or *nf1b*. The remaining steps are those that were carried out to generate and isolate founder animals that were germ line positive for ZFN-mediated mutations and to subsequently transmit these mutant alleles to heterozygous F₁ animals by wild type outcrosses.

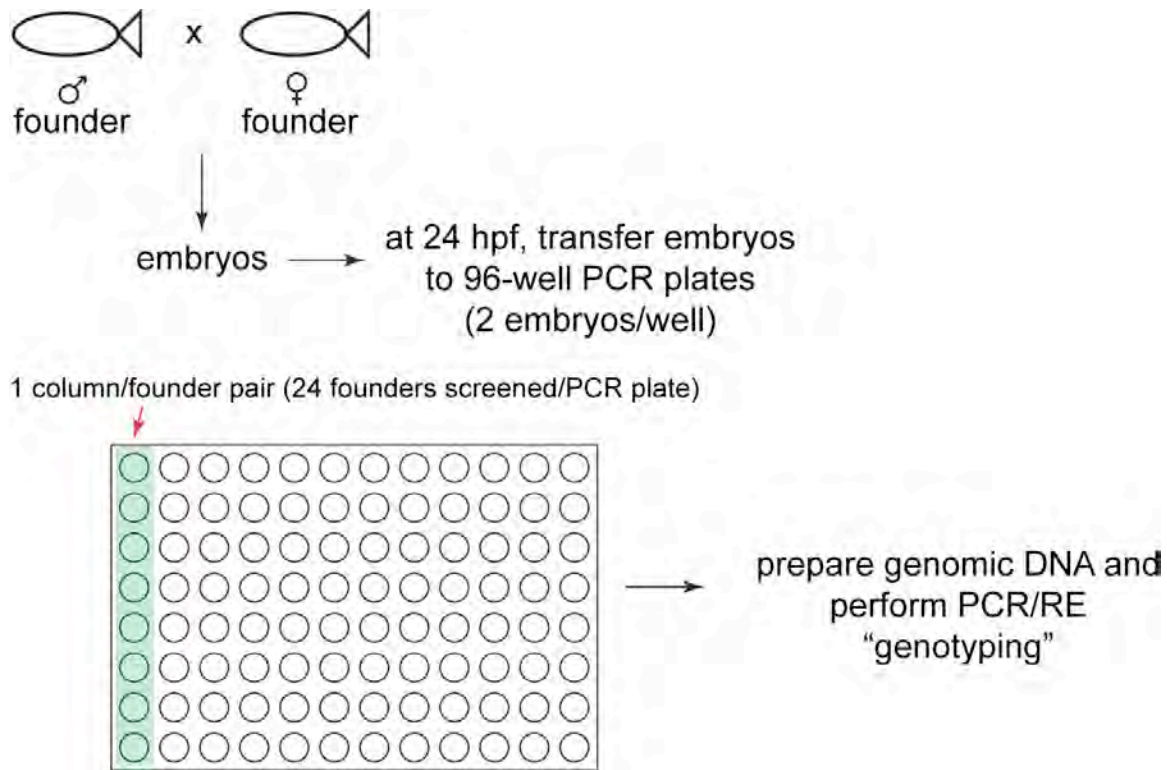


Figure 44. Strategy for identifying F_0 animals positive for germ line ZFN-induced mutations.

Embryos were collected from incrosses of founder pairs and 16 embryos were transferred to one column (8 wells) of a 96-well PCR plate (2 embryos per well). Genomic DNA was prepared from these embryos and subjected to our PCR/RE genotyping strategy. This methodology predicts that we should be able to identify founder animals with a degree of germ line mosaicism as low as 6.25% (1/16). Founder pairs producing embryos that are positive for ZFN-induced mutations in *nflb* were then individually outcrossed to wild type animals to identify which member of the pair harbored the germ line ZFN-mediated mutagenic lesion. Performing incrosses of founders doubled the throughput of our screening effort, as a negative result ruled out two founders as opposed to one.

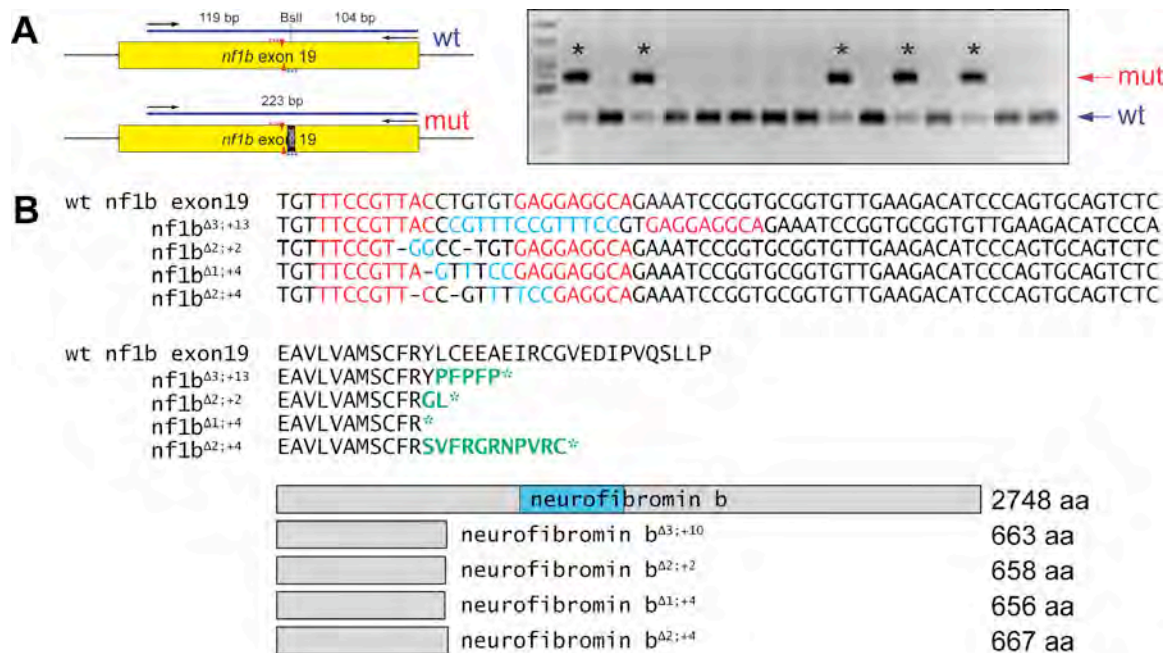


Figure 45. Germ line transmitted *nf1b* mutant alleles isolated from ZFN-injected founder animals.

(A) Schematic representation of the region of *nf1b* exon 19 targeted by our ZFNs. PCR using the depicted primers generates a 223 bp PCR product containing a BsiI restriction site in the spacer between the two unique ZFP binding sites (wt). Introduction of mutagenic lesions leads to insertions/deletions (indel) that render the PCR product resistant to BsiI digestion (mut). Retention of the uncut PCR product (denoted by an asterisk) following restriction digestion identifies the mutant *nf1b* allele as seen by gel electrophoresis of heterozygous *nf1b* mutant animals (mutant band (mut), top; wild type band (wt), bottom). (B) A summary of the nucleotide and corresponding protein sequences they encode for the four mutant alleles isolated for *nf1b*. All four alleles lead to frame shift mutations that produce premature translation stop codons and truncated proteins.



Figure 46. Germ line transmitted *nf1a* mutant alleles isolated from ZFN-injected founder animals.

(A) Schematic representation of the region of *nf1a* exon 25 targeted by our ZFNs. PCR using the depicted primers generates a 223 bp PCR product containing a BspCNI restriction site in the spacer between the two unique ZFP binding sites (wt). Introduction of mutagenic lesions leads to insertions/deletions (indel) that render the PCR product resistant to BspCNI digestion (mut). Retention of the uncut PCR product (denoted by an asterisk) following restriction digestion identifies the mutant *nf1a* allele as seen by gel electrophoresis of heterozygous *nf1a* mutant animals (mutant band (mut), top; wild type band (wt), bottom). (B) A summary of the nucleotide and corresponding protein sequences they encode for the four mutant alleles isolated for *nf1a*. Both alleles lead to frame shift mutations that produce premature translation stop codons and truncated proteins.

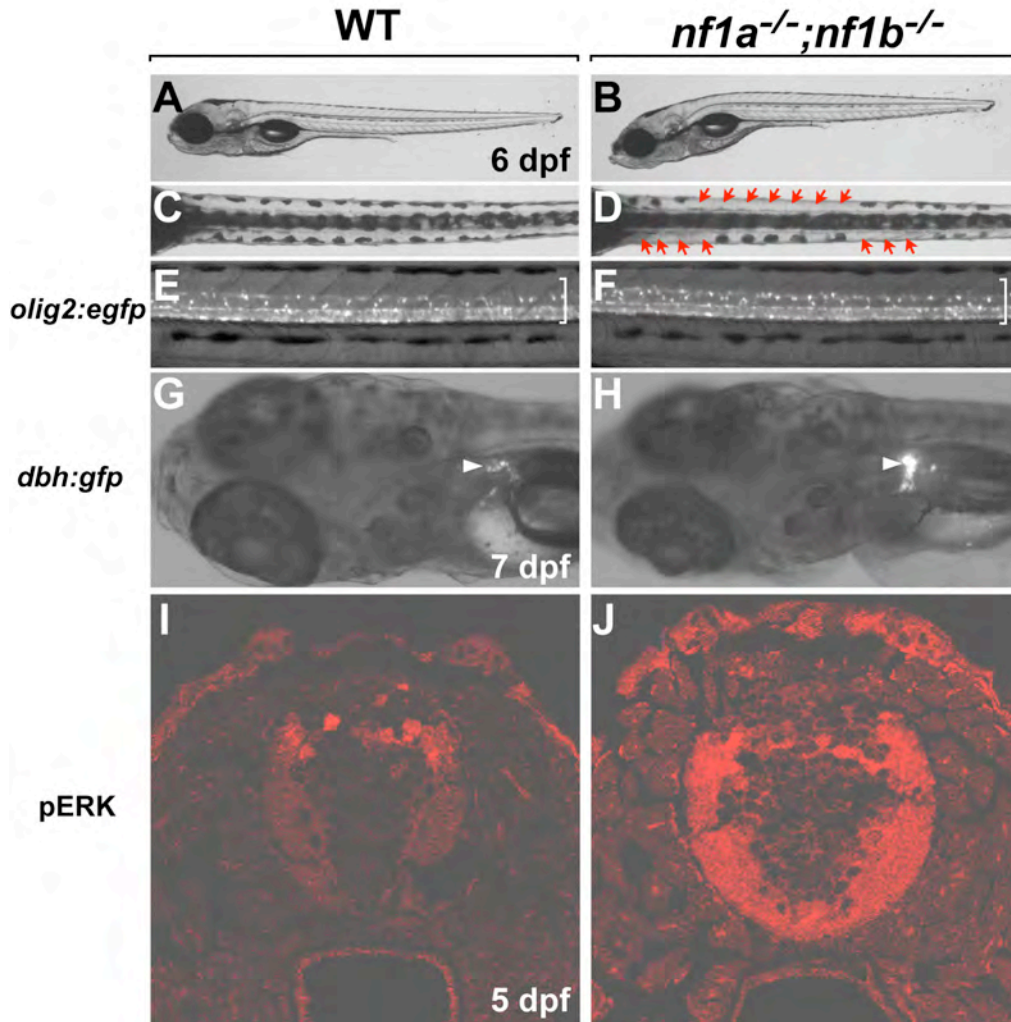


Figure 47. Phenotypes of *nf1a;nf1b* double mutant.

(A,C,E,G,I) Wild-type. (B,D,F,H,J) *nf1a;nf1b* double homozygous mutant. (A-D) Brightfield images. (E-H) Epi-fluorescent images. (I,J) Confocal images. (A,B) Overall morphology of the mutant looks normal at 6 dpf. (C,D) Dorsal view of the tail region. Arrows indicate missing melanocytes in the lateral strip of the mutant. (E,F) *nf1a;nf1b* mutant larva has more dorsally migrated *olig2*:EGFP⁺ OPCs than control (bracket). (G,H) At 7 dpf, *dbh*:GFP⁺ SCG (arrowhead) is enlarged in the mutant larva. (I,J) Transverse sections, dorsal up. Phospho-ERK1/2 is highly detected in a few neurons and white matter of the spinal cord of the *nf1a;nf1b* mutant larva.

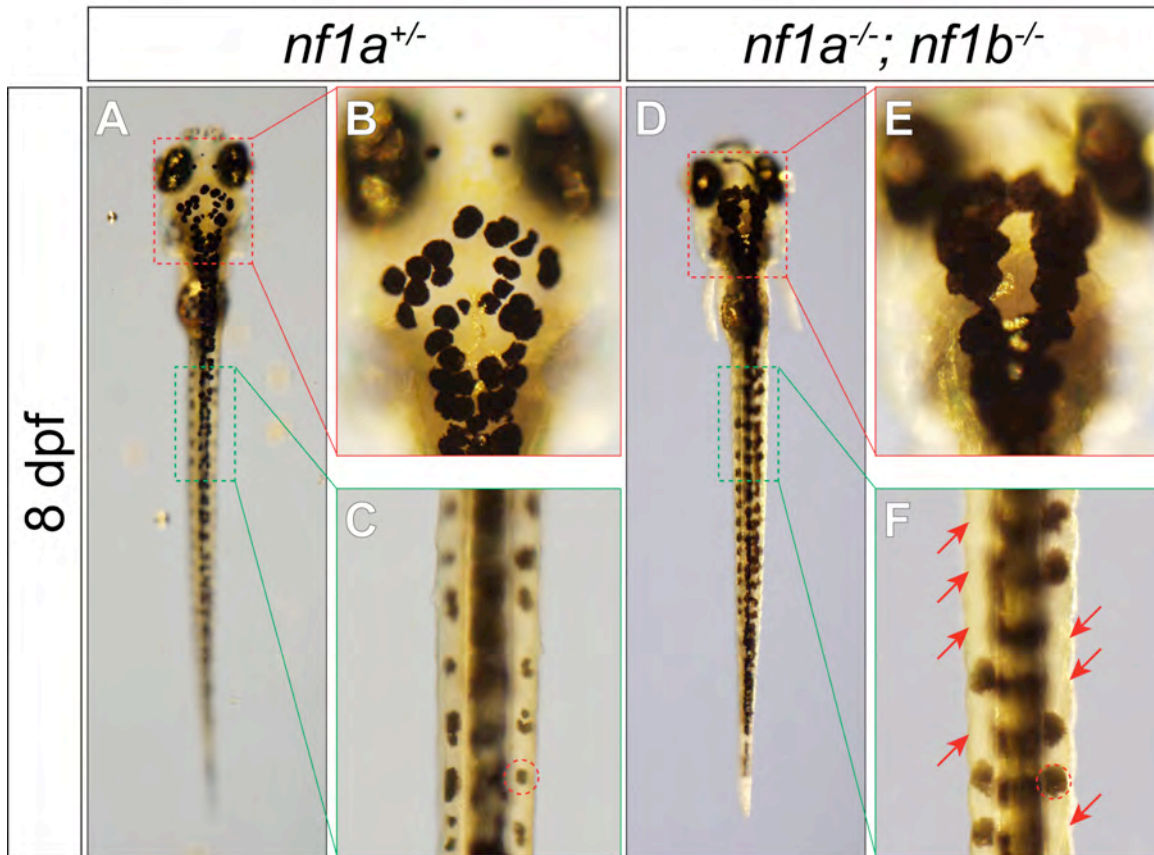


Figure 48. *nf1a*; *nf1b* double homozygous mutant embryos exhibit novel pigmentation phenotypes.

(A, D) Examination of dorsal views of 8 dpf *nf1a*; *nf1b* double homozygous mutant (A) and *nf1a* heterozygous mutant (D) larvae reveals a novel pigmentation abnormality in the head and along the lateral strip of double homozygous mutant embryos. (B, E) Double homozygous mutant embryos display increased pigmentation on the dorsal aspect of the head when compared with clutchmates. (C, F) The melanophores along the lateral stripe of double homozygous mutant larvae (F) do not display the normal repetitive pattern (arrows) seen in clutchmate controls (C). In addition, the individual melanophores along the lateral strip in double homozygous mutants appear enlarged when compared with their counterparts in clutchmate controls (dotted circles in C, F).

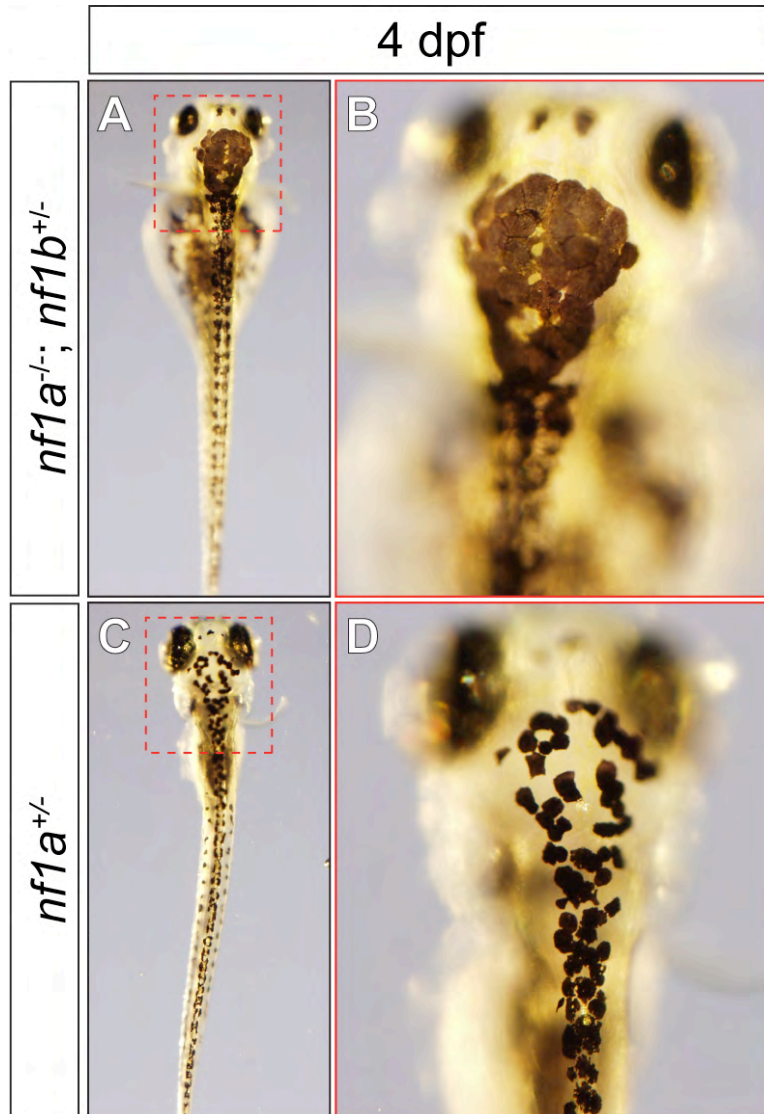


Figure 49. *nf1a/nf1b* mutant embryos positive for a valvular regurgitation phenotype are fully penetrant for pigmentation defects.

All *nf1a/nf1b* mutant zebrafish embryos displaying a valvular regurgitation phenotype at 3 dpf, as assessed by to-and-fro movement of blood between the atrium and ventricle, subsequently exhibit pigmentation defects that become evident at 4 dpf. (A) A *nf1a* homozygous; *nf1b* heterozygous mutant shown to exhibit valvular regurgitation at 3 dpf has increased pigmentation on the dorsal aspect of the head (B) when compared with a *nf1a* heterozygous mutant clutchmate (C, D).

Sample	Exon	Screening Method	Nucleotide Change	Amino Acid Change
P1C11	29	direct sequencing	CAG to CAC	Glutamine to Histidine
M82	21	CEL-I	ACG to ATG	Threonine to Methionine
F211	21	CEL-I	CCG to CTG	Proline to Lysine
74-11	28	CEL-I	TCA to CCA	Serine to Proline
VU180	28	CEL-I	ATG to AAG	Methionine to Lysine
T203	28	CEL-I	TTG to TAG	Leucine to STOP

Table 1. *nfla* mutant alleles identified by TILLING approaches.

Our collective TILLING efforts resulted in the isolation of 6 mutant alleles, with 5 representing missense mutations and 1 representing a nonsense mutation (highlighted in green). The exons the mutations appear in along with their respective nucleotide and amino acid changes are outlined.

Gene	Line Designation	Location of Proviral Insertion	Notes
<i>nfla</i>	ZM_00519422	6 bp upstream of exon 1	Line unrecoverable
<i>nflb</i>	ZM_00373494/ ZM_00346571	18 bp upstream of start codon	Line not recovered; Company ceased operations while in process of recovering line
<i>nflb</i>	ZM_00346420	137 bp downstream of exon 1 (in intron1/2)	Line successfully recovered; Proviral insertion is spliced out of <i>nflb</i> mRNA

Table 2. *nfla* and *nflb* retroviral insertional mutant lines identified in Znomics ZeneMark Library.

Overview of insertional mutant lines identified in Znomics ZeneMark library with location of proviral insertion, line designations, and other relevant notes.

Gene	Exon	ZFN Target Site	Score	RE Site in Spacer
<i>nfla</i>	1	cACAAGCCCGtggaatGGGTCCAGg	8	Yes
<i>nfla</i>	8	gAGCATCACCaagaaGTAGGGGAg	8	No
<i>nfla</i>	10	aCCAAACCTTtctcaaGAGGTACGGg	11	Yes
<i>nfla</i>	12	gTGCACATCCgcctctGAGGATGACa	7	Yes
<i>nfla</i>	25	cCTCTACAGCctgagGAGGGTGACg	10	Yes
<i>nfla</i>	25	cTTCCTCTACagcctGAGGAGGGTg	12	Yes
<i>nfla</i>	30	tTTCCTCCACagctgcGCAGTGTGTg	11	Yes
<i>nfla</i>	30	cCTCCACAGctgcgcaGTGTGTGCCa	11	Yes
<i>nflb</i>	1	gAGCGGCCATggcggcGCAGAAGCCc	7	Yes
<i>nflb</i>	2	tAGCTTCCTGtgaaaGTCGGTGTTc	7	No
<i>nflb</i>	9	gTCCACATACatcagcTGGGAGGATc	8	Yes
<i>nflb</i>	19	cCGTTACCTGtgtgagGAGGCAGAAa	10	Yes
<i>nflb</i>	17	tTCCGTTACctgtgtGAGGAGGCAg	11	Yes
<i>nflb</i>	27	tTGCCTCTTCagccaGAGGAAGGTg	10	Yes
<i>nflb</i>	28	gAACGACTGCagcgagGTGGAGGACg	10	Yes
<i>nflb</i>	28	cGACTGCAGCgaggtgGAGGACGAGg	10	Yes

Table 3. Potential ZFN target sites in *nfla* and *nflb*.

A list of the 16 potential ZFN target sites in *nfla* and *nflb* identified by a search algorithm developed by the Wolfe laboratory. Each ZFN pair is assigned a score that predicts how well it will function *in vivo*. Upper-case letters in ZFN target sites represent the nucleotides that are bound by the ZFPs. Mutagenic lesions induced by the ZFN pairs highlighted in red cannot be assayed for by a PCR based genotyping strategy. ZFN pairs highlighted in green represent those used to generate stable mutant lines.

Transgenic Line	Marked Cell Types	Reference
<i>Tg(mitfa:GFP)</i>	melanocytes	Curran K, Raible DW, Lister JA. Foxd3 controls melanophore specification in the zebrafish neural crest by regulation of Mitf. Dev Biol. 2009 Aug 15;332(2):408-17.
<i>Tg(sox10:GFP)</i> 2 different lines	early neural crest cells	Shannon Fisher (Unpublished); Jimann Shin (Unpublished)
<i>Tg(sox10:Cre);</i> Cre-reporter	early neural crest cells and derivatives	Shannon Fisher (Unpublished)
<i>Tg(tp1bglob:EGFP);</i> <i>Tg(fli1:DsRed)</i>	notch-responsive cells (green); endothelial cells (red)	Parsons MJ, Pisharath H, Yusuff S, Moore JC, Siekmann AF, Lawson N, Leach SD. Notch-responsive cells initiate the secondary transition in larval zebrafish pancreas. Mech Dev. 2009 Oct;126(10):898-912.
<i>Tg(kdr1:GRCFP)zn1</i>	endothelial cells	Cross LM, Cook MA, Lin S, Chen JN, Rubinstein AL. Rapid analysis of angiogenesis drugs in a live fluorescent zebrafish assay. Arterioscler Thromb Vasc Biol. 2003 May 1;23(5):911-2.
<i>Tg(fli1a:negfp)y7</i>	endothelial cells (nuclear)	Roman BL, Pham VN, Lawson ND, Kulik M, Childs S, Lekven AC, Garrity DM, Moon RT, Fishman MC, Lechleider RJ, Weinstein BM. Disruption of acvrl1 increases endothelial cell number in zebrafish cranial vessels. Development. 2002 Jun;129(12):3009-19.
<i>Tg(c236:GFP)</i>	AV valve	Davison JM, Akitake CM, Goll MG, Rhee JM, Gosse N, Baier H, Halpern ME, Leach SD, Parsons MJ. Transactivation from Gal4-VP16 transgenic insertions for tissue-specific cell labeling and ablation in zebrafish. Dev Biol. 2007 Apr 15;304(2):811-24.
<i>Tg(olig2:EGFP)</i>	OPCs; oligodendrocytes	Shin J, Park HC, Topczewska JM, Mawdsley DJ, Appel B. Neural cell fate analysis in zebrafish using olig2 BAC transgenics. Methods Cell Sci. 2003;25(1-2):7-14.
<i>Tg(dbh:EGFP)</i>	sympathetic ganglia	Jeong-Soo Lee (unpublished)
<i>Tg(nkx2.2a:mGFP)</i>	developing myelin; perineurial glia	Kirby BB, Takada N, Latimer AJ, Shin J, Carney TJ, Kelsh RN, Appel B. In vivo time-lapse imaging shows dynamic oligodendrocyte progenitor behavior during zebrafish development. Nat Neurosci. 2006 Dec;9(12):1506-11.
<i>Tg(brn3c:GFP)</i>	optic nerve	Xiao T, Roeser T, Staub W, Baier H. A GFP-based genetic screen reveals mutations that disrupt the architecture of the zebrafish retinotectal projection. Development. 2005 Jul;132(13):2955-67.
<i>Tg(GFAP:GFP)</i>	astrocytes	Xiao T, Roeser T, Staub W, Baier H. A GFP-based genetic screen reveals mutations that disrupt the architecture of the zebrafish retinotectal projection. Development. 2005 Jul;132(13):2955-67.
<i>Tg(nestin:GFP)</i>	neural precursors	Xiao T, Roeser T, Staub W, Baier H. A GFP-based genetic screen reveals mutations that disrupt the architecture of the zebrafish retinotectal projection. Development. 2005 Jul;132(13):2955-67.

Table 4. *nfla*; *nflb* compound heterozygous mutant lines were intercrossed with 16 different transgenic reporter lines to analyze tissue-specific effects of *nfla/nflb* loss.

A list of the various transgenic lines we have intercrossed our *nfla*; *nflb* compound heterozygous mutant lines with including the cells marked by reporter expression and references for lines that have been published.

Key research accomplishments:

- Characterization of zebrafish orthologs: *nf1a* and *nf1b*.
- *Additional analysis of gene expression of nf1a and nf1b.*
- *Additional analysis of morpholino knockdown phenotypes for nf1a and nf1b.*
- *Generation and validation of zebrafish lines harboring mutations in nf1a and nf1b via TILLING and through the use of engineered Zinc Finger Nucleases.*
- *Initial phenotypic analysis of nf1a/nf1b double homozygous mutant zebrafish embryos.*

Reportable outcomes:

Two manuscripts reporting our cardiovascular and neural findings following MO-mediated transient loss-of-function of *nf1a* and *nf1b* have been published in peer-reviewed journals. Notably, our paper was featured on the cover of Human Molecular Genetics.

Cardiac and vascular functions of the zebrafish orthologues of the type I neurofibromatosis gene NF1. Padmanabhan A*, Lee JS*, Ismat FA, Lu MM, Lawson ND, Kanki JP, Look AT[^], Epstein JA[^]. Proc Natl Acad Sci U S A. 2009 Dec 29;106(52):22305-10. Epub 2009 Dec 4. PMCID: PMC2799742

Oligodendrocyte progenitor cell numbers and migration are regulated by the zebrafish orthologs of the NF1 tumor suppressor gene. Lee JS*, Padmanabhan A*, Shin J, Zhu S, Guo F, Kanki JP, Epstein JA[^], Look AT[^]. Hum Mol Genet. 2010 Dec 1;19(23):4643-53. Epub 2010 Sep 21. PMCID pending

A third manuscript describing our work in generating *nf1a* and *nf1b* mutant alleles using the zinc finger nuclease technology has been submitted for publication and is presently under review.

Smith T*, Zhu, C*, McNulty J, Rayla A, Siekmann AF, Buffardi M, Meng X, Shin J, Padmanabhan A, Cifuentes D, Giraldez A, Look AT, Epstein JA, Lawson ND, Wolfe SA. Evaluation and application of modularly assembled zinc finger nucleases in zebrafish. Development. Submitted.

* = These authors contributed equally to this work

[^] = Corresponding authors

In addition, multiple abstracts and oral presentations stemming from this work have been presented at various local, national, and international meetings.

Conclusion:

In the final year of study, we have significantly furthered our advances towards meeting the goals set forth in the funded proposal. The target genes have been clearly identified and phenotypes due to morpholino knockdown have been characterized that are relevant to the understanding of human disease. Our efforts towards this end have resulted in two manuscripts published in peer-reviewed journals. While morpholino knockdown is informative, future experiments will be aided by the characterization of stable mutations within these genes in zebrafish. We have now obtained these mutant fish lines using

several different approaches and made significant strides towards their characterization. Following our complete phenotypic description of these reagents, we intend to freely share them with our colleagues in the NF1 and zebrafish communities. These reagents will be excellent candidates for use in screening small molecules and for use in performing genetic screens to identify modulators of this important disease.

Cardiac and vascular functions of the zebrafish orthologues of the type I neurofibromatosis gene *NF1*

Arun Padmanabhan^{a,1}, Jeong-Soo Lee^{b,1}, Fraz A. Ismat^c, Min Min Lu^a, Nathan D. Lawson^d, John P. Kanki^b, A. Thomas Look^{b,2}, and Jonathan A. Epstein^{a,2}

^aDepartment of Cell and Developmental Biology, Penn Cardiovascular Institute, and the Institute for Regenerative Medicine, University of Pennsylvania, Philadelphia, PA 19104; ^bDepartment of Pediatric Oncology, Dana-Farber Cancer Institute, Harvard Medical School, Boston, MA 02115; ^cDivision of Cardiology, Department of Pediatrics, Children's Hospital of Philadelphia, Philadelphia, PA 19104; and ^dProgram in Gene Function and Expression, University of Massachusetts Medical School, Worcester, MA 06105

Edited by Eric N. Olson, University of Texas Southwestern Medical Center, Dallas, TX, and approved October 14, 2009 (received for review February 20, 2009)

Von Recklinghausen neurofibromatosis is a common autosomal dominant genetic disorder characterized by benign and malignant tumors of neural crest origin. Significant progress in understanding the pathophysiology of this disease has occurred in recent years, largely aided by the development of relevant animal models. Von Recklinghausen neurofibromatosis is caused by mutations in the *NF1* gene, which encodes neurofibromin, a large protein that modulates the activity of Ras. Here, we describe the identification and characterization of zebrafish *nf1a* and *nf1b*, orthologues of *NF1*, and show neural crest and cardiovascular defects resulting from morpholino knockdown, including vascular and cardiac valvular abnormalities. Development of a zebrafish model of von Recklinghausen neurofibromatosis will allow for structure-function analysis and genetic screens in this tractable vertebrate system.

cardiovascular | neurofibromin

Von Recklinghausen neurofibromatosis (NF1) is caused by mutations in the *NF1* gene that result in a wide variety of symptoms expressed with variable penetrance among affected individuals (1). NF1 patients inherit a single mutated copy of *NF1* and may acquire additional somatic mutations in the wild-type allele that contribute to disease progression (2). Cutaneous neurofibromas, benign Schwann-cell tumors derived from the neural crest, are a pathognomonic lesion of this disease and often appear in large numbers. More serious oncogenic lesions, including neurofibrosarcomas and malignant peripheral nerve sheath tumors, may also develop. Additional neural crest-related pathologies include pheochromocytomas and hyperpigmented lesions arising from melanocyte abnormalities known as café-au-lait spots. Non-neural-crest-related abnormalities are also common and include cognitive and learning deficits, skeletal abnormalities, and leukemia. Affected individuals also display an increased incidence of cardiovascular pathologies, including hypertension, renal artery stenosis, and congenital heart disease (3).

Neurofibromin, the product of the *NF1* gene, is a protein of >2,800 aa. It contains a small region homologous to yeast IRA proteins that includes a Ras-GTPase-activating domain (GAP) capable of accelerating the hydrolysis of GTP-bound Ras, thus down-regulating the activity of Ras proto-oncogenes (4). Though additional extensive regions of neurofibromin have been conserved across evolution, other functions of this protein are largely unknown. Evidence from analysis of the *Drosophila NF1* orthologue (5, 6) and mouse models of NF1 (7, 8) implicate a role for neurofibromin in modulating cAMP-dependent protein kinase A signaling. Unrelated work suggests that neurofibromin can associate with microtubules (9) as well as other molecules able to induce cytoskeletal changes (10).

The past 15 years have seen the emergence of increasingly sophisticated mouse models of NF1 (11–23). Genetic inactivation of murine *Nf1* results in midgestation embryonic lethality with deficient embryos displaying congenital heart disease in-

volving the cardiac outflow tract and endocardial cushions. Heterozygous *Nf1*-deficient mice are viable and fertile, exhibit learning defects (24, 25), and develop malignancies, albeit at a low rate over a period of several years. Genetic inactivation of the *p53* tumor suppressor gene augments the disease phenotype in mouse models of NF1 and leads to a dramatic increase in the rate of malignancy (14, 15, 26, 27).

Tissue-specific *Nf1* gene inactivation using Cre-lox technology has led to the development of mouse models that more accurately reproduce aspects of the human disease. For example, Schwann cell-specific inactivation of *Nf1* results in the development of malignant peripheral nerve sheath tumors in all animals (19, 28). *Nf1* inactivation in the developing neural crest using Pax3- or Wnt1-Cre results uniformly in early neonatal lethality, with affected animals exhibiting massive overgrowths of peripheral nervous tissue, including the dorsal root and sympathetic ganglia (11, 20). Related investigations have implicated a role for the heterozygous tumor microenvironment as a major contributor to the development of disease (19, 28). Tissue-specific inactivation studies have also identified a critical role for neurofibromin in endothelial cells as Tie2-Cre-mediated *Nf1* inactivation reproduces the cardiac abnormalities associated with the *Nf1*^{-/-} phenotype (11, 20). *Nf1* inactivation in blood leads to the development of juvenile myelomonocytic leukemia (JMML), the specific form of leukemia found in NF1 patients (29–31). *Nf1* function in mast cells and neurofibromin-mediated modulation of Ras/Erk signaling downstream of c-Kit have also been implicated in tumor progression (32).

Though mouse and *Drosophila* models of NF1 have proven to be informative, additional information will be obtained from alternative model systems. In particular, vertebrate models that allow for high-throughput in vivo screens and rapid, cost-effective phenotypic analysis may facilitate discovery of novel functions and therapeutic approaches. Hence, we sought to develop a zebrafish model of NF1 and to use this model system to elucidate novel developmental functions of neurofibromin. Here, we describe two closely related zebrafish orthologues: *nf1a* and *nf1b*. Transient knockdown of either gene, or both together, during embryogenesis results in developmental defects of cardiac and neural crest structures that closely resemble murine models and aspects of the human disease. In addition, we identify

Author contributions: A.P., F.A.I., N.D.L., J.P.K., A.T.L., and J.A.E. designed research; A.P., J.-S.L., F.A.I., and M.M.L. performed research; J.-S.L. and N.D.L. contributed new reagents/analytic tools; A.P., F.A.I., and J.A.E. analyzed data; and A.P. and J.A.E. wrote the paper.

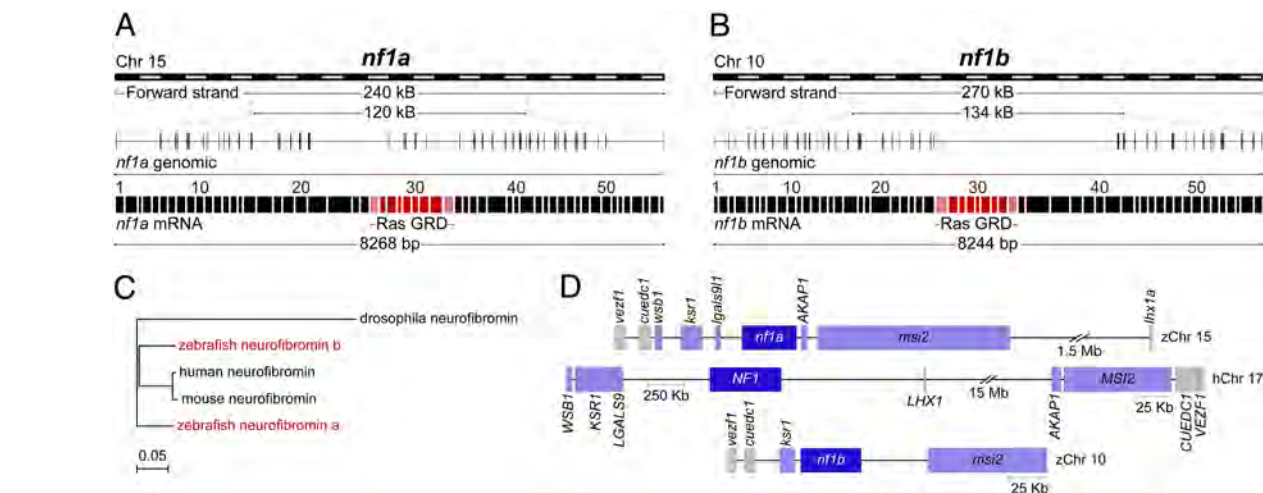
The authors declare no conflict of interest.

This article is a PNAS Direct Submission.

¹A.P. and J.-S.L. contributed equally to this work.

²To whom correspondence may be addressed at: 1154 BRB II/III, 421 Curie Boulevard, Philadelphia, PA 19104 or Mayer Building, Room 630, 44 Binney Street, Boston, MA 02115. E-mail: epsteinj@mail.med.upenn.edu or thomas_look@dfci.harvard.edu.

This article contains supporting information online at www.pnas.org/cgi/content/full/0901932106/DCSupplemental.



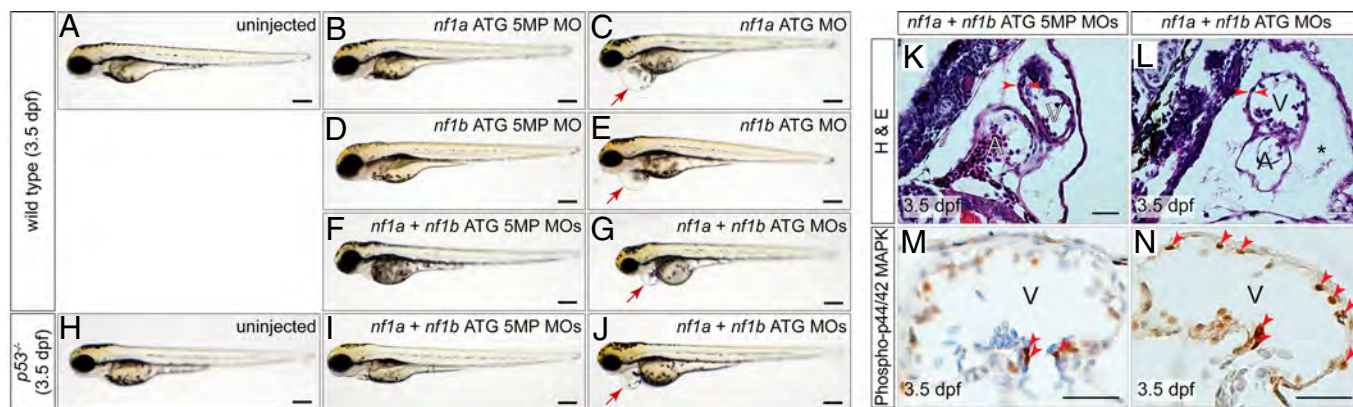


Fig. 3. MO knockdown of *nf1a*, *nf1b*, or both together results in pericardial effusions at 3.5 dpf and increased phospho-p44/42 MAPK in cardiac tissue. Analysis of 3.5-dpf wild-type embryos (A) or embryos injected with *nf1a* ATG 5-mispair (5MP) MO (B), *nf1b* ATG 5MP MO (D), or *nf1a* + *nf1b* ATG 5MP MO (F) reveal no apparent defects in gross morphology. Treatment with *nf1a* ATG MO (C), *nf1b* ATG MO (E), or a combination of both (G), however, results in a dilation of the pericardial space. (H–J) Injection of *p53*^{−/−} embryos with *nf1a* + *nf1b* ATG MO results in a gross dilation of the pericardial space (J), whereas uninjected (H) and *nf1a* + *nf1b* ATG 5MP MO-injected *p53*^{−/−} embryos (I) appear normal. (Scale bars: 0.25 mm.) (K and L) Transverse sections of 3.5-dpf *nf1a/nf1b* combined morphant embryos reveals a thinning of the ventricular myocardium and pericardial effusion (*) when compared with controls (A, atrium; V, ventricle). (M and N) Immunohistochemical analysis of transverse sections of 3.5-dpf *nf1a/nf1b* combined morphant embryos reveals an increase in the ratio of phospho-p44/42 MAPK-positive cardiac cells (arrows) to the total number of cardiac cells when compared with controls. (Scale bars: 25 μ m.)

pression, particularly in the vascular endothelium (Fig. S2B–G), whereas RNA from one-cell embryos indicate that both genes are expressed maternally (Fig. S2B). Queries of an expression database generated from sorted endothelial cells from Tg(fli1:egfp)y1 zebrafish identifies *nf1a* and *nf1b* in both GFP+ and GFP− cell populations, consistent with the expression of these genes in vascular endothelium (34).

Morpholino Knockdown of *nf1a* and *nf1b*. We used morpholino antisense oligonucleotides (MOs) to inhibit expression of *nf1a* and *nf1b* at early stages of development. Effectiveness of gene knockdown by translation blocking MO was confirmed by Western blot analysis (Fig. S3A). The ability of neurofibromin to function as a Ras-GAP, thereby down-regulating levels of active GTP-bound Ras, can result in decreased phosphorylation of downstream effectors, including Erk/MAPK. Western blots of 3.5-dpf whole-embryo extracts derived from *nf1a*, *nf1b*, or *nf1a/nf1b* morphants revealed a marked up-regulation of phospho-Erk in knockdown tissue, whereas levels of total Erk were unchanged (Fig. S3B). Efficacy of splice-blocking MOs was assessed by RT- and quantitative PCR using RNA collected from 24-hpf embryos (Fig. S3 C–G).

The phenotypes produced by MO treatment were compared in a blinded fashion to embryos injected with control MOs. We observed a marked increase in the intensity and domain of expression of glial fibrillary acidic protein (*GFAP*), a marker of Schwann and glial cells, by whole-mount in situ hybridization (Fig. S4). This finding is consistent with the increase in neural crest-derived tissue in *NfI*^{-/-} mice and the presence of neural crest-derived tumors in NF1 patients. We also examined the expression of myelin basic protein (*mbp*), sex-determining region Y-box 10 (*sox10*), forkhead box d3 (*foxd3*), and *crestin*, but did not observe changes. Therefore, the alterations observed in *nfla* and *nflb* morphant embryos appear to be restricted to the Schwann-glial lineages in the neural compartment.

served no readily apparent structural defects in the atrioventricular valves of morphants despite the observed functional deficits (Fig. S5). In addition, we observed pooling of blood in the common cardinal vein and a paucity of blood flow along the dorsal aorta and posterior cardinal vein. Valvular insufficiency and reduced blood flow were not seen in control morphants or wild-type embryos (Movie S3). Overall development of the embryos was relatively preserved through the first 3 days despite these cardiac defects. Histological analysis revealed a thinned ventricular myocardium and large pericardial effusions in MO-treated embryos (Fig. 3 K and L, and Fig. S6 A, B, F, and G). Immunohistochemical analysis of 3.5-dpf *nf1a*, *nf1b*, and *nf1a/nf1b* morphant zebrafish also reveals increases in phospho-Erk staining (Fig. 3 M and N, and Fig. S6 C–E and H–K). Gross morphological analysis showed an increased incidence of pericardial effusions beginning at 48 hpf, reflecting cardiac dysfunction, in *nf1a* and *nf1b* morphants when compared with controls (Fig. 3 A–G, and Fig. S6 L and M). Nonspecific toxicity arising from MO exposure as a cause of the observed cardiovascular defects was unlikely because unrelated control or scrambled MOs failed to produce similar levels of abnormalities, defects were observed even at low doses of specific MOs, and similar defects were observed with several unrelated but specific MOs directed against *nf1a* and *nf1b*. In addition, injection of specific MOs in *p53* mutant embryos also produced similar cardiovascular defects (Fig. 3 H–J), and off-target effects due to MO exposure are known to be partially mediated through *p53* activation (35). Defects in cardiac valve morphogenesis and a thinning of the ventricular myocardium are also seen in *Nf1*^{−/−} murine embryos.

We performed knockdown experiments using zebrafish embryos in which endothelial cells are marked by expression of a cytoplasmic enhanced green fluorescent protein (GFP) to allow for a more detailed analysis of vascular development. Dramatic abnormalities of vascular patterning in the intersomitic vessels of morphant embryos were seen at 48 and 72 hpf (Fig. 4). In *nf1a* MO-treated embryos, the leading edge of the sprouting vessels displayed claw-like projections at 48 hpf (Fig. 4C) and failed to pattern normally such that the dorsal longitudinal anastomotic vessel (DLAV) did not form or developed in a rudimentary fashion (Fig. 4F). This occurred in embryos that were otherwise normal in overall size and maturity. These defects were also noted in *nf1a/nf1b* compound morphants, and were present but

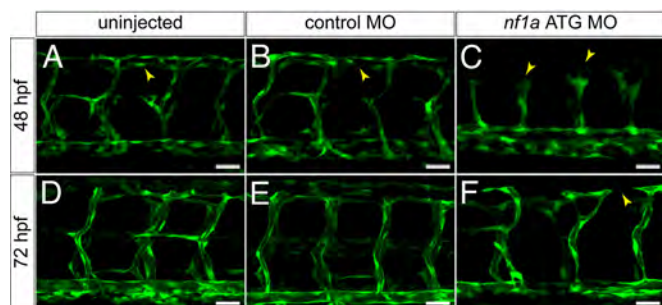


Fig. 4. MO knockdown of *nf1a* results in vascular patterning defects at 48 and 72 hpf. (A–C) At 48 hpf, *nf1a* ATG MO-treated Tg(fli:egfp)y1 (endothelial-specific GFP transgenic) zebrafish embryos display gross defects in vascular development compared with control MO-treated or uninjected samples. Morphant embryos (C) display abnormal claw-like projections at the leading edge of the developing intersomitic vessels and fail to develop the dorsal longitudinal anastomotic vessel (DLAV) present in both control MO-treated (B) and uninjected (A) samples. (D–F) At 72 hpf, *nf1a* ATG morphant embryos display only rudimentary DLAVs and a general disorganization of the trunk vasculature (F) when compared with control MO-treated (E) or uninjected (D) embryos. (Scale bars: 25 μ m.)

less severe in *nf1b* morphants. Vascular patterning defects did not appear to correlate directly with cardiac defects, as we observed embryos with vascular abnormalities that did not display pericardial effusion or valvular insufficiency as assessed by a to-and-fro movement of blood within the heart (36). Blood flow within the dorsal aorta and posterior cardinal vein appeared intact in these embryos (Movie S4).

At 24 hpf, analysis using zebrafish embryos expressing a nuclear-localized GFP in endothelial cells indicated that morphants displayed a complete (Fig. S4A) or partial absence of intersomitic vessels emanating from the dorsal aorta when compared with stage-matched controls (Fig. S4B). Overall morphology of morphant and control embryos appeared equivalent (Fig. S4A1 and A2), ruling out nonspecific developmental delay. These defects were apparent following MO-mediated knockdown of *nf1a* or *nf1b*, whereas knockdown of both together had an additive effect (Fig. 5B). The small percentage of embryos with defects produced by the 5MP MO may have been due to low-level knockdown of *nf1a*. Again, similar defects were observed with several unrelated but specific MOs directed against *nf1a* and *nf1b* (Fig. S7A). Our analysis of morphant embryos at 24 hpf also revealed a caudal vessel defect. Morphant embryos displayed a cystic expansion in the region of the caudal vein and exhibited inappropriate anastomoses between the caudal vein and artery (Fig. S7 D2–D4 and Movie S5) when compared with controls (Fig. S7D1). Identity of the expanded tissue as vascular was confirmed by expression of GFP (Fig. S7 D6–D8) and the observation of a pooling of red blood cells in the expanded region (Movie S5). This defect was present following knockdown of *nf1a*, *nf1b*, or both together (Fig. S7 C and D).

Additional confirmation of the role of *nf1a/nf1b* in vascular development derives from studies using a genetic background sensitized to vascular insult. Previous studies used MOs directed against *flt4*, the zebrafish VEGF receptor-3 orthologue, to investigate genetic interactions during zebrafish artery development (37). Additionally, *flt4* morphant zebrafish embryos display variable defects in segmental artery formation reminiscent of those identified in our *nf1a/nf1b* morphants. Endothelial-GFP expressing zebrafish embryos were injected with *flt4* MO alone and in combination with a MO directed against *nf1a*, *nf1b*, or a combination of both. At low MO doses, 85% of *flt4/nf1a*, 24% of *flt4/nf1b*, and 36% of *flt4/nf1a + nf1b* compound morphants displayed abnormal vascular shunts at 48 hpf compared with only 3–8% of individual *flt4*, *nf1a*, or *nf1b* morphants (Fig. 5C, Fig.

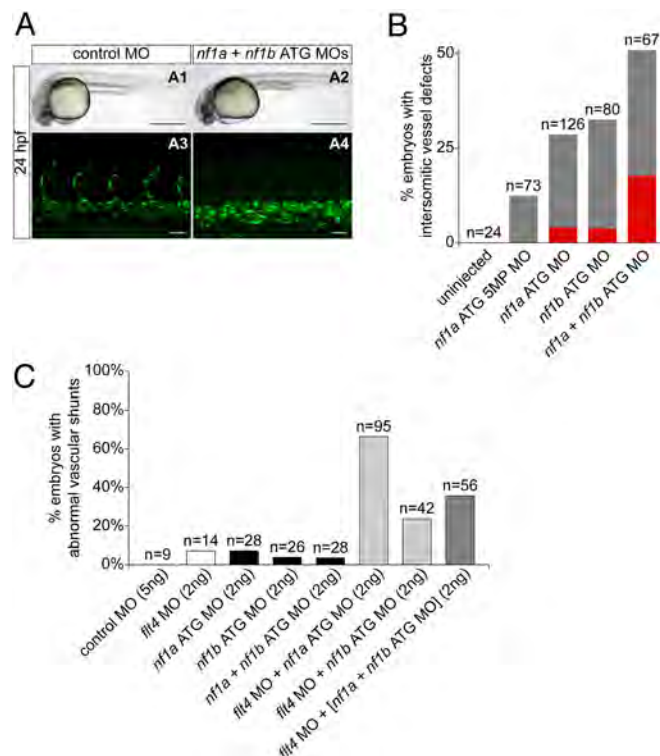


Fig. 5. MO knockdown of *nf1a*, *nf1b*, or both together result in vascular defects at 24 to 48 hpf. (A and B) Analysis and quantification of vascular defects at 24 hpf in uninjected and morphant Tg(fli:egfp)y1 (endothelial-specific nuclear GFP transgenic) zebrafish embryos. Control MO- (A1) and combined *nf1a/nf1b* MO-treated (A2) zebrafish embryos appear similar by gross morphological analysis at 24 hpf. (Scale bars: 500 μ m.) Development of intersomitic vessels is deficient at 24 hpf in *nf1a/nf1b* combined morphants (A4) when compared with controls (A3). (Scale bars: 25 μ m.) (B) Intersomitic vessel formation between somites 17–30 at 24 hpf was scored as absent (red), intermediate (gray), or normal following administration of 2 ng of the indicated MO(s). (C) MO-mediated knockdown of *flt4*, providing a sensitized background for the detection of vascular defects, was combined with *nf1a*, *nf1b*, and *nf1a + nf1b* ATG MO knockdown. Twenty-four to 85% of combined *flt4*(*nf1a*, *nf1b*, *nf1a + nf1b*) MO-treated embryos display abnormal vascular shunts compared with 3–8% of individual *flt4*, *nf1a*, *nf1b*, or *nf1a + nf1b* MO-treated embryos.

S7B, and Movie S6). This defect was not apparent in controls (Movie S7). The shunts occur between the dorsal aorta and the dorsal longitudinal anastomotic vessel with retrograde flow through segmental arteries back into the dorsal aorta or through intersegmental veins into the posterior cardinal vein. In some cases, there were interruptions of the dorsal aorta.

Vascular Patterning Defects in Mouse Embryos Lacking *Nf1*. Although cardiac defects have been reported in mouse embryos lacking *Nf1*, a phenotype that has been attributed to a role for neurofibromin in endothelium (11), abnormalities in vascular patterning have not been previously identified. *Nf1*^{−/−} mice succumb during midgestation and exhibit significant peripheral hemorrhage that has been hypothesized to be secondary to the intracardiac defects, although similar hemorrhage is not a common feature of mouse embryos with congenital heart disease. In light of our observation of peripheral vascular patterning defects in *nf1* morphant zebrafish embryos, we reevaluated murine *Nf1* knockouts by whole-mount platelet/endothelial cell adhesion molecule-1 (PECAM-1) staining to visualize endothelium at E10.5–E11.5 time points before the development of overt cardiac failure or significant endocardial cushion defects. Although no

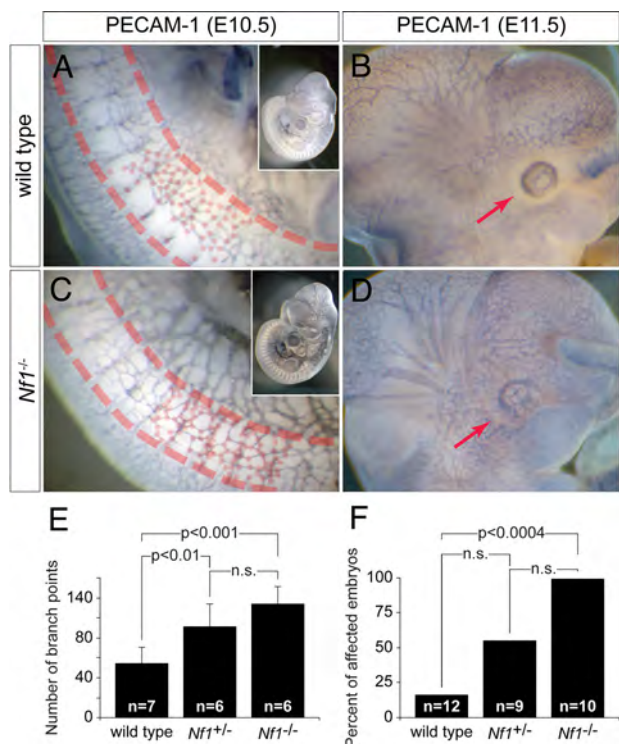


Fig. 6. *Nf1*^{-/-} mouse embryos display defects in vascular patterning. (A and C) Whole-mount PECAM-1 staining of E10.5 wild-type (A) and *Nf1*^{-/-} (C) mouse embryos reveals abnormal vascular patterning in *Nf1*^{-/-} embryos, with an increased number of vessels and branching (dots at branch points) particularly evident in the somites (between dashed lines). Low-magnification insets show an overall increase in vascular staining in *Nf1*^{-/-} embryos. (E) Quantification of vessel branch points over four somites immediately rostral to the anterior limb buds at E10.5 shows a significant increase in *Nf1*^{+/-} and *Nf1*^{-/-} embryos compared with wild type (\pm SD). (B and D) Similar staining of stage-matched littermates at E11.5 reveals loss of the normal avascular zone around the developing eye (D) in *Nf1*^{-/-} embryos compared with wild type (B). (F) Quantification of abnormal eye vasculature shows a significant increase in the number of affected *Nf1*^{-/-} embryos compared with wild types ($P < 0.004$).

overt differences were appreciated in E11.5 yolk sacs (Fig. S8), we identified vascular abnormalities in embryos, including an increase in overall vascularity and a failure of the primitive vascular plexuses in the somitic region and head to remodel as seen in wild-type embryos (Fig. 6). These findings suggest that peripheral hemorrhage commonly noted on *Nf1*^{-/-} mouse embryos may be related to an intrinsic vascular defect similar to that identified in MO knockdown zebrafish.

Discussion

We report the identification and initial characterization of the zebrafish orthologues of the human neurofibromatosis gene *NF1*. The two zebrafish *nf1* genes likely arose from a genome duplication event and are highly related to one another in structure, sequence, and expression pattern through early development. MO-mediated knockdown of either gene alone results in developmental defects involving cardiac and neural crest structures that are even more prominent when both genes are knocked down in concert, suggesting partial functional redundancy. Interestingly, the entire spectrum of cardiovascular defects we have identified, including pericardial effusions and functional valve abnormalities, segmental vessel defects, and aberrant arteriovenous shunts, are greater with knockdown of the *nf1a* orthologue compared with *nf1b*, suggesting that *nf1a* may play a more prominent role in cardiovascular development.

Nf1^{-/-} mice die during midgestation as a result of severe cardiac failure, and display gross cardiovascular and neural crest defects. Closer examination of these *Nf1*-deficient mice reveals hyperproliferative endocardial cushions, the precursors of the cardiac valves, which have been shown to result from a cell-autonomous role for *Nf1* in endothelial cells (11). Here, we show that zebrafish embryos also display cardiovascular and neural abnormalities following transient knockdown of the orthologous *nf1* genes. These defects resemble those seen in mouse models, including the presence of pericardial effusions, thinned myocardium, abnormal cardiac valves, and an increase in Schwann-glia derivatives.

Importantly, the generation of a new vertebrate model of NF1 allowed us to identify a previously unrecognized role for neurofibromin in vascular patterning during early zebrafish and murine development. The ability to distinguish a primary vascular defect from a phenotype resulting secondary to cardiac failure is possible in zebrafish because early vascular development does not require an intact circulation, and adequate oxygenation is achieved via passive diffusion (38). In mice, this distinction is much more difficult to define, emphasizing one of the advantages of developing a zebrafish model of NF1. It is worth noting that the degree of peripheral hemorrhage noted in *Nf1* knockout embryos is unusual for mouse models of congenital heart disease and is not seen in embryos with double-outlet right ventricle, truncus arteriosus, or atrioventricular canal defects despite pericardial effusions indicating heart failure (39). We hypothesize that a peripheral vascular defect produced by endothelial dysfunction in *Nf1*-deficient mouse embryos accounts for the observed degree of hemorrhage. Though the complexity and severity of vascular patterning defects in mouse and zebrafish embryos lacking neurofibromin are distinct, we suggest that they are highly likely to be related, and there is precedent for similar differences in the vascular manifestation of genetic mutations in fish and mice (40, 41).

Vascular patterning defects represent a well-recognized component of the pleiotropic spectrum of NF1 disease phenotypes in affected individuals (3). NF1 patients often exhibit a characteristic vascular lesion known as moyamoya, a name that derives from its appearance as a puff of smoke on computed tomography scans of the head due to abnormal small-vessel patterning in the brain (42, 43). Other vascular defects, including hypertension and renal artery stenosis, have also been documented (3). Neurofibromin has been shown to modulate the activity of Ras proto-oncogenes through its GAP-related domain (GRD), and multiple lines of evidence support a role for Ras signaling in normal vascular patterning and development. For example, mouse embryos deficient for p120 GAP activity display vascular defects such as abnormalities in endothelial cell organization (44). In addition, mutations in *RASA1*, the gene encoding p120 GAP, are associated with vascular anomalies in affected individuals (45, 46). Experiments in chicken and mouse endothelial tissues have identified a role for H-Ras in angiogenesis and vascular permeability (47). Studies in zebrafish also support a role for Ras signaling in vascular development; MO knockdown of *k-ras* or overexpression of a dominant negative mutant of *k-ras* both result in defective vascular development (48). These data, taken together with our own, suggest a necessity for tight regulation of Ras signaling in normal vascular development. The *flt4*(*nf1a*, *nf1b*, *nf1a* + *nf1b*) vascular shunting phenotype represents an inappropriate arteriovenous malformation, which is also present in the embryos with cystic expansion of the dorsal vein. Other vascular patterning defects observed in the *nf1a/nf1b* morphants may represent distinct functions of neurofibromin in the vasculature, or may be related by common underlying mechanisms. The genetic interaction between *nf1a/nf1b* and *flt4* that we show suggests that these molecules may function in a

common molecular pathway, although alternative interpretations cannot be ruled out.

In an effort to determine the degree to which neurofibromin function can be ascribed to its activity as a Ras-GAP, we have previously generated a mouse model in which the isolated neurofibromin GRD is expressed in a tissue-restricted manner upon Cre-mediated activation (20). These studies have shown that reconstitution of the neurofibromin GRD in endothelial cells of *Nf1*^{-/-} mice is sufficient to rescue cardiac development and midgestational lethality. The resulting mice, however, are abnormal and succumb in the early postnatal period. Analysis of these animals reveals massive overgrowth of peripheral nervous tissues that mimic those of the neural crest-specific *Nf1*-deleted mice. This finding strongly suggests that additional domains outside the GRD are important for neural crest growth and homeostasis. Our development of a zebrafish model of NF1 will be particularly useful for examining the potential activities of these domains through in vivo structure-function analyses. Enhancer and suppressor screens may identify signaling pathways, in addition to the Ras/MAPK and mTOR pathways, that impact disease progression. In addition, high-throughput small-molecule screens will allow for the rapid identification of compounds with the potential for modifying NF1 disease phenotypes. The generation of stable mutant lines for *nf1a* and *nf1b*

serve as a necessary prerequisite to pursue these exciting possibilities.

Materials and Methods

Morpholino Injections. Morpholino oligonucleotides (Gene Tools) corresponding to *nf1a*, *nf1b*, *flt4*, and associated controls were dissolved in water and supplemented with 0.1% vol/vol phenol red. One-cell zebrafish embryos were injected with ≈ 1 nL of the appropriate MO solution(s). MO sequences were as follows: *nf1a* ATG MO 5'-GGCTTGTGCGCCGATGCTCAGGG, *nf1a* ATG 5MP MO (*nf1a* ATG 5-mispair control MO) 5'-GGCTTGTGCCCCGGCATGGTACGCG, *nf1b* ATG MO 5'-CCGCTCAGCCGATAGTGATGAAGA, *nf1b* ATG 5MP MO 5'-CCCCTCAGGCCATAGTCATCAAGA, *nf1a* SB MO 5'-GTCCAAAGTAGTGTTCCTTACTGT, *nf1a* SB 5MP MO 5'-GTCCAACTACTCTTTGCTTACTGT, *nf1b* SB MO 5'-CTCAGTATTATCTGCACCTGTGG, *nf1b* SB 5MP MO 5'-CTGAGTATATATGTGCAGCTGTGG, *flt4* MO (37), and standard control MO 5'-CCTCTTACTCAGTTACAATTATA.

Additional information is available in *SI Materials and Methods*.

ACKNOWLEDGMENTS. We thank Jie He (University of Pennsylvania CDB Zebrafish Core) and Nicole Antonucci for assistance with animal husbandry, Andrea Stout (University of Pennsylvania CDB/CVI Microscopy Core) for assistance with microscopy, and Michael Pack and Mary Mullins for helpful discussions and reagents. This work was supported by National Institutes of Health Grants R01-HL062974 (to J.A.E.) and K08-HL075179 (to F.A.I.) and Department of Defense Grant NF050175 (to J.A.E. and A.T.L.). A.P. was supported by a fellowship from the Sarnoff Cardiovascular Research Foundation, and J.-S.L. was supported by a Young Investigator Award from the Children's Tumor Foundation.

1. Ferner RE, et al. (2007) Guidelines for the diagnosis and management of individuals with neurofibromatosis 1. *J Med Genet* 44(2):81–88.
2. Viskochil D (2002) Genetics of neurofibromatosis 1 and the NF1 gene. *J Child Neurol* 17(8):562–570; discussion: 571–562, 646–551.
3. Friedman JM, et al. (2002) Cardiovascular disease in neurofibromatosis 1: Report of the NF1 Cardiovascular Task Force. *Genet Med* 4(3):105–111.
4. Cichowski K, Jacks T (2001) NF1 tumor suppressor gene function: Narrowing the GAP. *Cell* 104(4):593–604.
5. Guo HF, The I, Hannan F, Bernards A, Zhong Y (1997) Requirement of Drosophila NF1 for activation of adenyl cyclase by PACAP38-like neuropeptides. *Science* 276(5313):795–798.
6. The I, et al. (1997) Rescue of a Drosophila NF1 mutant phenotype by protein kinase A. *Science* 276(5313):791–794.
7. Tong J, Hannan F, Zhu Y, Bernards A, Zhong Y (2002) Neurofibromin regulates G protein-stimulated adenylyl cyclase activity. *Nat Neurosci* 5(2):95–96.
8. Hegedus B, et al. (2007) Neurofibromatosis-1 regulates neuronal and glial cell differentiation from neuroglial progenitors in vivo by both cAMP- and Ras-dependent mechanisms. *Cell Stem Cell* 1(4):443–457.
9. Xu H, Gutmann DH (1997) Mutations in the GAP-related domain impair the ability of neurofibromin to associate with microtubules. *Brain Res* 759(1):149–152.
10. Hsueh Y, Roberts AM, Volta M, Sheng M, Roberts RG (2001) Bipartite interaction between neurofibromatosis type I protein (neurofibromin) and syndecan transmembrane heparan sulfate proteoglycans. *J Neurosci* 21(11):3764–3770.
11. Gitler AD, et al. (2003) NF1 has an essential role in endothelial cells. *Nat Genet* 33(1):75–79.
12. Brannan CI, et al. (1994) Targeted disruption of the neurofibromatosis type-1 gene leads to developmental abnormalities in heart and various neural crest-derived tissues. *Genes Dev* 8(9):1019–1029.
13. Jacks T, et al. (1994) Tumour predisposition in mice heterozygous for a targeted mutation in *Nf1*. *Nat Genet* 7(3):353–361.
14. Cichowski K, et al. (1999) Mouse models of tumor development in neurofibromatosis type 1. *Science* 286(5447):2172–2176.
15. Vogel KS, et al. (1999) Mouse tumor model for neurofibromatosis type 1. *Science* 286(5447):2176–2179.
16. Reilly KM, Loisel DA, Bronson RT, McLaughlin ME, Jacks T (2000) *Nf1*/Trp53 mutant mice develop glioblastoma with evidence of strain-specific effects. *Nat Genet* 26(1):109–113.
17. Costa RM, et al. (2001) Learning deficits, but normal development and tumor predisposition, in mice lacking exon 23a of *Nf1*. *Nat Genet* 27(4):399–405.
18. Zhu Y, et al. (2001) Ablation of NF1 function in neurons induces abnormal development of cerebral cortex and reactive gliosis in the brain. *Genes Dev* 15(7):859–876.
19. Zhu Y, Ghosh P, Charnay P, Burns DK, Parada LF (2002) Neurofibromas in NF1: Schwann cell origin and role of tumor environment. *Science* 296(5569):920–922.
20. Ismat FA, Xu J, Lu MM, Epstein JA (2006) The neurofibromin GAP-related domain rescues endothelial but not neural crest development in *Nf1* mice. *J Clin Invest* 116(9):2378–2384.
21. Joseph NM, et al. (2008) The loss of *Nf1* transiently promotes self-renewal but not tumorigenesis by neural crest stem cells. *Cancer Cell* 13(2):129–140.
22. Wu J, et al. (2008) Plexiform and dermal neurofibromas and pigmentation are caused by *Nf1* loss in desert hedgehog-expressing cells. *Cancer Cell* 13(2):105–116.
23. Zheng H, et al. (2008) Induction of abnormal proliferation by nonmyelinating Schwann cells triggers neurofibroma formation. *Cancer Cell* 13(2):117–128.
24. Silva AJ, et al. (1997) A mouse model for the learning and memory deficits associated with neurofibromatosis type I. *Nat Genet* 15(3):281–284.
25. Costa RM, et al. (2002) Mechanism for the learning deficits in a mouse model of neurofibromatosis type 1. *Nature* 415(6871):526–530.
26. Li H, Velasco-Miguel S, Vass WC, Parada LF, DeClue JE (2002) Epidermal growth factor receptor signaling pathways are associated with tumorigenesis in the *Nf1*:p53 mouse tumor model. *Cancer Res* 62(15):4507–4513.
27. Zhu Y, et al. (2005) Early inactivation of p53 tumor suppressor gene cooperating with NF1 loss induces malignant astrocytoma. *Cancer Cell* 8(2):119–130.
28. Le L, Parada L (2007) Tumor microenvironment and neurofibromatosis type I: Connecting the GAPs. *Oncogene* 26(32):4609–4616.
29. Side LE, et al. (1998) Mutations of the NF1 gene in children with juvenile myelomonocytic leukemia without clinical evidence of neurofibromatosis, type 1. *Blood* 92(1):267–272.
30. Le DT, et al. (2004) Somatic inactivation of NF1 in hematopoietic cells results in a progressive myeloproliferative disorder. *Blood* 103(11):4243–4250.
31. Gitler A, et al. (2004) Tie2-Cre-induced inactivation of a conditional mutant *Nf1* allele in mouse results in a myeloproliferative disorder that models juvenile myelomonocytic leukemia. *Pediatr Res* 55(4):581–584.
32. Yang FC, et al. (2008) *Nf1*-dependent tumors require a microenvironment containing *Nf1*^{+/−} and c-kit-dependent bone marrow. *Cell* 135(3):437–448.
33. Amores A, et al. (1998) Zebrafish *hox* clusters and vertebrate genome evolution. *Science* 282(5394):1711–1714.
34. Covassin L, et al. (2006) Global analysis of hematopoietic and vascular endothelial gene expression by tissue specific microarray profiling in zebrafish. *Dev Biol* 299(2):551–562.
35. Robu ME, et al. (2007) p53 activation by knockdown technologies. *PLoS Genet* 3(5):e78.
36. Isogai S, Lawson ND, Torrealday S, Horiguchi M, Weinstein BM (2003) Angiogenic network formation in the developing vertebrate trunk. *Development* 130(21):5281–5290.
37. Covassin LD, Villefranc JA, Kacergis MC, Weinstein BM, Lawson ND (2006) Distinct genetic interactions between multiple *Vegf* receptors are required for development of different blood vessel types in zebrafish. *Proc Natl Acad Sci USA* 103(17):6554–6559.
38. Vogel AM, Weinstein BM (2000) Studying vascular development in the zebrafish. *Trends Cardiovasc Med* 10(8):352–360.
39. Gruber PJ, Epstein JA (2004) Development gone awry: Congenital heart disease. *Circ Res* 94(3):273–283.
40. Gitler A (2004) PlexinD1 and semaphorin signaling are required in endothelial cells for cardiovascular development. *Dev Cell* 7(1):107–116.
41. Torresvazquez J (2004) Semaphorin-plexin signaling guides patterning of the developing vasculature. *Dev Cell* 7(1):117–123.
42. Norton KK, Xu J, Gutmann DH (1995) Expression of the neurofibromatosis I gene product, neurofibromin, in blood vessel endothelial cells and smooth muscle. *Neurobiol Dis* 2(1):13–21.
43. Cairns AG, North KN (2008) Cerebrovascular dysplasia in neurofibromatosis type 1. *J Neurol Neurosurg Psychiatr* 79(10):1165–1170.
44. Henkemeyer M, et al. (1995) Vascular system defects and neuronal apoptosis in mice lacking ras GTPase-activating protein. *Nature* 377(6551):695–701.
45. Eerola I, et al. (2003) Capillary malformation–arteriovenous malformation, a new clinical and genetic disorder caused by *RASA1* mutations. *Am J Hum Genet* 73(6):1240–1249.
46. Revencu N, et al. (2008) Parkes Weber syndrome, vein of Galen aneurysmal malformation, and other fast-flow vascular anomalies are caused by *RASA1* mutations. *Hum Mutat* 29(7):959–965.
47. Serban D, Leng J, Cheresch D (2008) H-ras regulates angiogenesis and vascular permeability by activation of distinct downstream effectors. *Circ Res* 102(11):1350–1358.
48. Liu L, Zhu S, Gong Z, Low BC (2008) K-ras/PI3K-Akt signaling is essential for zebrafish hematopoiesis and angiogenesis. *PLoS ONE* 3(8):e2850.

Oligodendrocyte progenitor cell numbers and migration are regulated by the zebrafish orthologs of the *NF1* tumor suppressor gene

Jeong-Soo Lee^{1,†}, Arun Padmanabhan^{2,†}, Jimann Shin¹, Shizhen Zhu¹, Feng Guo¹, John P. Kanki¹, Jonathan A. Epstein^{2,*} and A. Thomas Look^{1,3,*}

¹Department of Pediatric Oncology, Dana-Farber Cancer Institute, Harvard Medical School, Boston, MA 02115, USA,

²Department of Cell and Developmental Biology, Penn Cardiovascular Institute, and the Institute for Regenerative Medicine, University of Pennsylvania, Philadelphia, PA 19104, USA, and ³Division of Hematology/Oncology, Department of Pediatrics, Children's Hospital Boston, Harvard Medical School, Boston, MA 02115, USA

Received June 15, 2010; Revised and Accepted September 8, 2010

Neurofibromatosis type 1 is the most commonly inherited human cancer predisposition syndrome. Neurofibromin (*NF1*) gene mutations lead to increased risk of neurofibromas, schwannomas, low grade, pilocytic optic pathway gliomas, as well as malignant peripheral nerve sheath tumors and glioblastomas. Despite the evidence for *NF1* tumor suppressor function in glial cell tumors, the mechanisms underlying transformation remain poorly understood. In this report, we used morpholinos to knockdown the two *nf1* orthologs in zebrafish and show that oligodendrocyte progenitor cell (OPC) numbers are increased in the developing spinal cord, whereas neurons are unaffected. The increased OPC numbers in *nf1* morphants resulted from increased proliferation, as detected by increased BrdU labeling, whereas TUNEL staining for apoptotic cells was unaffected. This phenotype could be rescued by the forced expression of the GTPase-activating protein (GAP)-related domain of human *NF1*. In addition, the *in vivo* analysis of OPC migration following *nf1* loss using time-lapse microscopy demonstrated that *olig2*-EGFP⁺ OPCs exhibit enhanced cell migration within the developing spinal cord. OPCs pause intermittently as they migrate, and in *nf1* knockdown animals, they covered greater distances due to a decrease in average pause duration, rather than an increase in velocity while in motion. Interestingly, *nf1* knockdown also leads to an increase in ERK signaling, principally in the neurons of the spinal cord. Together, these results show that negative regulation of the Ras pathway through the GAP activity of *NF1* limits OPC proliferation and motility during development, providing insight into the oncogenic mechanisms through which *NF1* loss contributes to human glial tumors.

INTRODUCTION

Neurofibromatosis type 1 is a dominantly inherited autosomal disease that affects 1 in 3500 individuals worldwide. Inactivating mutations of the neurofibromin (*NF1*) gene responsible for the disease can arise in a diverse set of tissues, producing symptoms that range from mild to severe, the most prevalent of which include café-au-lait pigment spots in the skin and the cutaneous development of neurofibromas

from Schwann cells of the peripheral nervous system (PNS). Plexiform neurofibromas—non-circumscribed, thick, irregular and invasive benign tumors composed of Schwann cells, fibroblasts, mast cells and vascular components—often occur in this disease and are a major cause of disfigurement because they invade essential structures. *NF1* loss is the most common syndrome predisposing to tumorigenesis in humans, increasing the risk for the development of low grade, pilocytic optic pathway gliomas of the central

*To whom correspondence should be addressed at: Dana-Farber Cancer Institute, Mayer Building, Room 630, 44 Binney Street, Boston, MA 02115, USA. Tel: +1 6176325826; Fax: +1 6176326989; Email: thomas_look@dfci.harvard.edu (A.T.L.); University of Pennsylvania, 1154 BRB II, 421 Curie Boulevard, Philadelphia, PA 19104, USA. Tel: +1 2158988731; Email: epsteinj@mail.med.upenn.edu (J.A.E.)

[†]The authors wish it to be known that, in their opinion, the first two authors should be regarded as joint First Authors.

nervous system (CNS) (1), as well as malignant peripheral nerve sheath tumors (2) and high-grade astrocytomas (3). Recently, a large-scale genomic analysis identified somatic mutations and loss of heterozygosity of *NF1* in 25% of sporadic glioblastoma cases (4).

The *NF1* gene encodes a very large 2818 amino acid cytoplasmic protein (5). To date, the principal domain identified and analyzed in this protein is a 360 amino acid GTPase-activating protein (GAP)-related domain (GRD) whose activity is known to hydrolyze GTP to GDP bound to Ras (5,6). The loss of GRD function in *NF1*-deficient malignant peripheral nerve sheath tumors leads to increased Ras activity, which in turn activates downstream signaling cascades including the Ras/ERK and PI3K/Akt pathways, providing putative underlying mechanisms for the tumor suppressor function of *NF1* in these cancers. Studies using murine models suggested that *Nf1* loss of function in specific cell populations (e.g. Schwann cells), possibly in combination with a heterozygous microenvironment (e.g. mast cells), was critical for the formation of plexiform neurofibromas (7–9). However, conflicting data supporting the micro-environmental contribution of *NF1* may reflect both tissue-specific and developmental timing effects (10,11).

Astrocytes and oligodendrocytes comprise the main glial cell types in the CNS, the latter being responsible for producing the myelin that forms sheaths around axons. In both mammals and zebrafish, oligodendrocytes arise from the motoneuron progenitor (pMN) domain of the ventral spinal cord, where motoneurons form first and oligodendrocytes develop later (12). The transcription factor gene *olig2* is critical for oligodendrocyte specification, and its expression is first observed in the pMN domain and then maintained throughout the subsequent differentiation of oligodendrocyte progenitor cells (OPCs) (13). Although the role of oligodendrocytes in tumors associated with *NF1* loss remains unclear, optic pathway gliomas in neurofibromatosis type 1 patients expressed PEN5, a marker for oligodendrocyte precursors (14). Consistent with this finding, knockout mice and *in vitro* cell culture experiments demonstrated that deletion of the *Nf1* gene in neuroglial cells leads to their overproliferation and abnormal differentiation (15,16). Aberrant oligodendroglial phenotypes may also contribute to other neurofibromatosis type 1 CNS abnormalities, such as macrocephaly and learning disabilities, presumably due to abnormal increases in glial cell production (17,18).

We recently identified two zebrafish orthologs of *NF1* and analyzed their cardiac and vascular functions during embryologic development (19). Here we report the *in vivo* roles of *nf1* in zebrafish oligodendrocyte development. Both genes are expressed ubiquitously early in development, but become restricted to the CNS after 48 hpf (hours post-fertilization). Knockdown of the *nf1* genes resulted in an increase in OPC proliferation in the spinal cord, and time-lapse imaging demonstrated an enhancement of OPC migration during development. The increased numbers of OPCs in the spinal cord caused by *nf1* deficiency was rescued by forced expression of the GRD domain of human *NF1*, suggesting an essential role for Ras pathway activation and the GAP activity of *NF1* in regulating OPC numbers during development.

RESULTS

The number of OPCs is increased upon *nf1* knockdown

NF1 patients often have symptoms that may be related to glial abnormalities such as macrocephaly, and they are prone to develop glia-derived cancers including optic pathway glioma and astrocytoma (1,3,18). In order to test the role of *nf1a* and *nf1b* in zebrafish oligodendrocyte development, we used morpholinos (MOs) to knockdown each gene in the *Tg(olig2:EGFP)* transgenic zebrafish line (20) that had been bred into wild-type and *p53 e7/e7* backgrounds (21). The *Tg(olig2:EGFP)* transgenic line expresses EGFP in OPCs throughout oligodendrocyte development, allowing their analysis *in vivo* (20). The *Tg(olig2:EGFP)* transgenic line in the *p53* mutant background was used to circumvent off-target effects that are known to be due to MO toxicity (Supplementary Material, Fig. S2) (22). To knockdown *nf1* function, we designed and injected *nf1*-specific splice-blocking MOs [two for *nf1a* (*nf1a-e1* and *nf1a-e7*) and one for *nf1b* (*nf1b-e4*)] into the *Tg(olig2:EGFP)* transgenic zebrafish lines (19). The two MOs used to block *nf1a* function, *nf1a-e1* and *nf1a-e7*, yielded similar results, both in efficacy and in the resultant phenotypes (Supplementary Material, Figs S3 and S4); thus, for consistency, we only present our results with *nf1a-e7* and *nf1b-e4* to block *nf1a* and *nf1b* expression, respectively. The efficiency of the MOs was confirmed by RT-PCR at 3 dpf (days postfertilization), when the observed aberrant bands upon MO knockdown demonstrated inappropriate splicing [MOs for *nf1a* (*nf1a-e7*) and *nf1b* (*nf1b-e4*) are shown in Supplementary Material, Fig. S3]. The efficacy of the *nf1b* MO was further evaluated by quantitative real-time RT-PCR, which indicated an ~90% knockdown of the wild-type *nf1b* transcript (Supplementary Material, Fig. S3D). Because *nf1a-e7* injection led to several aberrant bands in addition to multiple cryptic donor splice sites within exon 7 of *nf1a*, the quantitative knockdown of *nf1a* transcripts could not be similarly evaluated by quantitative real-time RT-PCR. However, when these aberrant bands were subcloned and sequenced, they were found to contain either deletions of the targeted exons or insertions of additional introns that resulted in frame-shifts in coding sequence leading to the early termination of transcripts (see Supplementary Material, Fig. S3B for details).

In *Tg(olig2:EGFP)* transgenic zebrafish, a subset of GFP⁺ OPCs that arise in the ventral spinal cord migrate dorsally and differentiate into oligodendrocytes (brackets in Fig. 1A–C), whereas another GFP⁺ OPC subpopulation remains in the ventral spinal cord, intermingled with *olig2-EGFP*⁺ motoneurons and interneurons (Fig. 1A–C) (20,23). These *olig2-EGFP*⁺ motoneurons and interneurons can often be distinguished from the OPCs because of their lower level of EGFP expression, relatively round shape devoid of processes and their failure to migrate dorsally. When *nf1a* and *nf1b* were knocked down by MOs, we consistently found an increased number of dorsally positioned OPCs at 3 dpf (Fig. 1A–C; see also Supplementary Material, Fig. S4). The most dramatic OPC increase relative to the control was observed when both the *nf1a* and *nf1b* genes were knocked down simultaneously in the *p53 e7/e7* background (Fig. 1C), although significant increases in OPC numbers were also observed in embryos with the knockdown of an individual *nf1* gene (Fig. 1M; Sup-

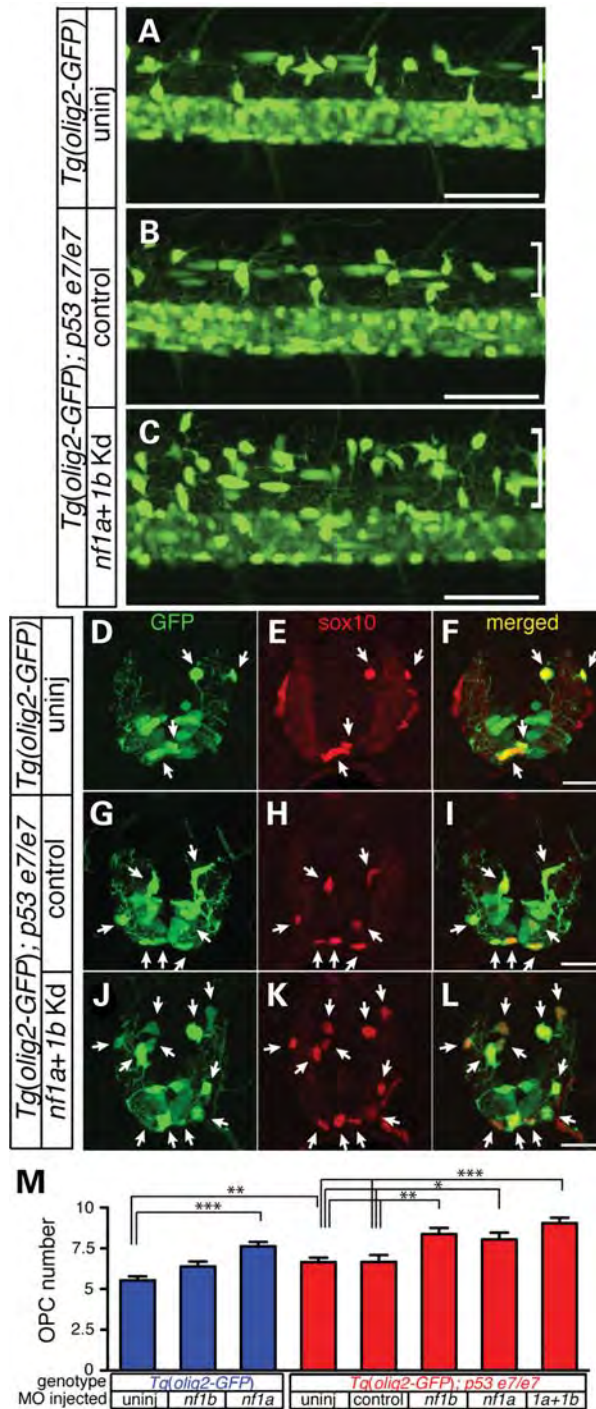


Figure 1. Knockdown of *nf1a* and *nf1b* leads to increased numbers of OPCs. (A–C) Projected confocal images showing a lateral view of the spinal cord in live transgenic animals at 3 dpf. (A, D–F) Uninjected *Tg(olig2:EGFP); p53+/+* transgenic zebrafish. (B, G–I) Control MO-injected *Tg(olig2:EGFP); p53 e7/e7* embryo. (C, J–L) *Tg(olig2:EGFP); p53 e7/e7* injected with *nf1a* and *nf1b* MOs [*nf1a + 1b* Kd (knockdown)]. (D–L) Transverse sections through the spinal cord of embryos at 3 dpf, with GFP (green) and sox10 (red) labeling to specifically visualize co-expressing OPCs (arrows). (M) Statistical analysis of mean ± SEM numbers of GFP⁺/sox10⁺ cells per section in *nf1a* or *nf1b* alone or in combination at 3 dpf. Asterisks indicate statistical significance (* $P < 0.05$; ** $P < 0.005$; *** $P < 0.0005$). Scale bars in (A–C) = 50 μ m; (F, I and L) = 20 μ m.

plementary Material, Fig. S4). These results indicate that both *nf1* genes contribute to the regulation of normal OPC numbers and that *nf1* knockdown results in an increased number of dorsally positioned OPCs.

We then extended our analysis to include ventrally positioned OPCs by co-immunostaining with an anti-sox10 antibody that labels OPCs, but not *olig2-EGFP*⁺ motoneurons and interneurons that are also located in the ventral spinal cord at this stage. Although the increase in *olig2-EGFP*⁺; sox10⁺ OPC numbers upon *nf1* knockdown was not apparent in transverse sections of the spinal cord at 2 dpf, when the dorsal migration of OPCs commences (Supplementary Material, Fig. S5), the increased numbers of OPCs did become evident by 3 dpf (Fig. 1J–L, compared with D–F and G–I). The mean number of OPCs was determined for *nf1a + nf1b* morphants and control embryos by counting these cells in immunostained transverse sections. The *nf1* morphants were found to have 36% more OPCs than control *p53 e7/e7* embryos (9.0 versus 6.6, with $n = 23$ and 26, respectively, $P < 0.0001$; Fig. 1M). These findings indicate that *nf1* negatively regulates the number of OPCs during development.

The observed increase in OPCs in *nf1* morphants could be due to an aberrant dorsal migration of OPCs that normally remain in the ventral spinal cord or to an overall increase in OPCs throughout the spinal cord. To distinguish between these possibilities, we assessed the differences in OPC numbers in dorsal and ventral spinal cord regions. A 36% increase in dorsally migrating OPCs was found in *nf1* versus control morphants in the *p53* background (4.0 versus 2.9; $n = 11$; $P < 0.05$), whereas a 26% increase in ventrally localized OPCs was observed (4.6 versus 3.7; $n = 11$; $P < 0.05$). These results indicate that increases in OPC numbers occur in both locations rather than reflecting an aberrant displacement of ventral cells to more dorsal regions. Although a slight increase in OPCs in the *p53* mutant background was observed, presumably due to the survival of cells that would otherwise succumb to MO toxicity, it is important to note that significant increases in OPCs in *nf1* morphants were also observed in the wild-type background (Fig. 1M; Supplementary Material, Fig. S4).

In order to further document the OPC increase upon *nf1a + 1b* knockdown, we also employed a second approach to block apoptosis and rescue the early cell death in the *p53* wild-type embryos that occurs with *nf1a + 1b* MO injection. In this approach, we co-injected zebrafish *bcl-X_L* RNA, which is known to block most cell death during early embryogenesis (24,25). Most of the embryos (>90%) co-injected with *bcl-X_L* RNA together with *nf1a + 1b* MOs did not exhibit cell death in the brain at 1 dpf (Supplementary Material, Fig. S12D) and developed relatively normally to 3 dpf. The numbers of OPCs in these *Tg(olig2:EGFP)* embryos were significantly increased compared with those in embryos co-injected with *bcl-X_L* RNA and the control MO (63.3 versus 52.9, $P < 0.05$; Supplementary Material, Fig. S12E–G), or embryos injected with control MO alone (Fig. 4D and E).

To determine whether *nf1* loss affects the differentiation of OPCs into oligodendrocytes, we counted myelin basic protein-positive oligodendrocytes in the dorsal spinal cord at 3 dpf in whole-mount RNA *in situ* hybridized embryos. No significant

differences between control and *nf1a + 1b* knockdown embryos were found at 3 dpf (Supplementary Material, Fig. S6). This finding suggests that the extra OPCs fail to differentiate during the 3 day time period shown in Supplementary Material, Figure S6; however, it is possible that the effects of MOs are diluted over time and genetic analysis at time points beyond 3 days will require the isolation of stable *nf1* mutants.

***nf1* loss specifically affects OPCs from the pMN of the ventral spinal cord**

Since OPCs and motoneurons are derived from common precursors in the *olig2*-positive pMN domain of the ventral spinal cord during development (26), we examined whether *nf1* deficiency might affect the development of motoneurons and contribute to the increased numbers of OPCs. Islet protein (Isl) is expressed in primary and secondary motoneurons, interneurons and sensory neurons of the spinal cord, and Zn5 is a marker specific for developing secondary motoneurons (27,28). Quantification of cell numbers using anti-Isl and Zn5 antibodies did not exhibit significant differences in cells expressing either of these markers in *nf1a + 1b* knockdown embryos compared with control at 80 hpf (Fig. 2F versus B; N versus J; Q and R, $n = 15$). In addition, *nf1a + 1b* loss did not affect the overall size or shape of developing secondary motoneurons (Fig. 2N versus J). These results suggest that *nf1* knockdown acted specifically on the cells of the oligodendrocyte lineage, whereas the neuronal lineages from the pMN domain, such as motoneurons, remain unaffected.

Loss of *nf1* causes an increase in OPC proliferation

The increase in OPC numbers caused by *nf1* deficiency could occur through several different mechanisms. We first investigated whether cell death played a role in this phenotype by comparing the numbers of TUNEL-positive OPCs in the spinal cord of control versus *nf1a + 1b* morphants; the numbers of TUNEL-positive OPCs were identical and, in fact, were extremely rare in embryos injected with either specific or control MOs (total 2–4 cells in >40 sections), suggesting that the increase OPC numbers due to *nf1* loss does not occur because of decreased levels of apoptosis.

Next we investigated whether the increase in OPC numbers in *nf1* morphants was due to the increased proliferation of OPCs. We pulse-labeled control- and MO-injected embryos with BrdU at 54 and 80 hpf, fixed them immediately after BrdU treatment and examined BrdU incorporation in GFP⁺/sox10⁺ OPCs. At 80 hpf, BrdU⁺ cells were much more abundant in sections of the spinal cord (>40% of total sections), and BrdU⁺-positive OPCs could be identified in both control and *nf1a + 1b* morphants. Importantly, when GFP⁺/sox10⁺/BrdU⁺ cells were counted; the number of BrdU-labeled as well as total OPCs in *nf1a + 1b* morphants was significantly higher compared with those in controls (1.08 versus 1.83 per section, $n = 12$, $P < 0.005$; Fig. 3). These results indicate that *nf1*-deficient OPCs exhibit a higher proliferation rate, thus accounting for the observed increase in OPC numbers. In contrast, at 54 hpf, when OPC numbers were not yet affected by *nf1* loss (Supplementary Material, Fig. S5), GFP⁺/sox10⁺/BrdU⁺ cells in

the spinal cord of both control and *nf1a + 1b* morphants were very rare and not significantly different (1/60 sections of control and 4/43 sections of *nf1a + 1b* morphant, Fisher's exact test, $P > 0.05$; Supplementary Material, Fig. S7).

Another potential contributor to increased OPC numbers may be through an increase in OPC progenitor cells. *olig2-EGFP*⁺ radial glial cells are slowly dividing cells that are thought to give rise to newly forming OPCs in the juvenile and adult spinal cord (29). Thus, hyperproliferation or trans-differentiation of radial glial cells into OPCs could contribute to the increase in OPCs observed in our *nf1a + 1b* morphants. However, the numbers of *olig2-EGFP*⁺ radial glia, which are co-labeled with GFAP, did not differ significantly in *nf1*-deficient versus control embryos (1.17 versus 1.11, $n = 18$, $P > 0.7$, Supplementary Material, Fig. S8A–F), and BrdU-incorporating radial glial cells in the spinal cord at 54 and 80 hpf were unchanged and extremely rare without or with *nf1* loss (3 BrdU⁺ radial glial cells/109 sections in control and 1 BrdU⁺ radial glial cell/138 sections in *nf1a + 1b* morphants at 80 hpf, Fisher's exact test, $P > 0.3$; Supplementary Material, Fig. S8G–N). Taken together, these data suggest that following OPC specification, *nf1* loss causes an increase in their proliferation between 54 and 80 hpf, which is responsible for the observed increase in OPC numbers in *nf1a + 1b* morphants.

The increase in OPCs due to *nf1* knockdown depends upon the GRD of NF1

The best known function of human NF1 is to act as a Ras-GAP to downregulate Ras signaling. To test whether the overproliferation of OPCs in *nf1* morphants was dependent upon GRD function, we co-injected mRNA encoding the GRD domain of human NF1 (5,6,30) into *nf1a + 1b*-morphant embryos [*Tg(olig2:EGFP): p53 e7/e7* background] and examined whether its expression could rescue this phenotype. To monitor GRD expression, we fused the coding sequence of the mCherryRed fluorescent protein in-frame at the N-terminus of the sequence encoding the GRD domain. The *nf1a + 1b*-morphant embryos [*Tg(olig2:EGFP): p53 e7/e7* background] co-injected with *mCherryRed* RNA served as a positive control and exhibited the expected increase in OPC numbers relative to control MO- and control RNA-injected *Tg(olig2:EGFP): p53 e7/e7* embryos (Fig. 4B–D). However, *nf1a + 1b*-morphant embryos that were co-injected with the GRD RNA exhibited a relative reduction in OPC numbers in the dorsal spinal cord from 67.7/embryo to 48.5/embryo ($n = 10$, $P < 0.001$; Fig. 4A, B and E), which did not differ significantly from the number of OPCs present in control MO- and control RNA-injected embryos (48.5 versus 47.5, $P > 0.7$, and 48.5 versus 57.5, $P > 0.1$, respectively; Fig. 4A and C–E). These results demonstrate that the expression of *NF1-GRD* alone can rescue the increased OPC phenotype due to *nf1* deficiency, indicating that NF1 regulates OPC proliferation through its GAP activity.

***nf1* loss promotes OPC migration**

To examine the behavior of OPCs following *nf1* knockdown, we performed *in vivo* live time-lapse imaging of these cells.

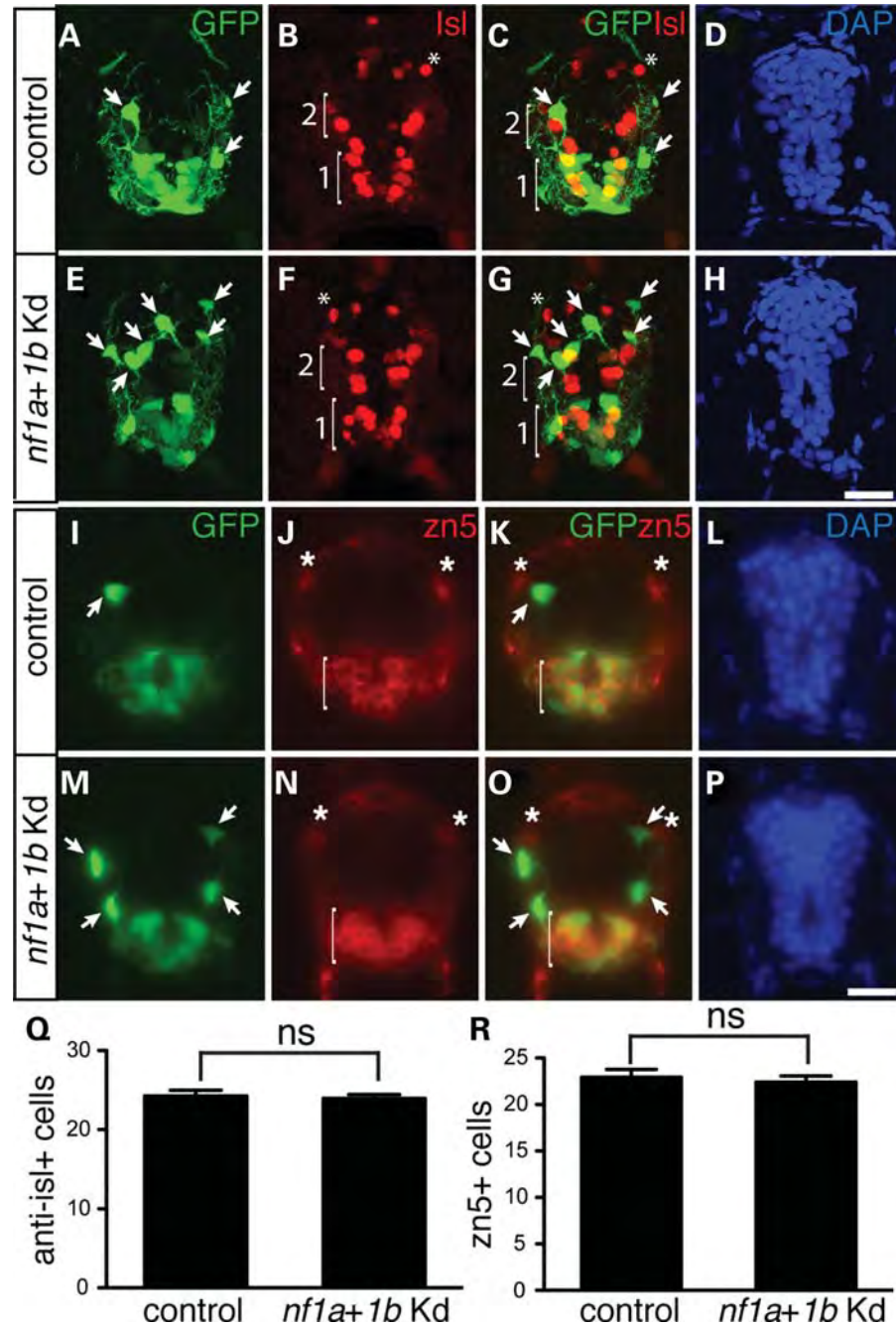


Figure 2. Spinal cord neurons are not affected by *nf1* loss. (A–D, I–L) *Tg(olig2:EGFP)*; *p53 e7/e7* embryos injected with the control MO (control). (E–H, M–P) An *Tg(olig2:EGFP)*; *p53 e7/e7* embryo injected with *nf1a* and *nf1b* MOs (*nf1a+1b* Kd). (A–H) Projected confocal images of transverse sections labeled with the anti-is1 antibody show subsets of primary/secondary motor neurons (bracket 1), interneurons (bracket 2) and putative Rohon Beard sensory neurons (asterisk). Green, *olig2*-GFP; red, anti-is1; blue, DAPI. Arrows in (A), (C), (E) and (G) designate dorsal OPCs. (I–P) Fluorescence images of transverse sections labeled with the zn5 antibody showing secondary motor neurons. Statistical analyses of the numbers of anti-is1-positive (Q) or zn5-positive (R) cells show no significant differences. Green, *olig2*-GFP; red, zn5; blue, DAPI. Arrows in (I), (K), (M) and (O) indicate dorsal OPCs; asterisks in (J), (K), (N) and (O) indicate the dorsal lateral fasciculus; brackets in (J), (K), (N) and (O) indicate secondary motoneurons. Scale bar = 20 μ m.

We monitored the *Tg(olig2:EGFP)* transgenic animals for 12 h, beginning at 60 hpf when OPCs start to actively migrate away from the ventral spinal cord. Compared with the findings in uninjected control animals, more OPCs in the *nf1a+1b*-knockdown embryos migrated into the dorsal spinal cord (Fig. 5A and B; Supplementary Material, Movies S1 and S2), consistent with our observations from fixed sec-

tions (Fig. 1). Interestingly, the time-lapse study also revealed that the *nf1a+1b*-morphant OPCs traveled longer distances relative to control animals (Fig. 5E; Supplementary Material, Movies S1 and S2). In the movies, *nf1a+1b*-knockdown OPCs migrated farther in the dorsal and rostro-caudal directions than did control OPCs, as indicated by the examination of representative migratory traces of individual cells

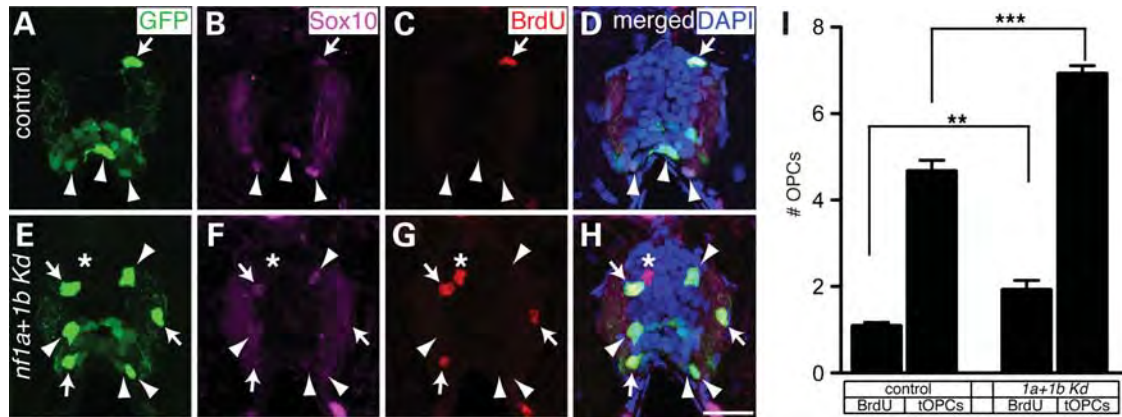


Figure 3. *nf1* loss leads to increased BrdU incorporation in OPCs. Projected confocal images of transverse spinal cord sections of *Tg(olig2:EGFP); p53 e7/e7* embryos at 80 hpf. (A and E) green, *olig2:EGFP*; (B and F) magenta, anti-sox10; (C and G) red, anti-BrdU; (D and H) overlay merged with DAPI (blue). (A–D) Embryos injected with the control MO (control). (E–H) Embryos injected with *nf1a + nf1b* MOs (*nf1a + 1b* Kd). (A–H) Arrows indicate dividing OPCs ($\text{GFP}^+/\text{sox10}^+/\text{BrdU}^+$), and arrowheads denote non-dividing OPCs ($\text{GFP}^+/\text{sox10}^+/\text{BrdU}^-$). (E–H) Asterisks denote a $\text{GFP}^-/\text{sox10}^-/\text{BrdU}^+$ cell in the spinal cord, representing a dividing neuron. (I) Statistical analysis of mean \pm SEM numbers of $\text{GFP}^+/\text{sox10}^+/\text{BrdU}^+$ ('BrdU⁺') or total OPCs ('tOPCs') per section in control or *nf1a + 1b* Kd at 3 dpf. OPCs incorporating BrdU are increased in the *nf1a + 1b* morphants compared with controls, indicating a higher proliferative activity. Asterisks indicate statistical significance (** $P < 0.005$; *** $P < 0.0005$). Scale bar = 20 μm .

(Fig. 5C and D). Analysis of the movement of all individual OPCs that could be observed over the 12 h imaging period showed a 35% increase in total distance traveled by the OPCs in *nf1* knockdown animals (32.05 μm in control versus 43.27 μm in *nf1a + 1b* morphant; $P < 0.05$; $n = 9$ and $n = 23$, respectively; Fig. 5E). In all cases, the OPCs display intermittent movements consisting of repeated cycles of active migration, separated by pauses before continuing, often in different directions from the original path. After *nf1* knockdown, the OPCs paused for shorter periods of time relative to controls (413.9 min in control versus 324.3 min in *nf1a + 1b* morphant; $P < 0.005$; Fig. 5F), whereas the frequency of the pauses did not differ significantly (2.28 h^{-1} in control versus 2.58 h^{-1} in *nf1a + 1b* morphant; $P > 0.1$). Furthermore, the migration velocity of OPCs was determined by dividing the distance traveled by the total traveling time, which excluded the periods when they were stationary. The migration velocity was unaffected by *nf1* knockdown (0.5203 $\mu\text{m}/5$ min in control versus 0.5343 $\mu\text{m}/5$ min in *nf1a + 1b* morphant; $P > 0.7$; Fig. 5G). Together, these findings show that OPCs in *nf1a + 1b* morphants exhibit a novel phenotype *in vivo*, spending more time actively migrating with shorter pauses than controls.

nf1 loss leads to the hyperactive ERK signaling in the spinal cord

To further investigate the effect of *nf1* deficiency on Ras signaling during OPC development, we examined two principal pathways downstream of activated Ras by evaluating the status of phosphorylated ERK and phosphorylated S6 to assess the Raf/ERK and PI3K/Akt/mTOR pathways, respectively (31). Labeling transverse sections of the spinal cord at 54 hpf of *Tg(olig2:EGFP); p53 e7/e7* embryos with a phospho-ERK antibody revealed few phospho-ERK⁺ cells in either control or *nf1*-knockdown conditions, suggesting low ERK signaling in the spinal cord at this stage that did not

respond to *nf1* loss (Supplementary Material, Fig. S9). However, at 80 hpf, *nf1* knockdown resulted in a marked increase in phospho-ERK-positive cells throughout the spinal cord of *Tg(olig2:EGFP); p53 e7/e7* embryos relative to controls, indicating an aberrant activation of the Ras pathway due to *nf1* deficiency (Fig. 6). Interestingly, phospho-ERK was not increased in OPCs (arrows in Fig. 6A–H), but rather was expressed in neighboring neurons that were identified by the co-expression of HuC/D, a pan-neuronal marker (arrows in Supplementary Material, Fig. S10). There was a subpopulation of OPCs that were weakly pERK positive in both control and *nf1a + 1b* morphants (asterisks in Fig. 6A–H and Supplementary Material, Fig. S9F–J); however, no significant change in pERK levels was detected upon *nf1* loss. We also assayed for the phosphorylation of the S6 ribosomal protein in the spinal cord at 3 dpf following *nf1* knockdown in *Tg(olig2:EGFP); p53 e7/e7* embryos and did not observe any significant differences in the numbers of phospho-S6-positive OPCs or other cell types (Supplementary Material, Fig. S11). Thus, *nf1* deficiency causes an aberrant upregulation of the ERK signaling pathway in neighboring spinal cord neurons, coincident with the overproliferation and abnormal migration of OPCs.

DISCUSSION

Inactivation of the *NF1* tumor suppressor gene has been found to contribute to a wide variety of pathologies that can affect glial development and predispose to tumorigenesis in both the PNS and CNS. In this study, we gain insight into the role of NF1 in gliogenesis by investigating how the loss of *nf1* affects oligodendrocyte development in zebrafish. We determined the expression patterns of the two zebrafish *nf1* genes during embryogenesis and showed that the loss of the *nf1* orthologs by MO knockdown resulted in increased numbers of OPCs. The increased number of OPCs was found to be due to overproliferation of the OPCs themselves,

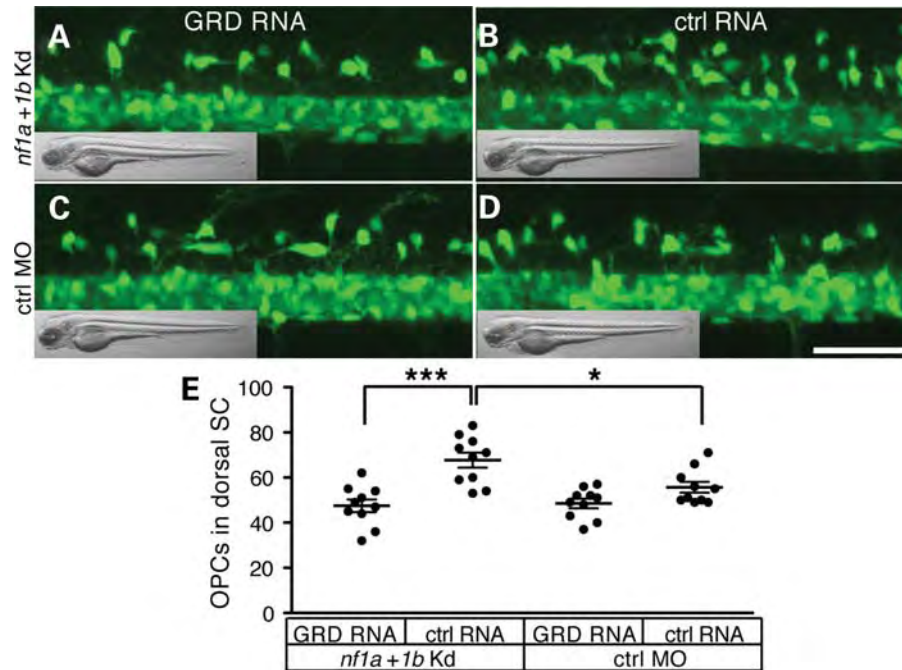


Figure 4. Forced expression of *NF1* GRD is sufficient to rescue the proliferative OPC phenotype. (A–D) Projected confocal images showing the lateral view of the spinal cord of *Tg(olig2:EGFP); p53 e7/e7* embryo at 3 dpf: (A and B) *nf1a + 1b Kd*; (C and D) control MO; (A and C) GRD RNA injected; (B and D) mCherryRed (control) RNA injected. Insets show the bright field images of the embryos used for confocal imaging and demonstrate normal overall morphologies in all cases. Scale bar = 50 μ m. (E) Graph showing the number of OPCs, represented by individual points, in the dorsal spinal cord (SC) of 10 embryos for each condition at 3 dpf (* $P < 0.05$; *** $P < 0.001$). The data are presented as means \pm SEM.

which was dependent upon the activation of the Ras pathway through the expression of the NF1-GRD. *nf1* deficiency also increased the motility of OPCs, leading to an enhancement of migration. The hyperproliferation and enhanced migration of OPCs after *nf1* knockdown occurred along with the aberrant activation of pERK signaling in neighboring neurons in the developing spinal cord.

Duplication of the whole genome in teleosts, which followed their divergence from tetrapods, accounts for the presence of two zebrafish *nf1* genes, in contrast to the single gene found in mammals (32). Both *nf1* genes are not only functional but also act redundantly during OPC development in zebrafish because: (i) they show exceptionally high amino acid sequence homology, especially in the GRD; (ii) both genes conserve syntenic relationships with human *NF1*; (iii) both are expressed during embryogenesis with partially overlapping expression patterns; and (iv) both genes contribute independently to an increase in OPC numbers as a result of MO knockdown. Our analysis indicates that zebrafish *nf1a* and *nf1b* act in an additive manner during OPC development, in that simultaneous knockdown of these genes increased OPC numbers more than knockdown of either gene alone.

Studies *in vivo* and *in vitro* indicate that astrocytes and oligodendrocytes, the two main glial cell types in the CNS, overproliferate in the context of either complete *Nf1* knockout or heterozygous *Nf1* mutant cells (11,15,16,33). Schwann cells, the myelin-producing glial population in the PNS, also overproliferate upon *Nf1* loss (34,35). We augment these findings by showing *in vivo* that the number of zebrafish OPCs in the spinal cord is increased upon *nf1* MO knockdown. We found that the numbers of zebrafish *olig2*⁺ OPCs co-labeled by

sox10 in the developing spinal cord are increased upon *nf1* MO knockdown. Furthermore, our TUNEL and BrdU pulse-labeling assays clearly show that excessive OPCs in *nf1*-deficient embryos results from the aberrant overproliferation of OPCs themselves (Fig. 4), rather than decreased OPC death or increased production from *olig2-EGFP*⁺ radial glial cells (29). Consistent with our finding, cultured cells from the E12.5 spinal cord of the *nf1* knockout mouse showed an increased number of BrdU-incorporating cells (15), and the numbers of both *olig2*-expressing cells and BrdU-incorporating cells were increased in the brains of BLBP-cre/*Nf1* flox mice, when *Nf1* was selectively deleted in neuroglial progenitors (16). Moreover, our GRD rescue experiment establishes that the OPC phenotype is due to the loss of GAP activity normally provided by Nf1. Our results are important because Nf1 has also been observed to have tissue-specific roles in development that are independent of the GRD. For example, GRD rescue in the context of *Nf1* deficiency can restore cardiovascular development, but does not inhibit the overgrowth of neural crest-derived tissues (30).

During development, neurons and glia of the vertebrate CNS originate from common neuroglial precursor cells in the pMN domain of the ventral spinal cord (26). Since MO injections were performed at the one-cell stage, it is possible that the increased OPC phenotype might reflect an earlier effect of *nf1* deficiency on neuroglial precursor cell proliferation, which might be evident from abnormal cell numbers in both neuronal and glial lineages. However, analysis of the neuronal derivatives (including motoneurons) in the *nf1* morphants revealed numbers that were essentially unchanged, indicating that the effect of *nf1* deficiency was specific to

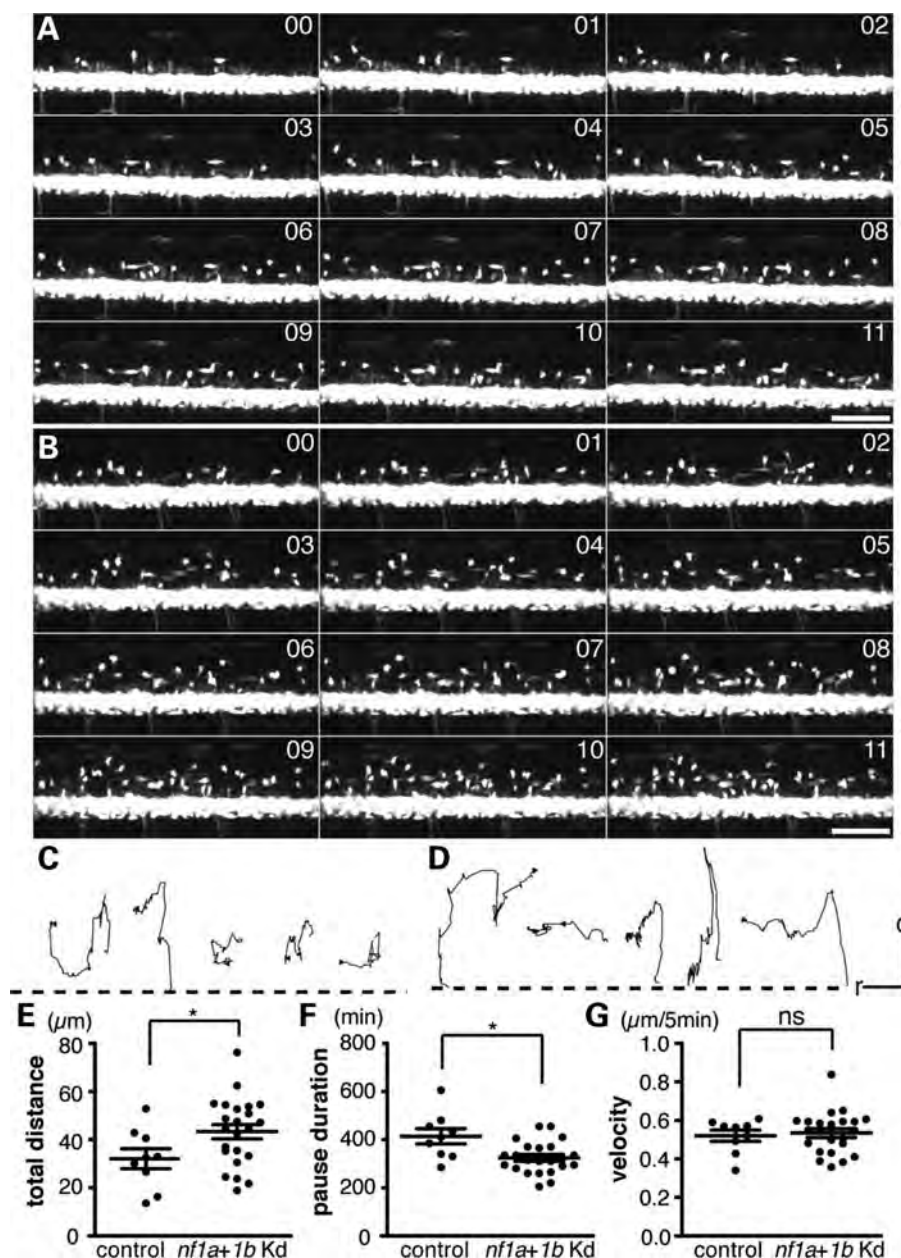


Figure 5. *nf1* loss affects the migration of OPCs. (A and C) An uninjected *Tg(olig2:EGFP): p53 e7/e7* control embryo; (B and D) A *Tg(olig2:EGFP): p53 e7/e7* embryo injected with *nf1a + 1b* MOs. (A and B) Montages of 12 h time-lapse images from 60 to 72 hpf, showing the movements of OPCs every hour. Numbers in each panel denote the hour(s) after the start of imaging. For the complete movies, refer to Supplementary Material, Movies S1 and S2. (C and D) Cell migration paths are shown for five OPCs that traveled the farthest during the observation period. In both conditions, migration patterns are highly dynamic. Arrowheads indicate the endpoint of the cell's migration. The dashed lines represent the dorsal-most GFP⁺ domains of the ventral spinal cord. Top, dorsal (d); left, rostral (r). (E) Graph showing the total distance OPCs travel with or without *nf1* loss. (F) Graph showing the total time individual OPCs spent pausing. (G) Graph showing the velocity of OPCs calculated from when they were actively migrating. All individual OPCs (represented by single points) that could be observed in the field of view throughout the entire period, spanning the 12 h imaging period, were traced and used in this analysis ($n = 9$ for uninjected control embryos, $n = 23$ for *nf1a + 1b*-morphant embryos). The data in (E–G) are reported as mean \pm SEM; asterisks indicate non-parametric statistical significance (* $P < 0.05$; ns, not significant). Scale bars in (A) and (B) = 25 μ m; (C) and (D) X-axis = 10 μ m and Y-axis = 5 μ m.

OPCs. These findings are interesting in light of the marked increase in levels of phosphorylated ERK observed after *nf1* knockdown in the neurons surrounding the OPCs (Fig. 6; Supplementary Material, Fig. S7). Although we do not believe that earlier changes in phospho-ERK signaling affect the OPCs themselves (Supplementary Material, Fig. S8), it is worthwhile to note that there remain additional signaling pathways regu-

lated by Ras that may contribute to the intrinsic control of OPC numbers in *nf1* morphants (31).

In vitro assays indicate that *Nf1* loss in astrocytes and Schwann cells can lead to enhanced motility. Astrocytes missing one or both alleles of *Nf1* exhibit an increase in cell motility, together with cytoskeletal abnormalities (36), that is dependent upon the mTOR pathway and requires

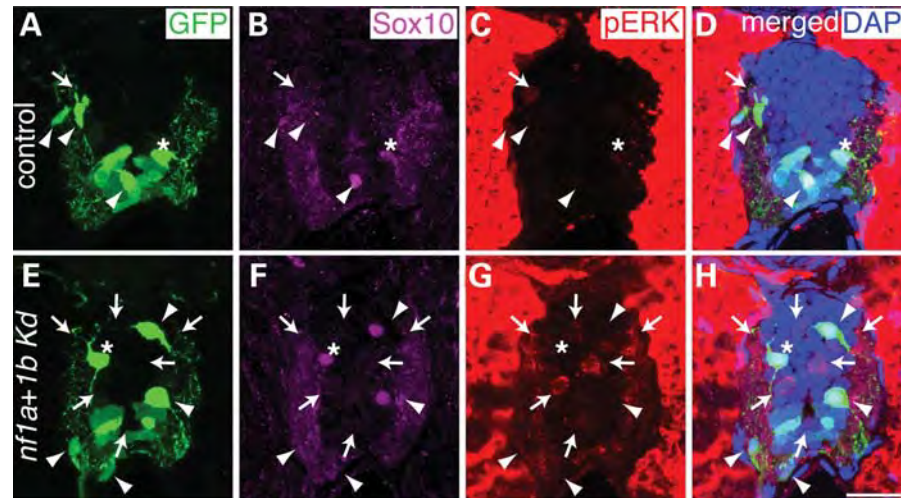


Figure 6. *nf1* loss activates the ERK pathway. Projected confocal images of transverse spinal cord sections at 80 hpf of *Tg(olig2:EGFP); p53 e7/e7* embryos. (A and E) green, *olig2:EGFP*; (B and F) magenta, anti-sox10; (C and G) red, anti-phospho-ERK; (D and H) overlay merged with DAPI (blue). (A–D) Control MO-injected embryo. (E–H) *nf1a + 1b* Kd. Increased numbers of phospho-ERK-positive cells were detected in the spinal cord of *nf1a + 1b* morphants (arrows in G), compared with control (arrow in C). Arrowheads denote $GFP^{+}/sox10^{+}$ OPCs, which are predominantly phospho-ERK1/2 negative. A minor OPC population is phospho-ERK positive (asterisks). Scale bars = 20 μ m.

nucleophosmin (37). Cultured Schwann cells deficient in *Nf1* have also demonstrated increased invasiveness (34) and motility via the enhanced activity of TC21/R-Ras2 (38). However, the motility of these cells has not been analyzed *in vivo* due to technical limitations, and the effect of *NF1* on oligodendrocyte motility has not been addressed. Here, we report the first *in vivo* analysis of OPC migration following *nf1* knockdown using time-lapse microscopy. Our studies show conclusively that the *nf1* deficiency leads to the enhanced migration of OPCs, which move intermittently as they migrate and cover greater distances owing to the decreased duration of pauses rather than to increased velocity of movement during active migration (Fig. 4). The increased migratory behavior of OPCs in *nf1* morphants might result from the cell-autonomous effects of *nf1* deficiency, such as cytoskeletal defects possibly mediated by the overexpression of GAP43 and T-cadherin (36), similar to the role of *nf1* in motility in other glial cell types. The increased numbers of OPCs might also indirectly affect their migratory properties in *nf1* morphants (39). At this time, we do not know whether the OPCs are responding to a non-cell-autonomous effect of *nf1* loss, possibly mediated by increased phospho-ERK activity in adjacent neurons, or whether the effects are mediated by cell-autonomous effects of *nf1* unrelated to phospho-ERK activation. The increased OPC numbers and motility due to *NF1* loss may contribute to the phenotypes observed in human patients, such as neurofibromatosis type 1-associated macrocephaly (18) and the increased invasiveness of *NF1*-deficient glioma cells (40).

In summary, we have shown that OPC numbers and migration are enhanced upon *nf1* knockdown and that forced expression of the GRD restores normal OPC numbers in *nf1*-deficient embryos. The experimental accessibility of the zebrafish embryo provides an excellent platform for further analysis of the mechanisms that underlie these changes. Furthermore, the eventual establishment of stable *nf1*-deficient zebrafish lines and the ability to conduct modifier genetic

and drug screens in the zebrafish embryo should contribute to the dissection of proteins and pathways that can be targeted to improve the treatment of human pathologies resulting from *NF1* loss.

MATERIALS AND METHODS

Zebrafish maintenance

All zebrafish were grown and maintained in accord with the DFCI IACUC-approved protocol. *Tg(olig2:EGFP)* transgenic animals were obtained from Dr Bruce Appel (20) and were crossed to our *p53 e7/e7* mutant fish (21) to generate the *Tg(olig2:EGFP); p53 e7/e7* line.

Cloning and plasmids

The predicted full-length cDNA for *nf1a* and *nf1b* was obtained from the Ensembl database (<http://www.ensembl.org>). EST clones CN024089 (GI: 45796859) for *nf1a* and CR930343 (GI: 56559576) for *nf1b* were identified and cloned into pBluescript to generate probes for whole-mount *in situ* hybridization assays.

MO injections

Approximately 1 nl of MO(s) in water with phenol red (0.5%), corresponding to 150 μ M *nf1a* MO and 200 μ M *nf1b* MO, was injected individually or together into embryos at the one-cell stage. The standard control MO was also used (Gene Tools). MO sequences: (1) *nf1a-e1*: 5'-GTC CAA GTA GTG TTT TCC TTA CCT G-3'; (2) *nf1a-e7*: 5'-TAG TAA ACA AGT GTC ACT CAC CGG C-3'; (3) *nf1b-e4*: 5'-CTC AGT ATT TAT CTG CAC CTG GTG G-3'; (4) MO control; 5'-CCT CTT ACC TCA GTT ACA ATT TAT A-3'.

Whole-mount *in situ* hybridization and immunofluorescence assays

Paraformaldehyde-fixed embryos were cryosectioned and immunostained using primary antibodies (rabbit anti-sox10, anti-GFP, anti-isl, zn5, anti-BrdU and anti-phospho-ERK), followed by incubation with Alexa 488- or 568-conjugated secondary antibodies. WISH assays were performed as by Thisse and Thisse (41).

Reverse transcription and PCR

Cells from the spinal cord of *Tg(olig2:EGFP)* at 3 dpf were FACS-sorted based on GFP expression. RNA from these cells were reverse-transcribed (RT) to prepare cDNA, which was used to perform PCR to test the expression of *nf1* and *nf1b*. Similarly, RT-PCR of MO-injected embryos detected aberrant splicing events, confirming the whole or partial deletion of the targeted exons, or insertions leading to aberrantly truncated proteins.

Imaging and statistical analyses

A Zeiss LSM 510 META confocal microscope and a Zeiss compound microscope Axio Imager.Z1 were used to capture confocal images and fluorescence/brightfield DIC images, respectively. For time-lapse movies, a Zeiss 200M inverted microscope equipped with a spinning-disk confocal system (Yokogawa) was used. The statistical significance of changes to OPC numbers and migration upon *nf1* knockdown was determined by *t*-test analysis (see Supplementary Material for further methodological details).

SUPPLEMENTARY MATERIAL

Supplementary Material is available at *HMG* online.

ACKNOWLEDGEMENTS

We thank Greg Molind and Lu Zhang for excellent care of our zebrafish facility. We also thank Bruce Appel (University of Colorado) for the anti-sox10 antibody, Jin Rong Peng for the *nf1b* EST CR930343 and the Pellman laboratory (DFCI) for use of their spinning-disk confocal microscope.

Conflict of Interest statement. None declared.

FUNDING

This work was supported by the Department of Defense (NF050175 to J.A.E. and A.T.L.). J.S.L. was supported by a Young Investigator Award (Children's Tumor Foundation) and A.P. by a fellowship from the Sarnoff Cardiovascular Research Foundation.

REFERENCES

- Listernick, R., Ferner, R.E., Liu, G.T. and Gutmann, D.H. (2007) Optic pathway gliomas in neurofibromatosis-1: controversies and recommendations. *Ann. Neurol.* **61**, 189–198.

- Rubin, J.B. and Gutmann, D.H. (2005) Neurofibromatosis type 1—a model for nervous system tumour formation? *Nat. Rev. Cancer* **5**, 557–564.
- Gutmann, D.H., James, C.D., Poyhonen, M., Louis, D.N., Ferner, R., Guha, A., Hariharan, S., Viskochil, D. and Perry, A. (2003) Molecular analysis of astrocytomas presenting after age 10 in individuals with NF1. *Neurology* **61**, 1397–1400.
- Network, T.C.G.A.R. (2008) Comprehensive genomic characterization defines human glioblastoma genes and core pathways. *Nature* **455**, 1061–1068.
- Ballester, R., Marchuk, D., Boguski, M., Saulino, A., Letcher, R., Wigler, M. and Collins, F. (1990) The NF1 locus encodes a protein functionally related to mammalian GAP and yeast IRA proteins. *Cell* **63**, 851–859.
- Xu, G.F., O'Connell, P., Viskochil, D., Cawthon, R., Robertson, M., Culver, M., Dunn, D., Stevens, J., Gesteland, R., White, R. *et al.* (1990) The neurofibromatosis type 1 gene encodes a protein related to GAP. *Cell* **62**, 599–608.
- Bajenaru, M.L., Hernandez, M.R., Perry, A., Zhu, Y., Parada, L.F., Garbow, J.R. and Gutmann, D.H. (2003) Optic nerve glioma in mice requires astrocyte *Nf1* gene inactivation and NF1 brain heterozygosity. *Cancer Res.* **63**, 8573–8577.
- Yang, F.C., Ingram, D.A., Chen, S., Zhu, Y., Yuan, J., Li, X., Yang, X., Knowles, S., Horn, W., Li, Y. *et al.* (2008) NF1-dependent tumors require a microenvironment containing NF1 +/– and c-kit-dependent bone marrow. *Cell* **135**, 437–448.
- Zhu, Y., Ghosh, P., Charnay, P., Burns, D.K. and Parada, L.F. (2002) Neurofibromas in NF1: Schwann cell origin and role of tumor environment. *Science* **296**, 920–922.
- Wu, J., Williams, J.P., Rizvi, T.A., Kordich, J.J., Witte, D., Meijer, D., Stemmer-Rachamimov, A.O., Cancelas, J.A. and Ratner, N. (2008) Plexiform and dermal neurofibromas and pigmentation are caused by NF1 loss in desert hedgehog-expressing cells. *Cancer Cell* **13**, 105–116.
- Zhu, Y., Harada, T., Liu, L., Lush, M.E., Guignard, F., Harada, C., Burns, D.K., Bajenaru, M.L., Gutmann, D.H. and Parada, L.F. (2005) Inactivation of NF1 in CNS causes increased glial progenitor proliferation and optic glioma formation. *Development* **132**, 5577–5588.
- Nicolay, D.J., Doucette, J.R. and Nazarali, A.J. (2007) Transcriptional control of oligodendrogenesis. *Glia* **55**, 1287–1299.
- Lu, Q.R., Sun, T., Zhu, Z., Ma, N., Garcia, M., Stiles, C.D. and Rowitch, D.H. (2002) Common developmental requirement for Olig function indicates a motor neuron/oligodendrocyte connection. *Cell* **109**, 75–86.
- Li, J., Perry, A., James, C.D. and Gutmann, D.H. (2001) Cancer-related gene expression profiles in NF1-associated pilocytic astrocytomas. *Neurology* **56**, 885–890.
- Bennett, M.R., Rizvi, T.A., Karyala, S., McKinnon, R.D. and Ratner, N. (2003) Aberrant growth and differentiation of oligodendrocyte progenitors in neurofibromatosis type 1 mutants. *J. Neurosci.* **23**, 7207–7217.
- Hegedus, B., Dasgupta, B., Shin, J.E., Emmett, R.J., Hart-Mahon, E.K., Elghazi, L., Bernal-Mizrachi, E. and Gutmann, D.H. (2007) Neurofibromatosis-1 regulates neuronal and glial cell differentiation from neuroglial progenitors in vivo by both cAMP- and Ras-dependent mechanisms. *Cell Stem Cell* **1**, 443–457.
- Ozonoff, S. (1999) Cognitive impairment in neurofibromatosis type 1. *Am. J. Med. Genet.* **89**, 45–52.
- Steen, R.G., Taylor, J.S., Langston, J.W., Glass, J.O., Brewer, V.R., Reddick, W.E., Mages, R. and Pivnick, E.K. (2001) Prospective evaluation of the brain in asymptomatic children with neurofibromatosis type 1: relationship of macrocephaly to T1 relaxation changes and structural brain abnormalities. *AJNR Am. J. Neuroradiol.* **22**, 810–817.
- Padmanabhan, A., Lee, J.S., Ismat, F.A., Lu, M.M., Lawson, N.D., Kanki, J.P., Look, A.T. and Epstein, J.A. (2009) Cardiac and vascular functions of the zebrafish orthologues of the type I neurofibromatosis gene NF1. *Proc. Natl Acad. Sci. USA* **106**, 22305–22310.
- Shin, J., Park, H.C., Topczewska, J.M., Mawdsley, D.J. and Appel, B. (2003) Neural cell fate analysis in zebrafish using olig2 BAC transgenics. *Methods Cell Sci.* **25**, 7–14.
- Berghmans, S., Murphey, R.D., Wienholds, E., Neubergh, D., Kutok, J.L., Fletcher, C.D., Morris, J.P., Liu, T.X., Schulte-Merker, S., Kanki, J.P. *et al.* (2005) tp53 mutant zebrafish develop malignant peripheral nerve sheath tumors. *Proc. Natl Acad. Sci. USA* **102**, 407–412.
- Robu, M.E., Larson, J.D., Nasevicius, A., Beiraghi, S., Brenner, C., Farber, S.A. and Ekker, S.C. (2007) p53 activation by knockdown technologies. *PLoS Genet.* **3**, e78.

23. Park, H.C., Shin, J. and Appel, B. (2004) Spatial and temporal regulation of ventral spinal cord precursor specification by Hedgehog signaling. *Development* **131**, 5959–5969.
24. Stewart, R.A., Sanda, T., Widlund, H.R., Zhu, S., Swanson, K.D., Hurley, A.D., Bentires-Alj, M., Fisher, D.E., Kontaridis, M.I., Look, A.T. *et al.* (2010) Phosphatase-dependent and -independent functions of Shp2 in neural crest cells underlie LEOPARD syndrome pathogenesis. *Dev. Cell* **18**, 750–762.
25. Chen, J., Ng, S.M., Chang, C., Zhang, Z., Bourdon, J.C., Lane, D.P. and Peng, J. (2009) p53 isoform delta113p53 is a p53 target gene that antagonizes p53 apoptotic activity via BclxL activation in zebrafish. *Genes Dev.* **23**, 278–290.
26. Rowitch, D.H. (2004) Glial specification in the vertebrate neural tube. *Nat. Rev. Neurosci.* **5**, 409–419.
27. Fashena, D. and Westerfield, M. (1999) Secondary motoneuron axons localize DM-GRASP on their fasciculated segments. *J. Comp. Neurol.* **406**, 415–424.
28. Pineda, R.H., Svoboda, K.R., Wright, M.A., Taylor, A.D., Novak, A.E., Gamse, J.T., Eisen, J.S. and Ribera, A.B. (2006) Knockdown of Nav1.6a Na⁺ channels affects zebrafish motoneuron development. *Development* **133**, 3827–3836.
29. Park, H.C., Shin, J., Roberts, R.K. and Appel, B. (2007) An olig2 reporter gene marks oligodendrocyte precursors in the postembryonic spinal cord of zebrafish. *Dev. Dyn.* **236**, 3402–3407.
30. Ismat, F.A., Xu, J., Lu, M.M. and Epstein, J.A. (2006) The neurofibromin GAP-related domain rescues endothelial but not neural crest development in Nf1 mice. *J. Clin. Invest.* **116**, 2378–2384.
31. Shaw, R.J. and Cantley, L.C. (2006) Ras, PI(3)K and mTOR signalling controls tumour cell growth. *Nature* **441**, 424–430.
32. Postlethwait, J.H., Woods, I.G., Ngo-Hazlett, P., Yan, Y.L., Kelly, P.D., Chu, F., Huang, H., Hill-Force, A. and Talbot, W.S. (2000) Zebrafish comparative genomics and the origins of vertebrate chromosomes. *Genome Res.* **10**, 1890–1902.
33. Gutmann, D.H., Loehr, A., Zhang, Y., Kim, J., Henkemeyer, M. and Cashen, A. (1999) Haploinsufficiency for the neurofibromatosis 1 (NF1) tumor suppressor results in increased astrocyte proliferation. *Oncogene* **18**, 4450–4459.
34. Kim, H.A., Ling, B. and Ratner, N. (1997) Nf1-deficient mouse Schwann cells are angiogenic and invasive and can be induced to hyperproliferate: reversion of some phenotypes by an inhibitor of farnesyl protein transferase. *Mol. Cell. Biol.* **17**, 862–872.
35. Zheng, H., Chang, L., Patel, N., Yang, J., Lowe, L., Burns, D.K. and Zhu, Y. (2008) Induction of abnormal proliferation by nonmyelinating schwann cells triggers neurofibroma formation. *Cancer Cell* **13**, 117–128.
36. Gutmann, D.H., Wu, Y.L., Hedrick, N.M., Zhu, Y., Guha, A. and Parada, L.F. (2001) Heterozygosity for the neurofibromatosis 1 (NF1) tumor suppressor results in abnormalities in cell attachment, spreading and motility in astrocytes. *Hum. Mol. Genet.* **10**, 3009–3016.
37. Sandsmark, D.K., Zhang, H., Hegedus, B., Pelletier, C.L., Weber, J.D. and Gutmann, D.H. (2007) Nucleophosmin mediates mammalian target of rapamycin-dependent actin cytoskeleton dynamics and proliferation in neurofibromin-deficient astrocytes. *Cancer Res.* **67**, 4790–4799.
38. Huang, Y., Rangwala, F., Fulkerson, P.C., Ling, B., Reed, E., Cox, A.D., Kamholz, J. and Ratner, N. (2004) Role of TC21/R-Ras2 in enhanced migration of neurofibromin-deficient Schwann cells. *Oncogene* **23**, 368–378.
39. Kirby, B.B., Takada, N., Latimer, A.J., Shin, J., Carney, T.J., Kelsh, R.N. and Appel, B. (2006) In vivo time-lapse imaging shows dynamic oligodendrocyte progenitor behavior during zebrafish development. *Nat. Neurosci.* **9**, 1506–1511.
40. Farin, A., Suzuki, S.O., Weiker, M., Goldman, J.E., Bruce, J.N. and Canoll, P. (2006) Transplanted glioma cells migrate and proliferate on host brain vasculature: a dynamic analysis. *Glia* **53**, 799–808.
41. Thisse, C. and Thisse, B. (2008) High-resolution in situ hybridization to whole-mount zebrafish embryos. *Nat. Protoc.* **3**, 59–69.

Zebrafish neurofibromatosis type 1 genes have redundant functions in tumorigenesis and embryonic development

Jimann Shin^{1,*‡}, Arun Padmanabhan^{2,‡}, Eric D. de Groh^{2,‡}, Jeong-Soo Lee^{1,§}, Sam Haidar³, Suzanne Dahlberg¹, Feng Guo¹, Shuning He¹, Marc A. Wolman², Michael Granato², Nathan D. Lawson⁴, Scot A. Wolfe⁴, Seok-Hyung Kim⁵, Lilianna Solnica-Krezel⁶, John P. Kanki¹, Keith L. Ligon³, Jonathan A. Epstein^{2,¶} and A. Thomas Look^{1,¶}

SUMMARY

Neurofibromatosis type 1 (NF1) is a common, dominantly inherited genetic disorder that results from mutations in the *neurofibromin 1* (*NF1*) gene. Affected individuals demonstrate abnormalities in neural-crest-derived tissues that include hyperpigmented skin lesions and benign peripheral nerve sheath tumors. NF1 patients also have a predisposition to malignancies including juvenile myelomonocytic leukemia (JMML), optic glioma, glioblastoma, schwannoma and malignant peripheral nerve sheath tumors (MPNSTs). In an effort to better define the molecular and cellular determinants of NF1 disease pathogenesis in vivo, we employed targeted mutagenesis strategies to generate zebrafish harboring stable germline mutations in *nf1a* and *nf1b*, orthologues of *NF1*. Animals homozygous for loss-of-function alleles of *nf1a* or *nf1b* alone are phenotypically normal and viable. Homozygous loss of both alleles in combination generates larval phenotypes that resemble aspects of the human disease and results in larval lethality between 7 and 10 days post fertilization. *nf1*-null larvae demonstrate significant central and peripheral nervous system defects. These include aberrant proliferation and differentiation of oligodendrocyte progenitor cells (OPCs), dysmorphic myelin sheaths and hyperplasia of Schwann cells. Loss of *nf1* contributes to tumorigenesis as demonstrated by an accelerated onset and increased penetrance of high-grade gliomas and MPNSTs in adult *nf1a*^{+/-}; *nf1b*^{-/-}; *p53*^{e7/e7} animals. *nf1*-null larvae also demonstrate significant motor and learning defects. Importantly, we identify and quantitatively analyze a novel melanophore phenotype in *nf1*-null larvae, providing the first animal model of the pathognomonic pigmentation lesions of NF1. Together, these findings support a role for *nf1a* and *nf1b* as potent tumor suppressor genes that also function in the development of both central and peripheral glial cells as well as melanophores in zebrafish.

INTRODUCTION

Type 1 neurofibromatosis (NF1) is an autosomal dominant inherited genetic disorder characterized by pigmented birthmarks known as café-au-lait spots, cutaneous and plexiform

neurofibromas arising in the glial cells of the peripheral nervous system (PNS), optic pathway gliomas, cardiovascular abnormalities and learning defects (Williams et al., 2009). The disease results from mutations in the *NF1* gene, encoding the large protein neurofibromin, which contains a GTPase-activating protein-related domain (GRD) capable of inactivating the *RAS* proto-oncogene (Cawthon et al., 1990; Viskochil et al., 1990; Wallace et al., 1990). Thus, *NF1* loss results in aberrant activation of Ras signaling, which may predispose NF1 patients to a variety of cancers (Cichowski and Jacks, 2001). Heterozygous *Nf1* mutant mice develop pheochromocytoma and myeloid leukemia, whereas the conditional loss of *Nf1* in a *p53*-deficient background results in highly penetrant malignant astrocytoma formation (Jacks et al., 1994; Zhu et al., 2005a; Powers et al., 2007). Furthermore, two recent reports have identified *NF1* mutations in approximately 15-23% of human glioblastoma patients (Parsons et al., 2008; The Cancer Genome Atlas Research Network, 2008). Although these studies demonstrate a strong link between *NF1* function and high-grade glioma, the crucial signaling pathways governing the development of tumorigenesis remain to be elucidated. An animal model facilitating the rapid interrogation of epistatic and functional relationships within signaling pathways would serve as a valuable tool for probing the pathology underlying NF1-induced cell transformation.

We recently developed a zebrafish model of *NF1* deficiency using antisense morpholino oligonucleotides to produce transient gene knockdown (Padmanabhan et al., 2009; Lee et al., 2010). Two

¹Department of Pediatric Oncology, Dana-Farber Cancer Institute, and Children's Hospital Boston, Harvard Medical School, Boston, MA 02115, USA

²Department of Cell and Developmental Biology, Penn Cardiovascular Institute, and the Institute for Regenerative Medicine, Perelman School of Medicine at the University of Pennsylvania, Philadelphia, PA 19104, USA

³Department of Medical Oncology, Center for Molecular Oncologic Pathology, Dana-Farber Cancer Institute, Harvard Medical School, Boston, MA 02215, USA

⁴Program in Gene Function and Expression, University of Massachusetts Medical School, Worcester, MA 06105, USA

⁵Department of Neurology, Vanderbilt University School of Medicine, Nashville, TN 37232, USA

⁶Department of Developmental Biology, Washington University School of Medicine in St Louis, St Louis, MO 63110, USA

*Present address: Department of Developmental Biology, Washington University School of Medicine in St Louis, St Louis, MO 63110, USA

‡These authors contributed equally to this work

§Present address: Aging Research Center, Korea Research Institute of Bioscience and Biotechnology, Daejeon 305-806, Korea

¶Authors for correspondence (epsteinj@mail.med.upenn.edu; thomas_look@dfci.harvard.edu)

Received 2 March 2012; Accepted 14 May 2012

© 2012. Published by The Company of Biologists Ltd
This is an Open Access article distributed under the terms of the Creative Commons Attribution Non-Commercial Share Alike License (<http://creativecommons.org/licenses/by-nc-sa/3.0/>), which permits unrestricted non-commercial use, distribution and reproduction in any medium provided that the original work is properly cited and all further distributions of the work or adaptation are subject to the same Creative Commons License terms.

zebrafish orthologues were identified that are highly homologous to human *NF1* at the amino acid level, sharing approximately 84% identity, including 91–93% identity within the GRD. Both genes maintain syntenic relationships with human *NF1* on chromosome 17q11.2 and are probably the result of the well-described genomic duplication event that occurred early in the evolution of teleosts (Amores et al., 1998). In our previous work with *nf1* morphants, we observed defects in both cardiovascular and nervous system development. However, due to the transient nature of morpholino gene knockdown, the analysis of *nf1*-deficient phenotypes beyond the first 3 days of life was not possible.

We report here the generation of stable mutant *nf1* zebrafish lines, using both zinc finger nuclease (ZFN) and targeting induced local lesions in genomes (TILLING) strategies, and the detailed phenotypic analysis of this new animal model of human NF1. We have successfully generated several independent null alleles of *nf1a* and *nf1b*. Mutant larvae carrying at least one wild-type *nf1a* or *nf1b* allele are viable, fertile and show no obvious phenotypes during early development. By contrast, *nf1a*^{-/-}; *nf1b*^{-/-} larvae exhibit overt pigmentation defects as early as 6 days post fertilization (dpf) and do not survive beyond 10 dpf. Beginning at 4 dpf, *nf1a*^{-/-}; *nf1b*^{-/-} larvae exhibit hyperplasia of oligodendrocyte progenitor cells (OPCs) and Schwann cells, as well as melanophore hypoplasia. Defects resulting from the loss of *nf1* in pigment cell and glial cell lineages mirror those often observed in the tissues of NF1 patients. In a *p53* mutant background (*p53*^{e7/e7}), *nf1a*^{-/-}; *nf1b*^{-/-} fish develop high-grade gliomas and malignant peripheral nerve sheath tumors (MPNSTs), demonstrating a tumor-suppressor function for the zebrafish *nf1* orthologues. **Therefore**, we have developed and characterized a heritable zebrafish model of NF1 that exhibits clinical hallmarks of the disorder, including nervous system defects and increased susceptibility to tumorigenesis. Furthermore, *nf1* mutant zebrafish represent the first vertebrate model of the pathognomonic pigmentation lesions associated with NF1.

RESULTS

Generation of zebrafish *nf1a* and *nf1b* mutants

We previously identified two zebrafish orthologues of human *NF1*, *nf1a* and *nf1b*, and described the phenotypes that result from their loss of function during early development induced by antisense morpholino oligonucleotides (Padmanabhan et al., 2009; Lee et al., 2010). **Although** this technology readily permits transient knockdown of gene expression, its efficacy is limited to only the first few days of life. In an effort to gain a better understanding of the roles of *nf1a* and *nf1b* during development, as well as in cancer predisposition, we employed multiple approaches to develop stable lines of zebrafish harboring germline mutations in each of these genes. Using a modular approach (Zhu et al., 2011), zinc finger nucleases (ZFNs) were engineered with binding specificities directed to exon 26 of *nf1a* and exon 17 of *nf1b* (Fig. 1A,B). Paired ZFN mRNAs were injected into zebrafish embryos and independent target-specific mutant alleles for *nf1a* (*nf1a*^{Δ5} and *nf1a*^{Δ8}) and *nf1b* (*nf1b*⁺¹⁰ and *nf1b*^{Δ55}) were identified in the F1 generation (Fig. 1C; **supplementary material** Fig. S1A–D). Each of these mutations included a deletion and/or insertion within a coding exon that resulted in a frameshift, introducing premature stop codons that would be expected to truncate the neurofibromin protein upstream of the GRD (Fig. 1D,E). In a separate effort, we screened a library

of *N-ethyl-N-nitrosourea* (ENU)-mutagenized zebrafish by targeting induced local lesions in genomes (TILLING) (Wienholds et al., 2002) and identified a single founder harboring a nonsense mutation in exon 29 of *nf1a* (*nf1a*^{L1247X}) (Fig. 1C; **supplementary material** Fig. S1E–G). To confirm that the targeted alleles disrupted production of full-length protein, we performed western blots using an antibody that should recognize both *nf1a* and *nf1b* with extracts prepared from 3 dpf wild-type, *nf1a*^{Δ5/Δ5}; *nf1b*^{+/+}, *nf1a*^{+/+}; *nf1b*^{+10/+10} and *nf1a*^{Δ5/Δ5}; *nf1b*^{+10/+10} larvae (Fig. 1F). We observed a complete loss of Nf1 signal in the double-homozygous null extracts. We detected only low levels of protein expression in *nf1a*^{Δ5/Δ5}; *nf1b*^{+/+} mutant extracts as compared with wild-type or *nf1a*^{+/+}; *nf1b*^{+10/+10} mutant extracts, which **might** reflect differences in expression levels of the two orthologues at 3 dpf. However, we cannot rule out the possibility that the neurofibromin antibody we used recognizes the two proteins with different affinities. We generated separate zebrafish lines with distinct null alleles of both *nf1a* and *nf1b* to provide evidence that the observed phenotypes were in fact due to *nf1* loss and did not involve any spurious passenger mutations specific to the isolation of any individual *nf1* mutant line (**supplementary material** Fig. S2). Because our data indicate that these various null alleles are equivalent, we refer to them without individual allelic designations henceforth (*nf1a*^{-/-} and *nf1b*^{-/-}).

Mutants carrying at least one wild-type allele of either *nf1a* or *nf1b* are viable and fertile. However, when crossing parental genotypes that would be expected to yield *nf1a*^{-/-}; *nf1b*^{-/-} progeny, none were observed in the adult population. To investigate this further, we performed quantitative survival studies. At 7 dpf, *nf1a*^{-/-}; *nf1b*^{-/-} larvae began to die, with none surviving beyond 10 dpf, **although** 100% of wild-type larvae survived to 10 dpf (Fig. 1G). Furthermore, 100% survival at 10 dpf was also observed in *nf1a*^{-/-}; *nf1b*^{+10/+10} (*n*=26), *nf1a*^{+10/+10}; *nf1b*^{-/-} (*n*=22), *nf1a*^{-/-}; *nf1b*^{+10/+10} (*n*=28), and *nf1a*^{+10/+10}; *nf1b*^{-/-} (*n*=24) larvae. The swim bladders of *nf1a*^{-/-}; *nf1b*^{-/-} larvae were frequently observed to be underinflated. However, *nf1a*^{-/-}; *nf1b*^{-/-} larvae maintained the ability to both consume and transit live paramecia, suggesting that premature death was not the result of starvation (**supplementary material** Fig. S3). Additionally, an incompletely penetrant valvular insufficiency phenotype was appreciated in *nf1a*^{-/-}; *nf1b*^{-/-} larvae, as well as in those harboring only a single wild-type *nf1* allele (*nf1a*^{+/-}; *nf1b*^{-/-} and *nf1a*^{-/-}; *nf1b*^{+/-}) (**supplementary material** Movies 1–3).

OPC and Schwann cell hyperplasia in *nf1a*^{-/-}; *nf1b*^{-/-} larvae

We previously described OPC hyperplasia after *nf1a* and *nf1b* morpholino knockdown in the context of a homozygous *p53* mutant background (Lee et al., 2010). To examine *nf1a* and *nf1b* function in OPCs and other tissues beyond the first few days of life, we crossed several cell-type-specific zebrafish reporter lines into *nf1a*/*nf1b* mutant backgrounds. At 2 dpf, *olig2* expression appeared normal in Tg(*olig2:GFP*); *nf1a*^{-/-}; *nf1b*^{-/-} embryos, as assessed by both whole-mount in situ hybridization analysis of endogenous *olig2* mRNA expression and GFP expression (**supplementary material** Fig. S4A–D). We also evaluated *nf1* loss in Tg(*sox10:GFP*) embryos. This transgene drives GFP expression in specified ventral spinal cord OPCs, but not the neighboring motoneurons that arise from a common progenitor cell, as well as in Schwann cells of the posterior lateral line nerve (PLLn). At 2 dpf, similar numbers of *sox10:GFP*-positive OPCs **were** detected

in the dorsal and ventral spinal cord of wild-type and *nf1a*^{-/-}; *nf1b*^{-/-} embryos (supplementary material Fig. S4E,F). Examination of *nf1*-null PNS Schwann cells at 2 dpf showed no effect on the number of *sox10*:GFP-expressing cells associated with the PLLn,

which innervate skin mechanosensory neuromast cells (supplementary material Fig. S4G,H).

However, *nf1a*^{-/-}; *nf1b*^{-/-} larvae exhibited increased numbers of OPCs at 4 dpf compared with controls, as evidenced by an excess

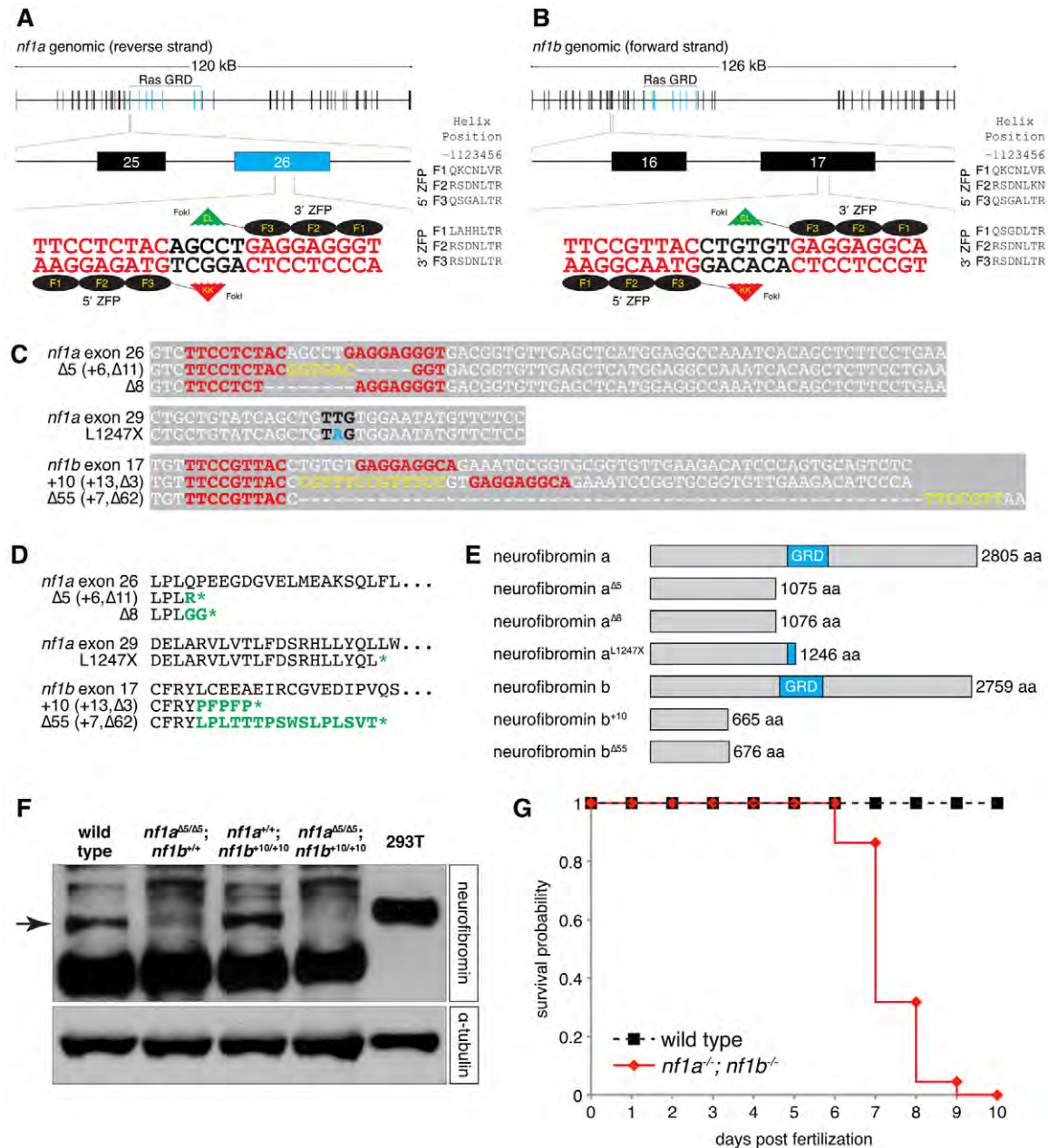


Fig. 1. ZFN and TILLING strategies generate null alleles of zebrafish *nf1a* and *nf1b*. (A,B) Scheme of site targeted for ZFN-mediated cleavage in exon 26 of *nf1a* and exon 17 of *nf1b*. (C) Alignments of nucleotide sequences from wild-type and mutant *nf1a* and *nf1b* alleles. ZFN target sites appear in red. Yellow bases represent insertions that arise from repair of ZFN-induced mutagenic lesions. Black bases correspond to the mutated codon in the *nf1a*^{L1247X} allele generated by a TILLING strategy, with the mutated base appearing in blue. (D) ZFN-induced mutagenic lesions in *nf1a* and *nf1b* produce frameshift mutations that lead to truncated protein products following short regions of altered translation, which are indicated in green. The nonsense mutation in the *nf1a*^{L1247X} allele generated by a TILLING strategy also appears in green. (E) The truncated protein products predicted by the ZFN- and TILLING-induced mutant *nf1a/nf1b* alleles all harbor complete or partial loss of the neurofibromin GAP-related domain (GRD). (F) Western blot analysis for neurofibromin in protein lysates from 3-dpf wild-type, *nf1a* ^{$\Delta 5/\Delta 5$} ; *nf1b*^{+/+}, *nf1a*^{+/+}; *nf1b* ^{$\Delta 5/\Delta 5$} and *nf1a* ^{$\Delta 5/\Delta 5$} ; *nf1b*^{+10/+10} zebrafish larvae (100 μ g each) or 293T cells (25 μ g) demonstrates absence of Nf1 protein in *nf1a*^{-/-}; *nf1b*^{-/-} larvae. Equal loading was confirmed by stripping the membrane and reprobing for α -tubulin. (G) Kaplan-Meier survival analysis demonstrates that 100% of *nf1a*^{-/-}; *nf1b*^{-/-} larvae ($n=22$) die by 10 dpf as compared with 0% of wild-type larvae ($n=27$).

of dorsally migrated *olig2*:GFP-positive OPCs (Fig. 2A,B) along with increased numbers of both dorsally and ventrally positioned *sox10*:GFP-positive OPCs (Fig. 2C,D), consistent with our analyses of *nf1* morphants at 3 dpf (Lee et al., 2010). In addition, we observed an increase in *sox10*:GFP-positive Schwann cells associated with the PLLn (Fig. 2E,F). This increase in PLLn Schwann cell number was not associated with altered proliferation of these cells (supplementary material Fig. S5A-F). To assess the roles of *nf1a* and *nf1b* in the developing radial glial cells of the spinal cord, *nf1a*/*nf1b* mutants were crossed into the *Tg(gfap:GFP)* line, which expresses GFP from the glial fibrillary acidic protein (*gfap*) promoter. At 4 dpf, *nf1a*^{-/-}; *nf1b*^{-/-} larvae harboring a *gfap:GFP* transgene demonstrated no readily discernible differences in *gfap*:GFP-positive spinal cord radial glial cells as compared with wild-type larvae (supplementary material Fig. S4I,J). However, *gfap* expression in the extensive processes of radial glial cells precludes precise quantification and might obscure subtle differences.

To determine whether neuronal numbers increased in concert with OPCs in *nf1a*/*nf1b* mutant larvae, we used anti-HuC/D and anti-SOX10 antibodies (see Materials and Methods) to discriminate between *olig2*:GFP-positive neurons and OPCs, respectively. No difference between the number of *olig2*:GFP-positive and HuC/D-positive neurons was appreciable in 4 dpf spinal cord sections from wild-type and *nf1a*^{-/-}; *nf1b*^{-/-} larvae (Fig. 2G,H, green and magenta; Fig. 2K). However, the numbers of *olig2*:GFP-positive and Sox10-positive OPCs (Fig. 2G,H, arrowheads; Fig. 2L) and PLLn Schwann cells (Fig. 2I,J,M) were significantly increased at 4 dpf in *nf1a*^{-/-}; *nf1b*^{-/-} larvae relative to wild-type controls. OPC cell numbers continued to increase in *nf1a*^{-/-}; *nf1b*^{-/-} larvae at 8 dpf, as reflected by increased numbers of dorsally localizing *olig2*:GFP-positive OPCs as well as both dorsally and ventrally localizing *sox10*:GFP-positive OPCs (supplementary material Fig. S4M-P). Increased numbers of *sox10*:GFP-expressing PLLn Schwann cells were also evident in *nf1a*^{-/-}; *nf1b*^{-/-} larvae at 8 dpf (supplementary material Fig. S4Q,R). Thus, loss of *nf1a* and *nf1b* does not affect the specification of OPCs at 2 dpf, but instead promotes the progressive expansion of OPCs without a concomitant increase in neuronal cell numbers. Furthermore, *nf1a*/*nf1b* loss triggers Schwann cell hyperplasia beginning at 4 dpf.

Immunohistochemical analysis using the Zrf1 antibody, which labels Gfap in zebrafish, showed coexpression with GFP expressed from the *gfap:GFP* transgene and revealed a similar pattern of expression in wild-type and *nf1a*^{-/-}; *nf1b*^{-/-} larvae at 4 dpf (supplementary material Fig. S6A,B). Zebrafish radial glial cells also express brain lipid-binding protein (Blbp), and immunohistochemical analysis of wild-type and *nf1a*^{-/-}; *nf1b*^{-/-} spinal cords with an anti-BLBP antibody at 4 dpf revealed an obvious decrease in Blbp expression in the *gfap*:GFP-positive radial glia of *nf1a*^{-/-}; *nf1b*^{-/-} larvae (supplementary material Fig. S6C,D). These results suggest that although *gfap*:GFP-positive radial glial cells in *nf1a*^{-/-}; *nf1b*^{-/-} larvae appear normal in number, they fail to express appropriate levels of Blbp indicating a defect in gliogenesis. An additional abnormality of gliogenesis was observed at 8 dpf as a disruption in the regular segmental pattern of glial process outgrowth in *Tg(gfap:GFP)*; *nf1a*^{-/-}; *nf1b*^{-/-} larvae (supplementary material Fig. S4K,L).

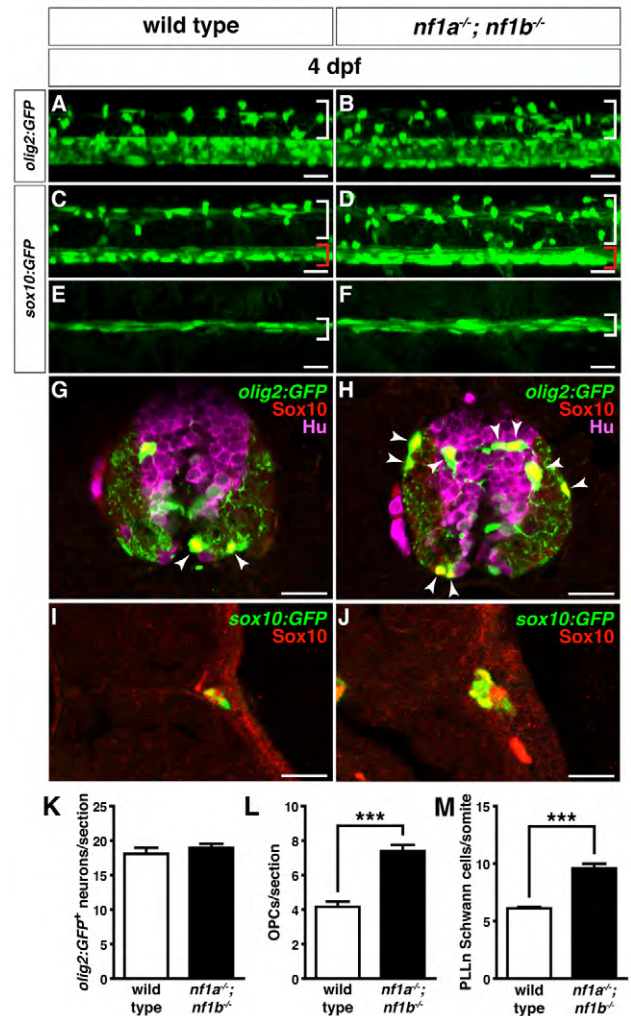


Fig. 2. Loss of *nf1a* and *nf1b* causes hyperplasia of OPCs and Schwann cells.

(A,B) Confocal images of spinal cords in *nf1a*^{-/-}; *nf1b*^{-/-}; *Tg(olig2:GFP)* larvae (B) demonstrate increased numbers of dorsally migrating (white brackets) *olig2*:GFP-positive OPCs as compared with wild-type; *Tg(olig2:GFP)* larvae (A) at 4 dpf. (C,D) Confocal images of spinal cord in *nf1a*^{-/-}; *nf1b*^{-/-}; *Tg(sox10:GFP)* larvae (D) demonstrate increased numbers of both dorsally (white brackets) and ventrally (red brackets) positioned *sox10*:GFP-positive OPCs as compared with wild-type; *Tg(sox10:GFP)* larvae (C) at 4 dpf. (E,F) *nf1a*^{-/-}; *nf1b*^{-/-}; *Tg(sox10:GFP)* larvae (F) show an increased number of *sox10*:GFP-positive Schwann cells associated with the peripheral lateral line nerve (PLLn; white brackets) as compared with wild-type; *Tg(sox10:GFP)* larvae (E) at 4 dpf. (G,H) Neuronal numbers (*olig2*:GFP- [green], HuC/D- [magenta] positive) do not increase in concert with OPCs (*olig2*:GFP- [green], Sox10- [red] positive; arrowheads) in transverse sections through the spinal cord of *nf1a*^{-/-}; *nf1b*^{-/-}; *Tg(olig2:GFP)* larvae (H) as compared with wild-type; *Tg(olig2:GFP)* larvae (G) at 4 dpf. (I,J) Increased numbers of PLLn Schwann cells (*sox10*:GFP- [green], Sox10- [red] positive) are appreciated in transverse sections of *nf1a*^{-/-}; *nf1b*^{-/-}; *Tg(sox10:GFP)* larvae (J) as compared with wild-type; *Tg(sox10:GFP)* larvae (I) at 4 dpf. (K,L) Quantification of neurons (*olig2*:GFP-, HuC/D-positive cells) (K) and OPCs (*olig2*:GFP-, Sox10-positive cells) (L) from transverse sections through the spinal cord of wild-type; *Tg(olig2:GFP)* and *nf1a*^{-/-}; *nf1b*^{-/-}; *Tg(olig2:GFP)* larvae at 4 dpf. Values indicate mean + s.e.m. per section ($n=30$ from five each of wild-type and *nf1a*^{-/-}; *nf1b*^{-/-} larvae). (M) Quantification of *sox10*:GFP-positive Schwann cells in the PLLn of wild-type; *Tg(sox10:GFP)* and *nf1a*^{-/-}; *nf1b*^{-/-}; *Tg(sox10:GFP)* larvae at 4 dpf. Values indicate mean + s.e.m. per hemisegment ($n=5$ each for wild-type and *nf1a*^{-/-}; *nf1b*^{-/-} larvae). *** $P<0.001$. Scale bars: 20 μ m.

OPC hyperplasia in *nf1a*^{-/-}; *nf1b*^{-/-} larvae results from increased proliferation

In *nf1a*^{-/-}; *nf1b*^{-/-} larvae, OPC numbers were increased relative to control animals at 4 dpf, but not at 2 dpf, suggesting that *nf1*-null OPCs might proliferate faster during this time period. We assessed OPC proliferation by labeling larvae with BrdU for 12 hours starting at 3.5, 4.5 and 5.5 dpf followed by immunohistochemical analysis of transverse sections through the spinal cord. By 4 dpf and continuing through 6 dpf, the number of *olig2*:GFP-positive and Sox10-positive OPCs in *nf1*-null larvae was significantly increased in comparison with wild-type controls (Fig. 3A–H, arrows; Fig. 3I). Mutant larvae further exhibited significantly increased numbers of *olig2*:GFP-, Sox10- and BrdU-positive OPCs at 4 and 5 dpf as compared with controls, indicating that neurofibromin normally suppresses the proliferation of OPCs during this period of development (Fig. 3A–H, arrowheads; Fig. 3J). There was little detectable BrdU incorporation at 6 dpf in either mutant or control populations

Myelination is aberrant in *nf1a*^{-/-}; *nf1b*^{-/-} larvae

We evaluated the ability of *nf1a*^{-/-}; *nf1b*^{-/-} OPCs to differentiate appropriately by examining the gene expression levels of proteolipid protein 1a (*plp1a*) and myelin basic protein (*mbp*), markers of differentiated oligodendrocytes, in wild-type and mutant larvae at 5 dpf. In *nf1*-null larvae, fewer *plp1a*-positive cells were detected in the midbrain and hindbrain regions (Fig. 4A,B) as well as along the dorsal and ventral spinal cords (Fig. 4C,D) as compared with

controls. Central nervous system (CNS) expression of *mbp*, on the other hand, was indistinguishable between wild-type and *nf1a*^{-/-}; *nf1b*^{-/-} larvae at 5 dpf (supplementary material Fig. S7). However, *mbp* expression was elevated in Schwann cells of the PLLn in *nf1a*^{-/-}; *nf1b*^{-/-} larvae as compared with controls (Fig. 4E,F, arrowheads). These data are consistent with perturbed oligodendrocyte differentiation in the CNS as well as in PNS Schwann cells associated with the PLLn of *nf1a*^{-/-}; *nf1b*^{-/-} larvae.

We went on to examine the ultrastructure of myelinated CNS axons in control and *nf1*-null larvae by transmission electron microscopy (TEM). At 8 dpf, oligodendritic myelin sheaths were tightly wrapped around CNS axons in the ventral spinal cord of wild-type larvae (Fig. 4G,I). By contrast, *nf1a*^{-/-}; *nf1b*^{-/-} axons were loosely encircled by multiple lamellae rather than by compact myelin sheaths, indicating that neurofibromin is required for the normal formation of the concentric layers of oligodendrocyte membranes that enwrap neuronal axons of the CNS to promote neural conduction (Fig. 4H,J).

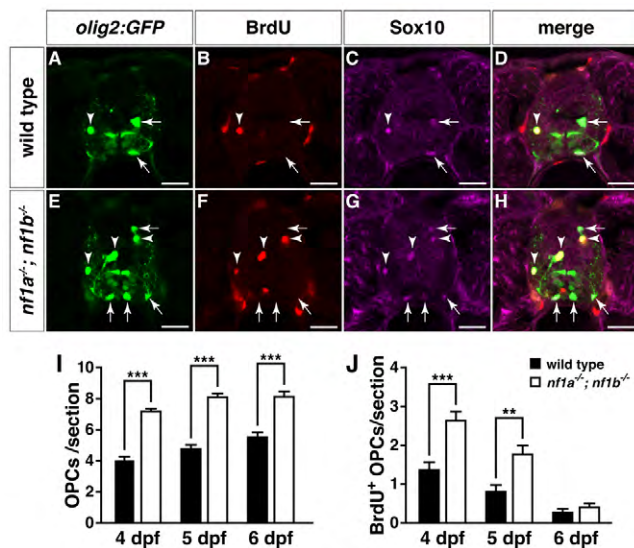


Fig. 3. Increased proliferation drives OPC hyperplasia in *nf1a*^{-/-}; *nf1b*^{-/-} larvae. (A–H) Transverse spinal cord sections of wild-type; Tg(*olig2*:GFP) (A–D) and *nf1a*^{-/-}; *nf1b*^{-/-}; Tg(*olig2*:GFP) larvae (E–H) labeled with anti-BrdU antibody (B,F, red) or anti-SOX10 antibody (C,G, magenta) at 4 dpf. Arrows indicate BrdU-negative, Tg(*olig2*:GFP)-, Sox10-positive OPCs. Arrowheads indicate BrdU-positive, Tg(*olig2*:GFP)-, Sox10-positive OPCs. (I,J) Quantification of total (I) and BrdU-positive OPCs (J) from transverse spinal cord sections of wild-type; Tg(*olig2*:GFP) and *nf1a*^{-/-}; *nf1b*^{-/-}; Tg(*olig2*:GFP) larvae at 4, 5 and 6 dpf. Values indicate mean + s.e.m. per section ($n=30$ from five each of wild-type and *nf1a*^{-/-}; *nf1b*^{-/-} larvae). ** $P<0.01$; *** $P<0.001$. Scale bars: 20 μ m.

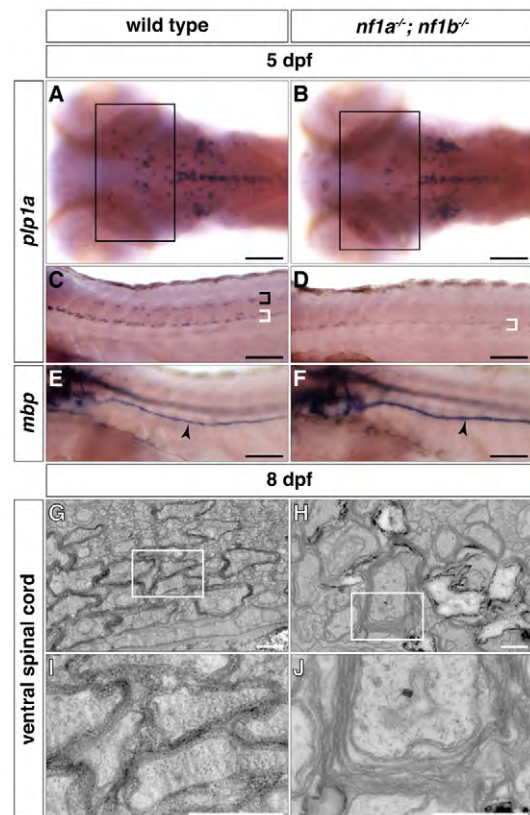


Fig. 4. *nf1a*^{-/-}; *nf1b*^{-/-} larvae exhibit myelination defects. (A–D) *plp1a* expression is decreased in glial cells of the midbrain and hindbrain regions (A,B, boxes) as well as the dorsal (black bracket) and ventral (white brackets) spinal cord of *nf1a*^{-/-}; *nf1b*^{-/-} larvae (B,D) as compared to wild-type larvae (A,C) by whole-mount in situ hybridization at 5 dpf. (E,F) *mbp* expression is elevated in Schwann cells of the PLLn (arrowheads) of *nf1a*^{-/-}; *nf1b*^{-/-} larvae (F) as compared to wild-type larvae (E) by whole-mount in situ hybridization at 5 dpf. (G–J) Transverse sections through the ventral spinal cord *nf1a*^{-/-}; *nf1b*^{-/-} larvae (H, boxed region magnified in J) demonstrate defects in formation of compact myelin sheaths as compared with wild-type larvae (G, boxed region magnified in I) at 8 dpf. Scale bars: 100 μ m (A–F) and 0.5 μ m (G–J).

Loss of *nf1a* and *nf1b* causes upregulation of Ras signaling in the spinal cord

Given the well-described role of neurofibromin as a negative regulator of Ras, we hypothesized that *nf1* loss in our mutants would lead to activation of downstream effector pathways. Western blot analysis of whole larvae extracts revealed an upregulation of phosphorylated ERK1 and ERK2 (pERK1/2) in *nf1a*^{-/-}; *nf1b*^{-/-} larvae at 3 dpf, whereas levels in *nf1a*^{-/-}; *nf1b*^{+/-} and *nf1a*^{+/-}; *nf1b*^{-/-} larvae remained unchanged (Fig. 5A). These data are consistent with the absence of functioning neurofibromin protein in *nf1a*^{-/-}; *nf1b*^{-/-} larvae and support functional redundancy between *nf1a* and *nf1b*. We next assessed the activation of Ras effector pathways in the spinal cords of wild-type, *nf1a*^{+/-}; *nf1b*^{-/-}, *nf1a*^{-/-}; *nf1b*^{+/-}, and *nf1a*^{-/-}; *nf1b*^{-/-} animals by immunohistochemical analysis of transverse larval sections. Antibodies directed against HuC/D, pERK1/2, and phosphorylated S6 (pS6) were used to label neurons and assess activation of ERK and mTOR signaling pathways, respectively (Fig. 5B–Q). Although pERK1/2 staining was only minimally observed in a few neurons and portions of spinal cord white matter at 4 dpf in wild-type larvae (Fig. 5B,N), a striking upregulation of pERK1/2 was detected in *nf1a*^{-/-}; *nf1b*^{-/-} larvae (Fig. 5E,Q). Increased ERK signaling was also noted at 3 dpf in spinal cord neurons and white matter of *nf1a*^{-/-}; *nf1b*^{-/-} larvae, but was absent at 2 dpf (supplementary material Fig. S8). Although pS6 signaling was evident in multiple spinal cord neurons, we observed no differences in these cells between wild-type and *nf1* mutant animals at 2, 3 or 4 dpf (supplementary material Fig. S8Ae–Ah, Be–Bh; Fig. 6F–I). These data suggest that activation of mTOR signaling (as assessed by S6 phosphorylation) is not altered, at least in the spinal cord following *nf1* loss.

nf1 and *p53* cooperate to accelerate zebrafish tumorigenesis in vivo

Mammalian *NF1* has been shown to be a potent tumor suppressor; however, we did not identify any tumors over 18 months of observation in adult zebrafish homozygous for either mutant *nf1* allele alone (*nf1a*^{-/-}; *nf1b*^{+/-} or *nf1a*^{+/-}; *nf1b*^{-/-}) or in combination with heterozygous loss of the remaining allele (*nf1a*^{+/-}; *nf1b*^{-/-} or *nf1a*^{-/-}; *nf1b*^{+/-}). Loss of *p53* has been shown to cooperate with *NF1* (Cichowski et al., 1999; Vogel et al., 1999) as well as other mutations that activate Ras signaling (Eliyahu et al., 1984; Parada et al., 1984; Kemp et al., 1994; Tanaka et al., 1994; Hundley et al., 1997) in mammalian tumorigenesis, so we next bred *p53* mutant zebrafish into an *nf1*-mutant background to generate *p53*^{e7/e7}; *nf1a*^{+/-}; *nf1b*^{-/-} fish. These animals were incrossed to derive *p53*^{e7/e7}; *nf1a*^{+/-}; *nf1b*^{-/-} and *p53*^{e7/e7}; *nf1a*^{-/-}; *nf1b*^{-/-} fish, which were subsequently monitored carefully for tumorigenesis. At 31 weeks post fertilization (wpf), *p53*^{e7/e7}; *nf1a*^{+/-}; *nf1b*^{-/-} fish began to develop tumors with high penetrance although only one *p53*^{e7/e7}; *nf1a*^{+/-}; *nf1b*^{-/-} fish developed a tumor at 44 wpf (Fig. 6A). At 45 wpf, tumor penetrance was higher in *p53*^{e7/e7}; *nf1a*^{+/-}; *nf1b*^{-/-} fish (24/39; 62%) than in *p53*^{e7/e7}; *nf1a*^{+/-}; *nf1b*^{-/-} fish (1/14; 7%). We have previously reported that *p53*^{e7/e7} fish with wild-type *nf1* alleles develop MPNSTs. These tumors did not begin to develop until 41 weeks of age, which was similar to the results with *nf1a*^{+/-}; *nf1b*^{-/-}; *p53*^{e7/e7} animals (Fig. 6A). Furthermore, the penetrance of tumors in *p53*-null animals was only 28% by 66 wpf (Berghmans et al., 2005). Thus, the combined loss of *p53* and 3 of 4 *nf1* alleles in zebrafish markedly

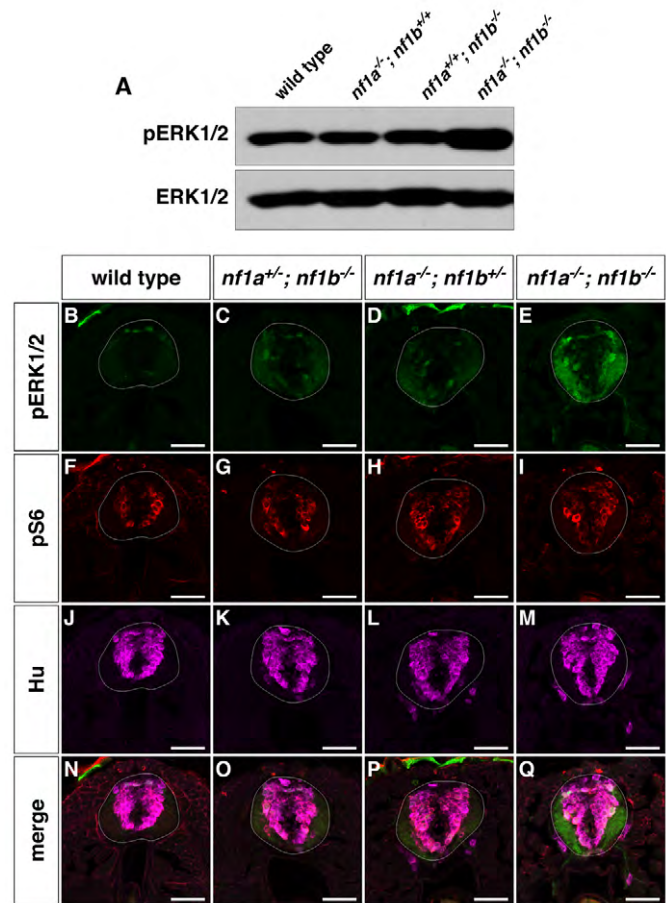


Fig. 5. *nf1a/nf1b* mutants exhibit upregulation of pERK1/2. (A) Western blot analysis for pERK1/2 in protein lysates prepared from wild-type, *nf1a*^{-/-}; *nf1b*^{+/-}, *nf1a*^{+/-}; *nf1b*^{-/-}, and *nf1a*^{-/-}; *nf1b*^{-/-} larvae (100 µg) reveals increased pERK1/2 levels *nf1a*^{-/-}; *nf1b*^{-/-} larvae as compared with wild-type or single allele *nf1*-null larvae at 3 dpf. Equal loading was confirmed by stripping the membrane and reprobing for total ERK1/2. (B–Q) Transverse spinal cord sections of wild-type (B,F,J,N), *nf1a*^{+/-}; *nf1b*^{-/-} (C,G,K,O), *nf1a*^{-/-}; *nf1b*^{+/-} (D,H,L,P) and *nf1a*^{-/-}; *nf1b*^{-/-} (E,I,M,Q) larvae labeled with anti-pERK1/2 antibody (B–E, green), anti-pS6 antibody (F–I, red), or anti-HuC/D antibody (J–M, magenta) demonstrate marked upregulation of pERK1/2 in *nf1a*^{-/-}; *nf1b*^{-/-} larvae and intermediate levels of pERK1/2 in larvae harboring a single functioning *nf1* allele as compared with wild-type larvae at 4 dpf (*n*=5 each for wild-type and mutant larvae). Scale bars: 40 µm.

accelerates the onset and increases the penetrance of tumors as compared with the loss of *p53* alone or the concomitant loss of *p53* and both alleles of *nf1b*, but with intact *nf1a*.

Tumors in *p53*^{e7/e7}; *nf1a*^{+/-}; *nf1b*^{-/-} fish were observed in the brain (*n*=2), eye (*n*=8), gill (*n*=1), abdomen (*n*=8) and trunk (*n*=5). Brain tumors developed very early (31 and 33 wpf) (Fig. 6A, arrows) and demonstrated features of diffuse high-grade gliomas, whereas all other tumor types were most consistent with MPNSTs (Fig. 6B–G). Histopathologically, the brain tumors were highly cellular and composed of ovoid to rounded cells with marked nuclear pleomorphism and diffuse single cell infiltration of parenchyma, including pre-existing neurons (Fig. 7A–F). Occasional mitoses were identified, but no necrosis or vascular proliferation was detected

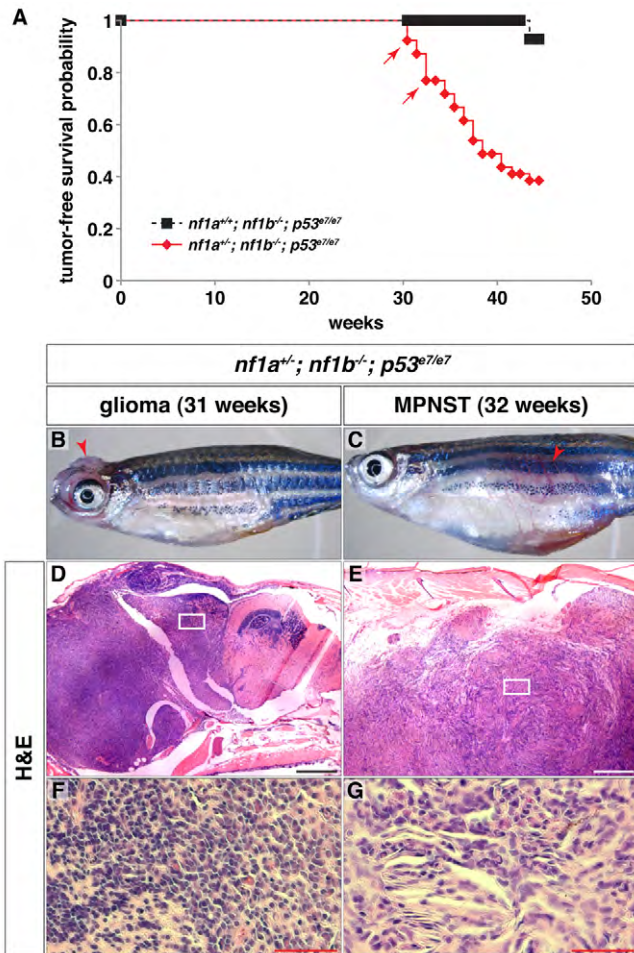


Fig. 6. $nf1a/nf1b$ mutants demonstrate increased susceptibility to tumorigenesis in a $p53$ mutant background. (A) Kaplan-Meier tumor-free survival analysis for $nf1a^{+/-}; nf1b^{-/-}; p53^{e7/e7}$ ($n=39$) animals demonstrates significantly decreased survival as compared with $nf1a^{+/+}; nf1b^{-/-}; p53^{e7/e7}$ ($n=14$) animals ($P<0.001$). Arrows indicate ages at which animals were identified with brain tumors demonstrating features of diffuse high-grade gliomas. (B,C) 31-week old $nf1a^{+/-}; nf1b^{-/-}; p53^{e7/e7}$ animal with a high-grade glioma (B, arrowhead) and 32-week-old $nf1a^{+/-}; nf1b^{-/-}; p53^{e7/e7}$ animal with a malignant peripheral nerve sheath tumor (MPNST) (C, arrowhead). (D-G) H&E staining of sagittal sections through the high-grade optic glioma (D, boxed area magnified in F) or MPNST (E, boxed area magnified in G). Scale bars: 200 μ m (D,E) and 50 μ m (F,G).

(Fig. 7G-I). Assessment of tumor lineage by immunohistochemical analysis showed that approximately 80% of tumor cells stained positive for the oligodendroglial marker Sox10, with little staining in matched wild-type tissue (Fig. 7J-L). The presence of a Sox10-negative tumor cell subpopulation is consistent with the level of heterogeneity for oligodendroglial transcription factors, such as Sox10 and Olig2, and is characteristic of astrocytic or mixed gliomas as compared with pure oligodendroglial class tumors (Fig. 7K, arrowhead) (Ligon et al., 2004; Bannykh et al., 2006). Staining for the astrocytic marker Gfap (Fig. 7M-O) highlighted a subpopulation of cells within the tumor with coarse, irregular cytoplasmic processes also consistent with the presence of an astrocytic lineage

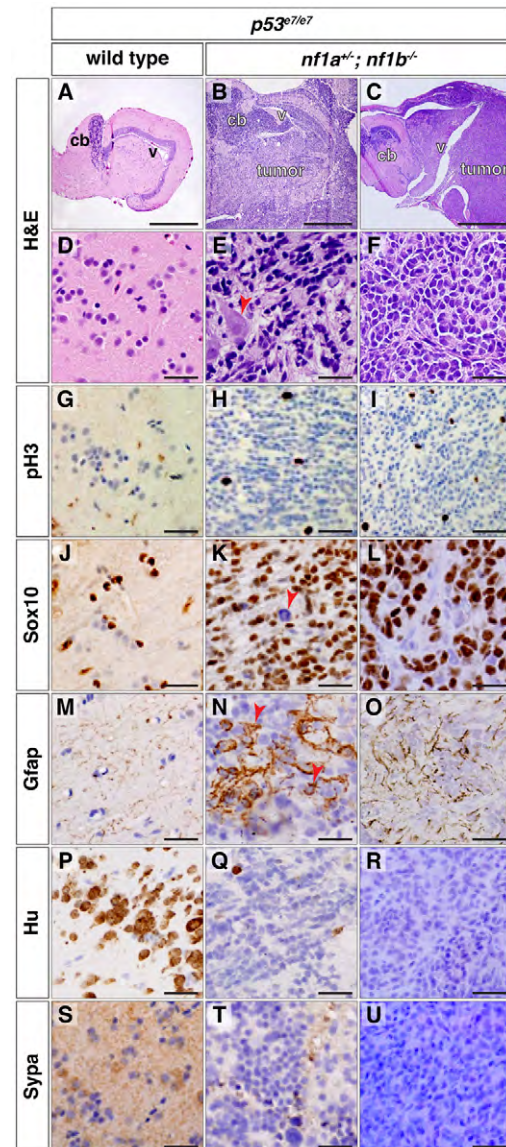


Fig. 7. Tumors from $nf1a^{+/-}; nf1b^{-/-}; p53^{e7/e7}$ animals express glial markers. (A-F) H&E staining of sagittal sections through $p53^{e7/e7}$ brain tissue (A,D) or brain tumors in $nf1a^{+/-}; nf1b^{-/-}; p53^{e7/e7}$ animals at 31 (B,E) and 33 (C,F) wpf (cb, cerebellum; v, ventricle). The arrowhead in E shows infiltration of a single cell through the parenchyma and around normal neurons. (G-U) Immunohistochemical analyses for phosphorylated histone H3 (G-I, pH3), SRY-box 10 (J-L, Sox10), glial fibrillary acidic protein (M-O, Gfap), HuC/D (P-R, Hu) and synaptophysin (S-U, Sypa) on sagittal sections through $p53^{e7/e7}$ brain tissue (G,J,M,P,S) or brain tumors in $nf1a^{+/-}; nf1b^{-/-}; p53^{e7/e7}$ animals at 31 (H,K,N,Q,T) and 33 (I,L,O,R,U) wpf demonstrate occasional mitoses in tumor tissue (H,I) with most tumor cells staining positive for the oligodendroglial marker Sox10 (K,L), a Sox10-negative subpopulation (K, arrowhead), an astrocytic component (N, arrowheads and O) and the absence of mature neuronal markers HuC/D (Q,R) or synaptophysin (T,U). Scale bars: 450 μ m (A-C) and 20 μ m (D-U).

component (Fig. 7N, arrowheads). Tumor cells did not express the mature neuronal markers HuC/D or synaptophysin (Sypa), consistent with their glial origin (Fig. 7P-U).

Immunohistochemical analysis for pERK1/2 and pS6 to assess activation of ERK and mTOR signaling pathways, respectively (supplementary material Fig. S9A-F) revealed increased pERK1/2 staining in the more malignant of these two brain tumors, with normal amounts of pS6 (supplementary material Fig. S9C,D). The more hyperplastic brain tumor showed increased pERK1/2 and pS6 staining (supplementary material Fig. S9E,F). These data demonstrate that some, but not all, brain tumors in *nf1a*^{+/-}; *nf1b*^{-/-}; *p53*^{e7/e7} animals demonstrate hyperactivation of ERK and mTOR pathways, consistent with mouse and human *NF1*-derived MPNSTs and gliomas (Dasgupta et al., 2005; Zhu et al., 2005b). Collectively, these findings suggest that the tumors were high-grade gliomas most closely resembling human anaplastic astrocytoma or anaplastic oligoastrocytoma WHO grade III. Furthermore, MPNSTs (Fig. 6C,E,G) exhibited spindle-shaped tumor cells and extensive necrosis consistent with this tumor type (Ducatman et al., 1986; Wanebo et al., 1993; Hirose et al., 1998). Taken together, we conclude that *nf1a* and *nf1b* mutations cooperate with *p53* loss to generate high-grade gliomas and MPNSTs.

nf1a^{-/-}; *nf1b*^{-/-} larvae show motor and learning deficits

Deficits in motor coordination and cognition, including learning and memory, are characteristic of NF1 patients and animal models. To examine motor behavior and cognition in *nf1a*^{-/-}; *nf1b*^{-/-} larvae, we performed kinematic analysis of the short-latency C-start (SLC), a highly stereotyped yet modifiable acoustic startle reflex in the zebrafish (Burgess and Granato, 2007a; Wolman et al., 2011). Unlike their siblings, *nf1a*^{-/-}; *nf1b*^{-/-} larvae showed a deficit in short-term SLC habituation when presented with repetitive acoustic stimulation (supplementary material Fig. S10A). Furthermore, *nf1a*^{-/-}; *nf1b*^{-/-} larvae performed kinematically weaker SLC responses, as indicated by decreased head turning angle, maximum angular velocity and distance traveled following delivery of an acoustic stimulus (supplementary material Fig. S10B-D). Taken together, these data support the hypothesis that *nf1a* and *nf1b* function redundantly during zebrafish development and that only one of the four wild-type *nf1* alleles is required for phenotypically normal embryonic development, motor behavior and cognition.

nf1 mutants exhibit melanophore defects

Notably, *nf1* null larvae displayed aberrant lateral stripe pigmentation as compared with wild-type controls at 6 dpf (Fig. 8A-D). This phenotype was first appreciable at 4 dpf and was manifested as a disruption in the uniform pattern of melanophores arranged along the lateral stripe (Fig. 8B,D, brackets). To further investigate this phenotype, we quantified melanophore numbers along the lateral stripe of 3 and 6 dpf wild-type and *nf1a*^{-/-}; *nf1b*^{-/-} larvae. No significant differences in the number of melanophores comprising the 3 dpf lateral stripe were appreciable in any combination of mutant *nf1* alleles as compared with sibling wild-type controls (supplementary material Fig. S11). However, at 6 dpf, *nf1a*^{-/-}; *nf1b*^{-/-} larvae exhibited a significant reduction in the number of lateral stripe melanophores (Fig. 8E). Less severe, but still significant, decreases were also noted in larvae carrying two or three mutant *nf1* alleles (Fig. 8E). No difference in the number of apoptotic cells between wild-type and mutant larvae was discernible at 3 dpf (68.1±11 cells/larva, *n*=12 wild-type versus

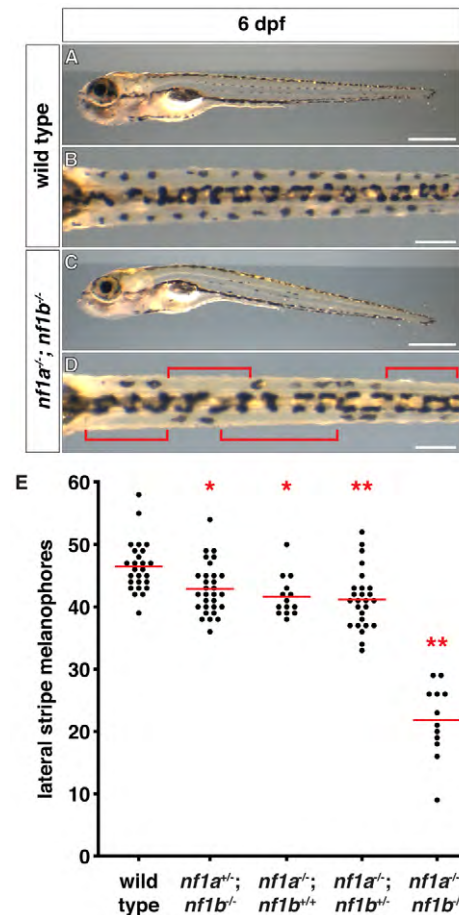


Fig. 8. *nf1* mutants display decreased lateral stripe melanophores. (A–D) Lateral stripe melanophores of wild-type (A,B) larvae demonstrate a normal uniform pattern that is absent in *nf1a*^{-/-}; *nf1b*^{-/-} larvae (C,D) at 6 dpf. The brackets in D highlight regions where melanophores are absent. (E) Quantification of lateral stripe melanophores from wild-type (*n*=26), *nf1a*^{+/-}; *nf1b*^{-/-} (*n*=30), *nf1a*^{-/-}; *nf1b*^{+/-} (*n*=14), *nf1a*^{-/-}; *nf1b*^{-/-} (*n*=26) and *nf1a*^{-/-}; *nf1b*^{-/-} (*n*=12) larvae at 6 dpf. Each point represents the number of lateral stripe melanophores in an individual embryo and red lines indicate mean values. **P*<0.05, ***P*<0.01. Scale bars: 0.5 mm (A,C) and 150 μm (B,D).

63.8±8.5, *n*=12 mutants; *P*=0.27) (supplementary material Fig. S12A-F). Serial observation of melanophore development in individual *nf1a*^{-/-}; *nf1b*^{-/-} and wild-type larvae revealed a defect of migration or differentiation of regeneration and metamorphic lineage melanophores. At 3 dpf, a time point at which embryonic or ontogenetic melanophore development is complete (Hultman et al., 2009), no difference in melanophore number along the lateral stripe was observed (supplementary material Fig. S13A,B,G), indicating that the melanophores develop normally in *nf1* mutants. To assess the regeneration and metamorphic lineage of melanophores, we suppressed melanin synthesis after 3 dpf by treatment with *N*-phenylthiourea (PTU) (Hultman and Johnson, 2010), which allowed us to identify newly formed melanophores by their melanin-negative and pale appearance (supplementary material Fig. S13C,D, red arrows). Removal of PTU at 5 dpf restored melanin synthesis and regeneration and metamorphic

melanophores appeared melanin-positive by 6 dpf ([supplementary material Fig. S13E,F](#), black arrows). The abnormal appearance of the lateral stripe in mutant larvae can be attributed to defects in patterning of regeneration and metamorphic melanophores ([supplementary material Fig. S13F,G](#), brackets), suggesting abnormal migration or differentiation of this lineage. Head melanophore numbers at 6 dpf were not significantly changed in *nf1* mutant larvae and sibling controls ([supplementary material Fig. S14](#)). Collectively, these data demonstrate a specific defect in lateral stripe melanophore numbers following *nf1* allele loss, most prominent in the setting of biallelic *nf1a/nf1b* loss. Each *nf1a*^{-/-}; *nf1b*^{-/-} larvae showed a unique pattern of lateral stripe melanophore loss, suggesting a stochastic defect in melanophore differentiation from neural crest, proliferation, migration or survival, rather than a defect specific to any particular somite of the developing embryo and larvae.

DISCUSSION

NF1 is a common tumor-predisposing, autosomal dominant genetic disorder characterized by café-au-lait macules and cutaneous neurofibromas. In addition to these pigmentation defects and tumors of the peripheral nervous system (PNS), NF1 patients demonstrate highly diversified clinical features with multiple tissue types affected. Prominent lesions include optic pathway gliomas, Lisch nodules, skeletal dysplasia, cardiovascular abnormalities, learning defects and various cancers such as leukemia and intestinal tumors (Side et al., 1997; Side et al., 1998; Bahuau et al., 2000; Andersson et al., 2005; Williams et al., 2009). It remains unclear how *NF1* mutations contribute to the diverse symptoms and tissue types affected in patients. Because neurofibromin is a very large protein that is highly conserved evolutionarily, it is likely to have activities related to functional domains other than those affecting Ras signaling. For example, in addition to Ras, neurofibromin can bind to microtubules, syndecan, phospholipids and amyloid precursor protein (Xu and Gutmann, 1997; Hsueh et al., 2001; D'Angelo et al., 2006; De Schepper et al., 2006). Intriguingly, recent studies indicate that neurofibromin [might](#) function as a positive regulator of adenylyl cyclase (Guo et al., 2000; Tong et al., 2002; Dasgupta et al., 2003). This function of neurofibromin modulates neuronal differentiation (Hegedus et al., 2007), suggesting the possibility that cognitive defects in NF1 patients [might](#) be related to defects in cAMP signaling rather than activated Ras. Furthermore, the tremendous clinical variability in the phenotypic spectrum seen among families with the same molecular *NF1* lesion posits the role of unlinked modifier loci in regulating the expressivity of disease characteristics (Easton et al., 1993; Sabbagh et al., 2009). Nevertheless, the identification of specific modifier genes and the relative contributions of Ras signaling versus other neurofibromin-regulated pathways for specific phenotypes have yet to be fully elucidated. The zebrafish model that we have developed offers an attractive tool for furthering this analysis because it is amenable to small molecule screens, genetic modifier screens and genetic rescue experiments.

A hallmark feature of human NF1 is the presence of pigmentation defects known as café-au-lait spots. Little is known about the underlying mechanisms responsible for this abnormality, and pigmentation abnormalities in other animal models of NF1 have not been described. In this regard, it is of interest that zebrafish

lacking neurofibromin exhibit abnormal patterning of the melanophores that compose the lateral stripe, a phenotype similar to that following pharmacologic inhibition of the upstream Ras effector ErbB (Hultman et al., 2009; Hultman and Johnson, 2010). This easily observable and quantifiable phenotype offers the opportunity to probe underlying molecular pathways modulated by *nf1* in melanophores.

Several studies employing murine models have previously shown a role for neurofibromin in regulating cell numbers of CNS OPCs and astrocytes as well as PNS Schwann cells and sympathetic neurons (Brannan et al., 1994; Gutmann et al., 1999; Bennett et al., 2003; Zhu et al., 2005b; Hegedus et al., 2007; Zheng et al., 2008). These are consistent with our findings in *nf1a/nf1b* mutants and indicative of a strong evolutionary conservation of Nf1 function in neural development. Our observation of impaired compact myelin formation and reduced CNS *plp1a* expression with unperturbed CNS and increased PNS *mbp* expression suggests that the differentiation programs of oligodendrocytes and Schwann cells respond differently to Nf1 deficiency. Alternatively, the observed ultrastructural defects in myelinated CNS axons [might](#) arise secondary to neuronal defects. The accessibility of the zebrafish embryo to mosaic analysis offers the ability to differentiate between these possibilities. Unlike *Nf1*-deficient mice, however, *nf1a/nf1b* mutant radial glia failed to demonstrate an appreciable increase in *Gfap* expression. Instead, we observed a decrease in *Blbp* expression and irregularities in patterning of *nf1a*^{-/-}; *nf1b*^{-/-} radial glial cells. This discrepancy [might](#) reflect species-specific differences in neural tissue as opposed to Nf1 function, because it remains unclear whether zebrafish radial glia-like ependymal cells are functionally equivalent to mammalian astrocytes.

We have previously characterized cardiovascular defects resulting from morpholino knockdown of *nf1a* and *nf1b* in zebrafish (Padmanabhan et al., 2009; Lee et al., 2010). These defects were observed at 48 and 72 hpf and probably resulted from impairment of both maternal and zygotic gene expression. In our stable compound mutants, we observed partially penetrant insufficiency of the atrioventricular valve at 3 dpf along with significant edema and impaired blood circulation associated with irregular heart rates beginning at 5–6 dpf (data not shown). However, we could not determine whether these effects were primary or secondary. It is possible that impaired cardiac function is the cause of death of these larvae. The absence of earlier cardiovascular phenotypes is most probably due to the activity of maternal transcripts (Abrams and Mullins, 2009); confirmation of this interpretation awaits the creation of a maternal zygotic mutation.

Ubiquitous and conditional *Nf1* knockout mice have been generated to investigate the role of neurofibromin in development and tumorigenesis (Cichowski and Jacks, 2001; Le and Parada, 2007). Conditional loss of *Nf1* with *p53* deficiency in mice results in the development of grade III and IV astrocytomas with full penetrance (Zhu et al., 2005a), indicating that *Nf1* mutations are associated not only with low-grade but also high-grade astrocytoma. Indeed, two independent studies have demonstrated that *NF1* mutations are found in about 15–23% of human [glioblastoma multiformes](#) (GBMs) (Parsons et al., 2008; The Cancer Genome Atlas Research Network, 2008). Interestingly, we also observed gliomas in zebrafish lacking *nf1* and *p53*. Likewise, MPNSTs are observed in both mouse and zebrafish models. Thus,

the relative advantages of murine and zebrafish systems can be leveraged for future studies aimed at developing therapeutics for these lethal complications of NF1.

In summary, we have developed and characterized zebrafish lines containing specific targeted mutations in *nf1a* and *nf1b*. Compound deficiency of *nf1a* and *nf1b* results in lethality and predisposes to tumor formation. These studies provide a powerful new tool for analysis of neurofibromin function and for the development of therapies for a common human disorder.

METHODS

Zebrafish lines

The *nf1a*^{Δ5}, *nf1a*^{Δ8}, *nf1b*⁺¹⁰ and *nf1b*^{Δ55} mutant alleles were generated by application of modularly assembled ZFNs. The *nf1a*^{L1247X} mutant allele was generated by TILLING. Our *nf1* mutant alleles were crossed into various transgenic lines, including Tg(*gfap:GFP*) (Lam et al., 2009), Tg(*sox10:GFP*) (Thermes et al., 2002; Carney et al., 2006) and Tg(*olig2:GFP*) (Shin et al., 2003), as well as the *p53*^{7/e7} mutant line (Berghmans et al., 2005). Zebrafish were maintained under standard conditions as previously described (Westerfield, 2000). All experiments involving animals were approved by the Institutional Animal Care and Use Committees of Harvard University and the University of Pennsylvania.

TILLING with screening by CEL-I method

Individual samples from a preconstructed 'live library' of pooled genomic DNA from ENU-mutagenized F1 animals were used as a template for PCR with the following PCR primer pairs: *nf1a*_outer_F, 5'-TGGCAAATAAATGCTGACAGA-3' and *nf1a*_inner_F, 5'-HEX-TTTTATATCTCATGTTTAGCTCAC-AA-3'; *nf1a*_outer_R, 5'-AAGTCTTAAATGGCCTGAGTGG-3' and *nf1a*_inner_R, 5'-6FAM-AAATGGCCTGAGTGGTAATAAA-3'. A nested PCR was performed first using the outer primer pair with the following PCR conditions: 94°C for 2 minutes; 30 cycles of 94°C for 30 seconds, 60°C for 40 seconds and 72°C for 1 minute; and 72°C for 5 minutes. Amplification was then performed using the inner primer pair with the following PCR conditions: 94°C for 2 minutes; 25 cycles of 94°C for 30 seconds, 60°C for 40 seconds and 72°C for 1 minute; and 72°C for 5 minutes. PCR products were denatured, allowed to re-anneal, subjected to CEL-I digestion and separated by acrylamide electrophoresis using a LI-COR DNA analyzer. Upon identification of a genomic DNA sample harboring a mutation in the analyzed region, the individual animals comprising that genomic DNA pool were rescreened to identify the appropriate F1 animal harboring the lesion of interest. This F1 animal was then outcrossed to wild-type fish and progeny were selected on the basis of the presence of the desired mutation. A genotyping strategy was developed to identify animals harboring the nonsense allele isolated by our TILLING strategy using the following PCR primers: *nf1a*_stop_PstI_F, 5'-CTCTCTTCGACTCTCGCCATCTGCTGTATCAGCTGC-3' and *nf1a*_stop_R, 5'-GAAGCAGAAGGTCATAATC-TTGCTGGCTAGGC-3'. PCR conditions were 95°C for 2 minutes; 32 cycles of 94°C for 30 seconds, 62°C for 30 seconds and 72°C for 30 seconds; and 72°C for 5 minutes. This generates a 134 bp PCR product. The wild-type allele is resistant to PCR digestion by *PstI*, but the mutant allele is not.

Modular assembly of ZFNs

The desired three finger zinc finger proteins (ZFPs) were constructed by a splice overlap extension PCR strategy, with individual finger modules amplified from a archive of ZFPs with defined DNA-binding specificities (Zhu et al., 2011). Three individual fingers (F1, F2 and F3) were amplified using primers specific to their desired backbone position, followed by an overlapping PCR step to place them together into a single ZFP fragment which was cloned, sequence verified and subsequently subcloned in frame with a *FokI* nuclease variant in a pCS2 expression plasmid. The primers for the three backbone positions were as follows: F1 forward, 5'-GCGATGG-GTACCCGCCCATATGCTTGC-3' and F1 reverse, 5'-CACTGGAAGGGCTTCTGGCCTGTGTGAATCCGGATGTG-3'; F2 forward, 5'-CATCCGGATTCACACAGGCCAGAA-GCCCTTCCAGTGTGCGCATCTGC-3' and F2 reverse, 5'-ATGTCGCATGCAAAAGGCTTCTCGCCTGTGTGGGTGCGG-ATGTG-3'; F3 forward, 5'-CGAGAAGCCTTTTGCATGCGACA-3' and F3 reverse, 5'-GCGTAGGATCCACCTGTGTGGATCTT-GGTGTG-3'. The PCR conditions for amplifying F1 were 98°C for 2 minutes and 15 cycles of 94°C for 30 seconds, 68°C for 30 seconds and 72°C for 20 seconds. The PCR conditions for F2 and F3 were 98°C for 2 minutes and 20 cycles of 94°C for 30 seconds, 57°C for 30 seconds and 72°C for 30 seconds. The three individual gel-purified PCR products for positions F1, F2 and F3 were combined (15 ng of each) in a PCR using Advantage 2 HiFi polymerase (Clontech) and subjected to the thermal cycling of 94°C for 2 minutes and five cycles of 94°C for 30 seconds, 55°C for 30 seconds and 72°C for 30 seconds. Following this cycling program, F1 forward and F3 reverse primers were added to the reaction and thermal cycling was continued as follows: 25 cycles of 94°C for 15 seconds and 68°C for 30 seconds. This PCR product of approximately 300 bp was gel-purified, cloned, sequence verified and subcloned in frame with the DD/RR or EL/KK *FokI* variants (Miller et al., 2007; Szczepek et al., 2007) with and without the 3'-UTR of *nanos1* (Koprunner et al., 2001).

ZFN mRNA injections and PCR/RE genotyping assays

We utilized protocols similar to those recently described (Zhu et al., 2011). pCS2-based expression plasmids containing our constructed ZFNs were linearized downstream of the SV40 polyadenylation signal and used as templates for in vitro transcription of *ZFN* mRNAs (Ambion). One-cell fertilized zebrafish embryos were injected with varying amounts of DD/RR or EL/KK *FokI* variant mRNAs. Site-specific ZFN function was verified by a PCR/RE genotyping strategy wherein introduction of mutagenic lesions at the target site leads to loss of a unique endogenous restriction site. This same strategy was later used to genotype F1 animals. For *nf1a* and *nf1b*, PCR was performed using the following primer pairs and PCR conditions: *nf1a* F genotyping primer, 5'-GGTGTGTATGTAAATGGGCTCAATG-3'; *nf1a* R genotyping primer, 5'-TACAGTTTCCATAAAACC-TGACATTTTC-3'; *nf1b* F genotyping primer, 5'-TGCTACCTGCCGGCAGGCTCAG-3'; and *nf1b* R genotyping primer, 5'-ACCTGTGACCATCATGTTACTGACA-3'. PCR conditions for *nf1a* were 94°C for 2 minutes; 35 cycles of 94°C for 30 seconds, 54.8°C for 30 seconds and 72°C for 40 seconds; and 72°C for 5 minutes. PCR conditions for *nf1b* were 94°C for 2

minutes; 35 cycles of 94°C for 30 seconds, 62°C for 30 seconds and 72°C for 40 seconds; and 72°C for 5 minutes. For both *nf1a* and *nf1b*, a 223-bp PCR product was generated. Mutant alleles were resistant to subsequent digestion with *Bsp*CNI or *Dde*I (*nf1a*) and *Bsl*II or *Eco*NI (*nf1b*), whereas the wild-type alleles were completely digested. The molecular identities of the various mutant alleles were determined by cloning and sequencing the restriction enzyme-resistant PCR products from individual embryos derived from outcrosses of F1 animals to wild-type fish.

Larval genotyping

A modified fin clip genotyping strategy was utilized to identify larval genotypes prior to sacrifice. Briefly, 2-dpf larvae were anesthetized with tricaine and stereomicroscopic amputation was performed on the caudal fin with an angled dissecting knife (Fine Science Tools, 10056-12). Genomic DNA from fin-clipped tissue samples was prepared by collecting specimens in 1.5 µl of the surrounding medium and dispensing into PCR tubes containing 7.5 µl of 60 mM NaOH, which were incubated at 95°C for 20 minutes followed by 4°C for 5 minutes with the subsequent addition of 1 µl of 1 M Tris-**HCl** pH 8. PCR/RE genotyping for *nf1a* or *nf1b* was performed as described with an increase in PCR cycle number to 40. Genomic DNA prepared by this strategy was sufficient for a single genotyping reaction. Thus, parental crosses were selected to ensure all progeny were homozygous for the non-genotyped *nf1* allele (e.g., *nf1a*^{+/−}; *nf1b*^{−/−} incross). This was verified by genotyping the homozygous mutant allele in sibling clutchmates.

Whole-mount in situ hybridization and TUNEL staining, immunohistochemistry and BrdU labeling

Antisense RNA probes were generated for *plp1a* (Park et al., 2002) and *mbp* (Lyons et al., 2005) using a digoxigenin RNA labeling kit (Roche). A previously published protocol (Thisse and Thisse, 2008) was followed with minor modifications. Terminal deoxynucleotidyl transferase dUTP nick-end labeling (TUNEL) staining of larvae was performed using the ApopTag Peroxidase In Situ Apoptosis Detection Kit (EMD Millipore) with minor modifications. Larvae were subsequently blocked in 2% blocking reagent (Roche) for 4 hours at room temperature and incubated overnight in anti-digoxigenin-POD antibody (Roche; 1:500) at 4°C. TUNEL-positive cells were detected using the TSA fluorescein system (PerkinElmer). Apoptotic cells were quantified by counting TUNEL-positive cells between somites 6 and 15. For immunohistochemical analysis of zebrafish larvae, we used mouse anti-BrdU (Developmental Studies Hybridoma Bank G3G4; 1:1000), mouse anti-HuC/D (Invitrogen A-21271; 1:100), mouse anti-pERK1/2 (Sigma; 1:200), mouse anti-Zrf1 (Zebrafish International Resource Center; 1:1000), rabbit anti-BLBP (Millipore AB9558; 1:1000), rabbit anti-pS6 (Cell Signaling 2211; 1:200), and rabbit anti-SOX10 (Park et al., 2005) (a generous gift from Bruce Appel, **University of Colorado, Denver, CO**; 1:5000) as primary antibodies. For fluorescent detection of antibody labeling, we used anti-mouse and anti-rabbit IgG antibodies conjugated with Alexa Fluors 488, 568 and 647 (Invitrogen; 1:200). Immunohistochemistry of adult zebrafish tumor samples was performed according to a previously published protocol (Ligon et al., 2004). Primary antibodies included anti-pERK1/2 (Cell Signaling 4370; 1:200), anti-pS6 (Cell Signaling 2211; 1:50), anti-phosphorylated histone H3 (Cell Signaling 9706 1:100), rabbit anti-SOX10 (Park et al., 2005) (1:3000), mouse anti-

GFAP (Sigma G3893; 1:10,000), anti-HuC/D (Invitrogen A-21271; 1:200) and anti-synaptophys (Millipore MAB5258; 1:1000). Antibody binding was detected using a diaminobenzidine-peroxidase visualization system (EnVision+, Dako). Mayer's hematoxylin was used for counterstaining. For BrdU labeling, embryos were incubated in BrdU solution (10 mM BrdU in 2% DMSO) for 12 hours. After BrdU incubation, embryos were fixed with 4% paraformaldehyde and embedded in 1.5% agarose. Sections from embedded frozen specimens were immersed in 2 M HCl for 15 minutes and processed for immunohistochemistry. Paraffin sectioning followed by hematoxylin and eosin (**H&E**) staining was performed at the **Dana-Farber/Harvard Cancer Center** Research Pathology Core.

Behavioral analysis

Startle behavioral experiments were performed on 5-dpf larvae raised as previously described (Burgess and Granato, 2007b). Larvae with underinflated swim bladders were excluded from behavioral testing. Acoustic startle responses were elicited and measured as previously described (Burgess and Granato, 2007a; Wolman et al., 2011), such that larvae could be tracked and analyzed individually. All startle stimuli were 1000 Hz waveforms of 3 milliseconds duration at an intensity of approximately 150 m/second². Stimulus intensity was calculated by measuring the displacement of the testing arena due to vibration. To evaluate short latency C-start (SLC) behavior, images were recorded 30 milliseconds prior to and 90 milliseconds following the delivery of the 3 millisecond acoustic stimulus. To examine acoustic startle larval motor behaviors, we captured video recordings using a MotionPro high-speed camera (Redlake) at 1000 frames per second with 512×512 pixel resolution using a 50 mm macro lens. Behavioral analyses were carried out with the FLOTE software package (Burgess and Granato, 2007b; Burgess and Granato, 2007a). Startle short-term habituation was performed and analyzed as previously described (Wolman et al., 2011). Larvae were genotyped following behavioral testing.

Western blotting

Protein lysates were prepared from 3-dpf wild-type, *nf1a*^{−/−}; *nf1b*^{+/+}, *nf1a*^{+/+}; *nf1b*^{−/−}, and *nf1a*^{−/−}; *nf1b*^{−/−} larvae. Briefly, groups of 10–20 larvae with identical genotype were anesthetized with tricaine, deyolked in a solution of ice-cold PBS with 0.1% Tween-20 (PBST), transferred to a pre-chilled microcentrifuge tube containing 5 µl of lysis buffer (150 mM NaCl, 50 mM Tris-**HCl** pH 8, 5 mM EDTA, 1 mM PMSE, 1% Igepal CA 630, 0.5% sodium deoxycholate, 0.1% SDS and 1× Halt protease inhibitor cocktail (Thermo Fisher Scientific) per larva, sonicated using a Bioruptor (Diagenode) and cleared by centrifugation. Larval (100 µg) and 293T (25 µg) protein lysates were separated by gel electrophoresis, transferred to PVDF membranes and probed overnight at 4°C with the following primary antibodies: anti-neurofibromin (Abcam ab17963; 1:1000), anti- α -tubulin (Sigma T6074; 1:1000), anti-pERK1/2 (Cell Signaling 4377; 1:1000), and anti-ERK1/2 (Cell Signaling 9102; 1:1000). Primary antibody binding was visualized on X-ray film using anti-mouse-HRP (Cell Signaling 7076; 1:10,000) or anti-rabbit-HRP (Cell Signaling 7074; 1:10,000) secondary antibodies along with LumiGLO (Cell Signaling) or SuperSignal West Femto (Thermo Fisher Scientific) chemiluminescent substrates. Each Western blot was performed in three independent replicates with a representative image of one presented.

Quantification of lateral line and head melanophores

Lateral stripe melanophores, including those observed along the horizontal myoseptum, were counted by a blinded observer in live progeny from *nf1a*^{+/-}; *nf1b*^{+/-} incrosses at 3 and 6 dpf. Each discrete melanized region was counted as a single melanophore. Following 6-dpf lateral stripe melanophore quantitation, larvae were immersed in E3 medium containing 5 mg/ml epinephrine (Sigma E4375) for 10 minutes to induce contraction of melanosomes around cell bodies and allow evaluation of head melanophore numbers. Larvae were fixed overnight in 4% paraformaldehyde in PBS at 4°C, washed twice with PBS for 5 minutes, and melanophores anterior to somite one across the crown of the head (supplementary material Fig. S9) were counted. Larvae were subsequently genotyped for *nf1a* and *nf1b*. Data analysis was performed by one-way ANOVA with Dunnett's post-test (GraphPad InStat 3.1a, GraphPad Software).

Serial tracking of lateral line melanophores

Lateral stripe melanophores of live progeny from *nf1a*^{+/-}; *nf1b*^{-/-} or wild-type incrosses were individually imaged at 3 dpf followed by incubation with 0.2 mM *N*-phenylthiourea (PTU, Sigma) to prevent melanin synthesis. At 5 dpf, lateral stripe melanophores were again imaged, after which PTU was washed out. Larvae were reimaged at 6 dpf and subsequently genotyped for *nf1a*. Images were acquired using a Nikon SMZ1500 microscope and NIS-Elements F2.20 software with identical settings. Melanophores in a 200-μm region, corresponding to roughly 12 somites at 3 dpf, were counted at 3 and 6 dpf for each larva. Statistical analysis was performed using a one-tail, unpaired *t*-test (GraphPad Prism 5, GraphPad Software).

Intestinal transit assays

Groups of 5-dpf wild-type and *nf1a*^{-/-}; *nf1b*^{-/-} larvae were placed in individual wells of six-well plates containing feeding medium [4 ml E3, 2 ml paramecia culture and 5 μl of 2-μm yellow-green microspheres (Polysciences 18338)]. Larvae were incubated at 28.5°C for 1 hour followed by several E3 washes. Individual larvae were transferred to 24-well plates and visually assessed for the presence of fluorescent microspheres in the intestinal bulb. Extent of intestinal transit was observed at 2, 4, 6 and 24 hours. Transit was considered to be complete when fluorescence was no longer detectable in the intestinal tract.

Transmission electron microscopy

TEM was carried out at the Harvard Medical School Electron Microscopy Facility. Briefly, embryos were fixed in 2% formaldehyde and 2.5% glutaraldehyde, post-fixed with 1% osmium tetroxide and embedded in epon. Sections were collected in the trunk region of embryos. Images were captured by a Tecnai G² Spirit BioTWIN electron microscope with an AMT 2k CCD camera.

Tumor identification

nf1a^{Δ8/+}; *nf1b*^{+10/+10}; *p53*^{e7/e7} fish were incrossed and progeny were manually evaluated weekly for 45 weeks. Animals identified as having tumors were separated and fin-clipped for genotyping purposes. These samples were subsequently subjected to histological and immunohistochemical analyses as described above for determination

TRANSLATIONAL IMPACT

Clinical issue

Neurofibromatosis type 1 (NF1) is one of the most commonly inherited human genetic disorders. Despite nearly complete penetrance, the clinical expression of NF1 varies widely, even within families harboring identical mutations at the *NF1* locus. Not surprisingly, few genotype-phenotype relationships have thus far been reported for NF1, suggesting important contributions from unlinked modifier genes and/or environmental factors. However, these observations do not preclude mutations or deletions within the *NF1* locus from influencing pathology. Instead, they highlight the need for better experimental tools to address this important and clinically relevant observation. Additional models of NF1 are needed to begin elucidating these mechanisms using scalable chemical and genetic approaches.

Results

The authors employ zinc finger nucleases and TILLING to isolate null alleles of the two zebrafish orthologues of human *NF1*, *nf1a* and *nf1b*. They report that zebrafish lacking *nf1a* and *nf1b* exhibit valvular insufficiency, defects in learning and behavior and early larval lethality. Larvae carrying a single wild-type allele of either *nf1a* or *nf1b* are viable and fertile, suggesting functional redundancy. The authors also observe hyperplasia and aberrant differentiation in the oligodendrocyte progenitor cells and Schwann cells populating the nervous systems of *nf1*-null larvae. This is accompanied by irregularities in the myelin sheaths surrounding the neuronal axons of the central nervous system. Human *NF1* is a potent tumor-suppressor gene and the authors provide evidence that zebrafish *nf1a* and *nf1b* function similarly: they demonstrate that Ras is hyperactivated in the spinal cords of *nf1*-null larvae, and that the combined loss of *nf1* and *p53* accelerates tumorigenesis. Finally, the authors characterize a melanophore defect resulting from *nf1* loss that disrupts the uniform pigmentation pattern observed along the lateral stripes.

Implications and future directions

Using zebrafish to probe the genetic, epistatic and environmental factors underlying NF1 pathology offers several important advantages over currently available murine models. The low costs and high fecundity of zebrafish coupled with their ability to survive for several days as haploid organisms make them amenable to large-scale genetic screens. Thus, *nf1*-deficient zebrafish should greatly facilitate the identification of modifier genes influencing NF1 pathogenesis. In addition, genetic rescue experiments using specific *NF1* mutations or deletions could clarify the molecular basis of pathology. The feasibility of high-throughput chemical screening using this model should provide additional valuable mechanistic insights and identify lead compounds for future therapeutics. Few treatment options are currently available for individuals affected with NF1, so advances in this area are urgently needed. Importantly, this represents the first animal model that demonstrates pigmentation defects analogous to the pathognomonic café-au-lait spots seen in affected individuals. Therefore, this model will provide a platform for further investigation of one of the most common clinical pathologies associated with NF1.

of tumor type. At the completion of 45 weeks, all tumor-free fish were genotyped for subsequent statistical analysis.

ACKNOWLEDGEMENTS

We thank members of the Epstein and Look laboratories for helpful discussions, especially Rajan Jain and Nikhil Singh. We are grateful to Jie He for her expert assistance with zebrafish husbandry; Michael Pack and Mary Mullins for thoughtful suggestions; Joshua Abrams, Jesse Isaacman-Beck and Allison Rosenberg for technical instruction; and Thomas Joseph for critical reading of the manuscript.

COMPETING INTERESTS

The authors declare that they do not have any competing or financial interests.

AUTHOR CONTRIBUTIONS

J.S., A.P., E.D.D., M.A.W., J.P.K., N.D.L., S.A.W., K.L.L., J.A.E. and A.T.L. conceived and designed the experiments. J.S., A.P., E.D.D., J-S.L., S.H., S.D., F.G. and M.A.W. performed the experiments. J.S., A.P., E.D.D., J.P.K., K.L.L., J.A.E. and A.T.L. analyzed

the data. M.G., N.D.L., S.A.W., S-H.K., L.S.-K. and K.L.L. contributed reagents, materials and analysis tools. A.P., J.S., E.D.D., J.P.K., A.T.L. and J.A.E. wrote the paper.

FUNDING

This work was supported by the Department of Defense [grant numbers W81XWH-07-1-0228 and W81XWH-12-1-0125 to J.A.E. and A.T.L.] and the National Institutes of Health [grant numbers R01 HL062974 to J.A.E.; R01 HL093766 to N.D.L. and S.A.W.; T32 HL007843-15 to E.D.D.; and R01 HG002995 to L.S.-K.]. A.P. was supported by a fellowship from the Sarnoff Cardiovascular Research Foundation, J.S. was supported by a fellowship from the **Dana-Farber Cancer Institute** (DFCI) Pediatric Low-Grade Astrocytoma Program, and J.-S.L. was supported by a Young Investigator Award from the Children's Tumor Foundation. This work was also supported by the Vanderbilt University Academic Venture Capital Fund to L.S.-K. as well as the Spain Fund for Regenerative Medicine and the W.W. Smith Endowed Chair to J.A.E.

SUPPLEMENTARY MATERIAL

Supplementary material for this article is available at <http://dmm.biologists.org/lookup/suppl/doi:10.1242/dmm.009779/-/DC1>

REFERENCES

- Abrams, E. W. and Mullins, M. C. (2009). Early zebrafish development: it's in the maternal genes. *Curr. Opin. Genet. Dev.* **19**, 396-403.
- Amores, A., Force, A., Yan, Y. L., Joly, L., Amemiya, C., Fritz, A., Ho, R. K., Langeland, J., Prince, V., Wang, Y. L. et al. (1998). Zebrafish hox clusters and vertebrate genome evolution. *Science (New York, N. Y.)* **282**, 1711-1714.
- Andersson, J., Sihto, H., Meis-Kinblom, J. M., Joensuu, H., Nupponen, N. and Kindblom, L. G. (2005). NF1-associated gastrointestinal stromal tumors have unique clinical, phenotypic, and genotypic characteristics. *Am. J. Surg. Pathol.* **29**, 1170-1176.
- Bahuau, M., Laurendeau, I., Pelet, A., Assouline, B., Lamireau, T., Taine, L., Le Bail, B., Vergnes, P., Gallet, S., Vidaud, M. et al. (2000). Tandem duplication within the neurofibromatosis type 1 gene (NF1) and reciprocal t(15;16)(q26.3;q12.1) translocation in familial association of NF1 with intestinal neuronal dysplasia type B (IND B). *J. Med. Genet.* **37**, 146-150.
- Bannykh, S. I., Stolt, C. C., Kim, J., Perry, A. and Wegner, M. (2006). Oligodendroglial-specific transcriptional factor SOX10 is ubiquitously expressed in human gliomas. *J. Neurooncol.* **76**, 115-127.
- Bennett, M. R., Rizvi, T. A., Karyala, S., McKinnon, R. D. and Ratner, N. (2003). Aberrant growth and differentiation of oligodendrocyte progenitors in neurofibromatosis type 1 mutants. *J. Neurosci.* **23**, 7207-7217.
- Berghmans, S., Murphey, R. D., Wienholds, E., Neuberg, D., Kutok, J. L., Fletcher, C. D., Morris, J. P., Liu, T. X., Schulte-Merker, S., Kanki, J. P. et al. (2005). tp53 mutant zebrafish develop malignant peripheral nerve sheath tumors. *Proc. Natl. Acad. Sci. USA* **102**, 407-412.
- Brannan, C. I., Perkins, A. S., Vogel, K. S., Ratner, N., Nordlund, M. L., Reid, S. W., Buchberg, A. M., Jenkins, N. A., Parada, L. and Copeland, N. G. (1994). Targeted disruption of the neurofibromatosis type-1 gene leads to developmental abnormalities in heart and various neural crest-derived tissues. *Genes Dev.* **8**, 1019-1029.
- Burgess, H. A. and Granato, M. (2007a). Sensorimotor gating in larval zebrafish. *J. Neurosci.* **27**, 4984-4994.
- Burgess, H. A. and Granato, M. (2007b). Modulation of locomotor activity in larval zebrafish during light adaptation. *J. Exp. Biol.* **210**, 2526-2539.
- Carney, T. J., Dutton, K. A., Greenhill, E., Delfino-Machin, M., Dufourcq, P., Blader, P. and Kelsh, R. N. (2006). A direct role for Sox10 in specification of neural crest-derived sensory neurons. *Development* **133**, 4619-4630.
- Cawthon, R. M., Weiss, R., Xu, G. F., Viskochil, D., Culver, M., Stevens, J., Robertson, M., Dunn, D., Gesteland, R., O'Connell, P. et al. (1990). A major segment of the neurofibromatosis type 1 gene: cDNA sequence, genomic structure, and point mutations. *Cell* **62**, 193-201.
- Cichowski, K. and Jacks, T. (2001). NF1 tumor suppressor gene function: narrowing the GAP. *Cell* **104**, 593-604.
- Cichowski, K., Shih, T. S., Schmitt, E., Santiago, S., Reilly, K., McLaughlin, M. E., Bronson, R. T. and Jacks, T. (1999). Mouse models of tumor development in neurofibromatosis type 1. *Science (New York, N. Y.)* **286**, 2172-2176.
- D'Angelo, I., Welti, S., Bonneau, F. and Scheffzek, K. (2006). A novel bipartite phospholipid-binding module in the neurofibromatosis type 1 protein. *EMBO Rep.* **7**, 174-179.
- Dasgupta, B., Dugan, L. L. and Gutmann, D. H. (2003). The neurofibromatosis 1 gene product neurofibromin regulates pituitary adenylate cyclase-activating polypeptide-mediated signaling in astrocytes. *J. Neurosci.* **23**, 8949-8954.
- Dasgupta, B., Yi, Y., Chen, D. Y., Weber, J. D. and Gutmann, D. H. (2005). Proteomic analysis reveals hyperactivation of the mammalian target of rapamycin pathway in neurofibromatosis 1-associated human and mouse brain tumors. *Cancer Res.* **65**, 2755-2760.
- De Schepper, S., Boucneau, J. M., Westbroek, W., Mommaas, M., Onderwater, J., Messiaen, L., Naeyaert, J. M. and Lambert, J. L. (2006). Neurofibromatosis type 1 protein and amyloid precursor protein interact in normal human melanocytes and colocalize with melanosomes. *J. Invest. Dermatol.* **126**, 653-659.
- Ducatman, B. S., Scheithauer, B. W., Piepgras, D. G., Reiman, H. M. and Ilstrup, D. M. (1986). Malignant peripheral nerve sheath tumors. A clinicopathologic study of 120 cases. *Cancer* **57**, 2006-2021.
- Easton, D. F., Ponder, M. A., Huson, S. M. and Ponder, B. A. (1993). An analysis of variation in expression of neurofibromatosis (NF) type 1 (NF1): evidence for modifying genes. *Am. J. Hum. Genet.* **53**, 305-313.
- Eliyahu, D., Raz, A., Gruss, P., Givol, D. and Oren, M. (1984). Participation of p53 cellular tumour antigen in transformation of normal embryonic cells. *Nature* **312**, 646-649.
- Guo, H. F., Tong, J., Hannan, F., Luo, L. and Zhong, Y. (2000). A neurofibromatosis-1-regulated pathway is required for learning in *Drosophila*. *Nature* **403**, 895-898.
- Gutmann, D. H., Loehr, A., Zhang, Y., Kim, J., Henkemeyer, M. and Cashen, A. (1999). Haploinsufficiency for the neurofibromatosis 1 (NF1) tumor suppressor results in increased astrocyte proliferation. *Oncogene* **18**, 4450-4459.
- Hegedus, B., Dasgupta, B., Shin, J. E., Emmett, R. J., Hart-Mahon, E. K., Elghazi, L., Bernal-Mizrachi, E. and Gutmann, D. H. (2007). Neurofibromatosis-1 regulates neuronal and glial cell differentiation from neuroglial progenitors in vivo by both cAMP- and Ras-dependent mechanisms. *Cell Stem Cell* **1**, 443-457.
- Hirose, T., Scheithauer, B. W. and Sano, T. (1998). Perineurial malignant peripheral nerve sheath tumor (MPNST): a clinicopathologic, immunohistochemical, and ultrastructural study of seven cases. *Am. J. Surg. Pathol.* **22**, 1368-1378.
- Hsueh, Y. P., Roberts, A. M., Volta, M., Sheng, M. and Roberts, R. G. (2001). Bipartite interaction between neurofibromatosis type I protein (neurofibromin) and syndecan transmembrane heparan sulfate proteoglycans. *J. Neurosci.* **21**, 3764-3770.
- Hultman, K. A. and Johnson, S. L. (2010). Differential contribution of direct-developing and stem cell-derived melanocytes to the zebrafish larval pigment pattern. *Dev. Biol.* **337**, 425-431.
- Hultman, K. A., Budi, E. H., Teasley, D. C., Gottlieb, A. Y., Parichy, D. M. and Johnson, S. L. (2009). Defects in ErbB-dependent establishment of adult melanocyte stem cells reveal independent origins for embryonic and regeneration melanocytes. *PLoS Genet.* **5**, e1000544.
- Hundley, J. E., Koester, S. K., Troyer, D. A., Hilsenbeck, S. G., Subler, M. A. and Windle, J. J. (1997). Increased tumor proliferation and genomic instability without decreased apoptosis in MMTV-ras mice deficient in p53. *Mol. Cell. Biol.* **17**, 723-731.
- Jacks, T., Shih, T. S., Schmitt, E. M., Bronson, R. T., Bernards, A. and Weinberg, R. A. (1994). Tumour predisposition in mice heterozygous for a targeted mutation in Nf1. *Nat. Genet.* **7**, 353-361.
- Kemp, C. J., Burns, P. A., Brown, K., Nagase, H. and Balmain, A. (1994). Transgenic approaches to the analysis of ras and p53 function in multistage carcinogenesis. *Cold Spring Harb. Symp. Quant. Biol.* **59**, 427-434.
- Koprunner, M., Thisse, C., Thisse, B. and Raz, E. (2001). A zebrafish nanos-related gene is essential for the development of primordial germ cells. *Genes Dev.* **15**, 2877-2885.
- Lam, C. S., Marz, M. and Strahle, U. (2009). gfap and nestin reporter lines reveal characteristics of neural progenitors in the adult zebrafish brain. *Dev. Dyn.* **238**, 475-486.
- Le L. Q. and Parada, L. F. (2007). Tumor microenvironment and neurofibromatosis type I: connecting the GAPs. *Oncogene* **26**, 4609-4616.
- Lee, J. S., Padmanabhan, A., Shin, J., Zhu, S., Guo, F., Kanki, J. P., Epstein, J. A. and Look, A. T. (2010). Oligodendrocyte progenitor cell numbers and migration are regulated by the zebrafish orthologs of the NF1 tumor suppressor gene. *Hum. Mol. Genet.* **19**, 4643-4653.
- Ligon, K. L., Alberta, J. A., Kho, A. T., Weiss, J., Kwaan, M. R., Nutt, C. L., Louis, D. N., Stiles, C. D. and Rowitch, D. H. (2004). The oligodendroglial lineage marker OLIG2 is universally expressed in diffuse gliomas. *J. Neuropathol. Exp. Neurol.* **63**, 499-509.
- Lyons, D. A., Pogoda, H. M., Voas, M. G., Woods, I. G., Diamond, B., Nix, R., Arana, N., Jacobs, J. and Talbot, W. S. (2005). erbb3 and erbb2 are essential for schwann cell migration and myelination in zebrafish. *Curr. Biol.* **15**, 513-524.
- Miller, J. C., Holmes, M. C., Wang, J., Guschin, D. Y., Lee, Y. L., Rupniewski, I., Beausejour, C. M., Waite, A. J., Wang, N. S., Kim, K. A. et al. (2007). An improved zinc-finger nuclease architecture for highly specific genome editing. *Nat. Biotechnol.* **25**, 778-785.
- Padmanabhan, A., Lee, J. S., Ismat, F. A., Lu, M. M., Lawson, N. D., Kanki, J. P., Look, A. T. and Epstein, J. A. (2009). Cardiac and vascular functions of the zebrafish orthologues of the type I neurofibromatosis gene NF1. *Proc. Natl. Acad. Sci. USA* **106**, 22305-22310.
- Parada, L. F., Land, H., Weinberg, R. A., Wolf, D. and Rotter, V. (1984). Cooperation between gene encoding p53 tumour antigen and ras in cellular transformation. *Nature* **312**, 649-651.

- Park, H. C., Mehta, A., Richardson, J. S. and Appel, B. (2002). *olig2* is required for zebrafish primary motor neuron and oligodendrocyte development. *Dev. Biol.* **248**, 356-368.
- Park, H. C., Boyce, J., Shin, J. and Appel, B. (2005). Oligodendrocyte specification in zebrafish requires notch-regulated cyclin-dependent kinase inhibitor function. *J. Neurosci.* **25**, 6836-6844.
- Parsons, D. W., Jones, S., Zhang, X., Lin, J. C., Leary, R. J., Angenendt, P., Mankoo, P., Carter, H., Siu, I. M., Gallia, G. L. et al. (2008). An integrated genomic analysis of human glioblastoma multiforme. *Science (New York, N. Y.)* **321**, 1807-1812.
- Powers, J. F., Evinger, M. J., Zhi, J., Picard, K. L. and Tischler, A. S. (2007). Pheochromocytomas in *Nf1* knockout mice express a neural progenitor gene expression profile. *Neuroscience* **147**, 928-937.
- Sabbagh, A., Pasmant, E., Laurendeau, I., Parfait, B., Barbarot, S., Guillot, B., Combemale, P., Ferkal, S., Vidaud, M., Aubourg, P. et al. (2009). Unravelling the genetic basis of variable clinical expression in neurofibromatosis 1. *Hum. Mol. Genet.* **18**, 2768-2778.
- Shin, J., Park, H. C., Topczewska, J. M., Mawdsley, D. J. and Appel, B. (2003). Neural cell fate analysis in zebrafish using *olig2* BAC transgenics. *Methods Cell Sci.* **25**, 7-14.
- Side, L., Taylor, B., Cayouette, M., Conner, E., Thompson, P., Luce, M. and Shannon, K. (1997). Homozygous inactivation of the *NF1* gene in bone marrow cells from children with neurofibromatosis type 1 and malignant myeloid disorders. *N. Engl. J. Med.* **336**, 1713-1720.
- Side, L. E., Emanuel, P. D., Taylor, B., Franklin, J., Thompson, P., Castleberry, R. P. and Shannon, K. M. (1998). Mutations of the *NF1* gene in children with juvenile myelomonocytic leukemia without clinical evidence of neurofibromatosis, type 1. *Blood* **92**, 267-272.
- Szcepek, M., Brondani, V., Buchel, J., Serrano, L., Segal, D. J. and Cathomen, T. (2007). Structure-based redesign of the dimerization interface reduces the toxicity of zinc-finger nucleases. *Nat. Biotechnol.* **25**, 786-793.
- Tanaka, M., Omura, K., Watanabe, Y., Oda, Y. and Nakanishi, I. (1994). Prognostic factors of colorectal cancer: K-ras mutation, overexpression of the p53 protein, and cell proliferative activity. *J. Surg. Oncol.* **57**, 57-64.
- The Cancer Genome Atlas, Research Network. (2008). Comprehensive genomic characterization defines human glioblastoma genes and core pathways. *Nature* **455**, 1061-1068.
- Thermes, V., Grabher, C., Ristoratore, F., Bourrat, F., Choulika, A., Wittbrodt, J. and Joly, J. S. (2002). I-SceI meganuclease mediates highly efficient transgenesis in fish. *Mech. Dev.* **118**, 91-98.
- Thisse, C. and Thisse, B. (2008). High-resolution in situ hybridization to whole-mount zebrafish embryos. *Nat. Protoc.* **3**, 59-69.
- Tong, J., Hannan, F., Zhu, Y., Bernards, A. and Zhong, Y. (2002). Neurofibromin regulates G protein-stimulated adenylyl cyclase activity. *Nat. Neurosci.* **5**, 95-96.
- Viskochil, D., Buchberg, A. M., Xu, G., Cawthon, R. M., Stevens, J., Wolff, R. K., Culver, M., Carey, J. C., Copeland, N. G., Jenkins, N. A. et al. (1990). Deletions and a translocation interrupt a cloned gene at the neurofibromatosis type 1 locus. *Cell* **62**, 187-192.
- Vogel, K. S., Klesse, L. J., Velasco-Miguel, S., Meyers, K., Rushing, E. J. and Parada, L. F. (1999). Mouse tumor model for neurofibromatosis type 1. *Science (New York, N. Y.)* **286**, 2176-2179.
- Wallace, M. R., Marchuk, D. A., Andersen, L. B., Letcher, R., Odeh, H. M., Saulino, A. M., Fountain, J. W., Brereton, A., Nicholson, J., Mitchell, A. L. et al. (1990). Type 1 neurofibromatosis gene: identification of a large transcript disrupted in three *NF1* patients. *Science (New York, N. Y.)* **249**, 181-186.
- Wanebo, J. E., Malik, J. M., VandenBerg, S. R., Wanebo, H. J., Driesen, N. and Persing, J. A. (1993). Malignant peripheral nerve sheath tumors. A clinicopathologic study of 28 cases. *Cancer* **71**, 1247-1253.
- Westerfield, M. (2000). *The Zebrafish Book: A Guide for the Laboratory Use of Zebrafish (Danio rerio)* (4th ed.). Eugene, OR: University of Oregon Press.
- Wienholds, E., Schulte-Merker, S., Walderich, B. and Plasterk, R. H. (2002). Target-selected inactivation of the zebrafish *rag1* gene. *Science* **297**, 99-102.
- Williams, V. C., Lucas, J., Babcock, M. A., Gutmann, D. H., Korf, B. and Maria, B. L. (2009). Neurofibromatosis type 1 revisited. *Pediatrics* **123**, 124-133.
- Wolman, M. A., Jain, R. A., Liss, L. and Granato, M. (2011). Chemical modulation of memory formation in larval zebrafish. *Proc. Natl. Acad. Sci. USA* **108**, 15468-15473.
- Xu, H. and Gutmann, D. H. (1997). Mutations in the GAP-related domain impair the ability of neurofibromin to associate with microtubules. *Brain Res.* **759**, 149-152.
- Zheng, H., Chang, L., Patel, N., Yang, J., Lowe, L., Burns, D. K. and Zhu, Y. (2008). Induction of abnormal proliferation by nonmyelinating schwann cells triggers neurofibroma formation. *Cancer cell* **13**, 117-128.
- Zhu, Y., Guignard, F., Zhao, D., Liu, L., Burns, D. K., Mason, R. P., Messing, A. and Parada, L. F. (2005a). Early inactivation of p53 tumor suppressor gene cooperating with *NF1* loss induces malignant astrocytoma. *Cancer cell* **8**, 119-130.
- Zhu, Y., Harada, T., Liu, L., Lush, M. E., Guignard, F., Harada, C., Burns, D. K., Bajenaru, M. L., Gutmann, D. H. and Parada, L. F. (2005b). Inactivation of *NF1* in CNS causes increased glial progenitor proliferation and optic glioma formation. *Development* **132**, 5577-5588.
- Zhu, C., Smith, T., McNulty, J., Rayla, A. L., Lakshmanan, A., Siekmann, A. F., Buffardi, M., Meng, X., Shin, J., Padmanabhan, A. et al. (2011). Evaluation and application of modularly assembled zinc-finger nucleases in zebrafish. *Development* **138**, 4555-4564.

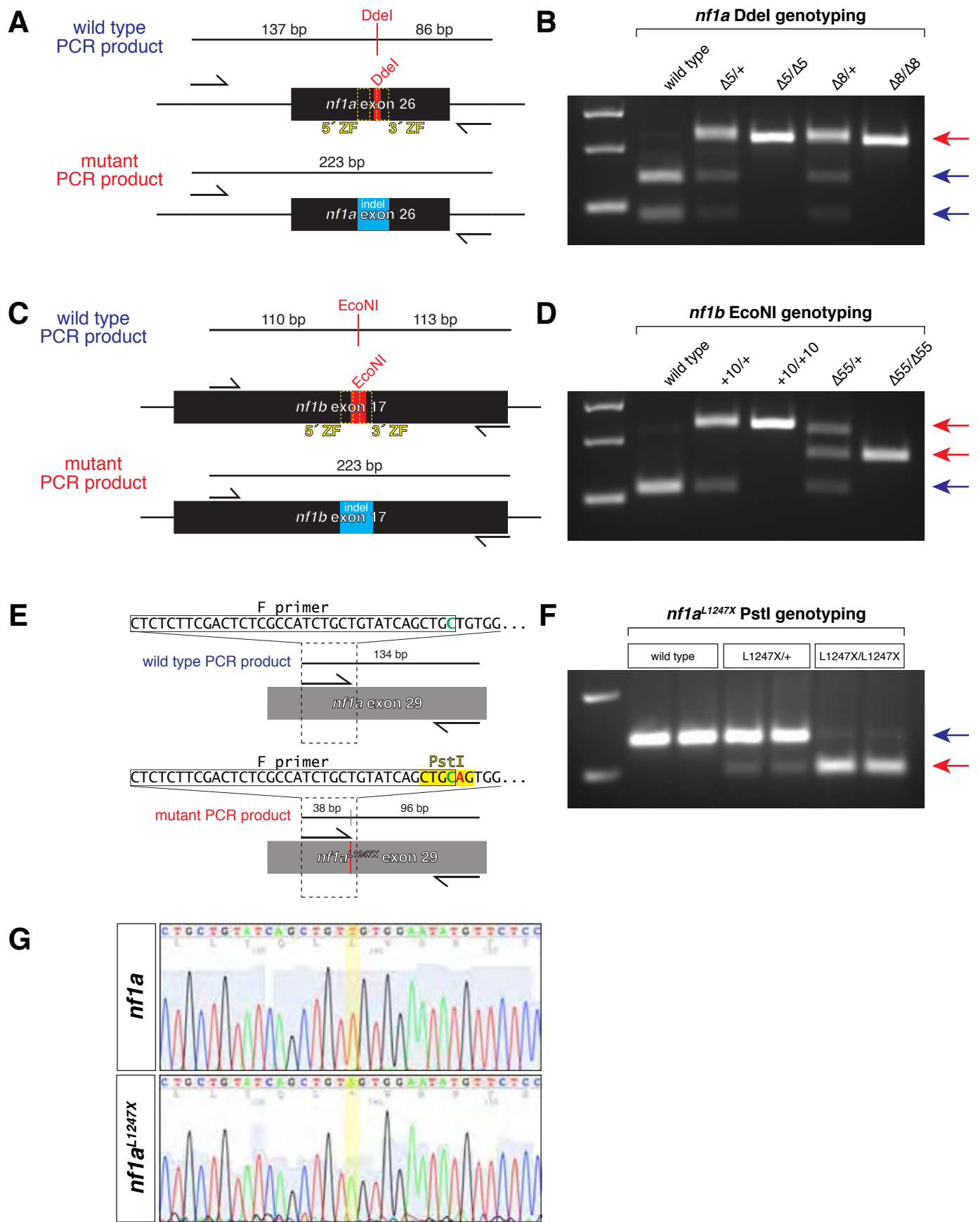


Fig. S1. Genotyping strategies for identification of *nf1* mutant alleles.

(A,B) Schematic diagram of PCR products generated from wild type and ZFN-induced mutant *nf1a* alleles (A). The indels (A, blue box) in the $\Delta 8$ and $\Delta 5$ *nf1a* alleles lead to loss of a native Ddel site, allowing for allelic discrimination by gel electrophoresis of Ddel digested PCR products (B, red arrow, mutant band; blue arrows, wild type bands). (C,D) Schematic diagram of PCR products generated from wild type and ZFN-induced mutant *nf1b* alleles (C). The indels (C, blue box) in the +10 and $\Delta 55$ *nf1b* alleles lead to loss of a native EcoNI site, allowing for allelic discrimination by gel electrophoresis of EcoNI digested PCR products (D, red arrows, mutant bands; blue arrow, co-migrating wild type bands). (E,F) Schematic diagram of PCR products generated from wild type and TILLING-induced *nf1a*^{L1247X} alleles (E). The forward primer (F primer) contains a 1 base pair mismatch with the native *nf1a* exon 29 sequence so as to create a PstI restriction site in the mutant, which harbors a T to A nonsense mutation, allowing for allelic discrimination by gel electrophoresis of PstI digested PCR products (F, red arrow, mutant band; blue arrow, wild type band). (G) Sequencing chromatograms from wild type and *nf1a*^{L1247X/L1247X} animals (TILLING-induced mutation highlighted).

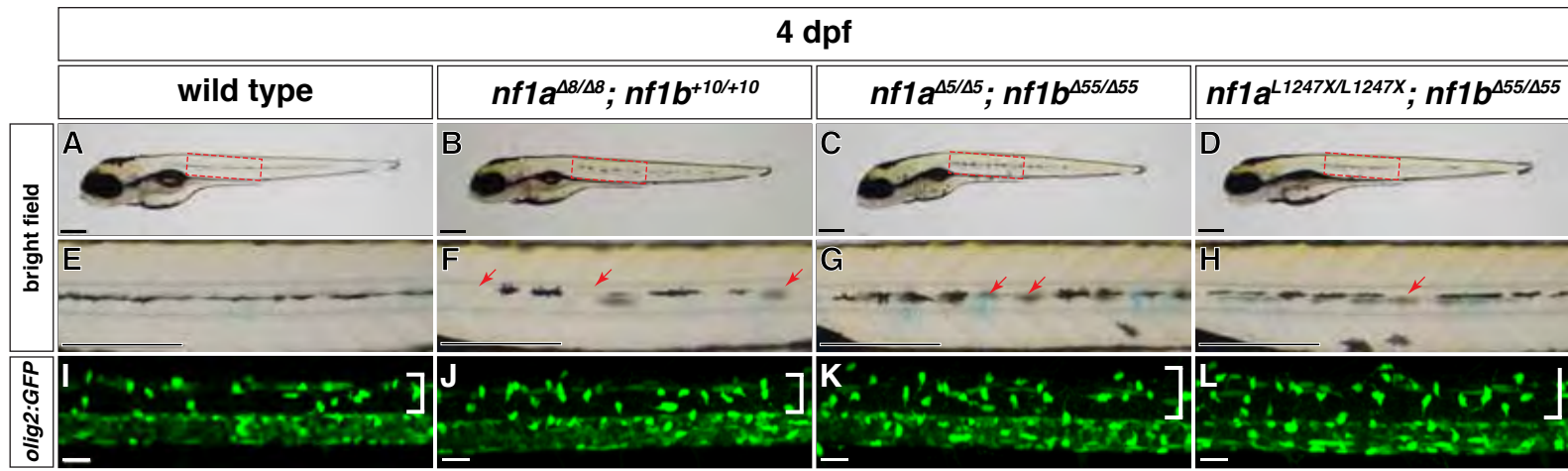


Fig. S2. *nf1*-null mutants with different allelic combinations of *nf1a* and *nf1b* are phenotypically identical.

(A-H) Lateral view of wild type (A,E,I), *nf1a*^{Δ8/Δ8}; *nf1b*^{+10/+10} (B,F,J), *nf1a*^{Δ5/Δ5}; *nf1b*^{Δ55/Δ55} (C,G,K), and *nf1a*^{L1247X/L1247X}; *nf1b*^{+10/+10} larvae (D,F,L) at 4 dpf. (E-H) Magnified views of the boxed region in A-D demonstrating absence of melanophores along the lateral line (arrows) in different allelic combinations of *nf1a*; *nf1b* double homozygous mutant alleles. Scale bars: 300 μm. (I-L) Confocal images of spinal cords in Tg(*olig2:GFP*) larvae harboring different allelic combinations of *nf1a*; *nf1b* homozygous mutant alleles at 4 dpf. OPC hyperplasia (brackets) is observed in all three allelic combinations of *nf1a*; *nf1b* double homozygous mutant alleles. Scale bars: 300 μm.

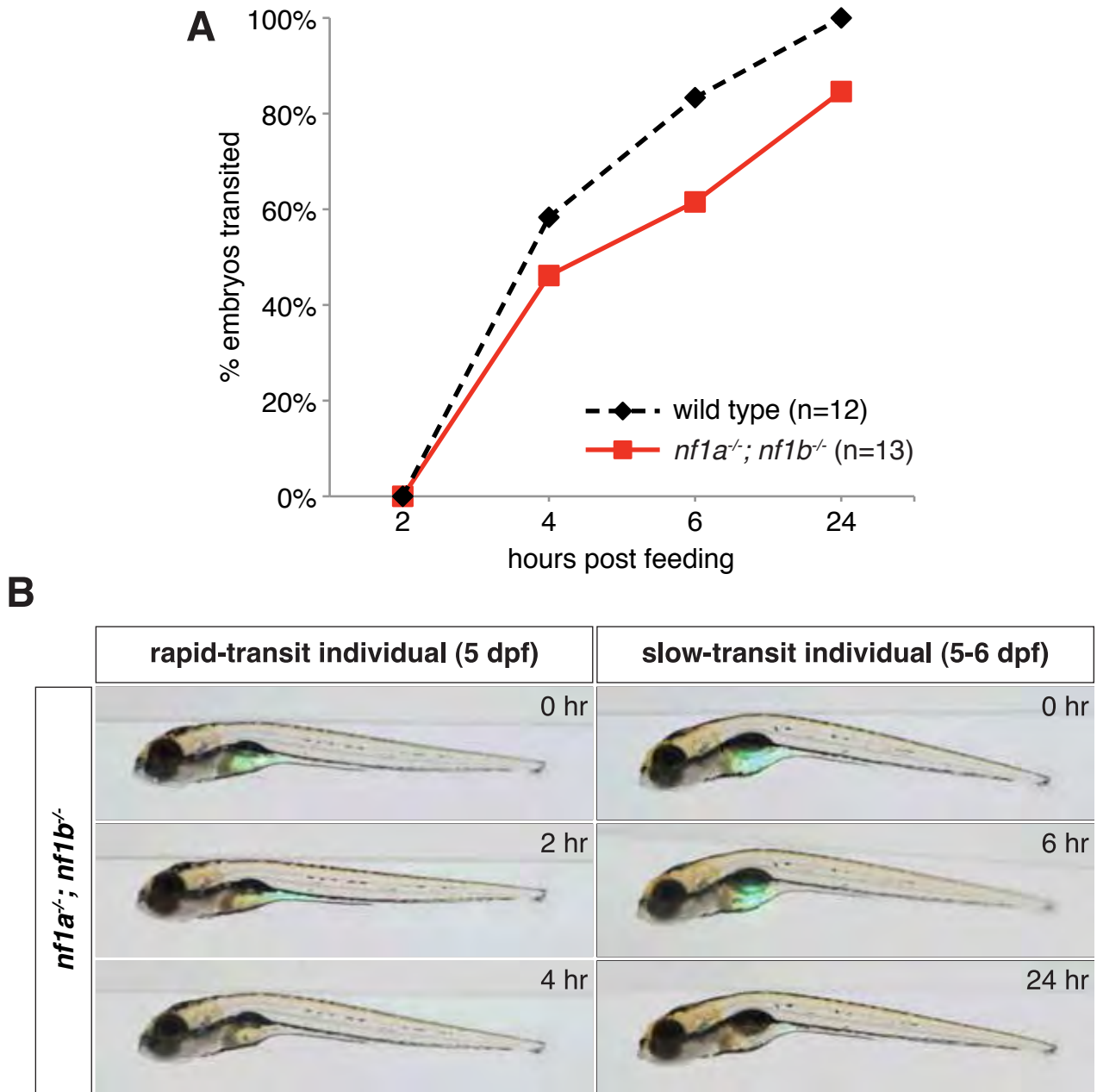


Fig. S3. Loss of *nf1a* and *nf1b* does not affect food consumption or transit.

(A) Graph depicting intestinal transit time for 5 dpf wild type (black line) and *nf1a*^{-/-}; *nf1b*^{-/-} (red line) larvae following a 1 hour feeding of paramecia and fluorescent microspheres. Transit was considered to be complete when fluorescent microspheres were no longer detected along the intestinal tract by fluorescent microscopy. (B) Representative overlays of bright field and fluorescent images from 5-6 dpf *nf1a*^{-/-}; *nf1b*^{-/-} larvae exhibiting rapid- or slow-transit.

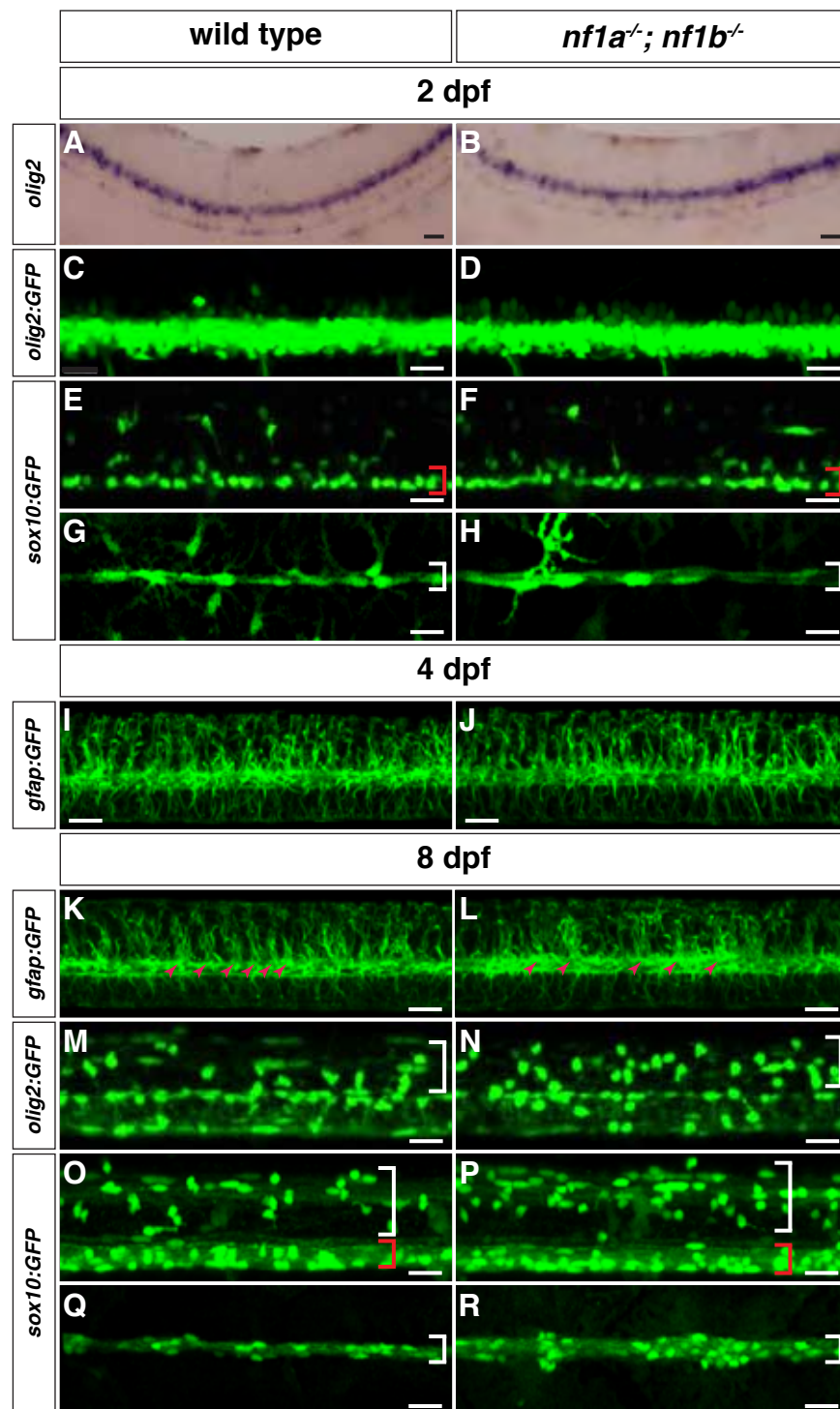


Fig. S4. Analysis of *nf1a/nf1b* mutant OPCs and Schwann cells at 2 dpf and radial glia at 4 dpf appear normal with defects appreciated in all three populations at 8 dpf.

(A,B) Whole-mount in situ hybridization for expression of endogenous *olig2* in wild type (A) and *nf1a*^{-/-}; *nf1b*^{-/-} (B) larvae at 2 dpf. Scale bars: 20 μ m. (C,D) Spinal cord of wild type; Tg(*olig2:GFP*) (C) and *nf1a*^{-/-}; *nf1b*^{-/-}; Tg(*olig2:GFP*) (D) larvae at 2 dpf. Scale bars: 20 μ m. (E,F) Spinal cord of wild type; Tg(*sox10:GFP*) (E) and *nf1a*^{-/-}; *nf1b*^{-/-}; Tg(*sox10:GFP*) (F) larvae at 2 dpf. Brackets indicate ventrally positioned *sox10:GFP*-positive OPCs. Scale bars: 20 μ m. (G,H) PLLn of wild type; Tg(*sox10:GFP*) (G) and *nf1a*^{-/-}; *nf1b*^{-/-}; Tg(*sox10:GFP*) (H) larvae at 2 dpf. Brackets indicate *sox10:GFP*-positive Schwann cells associated with the PLLn. Scale bars: 20 μ m. (I,J) Spinal cord of wild type; Tg(*gfap:GFP*) (I) and *nf1a*^{-/-}; *nf1b*^{-/-}; Tg(*gfap:GFP*) (J) larvae at 4 dpf. Scale bars: 20 μ m. (K,L) Spinal cord of wild type; Tg(*gfap:GFP*) (K) and *nf1a*^{-/-}; *nf1b*^{-/-}; Tg(*gfap:GFP*) (L) larvae at 8 dpf. Arrowheads depict the normal segmental expression of GFP in wild type larvae (K) that is absent in *nf1a*^{-/-}; *nf1b*^{-/-} larvae (L). Scale bars: 20 μ m. (M,N) Spinal cord of wild type; Tg(*olig2:GFP*) (M) and *nf1a*^{-/-}; *nf1b*^{-/-}; Tg(*olig2:GFP*) (N) larvae at 8 dpf. Brackets indicate dorsally positioned *olig2:GFP*-positive OPCs. Scale bars: 20 μ m. (O,P) Spinal cord of wild type; Tg(*sox10:GFP*) (O) and *nf1a*^{-/-}; *nf1b*^{-/-}; Tg(*sox10:GFP*) (P) larvae at 8 dpf. White and red brackets indicate dorsally and ventrally positioned *sox10:GFP*-positive OPCs, respectively. Scale bars: 20 μ m. (Q,R) PLLn of wild type; Tg(*sox10:GFP*) (Q) and *nf1a*^{-/-}; *nf1b*^{-/-}; Tg(*sox10:GFP*) (R) larvae at 8 dpf. Brackets indicate *sox10:GFP*-positive Schwann cells associated with the PLLn. Scale bars: 20 μ m.

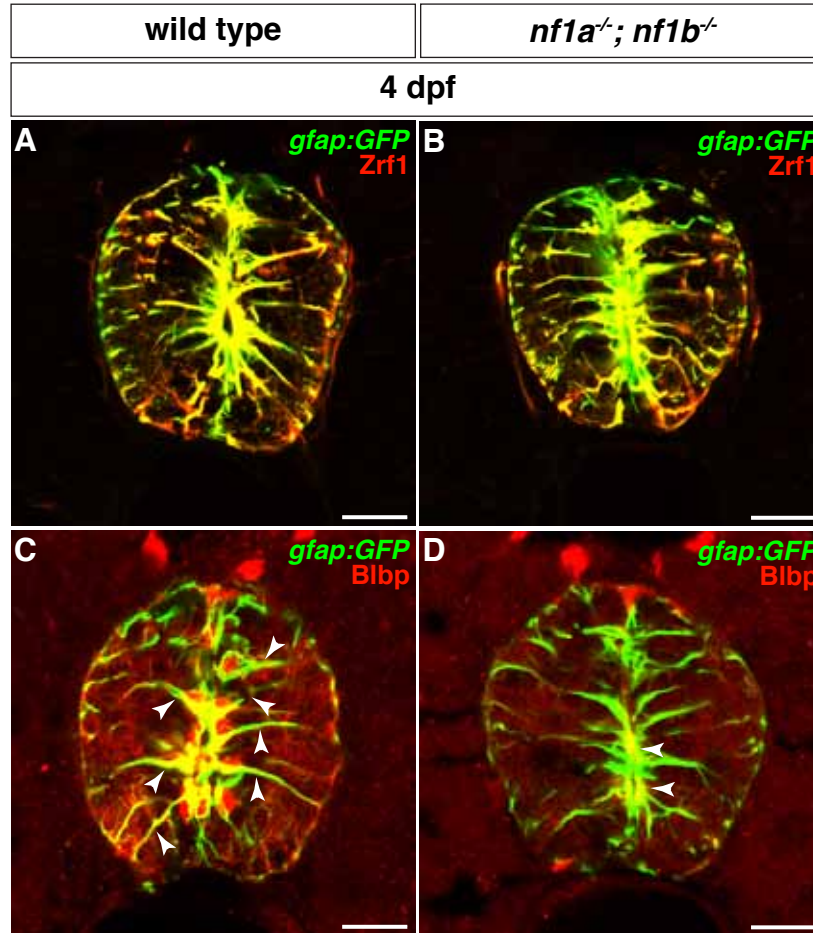


Fig. S5. Radial glia of *nf1a*^{-/-}; *nf1b*^{-/-} larvae express reduced amounts of brain lipid binding protein (Blbp). (A,B) Radial glia in transverse sections through the spinal cord of wild type; Tg(*gfap:GFP*) (A) and *nf1a*^{-/-}; *nf1b*^{-/-}; Tg(*gfap:GFP*) (B) larvae at 4 dpf are marked by expression of the *gfap:GFP* transgene (green) and the Zrf1 antibody (red). (C,D) Radial glia (green) in transverse sections through the spinal cord of *nf1a*^{-/-}; *nf1b*^{-/-}; Tg(*gfap:GFP*) larvae (D) demonstrate decreased Blbp expression (red), as identified by colocalization (yellow, arrowheads), when compared with wild type; Tg(*gfap:GFP*) larvae (C) at 4 dpf. Scale bars: 20 μ m.

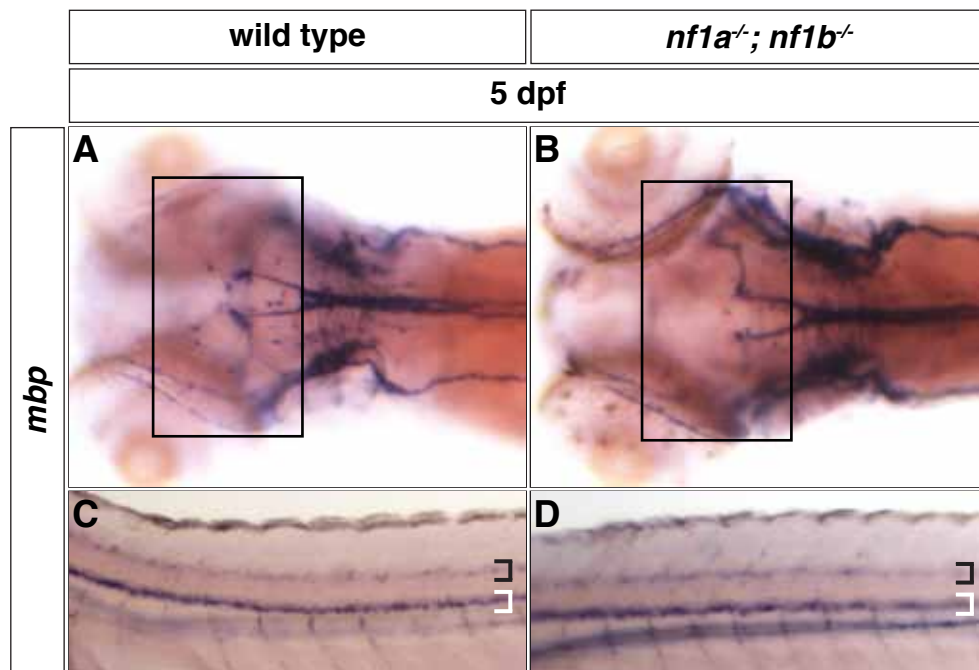


Fig. S6. Expression of *mbp* in the brain and spinal cord of *nf1a*^{-/-}; *nf1b*^{-/-} larvae appears normal.

(A,B) No difference in *mbp* expression is appreciated in the midbrain and hindbrain regions (A,B, boxes) as well as along the dorsal (black brackets) and ventral (white brackets) spinal cord of *nf1a*^{-/-}; *nf1b*^{-/-} larvae (B,D) when compared to wild type larvae (A,C) by whole mount in situ hybridization at 5 dpf.

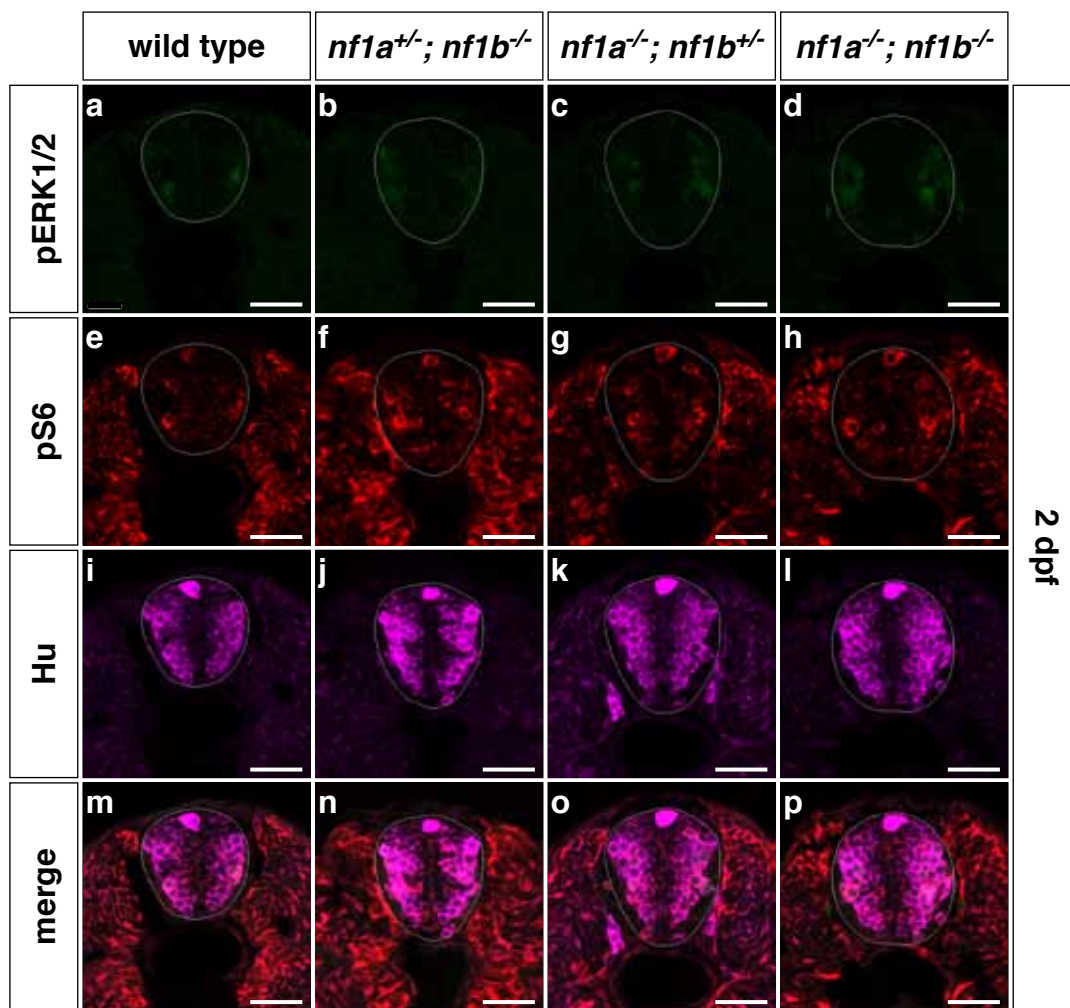
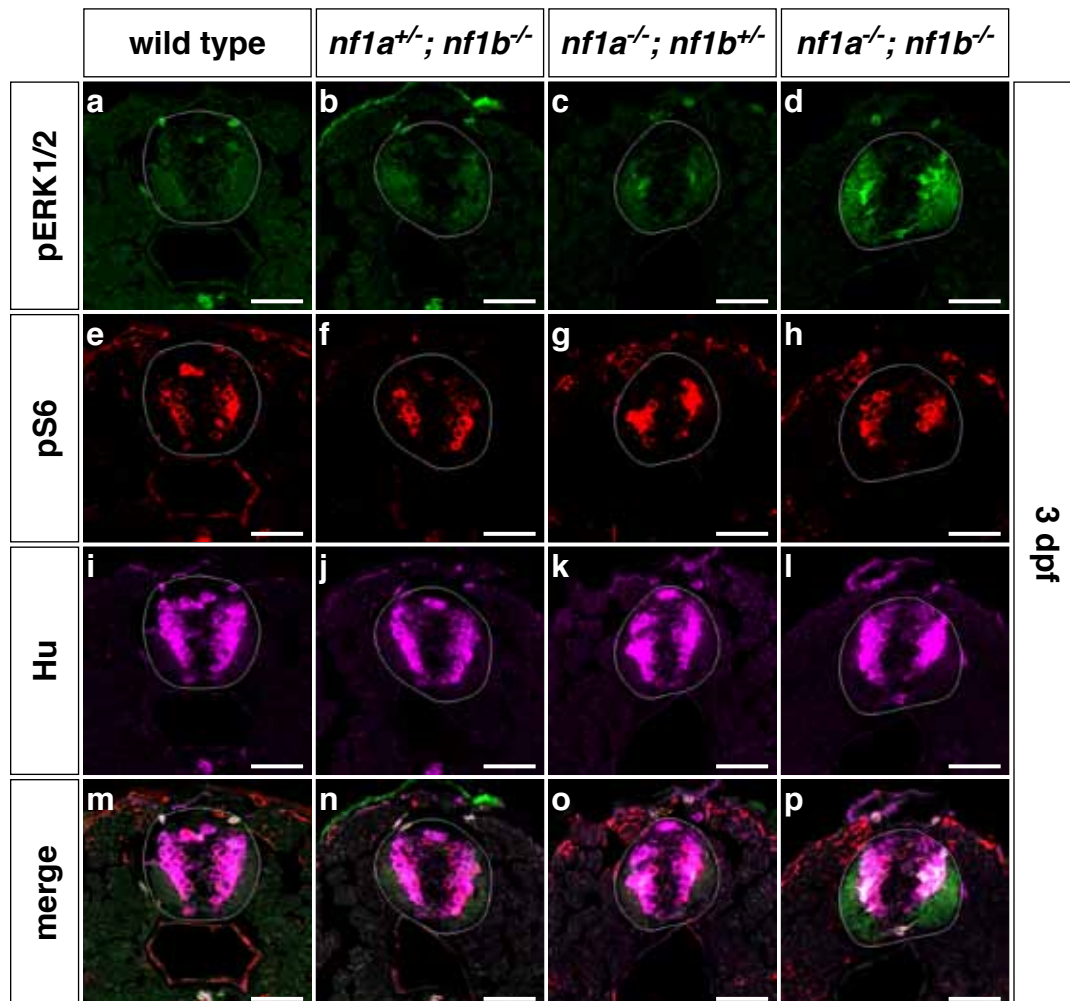
A**B**

Fig. S7. Increased ERK1/2 phosphorylation is appreciated in the spinal cords of *nf1a^{-/-}; nf1b^{-/-}* larvae by 3 dpf. Immunohistochemical analysis of transverse sections through the spinal cord of 2 dpf *nf1a^{-/-}; nf1b^{-/-}* larvae (Ad,Ah,AI,Ap) demonstrates no appreciable differences in pERK1/2 (green) or pS6 staining (red) when compared with *nf1a^{+/-}; nf1b^{-/-}* (Ab,Af,Aj,An), *nf1a^{-/-}; nf1b^{+/-}* (Ac,Ag,Ak,Ao), or wild type (Aa,Ae,Ai,Am) larvae. At 3 dpf, however, increased pERK1/2 signal is noted in *nf1a^{-/-}; nf1b^{-/-}* larvae (Bd,Bp) when compared with *nf1a^{+/-}; nf1b^{-/-}* (Bb,Bn), *nf1a^{-/-}; nf1b^{+/-}* (Bc,Bo), or wild type (Ba,Bm) larvae, with no differences noted in levels of pS6 (Be-Bh). Activated ERK1/2 signaling is most prominent in spinal cord neurons, as identified by colocalization (white) with HuC/D expression (magenta) (Bl,Bp). Scale bars: 20 μ m.

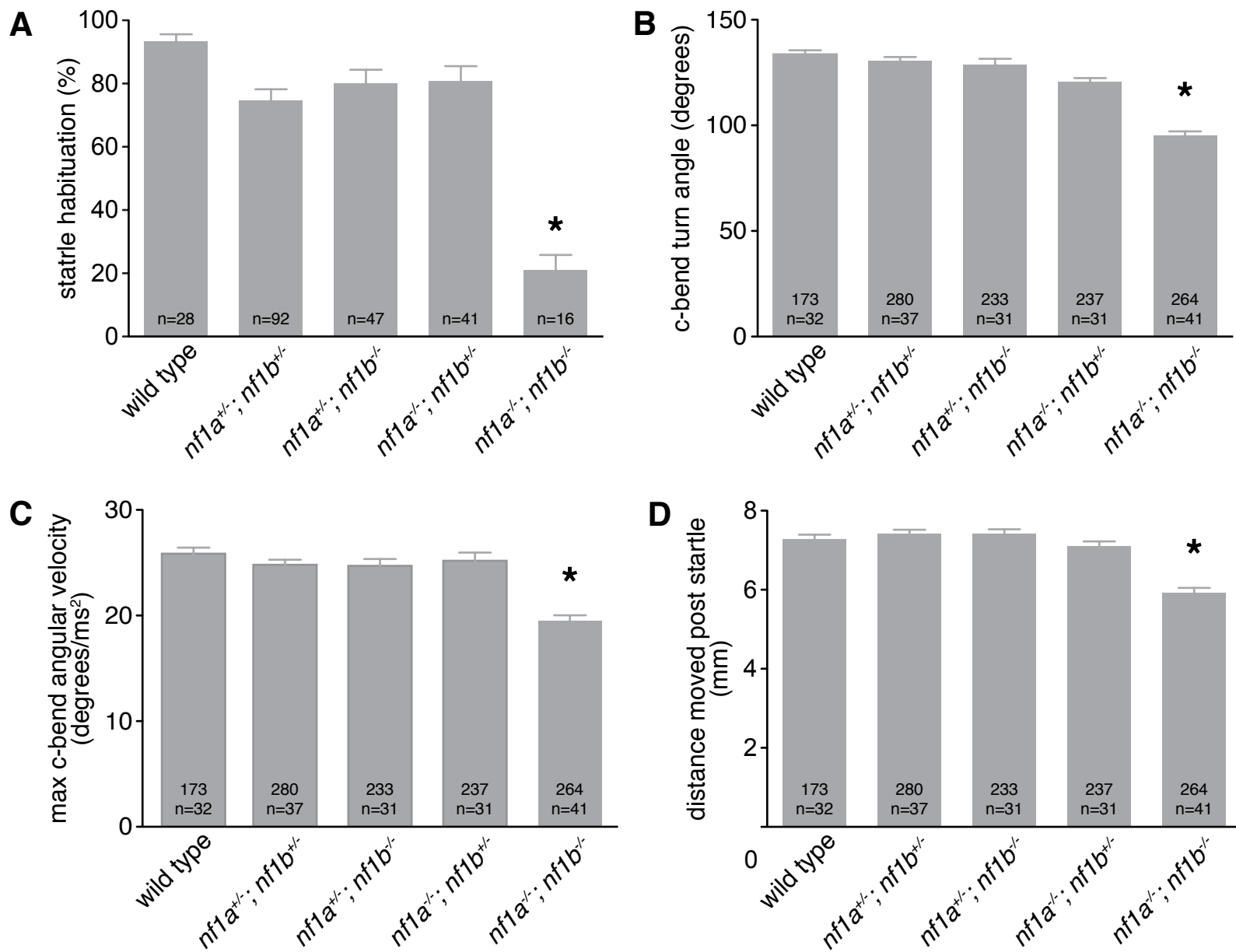


Fig. S8. *nf1a/nf1b* mutants exhibit acoustic startle C-start behavioral deficits.

(A) Mean degree of short-term SLC habituation is reduced in 5 dpf *nf1a^{-/-}; nf1b^{-/-}* larvae. (B-C) Measurement of mean head turning angle (B) and mean maximum angular velocity (C) of initial C-bend following delivery of acoustic stimulus demonstrates a significant reduction of both behavioral measures in 5 dpf *nf1a^{-/-}; nf1b^{-/-}* larvae. (D) Mean distance traveled over 90 milliseconds following delivery of acoustic stimulus, as a result of short latency C-start behavioral response, is also significantly reduced in 5 dpf *nf1a^{-/-}; nf1b^{-/-}* larvae. The total number of short latency C-bends and number of larvae tested per genotype appear at the base of each bar graph (* $P < 0.001$).

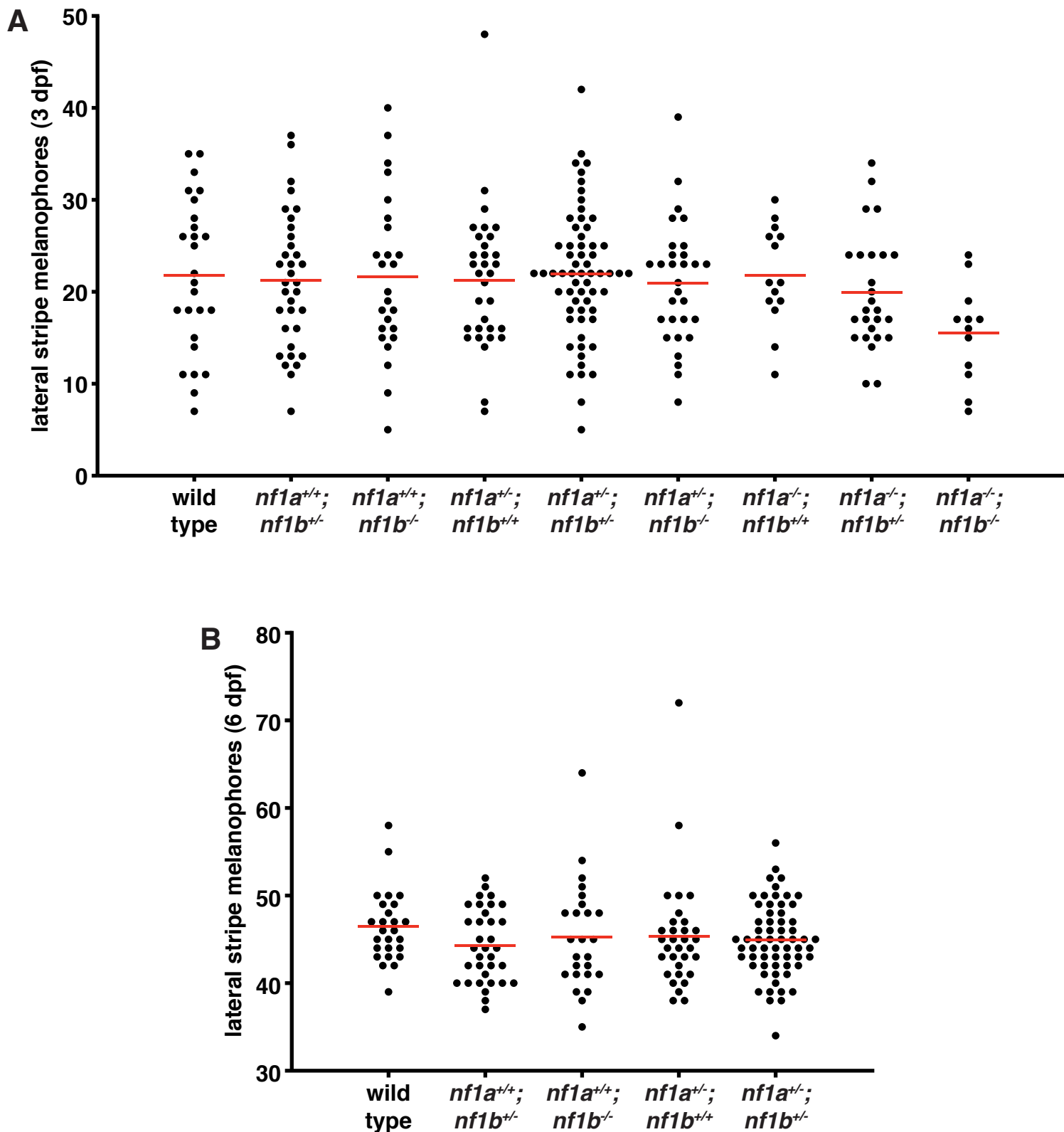


Fig. S9. Quantification of lateral stripe melanophores in wild type and *nf1a/nf1b* mutant larvae at 3 and 6 dpf. (A) Quantification of lateral stripe melanophores from wild type ($n=26$), $nf1a^{+/+}; nf1b^{+/-}$ ($n=34$), $nf1a^{+/+}; nf1b^{-/-}$ ($n=25$), $nf1a^{+/-}; nf1b^{+/-}$ ($n=32$), $nf1a^{+/-}; nf1b^{-/-}$ ($n=62$), $nf1a^{-/-}; nf1b^{+/-}$ ($n=30$), $nf1a^{-/-}; nf1b^{+/-}$ ($n=14$), $nf1a^{-/-}; nf1b^{+/-}$ ($n=26$), and $nf1a^{-/-}; nf1b^{-/-}$ ($n=12$) larvae at 3 dpf. Each point represents the number of lateral stripe melanophores in an individual embryo and red lines indicate mean values. (B) Quantification of lateral stripe melanophores from wild type ($n=26$; same as displayed in Fig. 8), $nf1a^{+/+}; nf1b^{+/-}$ ($n=34$), $nf1a^{+/+}; nf1b^{-/-}$ ($n=25$), $nf1a^{+/-}; nf1b^{+/-}$ ($n=32$), and $nf1a^{+/-}; nf1b^{-/-}$ ($n=62$) larvae at 6 dpf. Each point represents the number of lateral stripe melanophores in an individual embryo and red lines indicate mean values.

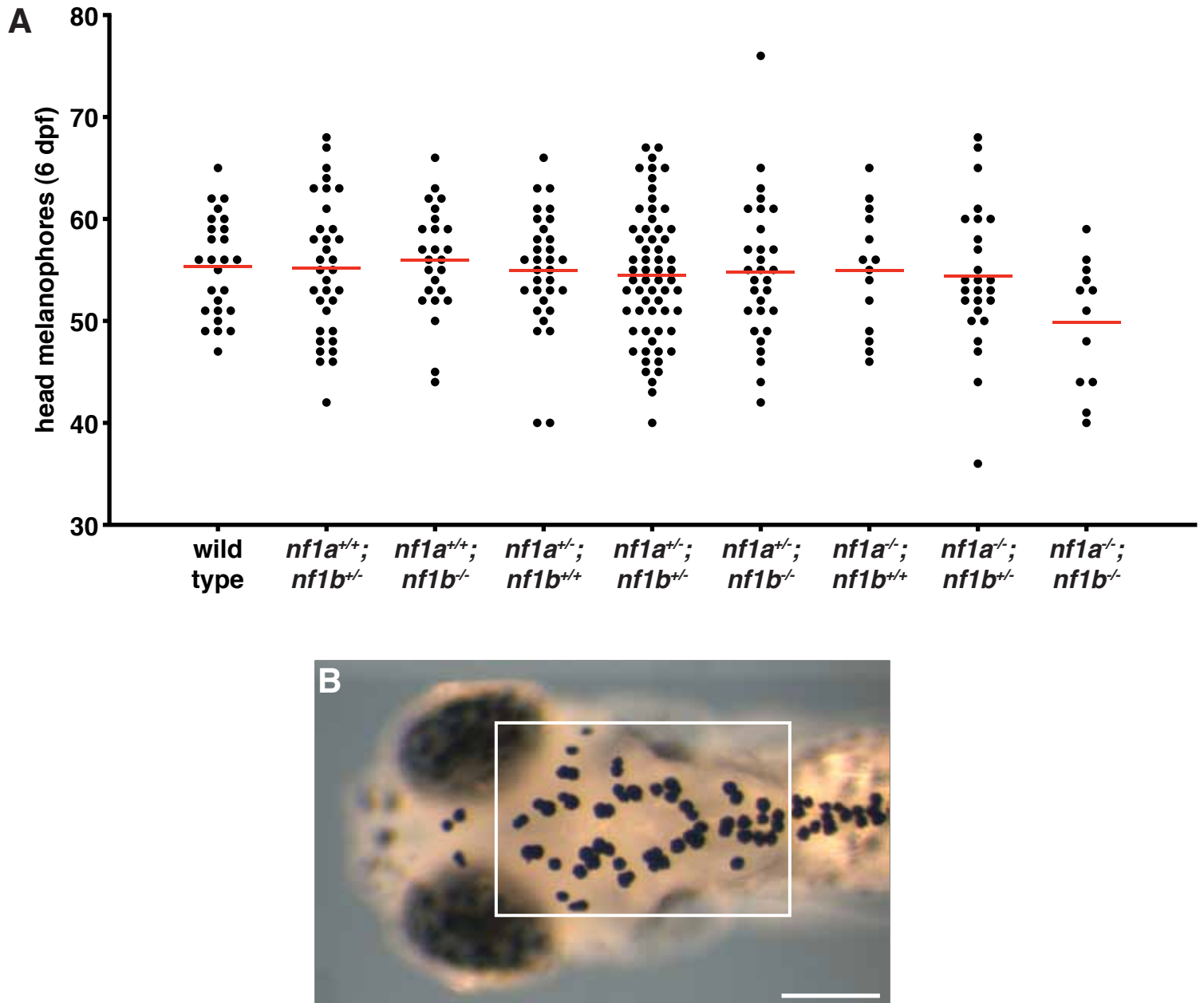


Fig. S10. Quantification of head melanophores in wild type and *nf1a/nf1b* mutant larvae at 6 dpf.

(A) Quantification of head melanophores from wild type ($n=26$), *nf1a*^{+/+}; *nf1b*^{+/-} ($n=34$), *nf1a*^{+/+}; *nf1b*^{-/-} ($n=25$), *nf1a*^{+/-}; *nf1b*^{+/+} ($n=32$), *nf1a*^{+/-}; *nf1b*^{+/-} ($n=62$), *nf1a*^{+/-}; *nf1b*^{-/-} ($n=30$), *nf1a*^{-/-}; *nf1b*^{+/+} ($n=14$), *nf1a*^{-/-}; *nf1b*^{+/-} ($n=26$), and *nf1a*^{-/-}; *nf1b*^{-/-} ($n=12$) larvae at 6 dpf. Each point represents the number of head melanophores in an individual embryo and red lines indicate mean values. (B) Representative image depicting head melanophores (boxed region) in a wild type larva at 6 dpf following epinephrine treatment and fixation. Scale bar: 200 μ m.